Quantifying short-range correlations in nuclei

Maarten Vanhalst

Promotor: Prof. Dr. Jan Ryckebusch

Proefschrift ingediend tot het behalen van de academische graad van
Doctor in de Wetenschappen: Fysica

Universiteit Gent
Faculteit Wetenschappen
Vakgroep Fysica en Sterrenkunde
Academiejaar 2013-2014

Dankwoord

Een doctoraatsthesis maak je niet alleen.

Jan,
bedankt voor de kans om bij u te kunnen doctoreren. Bedankt voor je vertrouwen, advies, sturing en geduld. Het was een verrijking en niet enkel op fysicavlak.

De vele collega's en ex-collega's,
Natalie, Pieter, Lesley, Tom, Marco, Tom, Kris, Jonas, Kris, Bart, Simon, Benjamin, Vishvas, Camille, Wim, Joe, Piet, ... Bedankt voor de uitleg, discussies, praatjes, middagpauzes, koffiepauzes en ontspanningen.

Mama en papa,
bedankt voor alle onvoorwaardelijke steun.

Kirsten,
bedankt om al die jaren jezelf te zijn. Bedankt voor je liefde en steun.

Contents

CHAPTER 1

Short-range correlations in nuclei

1.1 The nuclear many-body problem

In this thesis, the nucleus is considered as a non-relativistic A-body quantum-mechanical system. Its quantum states are described by the A-body wave functions Ψ_A^n, which are a solution to the Schrödinger equation

$$\hat{H}(\vec{x}_1, \vec{x}_2, \ldots, \vec{x}_A)\Psi_A^n(\vec{x}_1, \vec{x}_2, \ldots, \vec{x}_A) = E_n\Psi_A^n(\vec{x}_1, \vec{x}_2, \ldots, \vec{x}_A), \tag{1.1}$$

with a Hamiltonian of the type

$$\begin{aligned}\hat{H}(\vec{x}_1, \vec{x}_2, \ldots, \vec{x}_A) = &- \frac{\hbar^2}{2M_N}\sum_i^A \nabla_i^2 + \sum_{i<j}\hat{v}_2(\vec{x}_i, \vec{x}_j) \\ &+ \sum_{i<j<k=1}^A \hat{v}_3(\vec{x}_i, \vec{x}_j, \vec{x}_k) + \ldots .\end{aligned} \tag{1.2}$$

Here, $\vec{x} \equiv (\vec{r}, \vec{\sigma}, \vec{\tau}\,)$ is the shorthand notation for the combination of spatial, spin and isospin coordinates. The operator $\hat{v}_i$ stands for the i-body potential.

Solving the A-body Schrödinger equation for realistic nucleon-nucleon (NN) potentials is one of the major goals in present-day nuclear physics. It remains a challenging task to understand how nuclear structure and the observed symmetries come along from the underlying interaction between nucleons. A first major challenge is to determine a suitable form for the realistic NN potential.

A large amount of NN scattering data have been accumulated over the last decades [1, 2]. However, the NN potential is no direct observable and the NN scattering data is not enough to uniquely define the NN potential. First, at short distances, where the scattering nucleons

overlap strongly, there is no unique way to parametrize this complex many-body quantum problem. Second, when scattering off deuterium, the two nucleons are in an energy eigenstate with a well-defined relation between momentum or kinetic energy, potential energy, and total energy, usually labeled with on-shell. However, when going from the two-nucleon scattering state to the many-body case, another uncertainty arises. In the many-body case, a nucleon pair interacts with the surrounding other nucleons and has neither sharp energy nor is its relative momentum related to its energy. In this situation, the so-called off-shell behavior of the nuclear interaction is important but also not fully constrained by scattering data.

Consequently, several research groups have derived different effective NN potentials from these data sets. In general, research on the nuclear force has proceeded along three lines: the phenomenological approaches [3, 4], the boson exchange models [5–7] and the chiral effective field theory [8, 9]. The derived two-body interactions have a complex structure, but their most important features are the attraction at large distances, the strong repulsion at short distances and the tensor interaction at medium range.

The long-range part of the nuclear potential is fairly well established and agreement has been reached on the nature of the long-range part of the potential which is entirely due to one-pion exchange. All realistic NN interactions also possess a strong tensor force. It operates only in the $S = 1$ channels and induces there a strong correlation between the spatial orientation of the nucleons and the orientation of their spins. Among other things, the tensor force is responsible for the D-wave component of the deuteron wave function. The repulsive core at short distances suppresses the probability of finding two nucleons close to each other. The repulsive core is the most unknown part of the nuclear force but we know it prevent the nucleus from collapsing and is hence responsible for the stability of the atomic nuclei. The strong repulsive core and the tensor interaction induce short-range correlations in the nuclear many-body system, which complicate the theoretical description so much that exact solutions of the many-body Schrödinger equation can only be obtained for the lightest nuclei.

The NN phenomenology alone cannot reproduce the binding energies of nuclei containing three nucleons or more. This indicates that three-nucleon (3N) forces may play some significant role and should be included in the description [10, 11]. However, 3N forces are difficult to investigate [12] because they are expected to be weak in comparison with NN forces.

Summarized, several issues make the nuclear many-body problem very difficult to solve exactly: the rather complex structure of the complete two-body potential, the high number of particles involved and the lack of knowledge about higher-body potentials.

In the late 1940s, Maria Goeppert Mayer and J. Hans D. Jensen, who shared the 1963 Nobel Prize for Physics for their work, introduced independently the shell structure in nuclei [13–15]. The simplest model reproducing the nuclear shell structure is the independent particle model (IPM), in which each nucleon moves independently in a potential well created by the other nucleons. The IPM is based on the assumption that the mean free path for a nucleon is large compared to the size of the nucleon. The nuclear force acting on the nucleons is subsequently replaced by an average or mean-field potential and the motion of each nucleon is governed by this average attractive force which extends over ranges of the size of the nucleus. Essentially this amounts to approximating the nuclear A-body problem

by a sum of A single-body problems.

The mean-field potential can either be postulated based on empirical data, or can be derived from a variational principle based on a realistic two-body NN interaction which does not possess a hard core, i.e. the self-consistent or Hartree-Fock (HF) method. Examples of empirical scalar mean-field potentials are the harmonic oscillator (HO) potential and the Woods-Saxon (WS) potential. They can be extended with extra potentials like the spin-orbit coupling. The HF method with an effective interaction occupies an intermediate position between the microscopic methods and the various versions of IPM with phenomenological potentials.

Due to saturation, the central density of the nucleus is similar for all nuclei. The established value for the central density is 0.17 nucleons/fm^3. The average density is smaller, approximately 0.13 nucleons/fm^3. With this central density, the average internucleon distance is about 1.8 fm. The repulsive hard core of the NN interactions suggests a nucleon radius of at least 0.5 fm. Recent reanalysis of the electron scattering data resulted in a root-mean-square (rms) charge radius for the proton $r_p^c = \sqrt{\langle r_p^2 \rangle} = 0.897(18)$ fm [16]. From the above, it is clear that one expects that the nucleus is more like a saturated quantum liquid than a gas of freely moving nucleons with a large mean free path.

Despite these restrictions, the IPM provides an explanation of many nuclear properties: notably the extra stability of closed-shell nuclei, properties of nucleon binding energies, and spin and parity of many odd-mass nuclei. Figure 1.1 shows how IPM calculations using a Woods-Saxon potential, correspond well with the observed $(e, e'p)$ cross section obtained at the NIKHEF facility [17]. The $(e, e'p)$ reaction is a powerful method for probing single-nucleon properties of nuclei.

An IPM approach has two major drawbacks. First, any mean-field potential manifestly violates translational invariance [18, 19]. A wave function describing a real nucleus should be an eigenfunction of the total momentum operator, describing the center-of-mass motion of the nucleus as a plane wave. This is not the case for IPM wave functions. The position of the center-of-mass fluctuates about the origin of the coordinate system. These fluctuations are not present in real nuclei, and can influence the nucleon momentum distributions, especially for light nuclei. It should also be accounted for in the calculation of the kinetic energy and rms radii [20, 21].

A second drawback of IPM is that by treating the nucleons as moving independently from each other in an average potential, a lot of internucleon correlations (short, as well as long-range) are neglected.

In a many-body system, correlations between the constituents of a system are induced by the inter-particle forces. For a system with a one-body density $\rho^{[1]}(\vec{r})$, the two-body density $\rho^{[2]}(\vec{r}_1, \vec{r}_2)$ can be expressed as the conditional probability of finding a particle at $\vec{r}_1$ if there is one present at $\vec{r}_2$:

$$\rho^{[2]}(\vec{r}_1, \vec{r}_2) = \rho^{[1]}(\vec{r}_1)\rho^{[1]}(\vec{r}_2)g(|\vec{r}_1 - \vec{r}_2|), \tag{1.3}$$

with $g(r = |\vec{r}_1 - \vec{r}_2|)$ the correlation function. In absence of the correlations, $g(r) = 1$ and all particles move independently of each other. For an atomic ^{4}He liquid, the correlation function was measured with neutron [22] and X-ray [23] scattering and is shown in Figure 1.2. The correlations are a consequence of the hard repulsive core of the interatomic potential

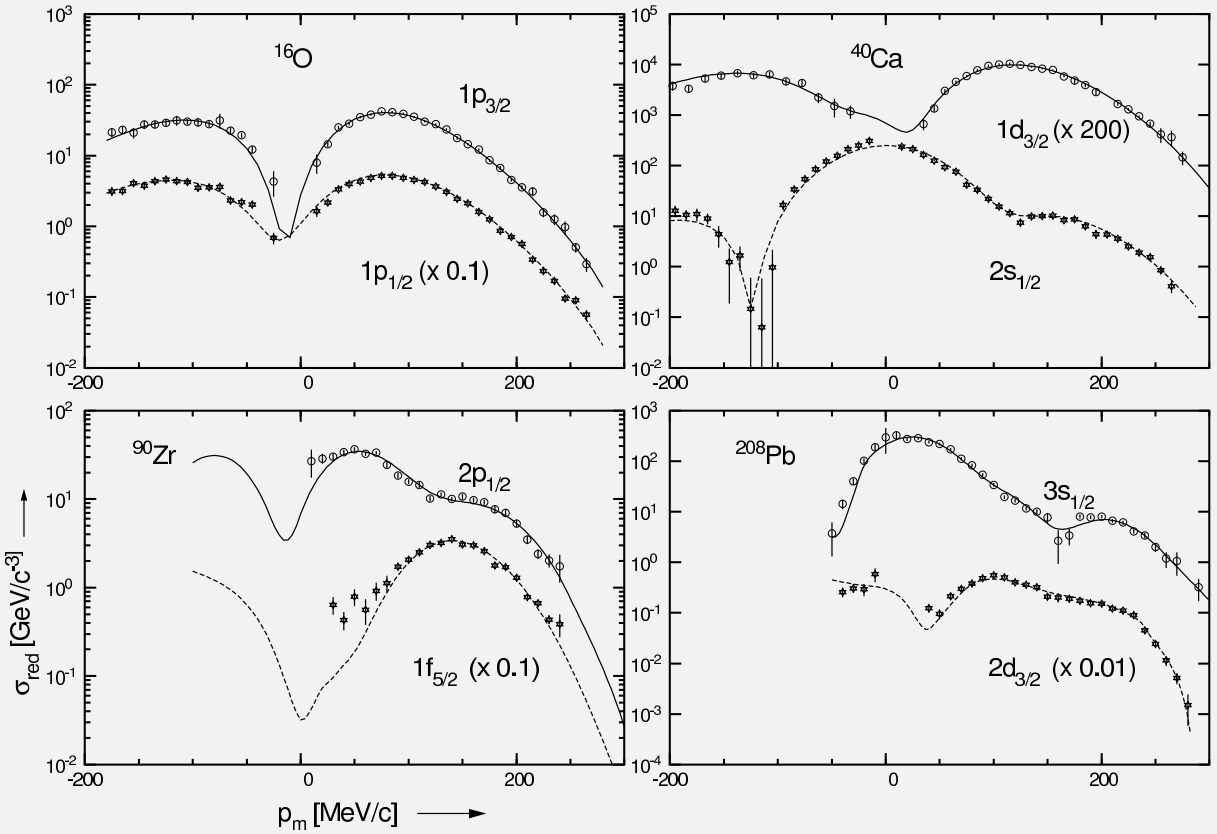

Figure 1.1 – Experimental momentum distributions in function of the missing momentum p_m for transitions in the reaction $(e, e'p)$ on ^{16}O, ^{40}Ca, ^{90}Zr and ^{208}Pb, involving knockout from the valence shell (upper data) and the next lower shell (lower data). The curves represent Complete Distorted Wave Impulse Approximation (CDWIA) calculations with the Woods-Saxon bound-state wave function of which normalization and rms radius were fitted to the data [17]. The CDWIA contains a model for final-state interactions (FSI) of the ejected proton. Missing momentum p_m is defined as in Figure 1.5a.

$v(r)$ which is also shown in Figure 1.2. The hard core reflects itself in $g(r)$ becoming zero for small internucleon separations. For larger distances $g(r)$ rises and then oscillates before reaching the asymptotic value of 1. The correlations connected with $g(r) \neq 1$ increase the high-momentum components in the momentum distribution of the atoms in the liquid.

Over the years, a lot of experimental evidence has been accumulated which advocates the importance of these correlations in the atomic nucleus. While the shape of the calculated nucleon momentum distributions in Figure 1.1 agrees with the data, there is a significant deviation between the calculated and observed occupation (or normalization) of the valence shell. Figure 1.3 shows the occupation probability, or spectroscopic strength, of the valence shells. The observed strength is 30 to 40% smaller than the naive mean-field result. A reduction of the spectroscopic strength is not limited to valence nucleons only, but is also observed in more deeply bound nucleons [25]. From the beginning it was assumed that this lower occupancy is caused by nucleon correlations within the nucleus.

The nuclear correlations are generally classified into two categories: the long-range correlations (LRC) and the short-range correlations (SRC). The LRC induce correlations between nucleon

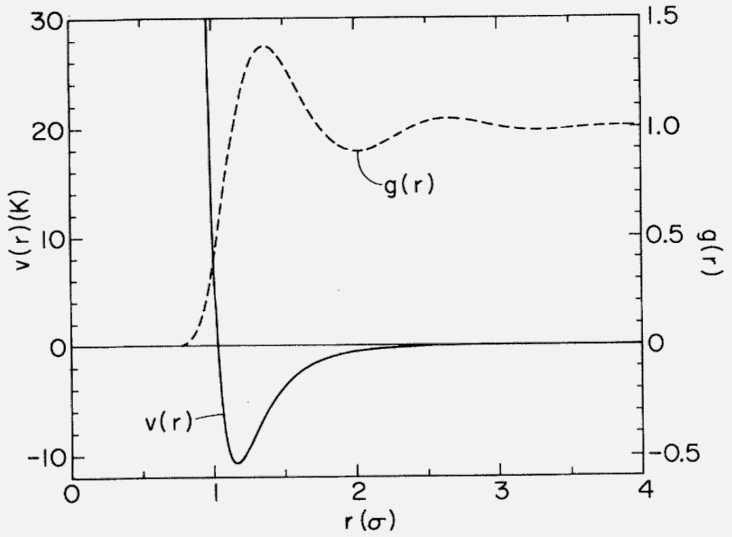

Figure 1.2 – The radial dependence of the inter-atomic potential $v(r)$ and correlation function $g(r)$ for an atomic ^{4}He liquid. The σ is a measure for the diameter of ^{4}He. Figure taken from Ref. [24].

at distances of several femtometers and are connected with the long-range attractive part of the NN interaction. They can account for 10 to 20% of the missing strength in the valence shells [25–27]. This loss of strength is redistributed around the Fermi energy. The correction to the mean-field model related to LRC can be physically captured by coupling the single-particle degrees-of-freedom to low-lying collective surface modes and higher-lying giant resonances. The SRC, which account for the remainder of the missing strength, are due to the repulsive core and tensor component of the NN interaction at short distances. The short-range part of the NN interaction leads to strong local fluctuations and can excite nucleons from the low-lying shells to higher energies and momenta, where neither the mean-field picture nor models including LRC predict substantial strength. The SRC deplete all single-particle levels and have a significant impact on the nuclear structure. These days it is common practice to implement a model for the effect of SRC in nuclear computations. Examples include the calculations of matrix elements for double-β decay [28], and of hadron transparencies in nuclei [29]. Most often, only central correlations are accounted for.

A first implication of SRC in nuclei is the presence of high-momentum and high-energy components in the nuclear wave functions. At lower nucleon momenta, the distribution in Figure 1.4a clearly shows the characteristics of a degenerate Fermi system (a gas of non-interacting Fermi particles at zero temperature) with a broad momentum distribution, falling off rapidly at momenta approaching the Fermi momentum, $k_F \approx 1.25$ fm^{-1}. For $k < k_F$, the IPM calculations and the calculations including SRC predict a momentum distribution which has comparable momentum dependence. However, the IPM calculation dramatically underestimates the strength at $k > k_F$, falling short by several orders of magnitude. The high-momentum tails in Figure 1.4b are similar for all nuclei, from deuterium to nuclear matter [31, 32]. The universality of the high-momentum tails can be understood as generated by the short-range part of the NN interaction.

Note that the SRC are often described as excitations of the nucleus where two nucleons

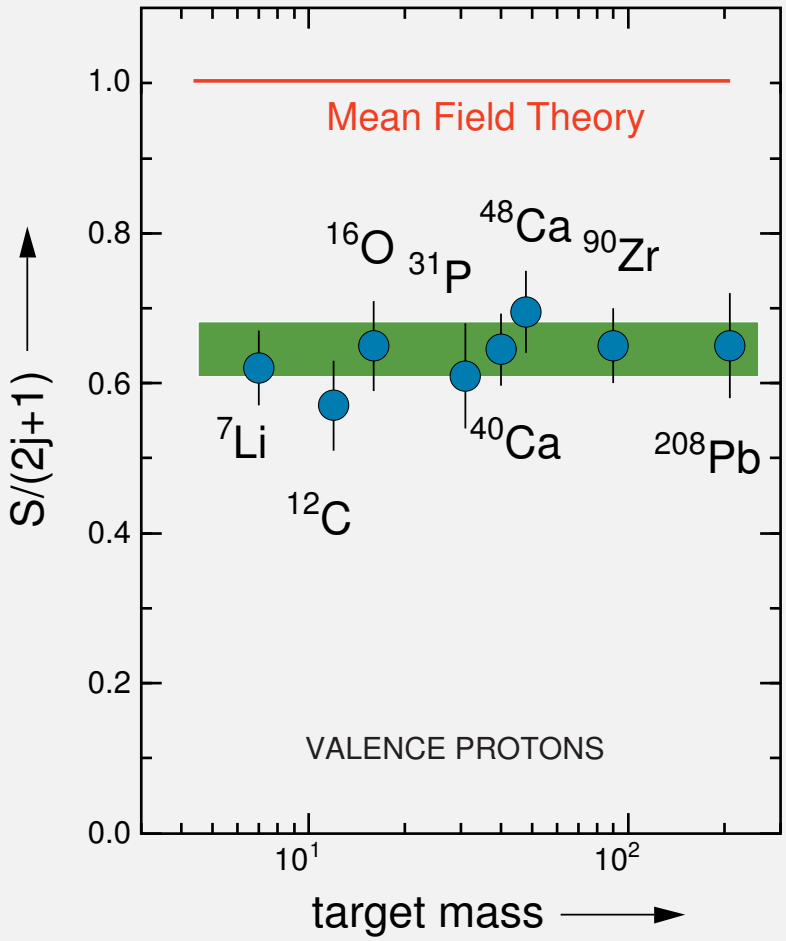

Figure 1.3 – Spectroscopic strength for the valence orbitals extracted from exclusive $A(e, e'p)$ reactions performed at NIKHEF as a function of the mass number of the target nucleus. Figure taken from Ref. [17].

undergo a hard interaction and both end up in a configuration with large momentum. These are excitations relative to a theoretical mean-field ground state of the nucleus and are not related to any real excited state of the nucleus; they are a contribution to the true nuclear ground state. One- and two-nucleon knock-out reactions have the potential to probe SRC. In the next sections, a brief overview of the experiments aimed at the observation of SRC is given. More detailed reviews on general issues related to SRC and more detailed surveys of recent experiments can be found in Refs. [33, 34].

1.2 Probing short-range correlations in nuclei

For decades, understanding the role played by SRC in nuclei has been a very elusive problem in nuclear physics due to the difficulties in isolating the signal of SRC. For intermediate-energy processes, the energy and momentum scales which characterize the measuring process and the structure of SRC are comparable. Consequently, the influence of the measuring process and the measured quantity are not separable.

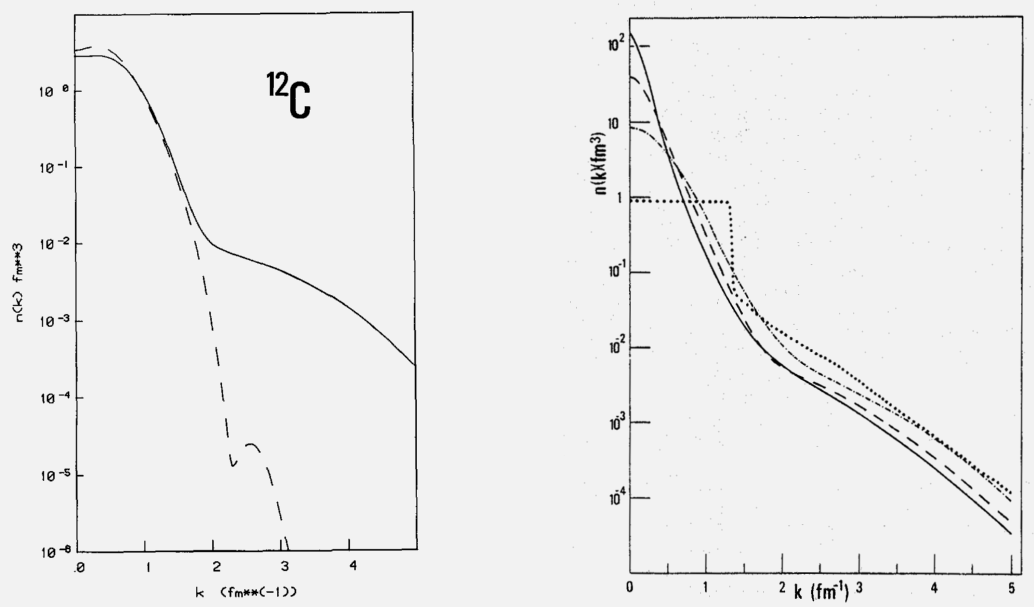

(a) **(b)**

Figure 1.4 – The momentum dependence of nucleon momentum distributions: (a) in ^{12}C. The full curve represents the results of the approach with SRC described in Ref. [30], whereas the dashed line has been obtained whithin the IPM using Woods-Saxon wave functions. Figure taken from Ref. [30]. (b) in few-body nuclei and in nuclear matter. The full line is the momentum distribution of the deuteron, the dashed line of ^{3}He, the dot-dashed line of ^{4}He and the dotted line is the nuclear matter momentum distribution. Figure taken from Ref. [31].

Figure 1.5 shows the diagrams of the quasi-elastic scattering off a correlated and uncorrelated nucleon and defines the variables used in this chapter. The removal of a nucleon which is involved in an SRC mechanism, can be treated as instantaneous (compared to nuclear motion within the SRC), if energy ω and momentum $\vec{q}$ transferred to one of the nucleons in the SRC significantly exceeds relevant energies and momenta in the SRC,

$$\omega \gg V_{NN}, \qquad |\vec{q}| \gg 2k_F. \tag{1.4}$$

Here, V_{NN} is a measure for the magnitude of the interaction potential between nucleons. The high-momentum probe will knock a nucleon out of the nucleus. The high relative momentum in the pair will also cause the correlated nucleon to be ejected.

Another challenge is the separation of the interactions with SRC nucleons from inelastic and/or quasi-elastic scattering with uncorrelated nucleons, and from competing reaction mechanisms such as meson exchange currents (MEC), delta isobar configurations (IC) and final-state interactions (FSI) [35, 36]. Though the complete elimination of MEC, IC and FSI is impossible, they are expected to be suppressed at high $Q^2 = q^2 - \omega^2$. The Bjorken scaling variable x_B can be used to separate the contribution from uncorrelated nucleons. It is defined as

$$x_B = \frac{Q^2}{2M_N\omega}, \tag{1.5}$$

where M_N is the nucleon mass. The value of x_B for quasi-elastic scattering from a stationary nucleus A ranges from 0 to M_A/M_N. Accordingly, the kinematic limit for scattering off a free

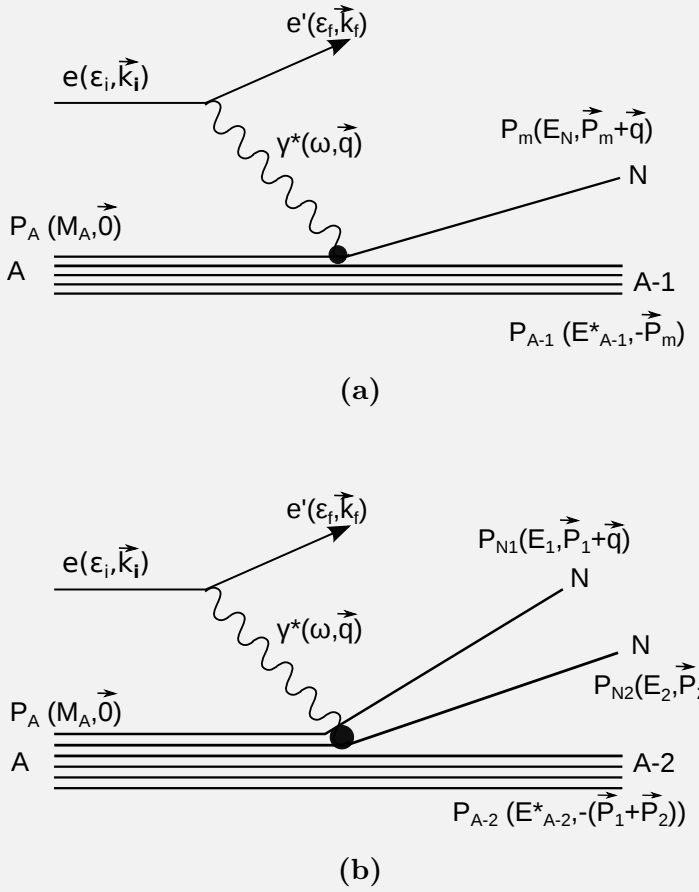

Figure 1.5 – Shown are the diagrams and variables of (a) quasi-elastic scattering off a uncorrelated nucleon with initial momentum $\vec{p}_m$. (b) quasi-elastic scattering off a nucleon involved in an SRC.

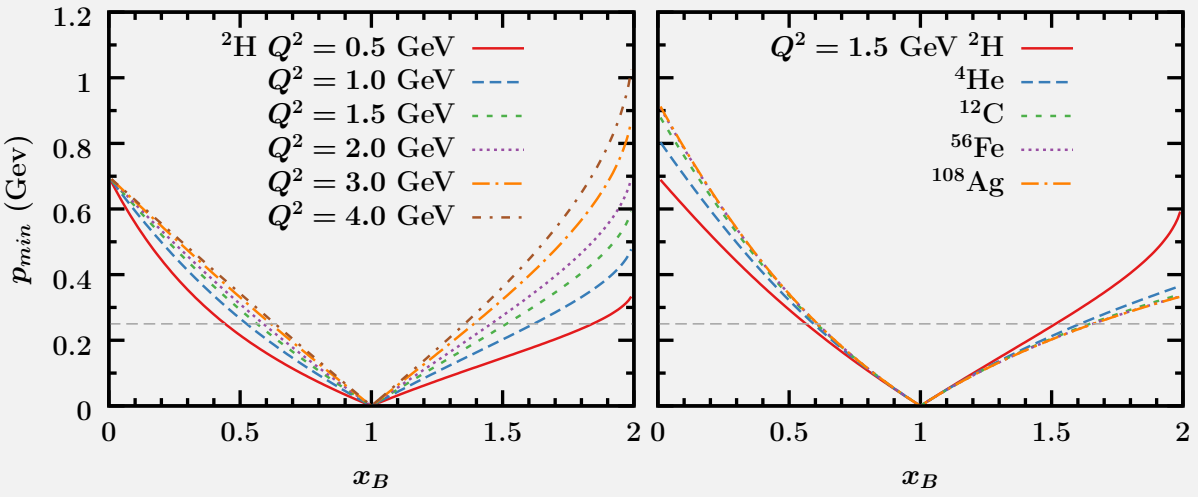

Figure 1.6 – The minimum missing momentum p_{min} as a function of Bjorken scaling x_B for quasi-elastic scattering off a single nucleon $\gamma^* + A \rightarrow (A-1) + N$. In the left panel scattering from ^{2}H for different four-momentum transfer Q^2. In the right panel scattering from different nuclei for $Q^2 = 1.5$ GeV.

nucleon is $x_B = 1$. For x_B slightly above 1, the dominant contribution is the quasi-elastic scattering off a bound nucleons inside the nucleus with a non-zero momentum smaller than k_F. Inelastic processes (with large values of ω) dominate at $x_B < 1$. Probing high-momentum nucleons on the $x_B > 1$ side of the quasi-elastic peak yields a significant suppression of inelastic and quasi-elastic scattering from uncorrelated nucleons. The limitation on Q^2 and x_B also determines a minimum possible momentum $\vec{p_{min}}$ for the removed nucleon. Figure 1.6 illustrates how selection criteria for x_B and Q^2 can suppress the background of quasi-elastic scattering from mean-field scattering with a momentum lower than k_F. For heavy nuclei, the minimum momentum for given $x_B > 1$ and Q^2 is somewhat smaller. This requires larger x_B and Q^2 values to fully suppress scattering from a mean-field nucleon.

The Bjorken scaling variable as defined in Eq. (1.5) can also be used to distinguish between two-, three- and higher-nucleon SRC. For scattering at $x_B > 1$ — neglecting the decreasing contribution from a moving bound nucleon slightly above $x_B = 1$ — at least two nucleons need to be involved. The probabilities of j-nucleon SRC ($j \geq 2$) drops with j. Due to the kinematic constrains, one can expect that scattering from j-nucleon SRC will dominate at $j - 1 \lesssim x_B \lesssim j$.

1.3 Scaling of the ratio of cross sections of inclusive reactions

The least complicated of the high-energy lepton-nucleon scattering measurements is inclusive electron scattering $A(e, e')$. At $Q^2 \geq 1.4$ GeV^2 and $1.5 \leq x_B \leq 2$, the conditions to probe NN SRC discussed in the previous section are satisfied. If the underlying SRC are indeed universal, one expects to see the same x_B dependence in the cross sections of different nuclei, with the cross section ratios providing an indication of the relative contributions related to SRC. Inclusive electron scattering experiments probing SRC were performed in SLAC [38], and at Hall B [39, 40] and Hall C [37, 41, 42] in Jefferson Lab (JLab). Figure 1.7 shows the measured cross section ratios

$$r(A/^2\mathrm{H}) = \frac{2}{A}\frac{\sigma_A(Q^2, x_B)}{\sigma_\mathrm{D}(Q^2, x_B)}, \tag{1.6}$$

of the most recent experiment at Hall C [37]. For $x_B > 1.5$ the data displays a plateau. The anomaly of the point at $x_B = 1.95$ is due to the approach to the kinematic threshold of the electron-deuteron scattering at $x_B = \frac{M_D}{M_p} \approx 2$.

Figure 1.8 shows the cross section ratio of a Hall C experiment [42] whereby the cross sections are expressed relative to the ^{3}He one,

$$r(A/^3\mathrm{He}) = \frac{3}{A}\frac{\sigma_A(Q^2, x_B)}{\sigma_{^3\mathrm{He}}(Q^2, x_B)}. \tag{1.7}$$

Beyond the scaling in the region $1.5 < x_B < 2$, the ratio increases with x_B for $2 < x_B < 2.25$ — which can be explained by scattering off NN SRC with a non-zero center-of-mass motion — and it displays a second scaling regime at $x_B > 2.25$ which may indicate that three-nucleon (3N) SRC dominate in that region. The ratios in the scaling region are often referred to as the a_j coefficient, $a_2(A/^3\mathrm{He})$ or $a_2(A/^2\mathrm{H})$ for the region $1.5 < x_B < 2$ and $a_3(A/^3\mathrm{He})$ for $x_B > 2.5$. These a_j coefficients will be discussed in greater detail in Chapter 3.

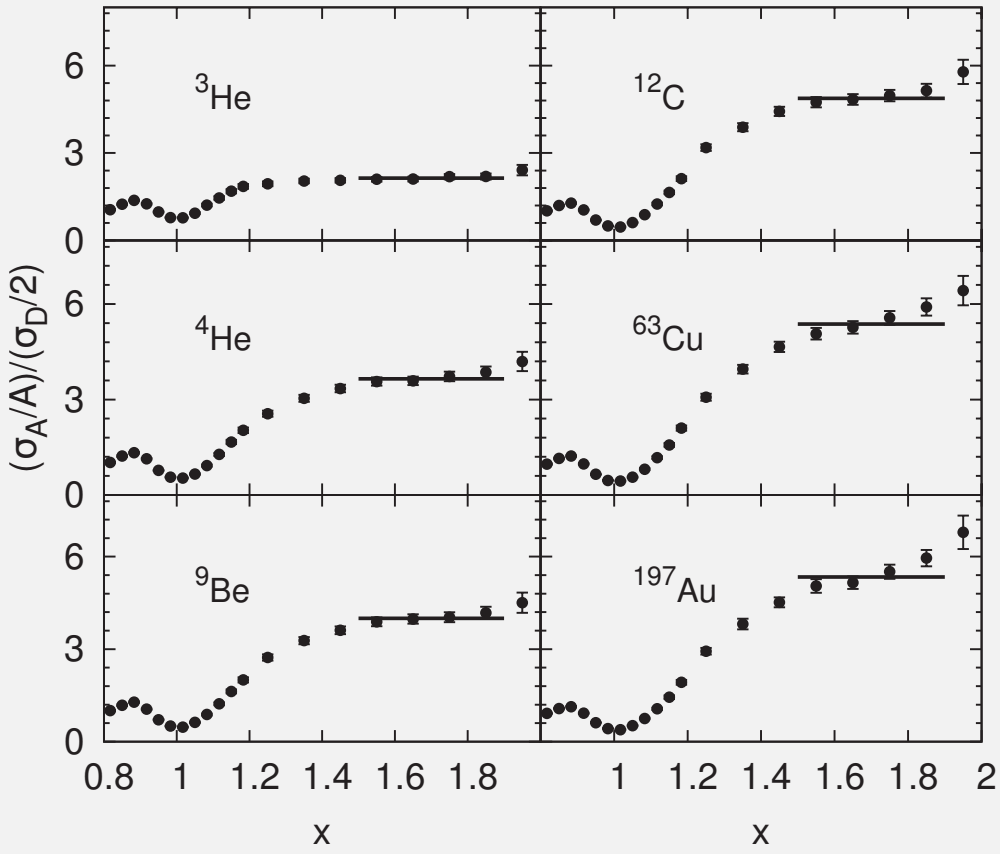

Figure 1.7 – The per-nucleon cross section ratios as a function of x_B (here represented by x) from the E02-019 experiment performed in Hall C at JLab [37]. An electron beam of 5.766 GeV impinged on targets of ^{2}H, ^{3}He, ^{4}He, ^{9}Be, ^{12}C, ^{63}Cu and ^{197}Au. Scattered electrons were detected at a scattering angle $\theta_e = 18°$. Figure taken from Ref. [37].

1.4 Probing short-range correlations in exclusive reactions

In Section 1.3, it is discussed how SRC can be probed via inclusive electron scattering. However, inclusive measurements do not display a large sensitivity to the details of the SRC pairs, for example the quantum numbers. Resolving the nature and further detailed structure of SRC involves nucleon knockout measurements in which two outgoing nucleons are detected. The kinematics of the experiments should correspond to the "asymmetric" situation in which a nucleon can be identified as the struck nucleon with a momentum close to the large momentum transfer. Thereby, the other nucleon can be identified as a recoil spectator nucleon from within the SRC, with a momentum exceeding the characteristic Fermi momentum of the nucleus, but well below the scale of the momentum transfer.

A triple-coincidence two-nucleon knockout experiment measuring $^{12}\mathrm{C}(p, ppn)$ was performed at Brookhaven National Laboratory (BNL) [43, 44]. From the results contained in Figure 1.9, it can be inferred that the momentum of protons with a high missing momentum is predominantly balanced by a single recoiling neutron with $\cos\gamma < 0$, where γ is the angle between the knocked out proton and neutron. This is consistent with the assumption that

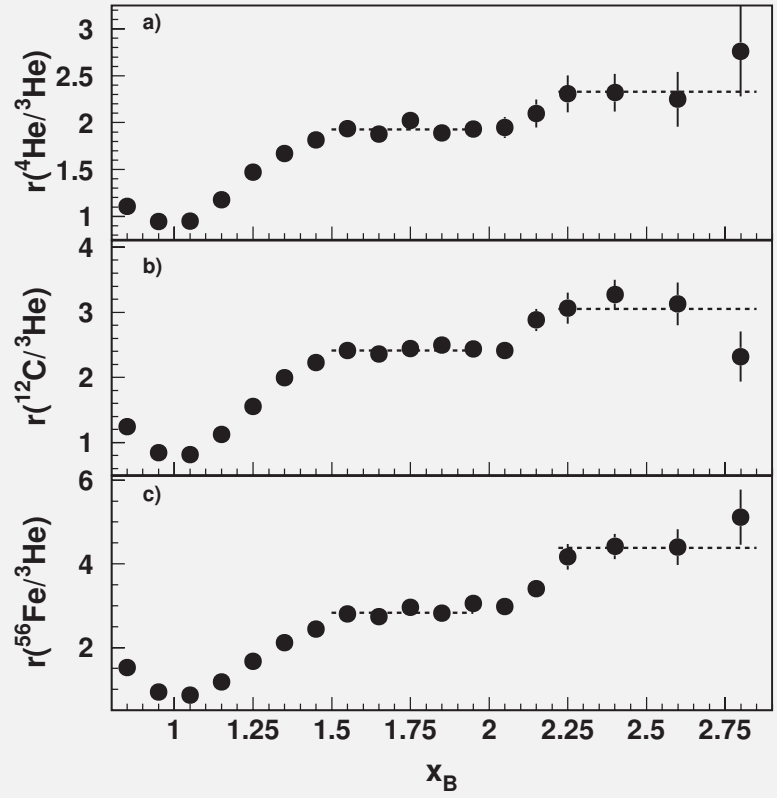

Figure 1.8 – The weighted cross section ratios of Eq. (1.7) for ^{4}He, ^{12}C and ^{56}Fe to ^{3}He as a function of x_B for $1.4 < Q^2 < 2.6$ GeV^2 from two sets of measurements performed in Hall C at JLab [42]. The first with 4.461 GeV electrons incident on ^{3}He, ^{4}He and ^{12}C targets. The second measurement used 4.471 GeV electrons on a ^{56}Fe target and 4.703 GeV electrons on a ^{3}He target. The horizontal dashed lines indicate the NN ($1.5 < x_B < 2$) and 3N ($x_B > 2.25$) scaling regions. Figure taken from Ref. [42].

high-momentum nucleons are the result of SRC, in which the two nucleons have large relative momenta but a small total momentum (both relative to the Fermi momentum).

Theoretical $(e, e'pn)$ and $(e, e'pp)$ calculations [36, 46, 47] have predicted that the tensor parts of the SRC are responsible for the fact that the correlated pn strength is typically a factor of 10 bigger than the correlated pp strength. By conducting triple-coincidence $A(e, e'pN)$ measurements whereby both recoil protons and neutrons are detected, one can learn about the isospin structure of SRC in the nucleus. Such experiments were studied in Hall A at JLab for ^{4}He [48] and ^{12}C [49, 50]. The scattered electron and the knocked-out proton in these $A(e, e'pN)$ reactions were detected in coincidence with a large-acceptance detector which looks for an associated recoil proton or neutron. For every $A(e, e'p)$ event, the ratios $A(e, e'pp)/A(e, e'p)$ and $A(e, e'pn)/A(e, e'p)$ were determined. Figure 1.10 shows the results for ^{12}C. With the information in Figure 1.10, a pp over pn ratio of 18 ± 5 can be deduced for SRC pairs in the ground state of ^{12}C. In combination with the observed strength of LRC and mean-field nucleons, one gets a comprehensive schematic picture of the structure of ^{12}C, as is shown in Figure 1.11. There will also be SRC with more than two nucleons, but their contribution is expected to be small.

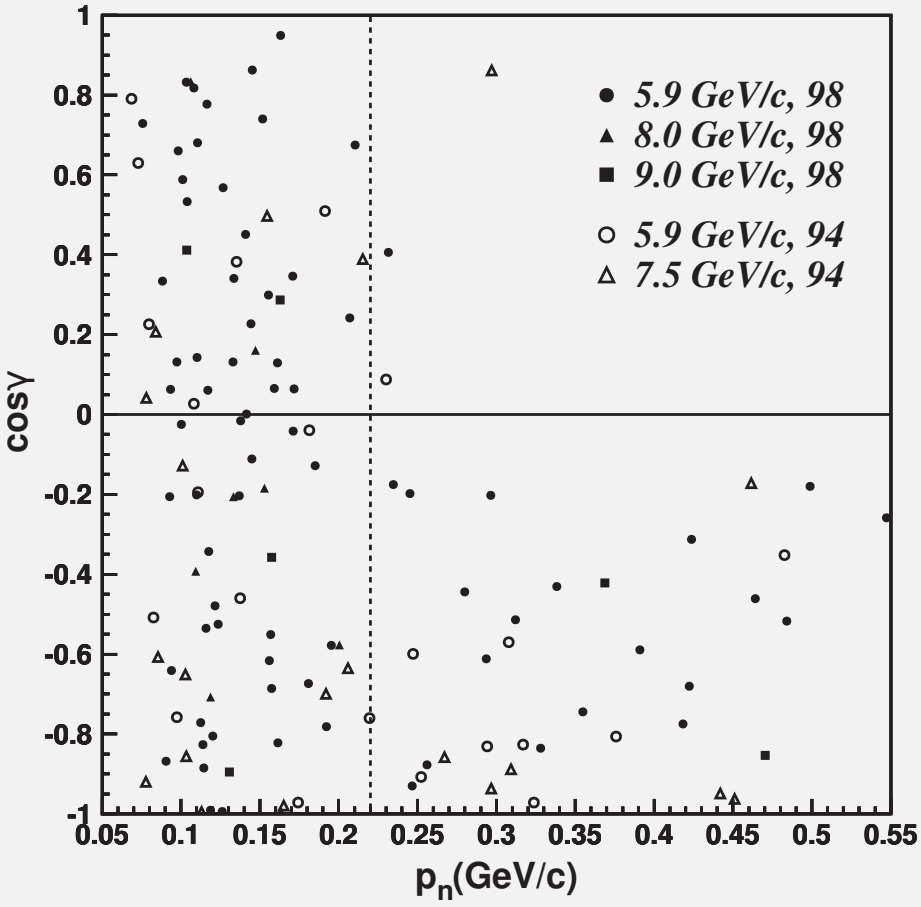

Figure 1.9 – The correlations between neutron momentum p_n and its direction γ relative to the initial momentum of the knocked out proton, from the measurement of $^{12}\mathrm{C}(p, ppn)$ reactions at BNL. Data labeled by 94 and 98 are from Refs. [43, 44] respectively. The momenta are the beam momenta. The dotted vertical line corresponds to $k_F = 220$ MeV. Figure taken from Ref. [45].

1.5 The EMC effect

Deep inelastic scattering provides access to the quark distributions in nuclei via measurements of inclusive cross sections. This cross section for electron (or muon) scattering from a nucleus can be written as

$$\frac{d^2\sigma}{dx_B dQ^2} = \frac{4\pi\alpha E'^2}{x_B Q^4}\frac{E'}{E}\left[F_2 \cos^2\frac{\theta}{2} + \frac{2\omega}{M}F_1 \sin^2\frac{\theta}{2}\right] \tag{1.8}$$

where E (E') is the energy of the initial (scattered) electron, θ the electron scattering angle in the lab frame and M the proton mass. The structure functions F_1 and F_2 depend on x_B and Q^2. In the parton model, information about quark distribution functions is contained in the F_1 and F_2. In the Bjorken limit (Q^2, $\omega \to \infty$, fixed $\frac{\omega}{Q^2}$), the structure functions become

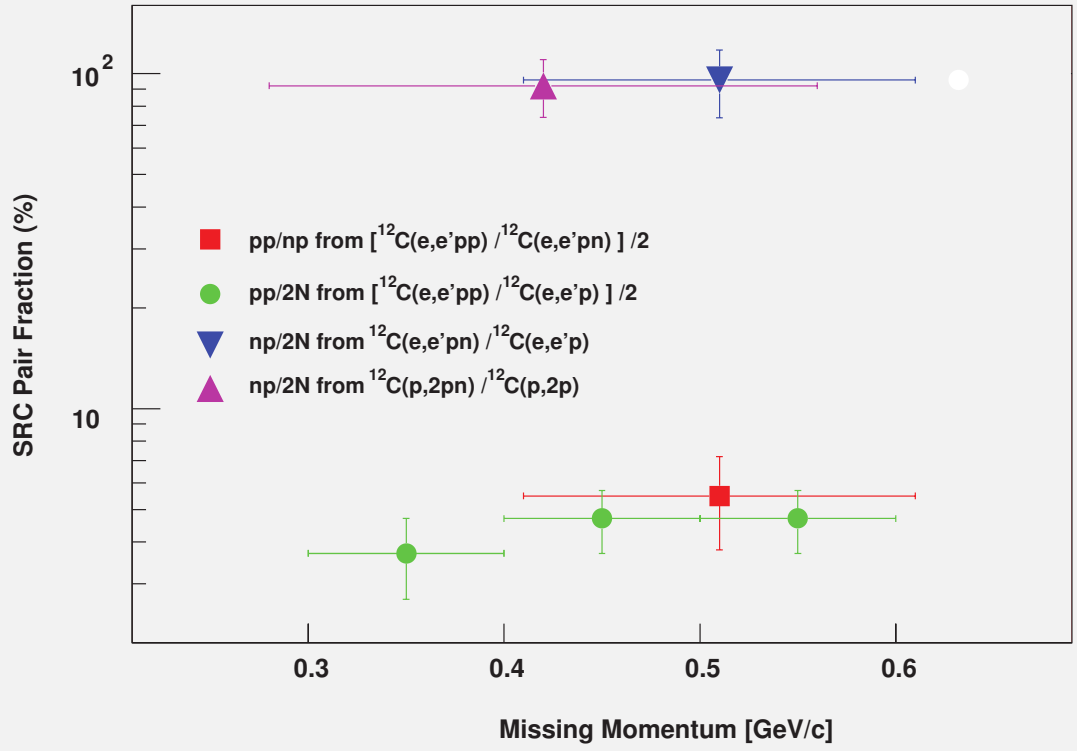

Figure 1.10 – The fractions of correlated pair combinations in ^{12}C as obtained from $(e, e'pp)$, $(e, e'pn)$ reactions from Refs. [49, 50], and $(p, 2pn)$ data from Ref. [45]. Figure from Ref. [50]

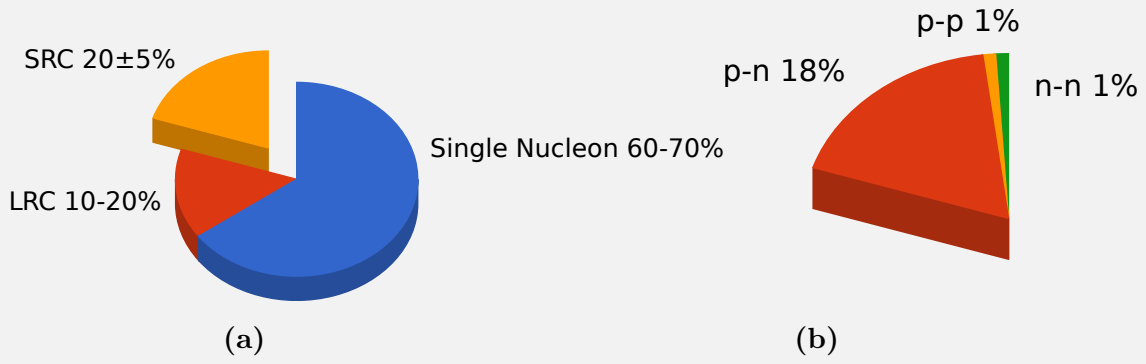

Figure 1.11 – Schematic picture of the structure of ^{12}C. (a) Most of the time the nucleons behave independently, 10 to 20 % of the time they are correlated over long distances, the rest of the time they are correlated over short distances. (b) The majority of the SRC pairs are proton-neutron (p-n) pairs.

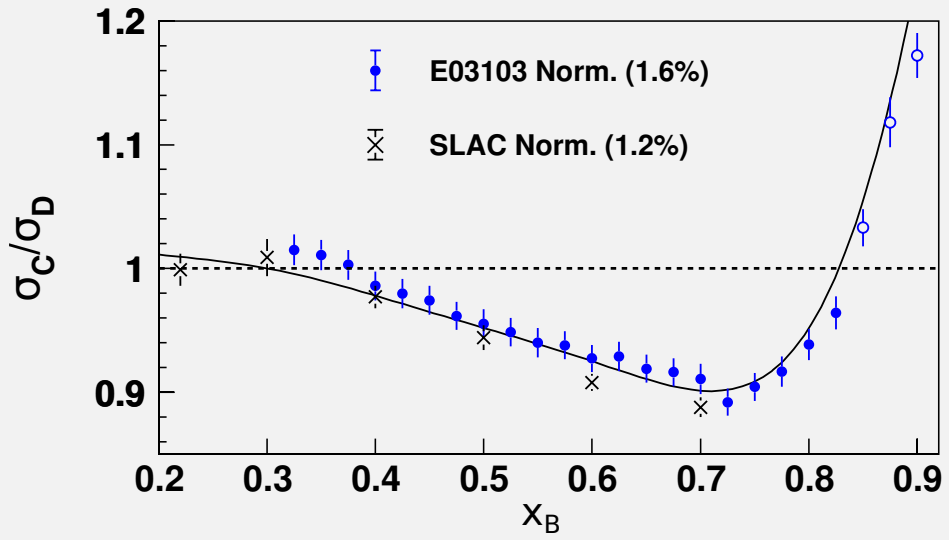

Figure 1.12 – Ratio of the per-nucleon cross section R_{EMC} of ^{12}C (here denoted by σ_C/σ_D) as a function of the Bjorken scaling variable x_B for the newest JLab [51] and the SLAC [52] data. The solid curve is a fit to the SLAC data. The EMC effect is the reduction of the ratio in the range $0.3 < x_B < 0.8$. Figure taken from Ref. [51].

independent of Q^2,

$$F_1(x_B) = \frac{1}{2}\sum_f e_f^2 \left[q_f(x_B) + \bar{q}_f(x_B)\right], \tag{1.9}$$

$$F_2(x_B) = 2x_B F_1, \tag{1.10}$$

where $q_f(x_B)$ ($\bar{q}_f(x_B)$) is the (anti-)quark distribution function and e_f is the quark charge for a given flavor f. The per-nucleon ratio of the F_2 structure functions between a nucleus and the deuteron is then a direct measure of the modification of quark distributions in nuclei.

In 1983, the European Muon Collaboration (EMC) discovered that the per-nucleon deep inelastic structure function F_2 in iron was significantly different from the one in deuterium [53]. They showed a clear suppression of quarks for $0.3 < x_B < 0.8$, confirmed for several nuclei in more extensive measurements at SLAC [51, 52]. This phenomenon, dubbed the "EMC effect", has become the subject of a vigorous theoretical effort aimed at understanding the underlying physics but a satisfying explanation remains elusive. Figure 1.12 shows the EMC effect in ^{12}C as the ratio of cross sections per nucleon,

$$R_{\mathrm{EMC}} = \frac{2}{A}\frac{\sigma_A}{\sigma_{^2\mathrm{H}}}, \tag{1.11}$$

rather than the F_2 structure functions. There are corrections involved in going from cross section ratios to the F_2 ratios [54].

If it is assumed that the shape of the EMC effect is universal and only the magnitude varies with target nucleus. The size of the EMC effect can be measured by the slope $-\frac{\mathrm{d}R_{\mathrm{EMC}}}{\mathrm{d}x_B}$. of the per-nucleon cross section ratios in the interval $0.3 < x_B < 0.7$.

The early assumption was that the size of the effect scales with the nuclear density. As is shown in Figure 1.13, however, the results of ^{9}Be are not consistent with simple density-

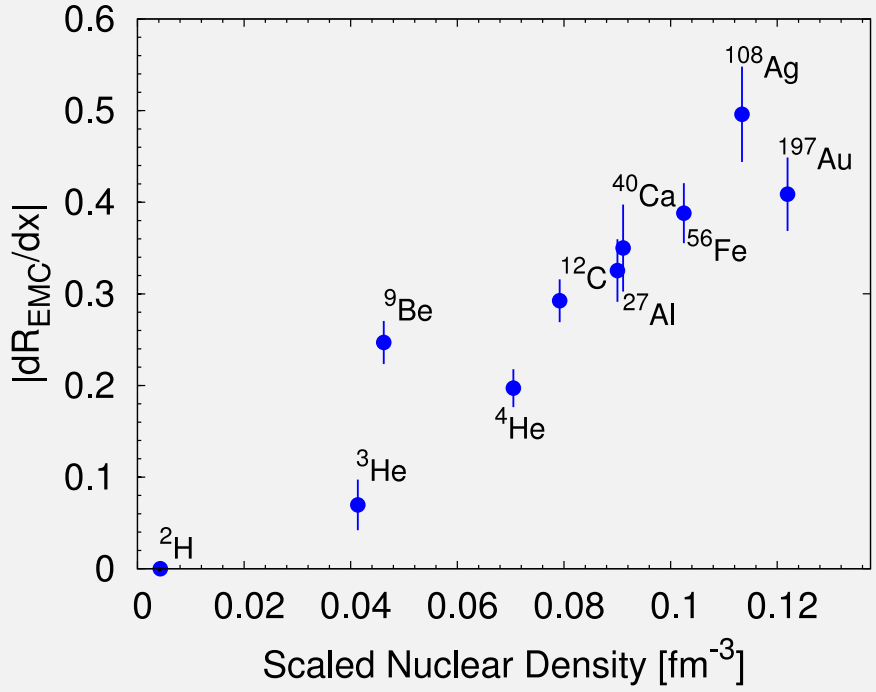

Figure 1.13 – The slope of the EMC ratio for $0.35 < x_B < 0.70$ as a function of nuclear density as a function of the Bjorken scaling variable x_B. Figure taken from Ref. [55].

dependent fits. The observed EMC effect in ^{9}Be is essentially almost identical to what is seen in ^{12}C, even though the average density of ^{9}Be is much lower. One explanation for the anomalous behavior of ^{9}Be is that it can be described as a pair of tightly bound alpha particles plus one additional neutron [56]. While most of the nucleons are in a dense environment, similar to ^{4}He, the average density is much lower, as the alphas (and an additional neutron) orbit in a larger volume. This suggests that it is the local density that drives the EMC modification. The strong clustering of nucleons in ^{9}Be leads to a special situation whereby the average density doesn't reflect the local environment of the bulk of the protons and neutrons.

1.6 Nuclear scaling and the EMC effect

The EMC effect discussed in the previous section can be associated with modified nucleon structure. The nuclear scaling discussed in Section 1.3 can be associated with large nucleon momenta. Both have been attributed to local nuclear density effects and not to properties of the bulk nuclear system. In Ref. [57], it is suggested that there exists a relation between these two observations. Figure 1.14 shows quantitatively that the magnitude of the EMC effect, $-\frac{\mathrm{d}R_{\mathrm{EMC}}}{\mathrm{d}x_B}$, is linearly related to the SRC scale factor $a_2(A/^2\mathrm{H})$.

The underlying physical reason for the EMC-SRC relation is so far only speculative. Assuming that the EMC effect is due to a difference in the quark distributions in bound and free nucleons, these differences could occur predominantly in both mean-field nucleons and nucleons affected by SRC. The linear correlation between the strength of the EMC and the SRC may hint that modifications of the quark distributions occur whenever nucleons are

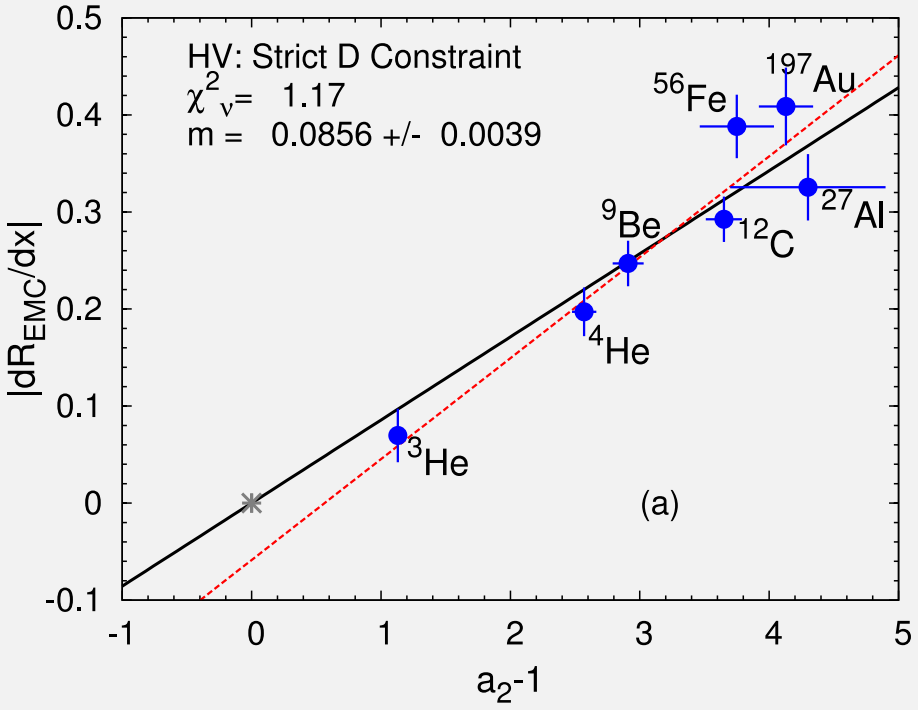

Figure 1.14 – The EMC slopes versus the SRC scale factors. The solid line is the one-parameter fit with slope m, constrained to yield zero for the deuteron. The dashed red line shows the result of a two-parameter fit. Figure taken from Ref. [55].

affected by SRC.

1.7 Outline

One of the goals of nuclear physics is providing a complete picture of the structure and dynamics of nuclei. This work focuses on the effect of the SRC. Whereas the existence of SRC was proposed in the early days of nuclear physics, finding direct experimental evidence has been difficult. For a long time, SRC has been one of the most elusive features of the nuclear system. In recent years, substantial progress has been made in exploring the dynamics of the SRC in nuclei. This chapter gave an overview of experimental results at high-luminosity and high-energy electron and proton accelerators that provided convincing evidence of SRC. Inclusive $A(e, e')$ measurements in kinematics favoring correlated pair knockout have provided an estimate for the magnitude of NN SRC in the target nucleus relative to the deuteron (or ^{3}He). Exclusive $A(e, e'pN)$ and $A(p, ppn)$ measurements probed correlated NN pairs and identified pn pairs as the dominant contribution.

On the theoretical side, momentum distributions contain information about SRC properties of the nuclear ground state. Over the years, various methods to compute the nuclear one-nucleon and two-nucleon momentum distributions have been developed. Ab-initio methods with variational wave functions compute the momentum distribution for nuclei up to $A = 12$ [21, 58–61]. Also for atomic mass number infinity, or nuclear matter, exact calculations with realistic NN interactions are performed [62, 63]. Momentum distributions for mid-heavy and heavy nuclei cannot be computed with exact methods to date. Advanced approximate

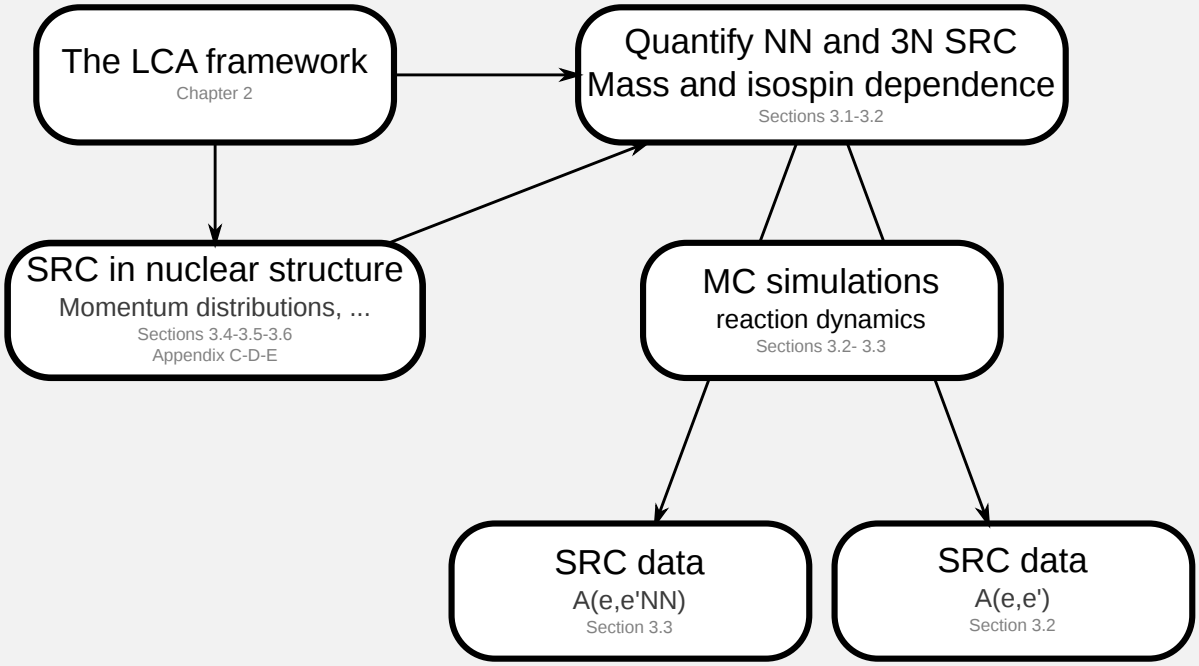

Figure 1.15 – Flowchart for the hierarchy of the different chapters. The LCA framework in Chapter 2 plays a central role. Based on the properties of the LCA, a method for quantifying NN and 3N SRC and the study of their mass and isospin dependence is exposed in Sections 3.1 and 3.2. The LCA framework is also used to calculate structure related properties like the one- and two-nucleon momentum distributions in Sections 3.4, 3.5 and 3.6. The results obtained here confirm the assumption made in Sections 3.1 and 3.2. The quantified NN and 3N SRC are related to SRC susceptible observables in inclusive $A(e, e')$ and exclusive $A(e, e'NN)$ reactions in Sections 3.2 and 3.3. In doing so, use was made of Monte Carlo (MC) simulations for the reaction dynamics.

schemes like cluster expansions [61, 64, 65] and correlated basis function theory [66, 67] are able to compute momentum distributions for heavier nuclei.

These calculations provided insight in the fat high-momentum tails of the momentum distributions attributable to multinucleon correlations. It is notoriously challenging, though, to establish quantitative relationships between observables and the computed momentum distributions [33, 34, 68–70].

Many questions related to SRC have remained unanswered for many years. In this thesis, we formulate an answer to the following research questions

- How can one quantify SRC in a nucleus?
- What is the isospin and mass dependence of SRC susceptible nucleons?
- How can the quantified amount of SRC be related to the experimental observations? As the SRC are predominantly connected with the relative motion of pairs, what is the contribution of the center-of-mass motion of the SRC susceptible observables?
- How do SRC manifest themselves in structure related properties like the nucleon kinetic energy, nucleon momentum distributions and nuclear radii?

The outline of this work is schematically represented in Figure 1.15 and is as follows:

- Chapter 2 describes the low-order correlation operator approximation (LCA). The LCA corrects IPM for SRC by shifting the complexity induced by the SRC from the wave functions to the operators. The expansion of these operators can be truncated to a low order due to the local character of the SRC.
- Chapter 3 presents published and unpublished results which are based on the LCA described in Chapter 2.
  - In Section 3.1, it is suggested that the number of correlated nucleon pairs in an arbitrary nucleus can be estimated by counting the number of nucleon pairs residing in a relative S state. This is based on the observation that correlation operators in the LCA mainly affect nucleon pairs in this state. The estimates are compared to the $a_2(A/^2\mathrm{H})$ coefficient.
  - In Section 3.2 a method for quantifying 3N SRC is exposed and the mass and isospin dependence of NN and 3N SRC are studied. In order to better relate the estimated number of SRC to the inclusive electro-induced scaling ratios, a Monte Carlo method for the effect of center-of-mass motion of SRC on inclusive reactions is proposed.
  - Section 3.3 derives a factorized expression for the exclusive electro-induced two-nucleon knockout $A(e, e'pN)$ processes. The $A(e, e'pN)$ cross section is shown to be proportional to the conditional center-of-mass momentum distribution for close-proximity pairs with zero relative and angular momentum. The effect of FSI and kinematic cuts on the factorization scheme is also considered.
  - Sections 3.4 and 3.6 report studies of the impact of the nuclear SRC on structure related properties: the one- and two-nucleon momentum distributions, nucleon kinetic energies and nuclear radii. The dominance of nucleon pairs with zero relative and angular momentum confirms the assumption made in the Sections 3.1 and 3.2. Section 3.5 looks at spin-isospin correlations in SRC and their influence on the single-nucleon momentum distributions.
- Chapter 4 provides a brief summary of the chief achievements and an outlook on the research of SRC and the possibilities of the developed framework.
- Appendix A gives more detailed information on Moshinsky transformation brackets. The Woods-Saxon potentials are discussed in Appendix B. The considered correlation functions and their parametrization are given in Appendix C. Appendix D provides the technical details on the calculation of the considered matrix elements. Finally, Appendix E gives details on the structure of the software developed in the context of this work.

1.8 References

[1] V. G. J. Stoks, R. A. M. Klomp, M. C. M. Rentmeester, and J. J. de Swart, Phys. Rev. C **48**, 792 (1993).

[2] R Machleidt and I Slaus, J. Phys. G: Nucl. Part. Phys. **27**, R69 (2001).

[3] R. B. Wiringa, V. G. J. Stoks, and R. Schiavilla, Phys. Rev. C **51**, 38 (1995).
[4] R. V. Reid Jr., Annals of Physics **50**, 411 (1968).
[5] R. Machleidt, Phys. Rev. C **63**, 024001 (2001).
[6] V. G. J. Stoks, R. A. M. Klomp, C. P. F. Terheggen, and J. J. de Swart, Phys. Rev. C **49**, 2950 (1994).
[7] M. Lacombe, B. Loiseau, J. M. Richard, et al., Phys. Rev. C **21**, 861 (1980).
[8] R. Machleidt and D. Entem, Physics Reports **503**, 1 (2011).
[9] E. Epelbaum, H.-W. Hammer, and U.-G. Meißner, Rev. Mod. Phys. **81**, 1773 (2009).
[10] J. Carlson and V. Pandharipande, Nucl. Phys. A **371**, 301 (1981).
[11] E. Epelbaum, A. Nogga, W. Glöckle, et al., Phys. Rev. C **66**, 064001 (2002).
[12] P. Mermod, J. Blomgren, B. Bergenwall, et al., Phys. Lett. B **597**, 243 (2004).
[13] M. G. Mayer, Phys. Rev. **74**, 235 (1948).
[14] M. G. Mayer, Phys. Rev. **75**, 1969 (1949).
[15] O. Haxel, J. H. D. Jensen, and H. E. Suess, Phys. Rev. **75**, 1766 (1949).
[16] P. G. Blunden and I. Sick, Phys. Rev. C **72**, 057601 (2005).
[17] L. Lapikàs, Nucl. Phys. A **553**, 297 (1993).
[18] H. J. Lipkin, Phys. Rev. **110**, 1395 (1958).
[19] S. Gartenhaus and C. Schwartz, Phys. Rev. **108**, 482 (1957).
[20] H. Feldmeier, T. Neff, R. Roth, and J. Schnack, Nucl. Phys. A **632**, 61 (1998).
[21] H. Feldmeier, W. Horiuchi, T. Neff, and Y. Suzuki, Phys. Rev. C **84**, 054003 (2011).
[22] E. C. Svensson, V. F. Sears, A. D. B. Woods, and P. Martel, Phys. Rev. B **21**, 3638 (1980).
[23] R. B. Hallock, Phys. Rev. A **5**, 320 (1972).
[24] O. Benhar, V. R. Pandharipande, and S. C. Pieper, Rev. Mod. Phys. **65**, 817 (1993).
[25] W. Dickhoff and C. Barbieri, Prog. Part. Nucl. Phys. **52**, 377 (2004).
[26] J. Ryckebusch, M. Waroquier, K. Heyde, et al., Nucl. Phys. A **476**, 237 (1988).
[27] J. Ryckebusch, K. Heyde, D. Van Neck, and M. Waroquier, Nucl. Phys. A **503**, 694 (1989).
[28] J. Engel, J. Carlson, and R. Wiringa, Phys. Rev. C **83**, 034317 (2011).
[29] W. Cosyn, M. C. Martinez, and J. Ryckebusch, Phys. Rev. C **77**, 034602 (2008).
[30] O. Benhar, C. Ciofi degli Atti, S. Liuti, and G. Salmè, Phys. Lett. B **177**, 135 (1986).
[31] R. Schiavilla, V. Pandharipande, and R. Wiringa, Nucl. Phys. A **449**, 219 (1986).
[32] C. Ciofi degli Atti and S. Simula, Phys. Rev. C **53**, 1689 (1996).
[33] J. Arrington, D. Higinbotham, G. Rosner, and M. Sargsian, Prog. Part. Nucl. Phys. **67**, 898 (2012).
[34] L. Frankfurt, M. Sargsian, and M. Strikman, Int. J. Mod. Phys. A **23**, 2991 (2008).
[35] J. Ryckebusch, V. V. der Sluys, K. Heyde, et al., Nucl. Phys. A **624**, 581 (1997).
[36] S. Janssen, J. Ryckebusch, W. Van Nespen, and D. Debruyne, Nucl. Phys. A **672**, 285 (2000).
[37] N. Fomin, J. Arrington, R. Asaturyan, et al., Phys. Rev. Lett. **108**, 092502 (2012).
[38] L. Frankfurt, M. Strikman, D. Day, and M. Sargsian, Phys. Rev. C **48**, 2451 (1993).
[39] J. Arrington, C. S. Armstrong, T. Averett, et al., Phys. Rev. Lett. **82**, 2056 (1999).
[40] J. Arrington, C. S. Armstrong, T. Averett, et al., Phys. Rev. C **64**, 014602 (2001).
[41] K. S. Egiyan, N. Dashyan, M. Sargsian, et al., Phys. Rev. C **68**, 014313 (2003).
[42] K. Egiyan, N. Dashyan, M. Sargsian, et al., Phys. Rev. Lett. **96**, 082501 (2006).
[43] A. Tang, J. W. Watson, J. Aclander, et al., Phys. Rev. Lett. **90**, 042301 (2003).
[44] J. Aclander, J. Alster, D. Barton, et al., Phys. Lett. B **453**, 211 (1999).

[45] E. Piasetzky, M. Sargsian, L. Frankfurt, et al., Phys. Rev. Lett. **97**, 162504 (2006).
[46] J. Ryckebusch, S. Janssen, W. Van Nespen, and D. Debruyne, Phys. Rev. C **61**, 021603R (2000).
[47] C. Barbieri, C. Giusti, F. Pacati, and W. Dickhoff, Phys. Rev. C **70**, 014606 (2004).
[48] I. Korover, N. Muangma, O. Hen, et al., ArXiv e-prints, 1401.6138 (2014).
[49] R. Shneor, P. Monaghan, R. Subedi, et al., Phys. Rev. Lett. **99**, 072501 (2007).
[50] R. Subedi, R. Shneor, P. Monaghan, et al., Science **320**, 1476 (2008).
[51] J. Seely, A. Daniel, D. Gaskell, et al., Phys. Rev. Lett. **103**, 202301 (2009).
[52] J. Gomez, R. G. Arnold, P. E. Bosted, et al., Phys. Rev. D **49**, 4348 (1994).
[53] J. Aubert, G. Bassompierre, K. Becks, et al., Phys. Lett. B **123**, 275 (1983).
[54] D. F. Geesaman, K Saito, and A. W. Thomas, Annu. Rev. Nucl. Part. Sci. **45**, 337 (1995).
[55] J. Arrington, A. Daniel, D. B. Day, et al., Phys. Rev. C **86**, 065204 (2012).
[56] K. Arai, Y. Ogawa, Y. Suzuki, and K. Varga, Phys. Rev. C **54**, 132 (1996).
[57] D. Higinbotham, J. Gomez, and E. Piasetzky, ArXiv e-prints, 1003.4497 (2010).
[58] R. Schiavilla, R. B. Wiringa, S. C. Pieper, and J. Carlson, Phys. Rev. Lett. **98**, 132501 (2007).
[59] R. B. Wiringa, R. Schiavilla, S. C. Pieper, and J. Carlson, Phys. Rev. C **78**, 021001 (2008).
[60] R. B. Wiringa, R. Schiavilla, S. C. Pieper, and J. Carlson, Phys. Rev. C **89**, 024305 (2014).
[61] M. Alvioli, C. Ciofi degli Atti, L. P. Kaptari, et al., Phys. Rev. C **87**, 034603 (2013).
[62] O. Benhar, A. Fabrocini, and S. Fantoni, Nucl. Phys. A **505**, 267 (1989).
[63] A. Rios, A. Polls, and W. H. Dickhoff, Phys. Rev. C **89**, 044303 (2014).
[64] M. Alvioli, C. Ciofi degli Atti, and H. Morita, Phys. Rev. Lett. **100**, 162503 (2008).
[65] M. Alvioli, C. Ciofi degli Atti, L. P. Kaptari, et al., Phys. Rev. C **85**, 021001 (2012).
[66] F. Arias de Saavedra, C. Bisconti, G. Co', and A. Fabrocini, Phys. Rept. **450**, 1 (2007).
[67] C. Bisconti, F. A. d. Saavedra, and G. Co', Phys. Rev. C **75**, 054302 (2007).
[68] R. Shneor, P. Monaghan, R. Subedi, et al., Phys. Rev. Lett. **99**, 072501 (2007).
[69] J. Ryckebusch, Phys. Rev. C **64**, 044606 (2001).
[70] J. Ryckebusch, Phys. Lett. B **383**, 1 (1996).

CHAPTER 2

Formalism

This chapter presents the formalism that will be used in Chapter 3 to quantify the mass and isospin dependence of SRC in nuclei. Section 2.1 deals with two- and three-body states in independent particle models (IPMs). First, useful transformations for two- and three-body states are derived for a harmonic oscillator (HO) basis. Then, similar transformations are derived for two- and three-body states in alternate bases. Section 2.2 introduces a flexible method dubbed the low-order correlation operator approximation (LCA). The LCA corrects mean-field models, for short-range correlations (SRC) by shifting the complexity induced by the SRC from the wave functions to the operators. It is argued that the expansion of these operators can be truncated to a low order due to the local character of the SRC. We stress that throughout this thesis, we neglect the role of long-range correlations. The latter marginally affect the high-momentum and high-energy component of the nuclear wave functions, which constitute the subject of investigation in this thesis.

2.1 Few-body states in independent particle models

In an IPM, the nucleus is described as a set of nucleons which move independently in a central potential well created by the other nucleons. The three-dimensional HO is one of the few three-dimensional IPMs that can be solved analytically. Therefore, it is often used as a basic model for the mean-field nucleus. A major advantage is that the two-nucleon Hamiltonian can be exactly written as a sum of relative and center-of-mass (cm) parts. The three-nucleon Hamiltonian can be written in function of three-body Jacobi coordinates. Accordingly, the HO is a good basis for the study of two- and three-body states.

2.1.1 The three-dimensional harmonic oscillator

The time-independent Schrödinger equation for the spherically-symmetric three-dimensional HO

$$\left(-\frac{\hbar^2}{2M_N}\nabla^2 + \frac{1}{2}M_N\omega^2 r^2\right)\psi = E\psi, \tag{2.1}$$

can be solved analytically. Here, M_N is the nucleon mass and ω is the angular frequency parameter of the oscillator. In polar coordinates, the solution is

$$\psi_{nlm}(\vec{r}\,) \equiv \langle \vec{r}\,|nlm\rangle = R_{nl}(r)Y_{lm}(\Omega), \tag{2.2}$$

where $Y_{lm}(\Omega)$ are the spherical harmonics and the radial wave functions are given in terms of the Laguerre polynomials $L_n^\alpha(r)$ by

$$R_{nl}(r) = \Big[\frac{2n!}{\Gamma(n+l+\frac{3}{2})}\nu^{l+3/2}\Big]^{1/2} r^l e^{-\frac{\nu r^2}{2}} L_n^{l+\frac{1}{2}}(\nu r^2), \tag{2.3}$$

where

$$\nu \equiv \frac{M_N\omega}{\hbar}. \tag{2.4}$$

In order to fit the nuclear properties, the HO parameter $\hbar\omega$ is generally parameterized as [1]

$$\hbar\omega(\mathrm{MeV}) = 45A^{-1/3} - 25A^{-2/3}. \tag{2.5}$$

2.1.2 Two-nucleon states

The single-particle states of a nucleon in a HO potential are denoted by $\alpha \equiv (nljm_jt)$, where $t = \pm\frac{1}{2}$ is the isospin quantum number and $\vec{j} = \vec{l} + \vec{s}$ is the total angular momentum. The normalized, antisymmetric (nas) uncoupled state of two independent nucleons with coordinates $\vec{r}_1$ and $\vec{r}_2$ in a HO potential, $|\alpha_1\rangle \equiv |n_1l_1j_1m_{j_1}t_1(\vec{r}_1)\rangle$ and $|\alpha_2\rangle \equiv |n_2l_2j_2m_{j_2}t_2(\vec{r}_2)\rangle$, is

$$|\alpha_1\alpha_2\rangle_{\mathrm{nas}} = \frac{1}{\sqrt{2}}\left(1 - \mathcal{P}_{12}\right)|\alpha_1\alpha_2\rangle\,, \tag{2.6}$$

where $\mathcal{P}_{12}$ is the interchange operator for the position, spin and isospin coordinates. The state with the total angular momenta of the two nucleons $\vec{j}_1$ and $\vec{j}_2$ coupled to total angular momenta $\vec{J}$,

$$|\alpha_1\alpha_2\rangle = \sum_{JM_J}\langle j_1m_{j_1}j_2m_{j_2}|JM_J\rangle\,|n_1l_1j_1t_1n_2l_2j_2t_2; JM_J\rangle\,, \tag{2.7}$$

can be transformed from jj coupling, $|n_1l_1j_1n_2l_2j_2; JM_J\rangle$ to LS coupling, $|n_1l_1n_2l_2; (\Lambda S)JM_J\rangle$,

$$|n_1l_1j_1n_2l_2j_2; JM_JTM_T\rangle = \sum_{\Lambda S}\hat{j}_1\hat{j}_2\hat{\Lambda}\hat{S}\begin{Bmatrix} l_1 & \frac{1}{2} & j_1 \\ l_2 & \frac{1}{2} & j_2 \\ \Lambda & S & J\end{Bmatrix}|n_1l_1n_2l_2; (\Lambda S)JM_JTM_T\rangle\,, \tag{2.8}$$

where $\vec{\Lambda} = \vec{l}_1 + \vec{l}_2$ and $\vec{S}$ are respectively the total angular momentum and the total spin, and the shorthand notation $\hat{j} = \sqrt{2j+1}$ is introduced.

Two particles moving in a harmonic potential can be described either by using the center-of-well (cw) coordinates $\vec{r}_1$ and $\vec{r}_2$ or the relative and cm (rcm) coordinates $\vec{r}$ and $\vec{R}$, respectively, which are related to each other by

$$\vec{r} = \frac{1}{\sqrt{2}}(\vec{r}_1 - \vec{r}_2), \qquad \vec{R} = \frac{1}{\sqrt{2}}(\vec{r}_1 + \vec{r}_2). \tag{2.9}$$

The transformation coefficients $\langle nlNL;\Lambda|n_1l_1n_2l_2;\Lambda\rangle$ for the transformation of coupled HO states in cw coordinates to coupled HO states in rcm coordinates,

$$|n_1l_1n_2l_2;\Lambda M_\Lambda\rangle = \sum_{nlNL} \langle nlNL;\Lambda|n_1l_1n_2l_2;\Lambda\rangle \, |nlNL;\Lambda M_\Lambda\rangle \,, \tag{2.10}$$

are known as the Moshinsky brackets [2]. Properties and relations of the Moshinsky brackets are given in Appendix A. Using the symmetry relation of Eq. (A.18),

$$\langle nlNL;\Lambda|n_1l_1n_2l_2;\Lambda\rangle = (-1)^{L-\Lambda}\langle nlNL;\Lambda|n_2l_2n_1l_1;\Lambda\rangle, \tag{2.11}$$

and the transformations

$$\begin{aligned} &|nlNL(\Lambda S);JM_J,TM_T\rangle \\ &= \sum_j \hat{\Lambda}\hat{j}(-1)^{j+L+S+\Lambda} \begin{Bmatrix} j & L & J \\ \Lambda & S & l \end{Bmatrix} |n(lS)jNL;JM_J,TM_T\rangle \,, \end{aligned} \tag{2.12}$$

$$\begin{aligned} &|n(lS)jNL;JM_J,TM_T\rangle \\ &= \sum_{M_Lm_j} \langle jm_jLM_L|JM_J\rangle \, |n(lS)jm_j,NLM_L,TM_T\rangle \,, \end{aligned} \tag{2.13}$$

the nas uncoupled two-nucleon state of Eq. (2.6) can be expanded in terms of uncoupled relative and cm two-nucleon states:

$$\begin{aligned} |\alpha_1\alpha_2\rangle_{nas} = &\sum_{n(lS)jm_j} \sum_{NLM_L} \sum_{TM_T} \sum_{JM_J} \sum_{\Lambda} \frac{1}{\sqrt{2}}(1-(-1)^{l+S+T}) \\ &\times \langle \tfrac{1}{2}t_1\tfrac{1}{2}t_2|TM_T\rangle\langle j_1m_{j_1}j_2m_{j_2}|JM_J\rangle\langle jm_jLM_L|JM_J\rangle \\ &\times \langle nlNL;\Lambda|n_1l_1n_2l_2;\Lambda\rangle\hat{\Lambda}\hat{j}(-1)^{j+L+S+\Lambda} \begin{Bmatrix} j & L & J \\ \Lambda & S & l \end{Bmatrix} \\ &\times \hat{j}_1\hat{j}_2\hat{\Lambda}\hat{S} \begin{Bmatrix} l_1 & \frac{1}{2} & j_1 \\ l_2 & \frac{1}{2} & j_2 \\ \Lambda & S & J \end{Bmatrix} \left| n(lS)jm_j(\vec{r}),NLM_L(\vec{R}),TM_T \right\rangle . \end{aligned} \tag{2.14}$$

Here, n and l are the radial and angular momentum quantum numbers corresponding with the relative motion of the pair. The TM_T (S) determine the isospin (spin) quantum numbers of the pair and $\vec{j} = \vec{l} + \vec{S}$ is the total angular momentum. The cm wave function is described by the quantum numbers NLM_L.

2.1.3 Three-nucleon states

In the previous section, the nas uncoupled states of two nucleons in a HO potential, $|\alpha_1\alpha_2\rangle_{\rm nas}$, are expanded in terms of uncoupled relative and cm two-nucleon states. In this section, a

similar expansion is derived for the uncoupled three-nucleon states $|\alpha_1\alpha_2\alpha_3\rangle_{\rm nas}$. Similar to the transformation to rcm coordinates of Eq. (2.9), is it the purpose to describe the three-nucleon system in terms of the Jacobi coordinates $\vec{r}_{12}$, $\vec{r}_{(12)3}$ and $\vec{R}_{123}$, defined as

$$\vec{r}_{12} = \frac{1}{\sqrt{2}}(\vec{r}_1 - \vec{r}_2), \qquad \vec{R}_{12} = \frac{1}{\sqrt{2}}(\vec{r}_1 + \vec{r}_2), \tag{2.15}$$

$$\vec{r}_{(12)3} = \frac{1}{\sqrt{3}}(\vec{R}_{12} - \sqrt{2}\vec{r}_3), \qquad \vec{R}_{123} = \frac{1}{\sqrt{3}}(\sqrt{2}\vec{R}_{12} + \vec{r}_3). \tag{2.16}$$

The uncoupled nas three-nucleon state reads

$$\begin{aligned} |\alpha_1\alpha_2\alpha_3\rangle_{\rm nas} &= \frac{1}{\sqrt{6}}(1-\mathcal{P}_{12})(|\alpha_1\alpha_2\alpha_3\rangle + |\alpha_2\alpha_3\alpha_1\rangle + |\alpha_3\alpha_1\alpha_2\rangle) \\ &= \frac{1}{\sqrt{3}}(|\alpha_1\alpha_2\rangle_{\rm nas}\,|\alpha_3\rangle + |\alpha_2\alpha_3\rangle_{\rm nas}\,|\alpha_1\rangle + |\alpha_3\alpha_1\rangle_{\rm nas}\,|\alpha_2\rangle). \end{aligned} \tag{2.17}$$

The nas two-nucleon state in the first term, $|\alpha_1\alpha_2\rangle_{\rm nas}$, can be expanded into relative and cm states $\left|n_{12}(l_{12}S_{12})j_{12}m_{j_{12}}(\vec{r}_{12}), N_{12}L_{12}M_{L_{12}}(\vec{R}_{12})\right\rangle$ with Eq. (2.14). The cm states, $\left|N_{12}L_{12}M_{L_{12}}(\vec{R}_{12})\right\rangle$, coupled to the third particle, $|n_3l_3m_{l_3}(\vec{r}_3)\rangle$, are

$$\begin{aligned} \left|N_{12}L_{12}M_{L_{12}}(\vec{R}_{12})n_3l_3m_{l_3}(\vec{r}_3)\right\rangle = \sum_{\Lambda_{123}M_{\Lambda_{123}}} &\langle L_{12}M_{L_{12}}l_3m_{l_3}|\Lambda_{123}M_{\Lambda_{123}}\rangle \\ &\times \left|N_{12}L_{12}(\vec{R}_{12})n_3l_3(\vec{r}_3);\Lambda_{123}M_{\Lambda_{123}}\right\rangle. \end{aligned} \tag{2.18}$$

This coupled two-particle state with coordinates $\vec{R}_{12}$ and $\vec{r}_3$ can be expanded into states with coordinates $\vec{R}_{123}$ and $\vec{r}_{(12)3}$ by the standard transformation brackets (STB)

$$\langle N_{123}L_{123}(\vec{R}_{123})n_{(12)3}l_{(12)3}(\vec{r}_{(12)3});\Lambda_{123}|N_{12}L_{12}(\vec{R}_{12})n_3l_3(\vec{r}_3);\Lambda_{123}\rangle_\beta, \tag{2.19}$$

with $\cos\frac{\beta}{2} = \frac{1}{\sqrt{3}}$. The STB are defined in Appendix A.2. After some trivial Racah-Wigner algebra, the first term of Eq. (2.17), $|\alpha_1\alpha_2\rangle_{\rm nas}\,|\alpha_3\rangle$, can be expanded in terms of the states

$$\begin{aligned} &\left|n_{12}(l_{12}S_{12})j_{12}m_{j_{12}}T_{12}M_{T_{12}}(\vec{r}_{12})N_{123}L_{123}M_{L_{123}}(\vec{R}_{123})\right\rangle \\ &\times \left|n_{(12)3}l_{(12)3}m_{l_{(12)3}}(\vec{r}_{(12)3})m_{s_3}t_3\right\rangle, \end{aligned} \tag{2.20}$$

where m_{s_3} is the spin of the third particle. The $\left|N_{123}L_{123}M_{L_{123}}(\vec{R}_{123})\right\rangle$ state describes the cm motion of the three-nucleon system. The $|n_{12}(l_{12}S_{12})j_{12}m_{j_{12}}T_{12}M_{T_{12}}(\vec{r}_{12})\rangle$ describes the relative motion of the $(\alpha_1\alpha_2)$ nucleon pair. Here, $T_{12}M_{T_{12}}$ (S_{12}) determine the total isospin (spin) of the $(\alpha_1\alpha_2)$ pair and $\vec{j}_{12} = \vec{l}_{12} + \vec{S}_{12}$. The $\left|n_{(12)3}l_{(12)3}m_{l_{(12)3}}(\vec{r}_{(12)3})\right\rangle$ describes the relative motion of the nucleon α_3 and the cm of the $(\alpha_1\alpha_2)$ pair.

Similar, the second and third term of Eq. (2.17) can respectively be expanded into the states

$$\begin{aligned} &\left|n_{23}(l_{23}S_{23})j_{23}m_{j_{23}}T_{23}M_{T_{23}}(\vec{r}_{12})N_{123}L_{123}M_{L_{123}}(\vec{R}_{123})\right\rangle \\ &\times \left|n_{(23)1}l_{(23)1}m_{l_{(23)1}}(\vec{r}_{(12)3})m_{s_1}t_1\right\rangle, \end{aligned} \tag{2.21}$$

and

$$\left|n_{13}(l_{13}S_{13})j_{13}m_{j_{13}}T_{13}M_{T_{13}}(\vec{r}_{12})N_{123}L_{123}M_{L_{123}}(\vec{R}_{123})\right\rangle \times \left|n_{(13)2}l_{(13)2}m_{l_{(13)2}}(\vec{r}_{(12)3})m_{s_2}t_2\right\rangle . \tag{2.22}$$

2.1.4 The Woods-Saxon potential

The Woods-Saxon (WS) Hamiltonian is defined by

$$\widehat{H} = -\frac{\hbar^2}{2\mu}\nabla^2 + V(r) + V_C(r) + \frac{1}{r}\frac{\partial}{\partial\, r}V_{SO}(r)\vec{l}\cdot\vec{s}. \tag{2.23}$$

Considering the WS potential as a two-body problem (nucleon and $A-1$ core) lead to the introduction of a reduced mass,

$$\mu = \left(\frac{1}{m_{n/p}} + \frac{1}{M'}\right)^{-1}, \tag{2.24}$$

where $m_{n/p}$ is the neutron/proton mass and M' is the total mass of the $A-1$ core. The radial potential consists of three components: a central $V(r)$, a Coulomb $V_C(r)$ and a spin-orbit $V_{SO}(r)$ potential. A more detailed discussion of the origin, shape and parametrization of the WS potential is given in Appendix B. The solution of the corresponding Schrödinger equation can be written in spatial polar coordinates as

$$\begin{aligned}\psi^{\rm WS}_{nljm_jt}(\vec{x}) \equiv& \langle\vec{x}|nljm_jt\rangle_{\rm WS}\\ =& \sum_{ms}\langle lm\frac{1}{2}s|jm_j\rangle R^{\rm WS}_{nlj}(r)Y_{lm}(\Omega)\chi_{\frac{1}{2}s}(\vec{\sigma})\xi_{\frac{1}{2}t}(\vec{\tau}),\end{aligned} \tag{2.25}$$

where $\vec{x}\equiv(\vec{r},\vec{\sigma},\vec{\tau})$ is the shorthand notation for the spatial, spin and isospin coordinates, and $\chi_{\frac{1}{2}s}$ and $\xi_{\frac{1}{2}t}$ are the spin and isospin wave function respectively. Unlike the HO radial wave functions $R_{nl}(r)$ in Eq. (2.3), the WS radial wave functions $R^{WS}_{nlj}(r)$ depend on the total angular momentum j of the single-particle state. It would be convenient if one could transform the two-nucleon WS states from cw coordinates to rcm coordinates, as is done for the two-nucleon HO states in Section 2.1.2. However, there is no WS equivalent of the HO Moshinsky transformation bracket. Therefore, the WS single-particle wave functions $R^{WS}_{nlj}(r)Y_{lm}(\Omega)$ are expanded in HO single-particle wave functions $\psi_{n'l'm'}(\vec{r})$,

$$\begin{aligned}R^{\rm WS}_{nlj}(r)Y_{lm}(\Omega) =& \sum_{n'l'm'}\psi_{n'l'm'}(\vec{r})\int d\vec{r}\,'\ \psi_{n'l'm'}(\vec{r}\,')R^{\rm WS}(r')Y_{lm}(\Omega')\\ =& \sum_{n'}\psi_{n'lm}(\vec{r})\int dr'\ r'^2R_{n'l}(r')R^{\rm WS}_{nlj}(r')\\ =& \sum_{n'}\psi_{n'lm}(\vec{r})\langle n'l|nlj\rangle_{\rm WS}.\end{aligned} \tag{2.26}$$

The sum over n' is cut off when $\langle n'l|nlj\rangle_{\rm WS}\leq 10^{-5}$ for n' at least 3. The accuracy of the integrals is same as the accuracy of the numerical integrations discussed Appendix E.3 For most WS wave function, the expansion up to $n'=5$ give a very good approximation.

With the Eq. (2.26), the nas uncoupled state of two nucleons in a WS basis can be expanded into HO states

$$|\alpha_1\alpha_2\rangle_{\text{WS, nas}} = \sum_{n_1'n_2'} \langle n_1'l_1|n_1l_1j_1\rangle_{\text{WS}}\ \langle n_2'l_2|n_2l_2j_2\rangle_{\text{WS}} \times |n_1'l_1j_1m_{j_1}t_1n_2'l_2j_2m_{j_2}t_2\rangle_{\text{nas}}\,. \tag{2.27}$$

Subsequently, the two-nucleon HO state $|n_1'l_1j_1m_{j_1}t_1n_2'l_2j_2m_{j_2}t_2\rangle_{\text{nas}}$ can be transformed to rcm coordinates and quantum numbers using Eq. (2.14). The two-nucleon WS state $|\alpha_1\alpha_2\rangle_{\text{WS, nas}}$ is now expanded into relative and cm two-nucleon HO states. An analogous derivation of the three-nucleon WS states can be outlined. The expansion of Eq. (2.27) is also applicable for two-nucleon states in alternate potentials.

2.2 Ground-state correlations

A time-honored method to account for correlations in IPMs is to shift the complexity induced by the correlations from the wave functions to the operators [3, 4]. The correlated wave functions $|\Psi\rangle$ are constructed by applying a many-body correlation operator $\widehat{\mathcal{G}}$ to the uncorrelated wave functions $|\Phi\rangle$. The (uncorrelated) IPM model ground-state of nucleus A, $|\Phi\rangle$ can be written as a Slater determinant of single-nucleon wave functions $|\phi_{\alpha_i}\rangle$,

$$\Phi\left(\vec{x}_1, \vec{x}_2, \ldots, \vec{x}_A\right) = \frac{1}{\sqrt{A!}} \det\left[\phi_{\alpha_i}\left(\vec{x_j}\right)\right], \tag{2.28}$$

where $\vec{x}_i \equiv (\vec{r}_i, \vec{\sigma}_i, \vec{\tau}_i)$ is the shorthand notation of the spatial, spin and isospin coordinate of nucleon i. As in Section 2.1, $\alpha_i \equiv n_i l_i j_i m_{j_i} t_i$ are the single-nucleon quantum numbers. Unless otherwise stated, it is implicitly assumed that the IPM under consideration is the HO model. The introduction of correlation functions is effective in correcting IPM wave functions. However, it is important to keep in mind that is does not restore translational invariance.

The correlation operator $\widehat{\mathcal{G}}$ corrects the IPM Slater determinant $|\Phi\rangle$ for short-range and other correlations:

$$|\Psi\rangle = \frac{1}{\sqrt{\mathcal{N}}} \widehat{\mathcal{G}}\,|\Phi\rangle\,, \tag{2.29}$$

with the normalization factor $\mathcal{N} \equiv \langle\Phi|\,\widehat{\mathcal{G}}^\dagger\widehat{\mathcal{G}}\,|\Phi\rangle$. Determining $\widehat{\mathcal{G}}$ represents a major challenge. One can, however, be guided by the knowledge of the basic features of the nucleon-nucleon (NN) force. For the correlation operator $\widehat{\mathcal{G}}$, one often considers a similar structure as the one-boson exchange parametrization of the NN force. Therefore, one obtains several terms,

$$\widehat{\mathcal{G}} = \widehat{\mathcal{S}} \prod_{i<j}^{A} \hat{f}(r_{ij}), \tag{2.30}$$

where $r_{ij} = |\vec{r}_i - \vec{r}_j|$, $\widehat{\mathcal{S}}$ is the symmetrization operator and

$$\hat{f}(r_{ij}) = \sum_{p=1}^{N} \hat{f}^p(r_{ij}) = \sum_{p=1}^{N} f^p(r_{ij})\mathcal{O}_{ij}^p. \tag{2.31}$$

The following operators are usually part of the NN force parametrization

$$\begin{aligned}
&\mathcal{O}^{p=1}(i,j) \equiv \mathcal{O}^{c}(i,j) = 1, && \mathcal{O}^{p=4}(i,j) \equiv \mathcal{O}^{\sigma\tau}(i,j) = (\vec{\sigma}_i \cdot \vec{\sigma}_j)(\vec{\tau}_i \cdot \vec{\tau}_j),\\
&\mathcal{O}^{p=2}(i,j) \equiv \mathcal{O}^{\sigma}(i,j) = \vec{\sigma}_i \cdot \vec{\sigma}_j, && \mathcal{O}^{p=5}(i,j) \equiv \mathcal{O}^{t}(i,j) = \widehat{S}_{ij}, \\
&\mathcal{O}^{p=3}(i,j) \equiv \mathcal{O}^{\tau}(i,j) = \vec{\tau}_i \cdot \vec{\tau}_j, && \mathcal{O}^{p=6}(i,j) \equiv \mathcal{O}^{t\tau}(i,j) = \widehat{S}_{ij}(\vec{\tau}_i \cdot \vec{\tau}_j),
\end{aligned} \tag{2.32}$$

where $\widehat{S}_{ij}$ is the tensor operator, $\widehat{S}_{ij} = \frac{3}{r_{ij}^2}(\vec{\sigma}_i \cdot \vec{r}_{ij})(\vec{\sigma}_j \cdot \vec{r}_{ij}) - \vec{\sigma}_i \cdot \vec{\sigma}_j$. This is only a selection of the operators which are commonly considered.

Often, it has been reported [5–8] that of all of the above components the central (or Jastrow) ($p = 1$), the spin-isospin ($p = 4$) and the tensor ($p = 6$) term are responsible for the majority of the correlation effects in the nuclear system. So, for the remainder of this thesis, the correlation operator is considered to contain at most these terms

$$\begin{aligned}
\widehat{\mathcal{G}} &= \widehat{\mathcal{S}}\left(\prod_{i<j=1}^{A}\left[1 - \hat{g}(i,j) + \hat{s}(i,j) + \hat{t}(i,j)\right]\right) \\
&= \widehat{\mathcal{S}}\left(\prod_{i<j=1}^{A}\left[1 + \hat{l}(i,j)\right]\right).
\end{aligned} \tag{2.33}$$

The introduced shorthand notations for the central, spin-isospin and tensor correlation operators are

$$\hat{g}(i,j) \equiv 1 - f^{p=1}(r_{ij}) = g(r_{ij}), \tag{2.34}$$

$$\hat{s}(i,j) \equiv f^{p=4}(r_{ij})(\vec{\sigma}_i \cdot \vec{\sigma}_j)(\vec{\tau}_i \cdot \vec{\tau}_j) = s(r_{ij})(\vec{\sigma}_i \cdot \vec{\sigma}_j)(\vec{\tau}_i \cdot \vec{\tau}_j), \tag{2.35}$$

$$\hat{t}(i,j) \equiv f^{p=6}(r_{ij})\widehat{S}_{ij}(\vec{\tau}_i \cdot \vec{\tau}_j) = t(r_{ij})\widehat{S}_{ij}(\vec{\tau}_i \cdot \vec{\tau}_j). \tag{2.36}$$

In general, the correlations are introduced as a variational degree of freedom in the nuclear wave function [4, 6, 9]. The optimized correlation function is then determined by minimizing the energy. In principle, the correlations functions can not be considered as universal. They depend for example on the choices made with regard to the NN interaction, the single-particle IPM basis and the approximation scheme. However, as will be pointed out in Section 3.2, tensor correlation function obtained in different models, show great similarity. In contrast, the shape of the central correlation function is far less constraint. Therefore, it could be interesting to study of the effect of different correlation functions on the quantities calculated in this disseration. It is worth stressing that the correlation functions are conceived to constitute a general feature of atomic nuclei and that the correlation functions are predicted to exhibit a very small A dependence.

In the numerical calculations presented in this thesis, we use a set of correlation functions as they have been determined in sophisticated many-body theories. For the central correlation function g, the correlation function from the G-matrix calculations in nuclear matter with the Reid potential by W.H. Dickhoff and C. Gearheart is used [10]. This correlation function heals to zero at $r_{12} \geq \frac{2.5}{\sqrt{2}}$ fm. It has a hard core at short internucleon distances r_{12}, guaranteeing that the nucleons repel each other strongly enough when they come too close. This correlation function has been used succesfully in semi-exclusive $^{16}\mathrm{O}(e,e'p)$ [11] and exlusive $^{12}\mathrm{C}(e,e'pp)$ [12] and $^{16}\mathrm{O}(e,e'pp)$ [13, 14] reactions. For the spin-isospin and tensor correlation functions,

we use those obtained by S. Pieper et al. [6] in a variational calculation for the ground state of ^{16}O with the Argonne v_{14} NN potential [15] and the Urbana VII three-nucleon [16] potential.

The correlation functions are further discussed in Section 3.2 and Appendix C gives their parametrizations.

Usually, evaluating transition matrix elements between correlated states is far from a trivial task. Formally, the procedure in outlined in Ref. [11] amounts to rewriting the matrix element between correlated states

$$\langle \Psi | \, \widehat{\Omega} \, | \Psi \rangle \, , \tag{2.37}$$

as a matrix element between uncorrelated states

$$\frac{1}{\mathcal{N}} \langle \Phi | \, \widehat{\Omega}^{eff} \, | \Phi \rangle \, , \tag{2.38}$$

where the effect of the correlations are implemented in an effective transition operator $\widehat{\Omega}^{eff}$ that combines the effect of the NN correlations and the operator $\widehat{\Omega}$,

$$\widehat{\Omega}^{eff} = \widehat{\mathcal{G}}^{\dagger} \, \widehat{\Omega} \, \widehat{\mathcal{G}} = \left(\prod_{i<j=1}^{A} \left[1 + \hat{l}(i,j) \right] \right)^{\dagger} \widehat{\mathcal{S}}^{\dagger} \, \widehat{\Omega} \, \widehat{\mathcal{S}} \left(\prod_{k<l=1}^{A} \left[1 + \hat{l}(k,l) \right] \right) \tag{2.39}$$

In this work, only one- and two-body operators $\widehat{\Omega}$ are considered,

$$\widehat{\Omega} \equiv \sum_{i=1}^{A} \widehat{\Omega}^{[1]}(i) + \sum_{i<j=1}^{A} \widehat{\Omega}^{[2]}(i,j). \tag{2.40}$$

2.2.1 The low-order correlation operator approximation

The universal character of SRC hints at a local phenomenon, which naturally truncates the corresponding expansions of Eq. (2.39). Recent experimental results discussed in Chapter 1 provide good arguments to justify a low-order correlation operator approximation (LCA) and allows one to treat the short-range nuclear correlations as pair correlations. In the LCA, upon expanding Eq. (2.39) one retains terms linear and quadratic in the correlation operator $\hat{l}$. For the quadratic terms, terms with both correlation operators acting on the same particle pair are retained. Disconnected terms are not considered. This results in the following approximation for the effective operator

$$\begin{aligned} \widehat{\Omega}^{eff} \approx \widehat{\Omega}^{\mathrm{LCA}} = & \left[\sum_{i=1}^{A} \widehat{\Omega}^{[1]}(i) + \sum_{i<j=1}^{A} \widehat{\Omega}^{[2]}(i,j) \right] \\ & + \left(\widehat{\Omega}^{[1],\mathrm{l}} + \widehat{\Omega}^{[2],\mathrm{l}} + \left[\widehat{\Omega}^{[1],\mathrm{l}} \right]^{\dagger} + \left[\widehat{\Omega}^{[2],\mathrm{l}} \right]^{\dagger} + \widehat{\Omega}^{[1],\mathrm{q}} + \widehat{\Omega}^{[2],\mathrm{q}} \right). \end{aligned} \tag{2.41}$$

Here, the index 'l' ('q') refers to the term linear (quadratic) in the correlation operators. The linear correlation operators are

$$\widehat{\Omega}^{[1],\mathrm{l}} = \sum_{i<j} [\Omega^{[1]}(i) + \Omega^{[1]}(j)] \hat{l}(i,j) \tag{2.42}$$

$$\begin{aligned}\widehat{\Omega}^{[2],\mathrm{l}} = &\sum_{i<j} \Omega^{[2]}(i,j)\hat{l}(i,j) + \sum_{i<j<k} \Big[\widehat{\Omega}^{[2]}(i,j)\hat{l}(i,k) + \widehat{\Omega}^{[2]}(i,j)\hat{l}(j,k) \\ &+\widehat{\Omega}^{[2]}(i,k)\hat{l}(i,j) + \widehat{\Omega}^{[2]}(i,k)\hat{l}(j,k) + \widehat{\Omega}^{[2]}(j,k)\hat{l}(i,j) + \widehat{\Omega}^{[2]}(j,k)\hat{l}(i,k)\Big] .\end{aligned} \tag{2.43}$$

The quadratic ones are

$$\widehat{\Omega}^{[1],\mathrm{q}} = \sum_{i<j} \hat{l}^{\dagger}(i,j) \left[\widehat{\Omega}^{[1]}(i) + \widehat{\Omega}^{[1]}(j)\right] \hat{l}(i,j) \tag{2.44}$$

$$\begin{aligned}\widehat{\Omega}^{[2],\mathrm{q}} = &\sum_{i<j} \hat{l}^{\dagger}(i,j)\widehat{\Omega}^{[2]}(i,j)\hat{l}(i,j) \\ &+ \sum_{i<j<k} \Big[\hat{l}^{\dagger}(i,k)\widehat{\Omega}^{[2]}(i,j)\hat{l}(i,k) + \hat{l}^{\dagger}(j,k)\widehat{\Omega}^{[2]}(i,j)\hat{l}(j,k) \\ &\quad +\hat{l}^{\dagger}(i,j)\widehat{\Omega}^{[2]}(i,k)\hat{l}(i,j) + \hat{l}^{\dagger}(j,k)\widehat{\Omega}^{[2]}(i,k)\hat{l}(j,k) \\ &\quad +\hat{l}^{\dagger}(i,j)\widehat{\Omega}^{[2]}(j,k)\hat{l}(i,j) + \hat{l}^{\dagger}(i,k)\widehat{\Omega}^{[2]}(j,k)\hat{l}(i,k)\Big] .\end{aligned} \tag{2.45}$$

In the absence of correlations only the first term in the expansion of Eq. (2.41) would not vanish. At large internucleon distances ($r_{ij} \geq 2.5$ fm), $\hat{l}(i,j) \to 0$ and the effective operator $\widehat{\Omega}^{\mathrm{LCA}}$ heals to the uncorrelated operator $\widehat{\Omega}$. It is worth remarking that the correlations in the bra and ket of the overlap matrix elements are to be treated on the same footing in order to guarantee that the effective operator formalism produces Hermitian operators.

A diagrammatic visualization of the LCA expansion in Eq. (2.41) is shown in Figures 2.1 and 2.2 for the one- and two-body operator respectively.

The LCA effective operator of Eq. (2.41) can be conveniently written as,

$$\widehat{\Omega}^{\mathrm{LCA}} = \widehat{\Omega} + \widehat{\Omega}^{\mathrm{corr}}, \tag{2.46}$$

whereby the operator $\widehat{\Omega}^{\mathrm{corr}}$ contains that part of the operator associated with the correlations,

$$\widehat{\Omega}^{\mathrm{corr}} = \widehat{\Omega}^{[1],\mathrm{l}} + \widehat{\Omega}^{[2],\mathrm{l}} + \left[\widehat{\Omega}^{[1],\mathrm{l}}\right]^{\dagger} + \left[\widehat{\Omega}^{[2],\mathrm{l}}\right]^{\dagger} + \widehat{\Omega}^{[1],\mathrm{q}} + \widehat{\Omega}^{[2],\mathrm{q}}. \tag{2.47}$$

The correlated operator $\widehat{\Omega}^{\mathrm{corr}}$ contains two- and three-body terms and can in general be written as

$$\widehat{\Omega}^{\mathrm{corr}} = \sum_{i<j} \widehat{\Omega}^{\mathrm{corr},[2]}(i,j) + \sum_{i<j<k} \widehat{\Omega}^{\mathrm{corr},[3]}(i,j,k). \tag{2.48}$$

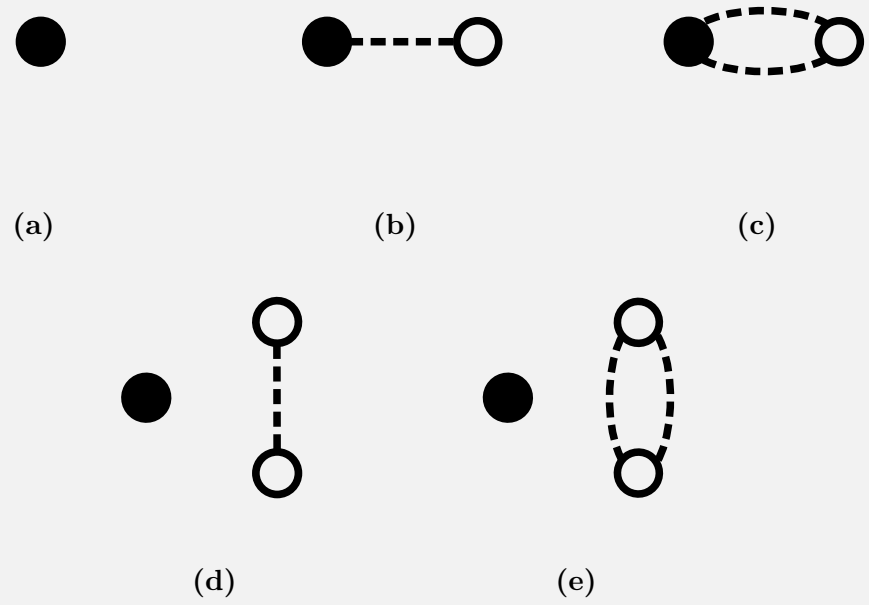

Figure 2.1 – Diagrammatic representation of the LCA expansion of a one-body operator in Eq. (2.41): (a) is the uncorrelated operator $\widehat{\Omega}^{[1]}$, (b) is the linear correlated operator $\widehat{\Omega}^{[1],\mathrm{l}}$ of Eq. (2.42), (c) is the quadratic correlated operator $\widehat{\Omega}^{[1],\mathrm{q}}$ of Eq. (2.44), (d) and (e) are the disconnected term not considered in the LCA. Particles on which operators act are represented by dots. Solid dots are subject to the uncorrelated operator $\widehat{\Omega}^{[1]}$. The correlation operators are represented by dashed lines. Open dots stand for a vertex involving a correlated nucleon. A single dashed line represents an initial $\hat{l}$ or a final $\hat{l}^\dagger$ correlation. A double dashed line represents the combined effect of initial and final correlations.

2.2.2 Matrix elements in the low-order correlation operator approximation

The (uncorrelated) IPM model ground-state of nucleus A, $|\Phi\rangle$ is in Eq. (2.28) defined as a Slater determinant of single-nucleon wave functions $|\phi_{\alpha_i}\rangle$. In the LCA, the matrix element of Eq. (2.38) is then,

$$\begin{aligned}\frac{1}{\mathcal{N}}\langle\Phi|\,\widehat{\Omega}^{\mathrm{LCA}}\,|\Phi\rangle = \frac{1}{\mathcal{N}}\sum_{\alpha}\langle\alpha|\,\widehat{\Omega}^{[1]}(1)\,|\alpha\rangle \\ + \frac{1}{\mathcal{N}}\sum_{\alpha<\beta}\mathrm{nas}\,\langle\alpha\beta|\,\widehat{\Omega}^{[2]}(1,2)\,|\alpha\beta\rangle_{\mathrm{nas}} \\ + \frac{1}{\mathcal{N}}\sum_{\alpha<\beta}\mathrm{nas}\,\langle\alpha\beta|\,\widehat{\Omega}^{\mathrm{corr},[2]}(1,2)\,|\alpha\beta\rangle_{\mathrm{nas}} \\ + \frac{1}{\mathcal{N}}\sum_{\alpha<\beta<\gamma}\mathrm{nas}\,\langle\alpha\beta\gamma|\,\widehat{\Omega}^{\mathrm{corr},[3]}(1,2,3)\,|\alpha\beta\gamma\rangle_{\mathrm{nas}}\,. \end{aligned} \tag{2.49}$$

Here, $|\alpha\beta\rangle_{\mathrm{nas}}$ and $|\alpha\beta\gamma\rangle_{\mathrm{nas}}$ are the uncoupled nas two-nucleon and three-nucleon states discussed in Sections 2.1.2 and 2.1.3, respectively.

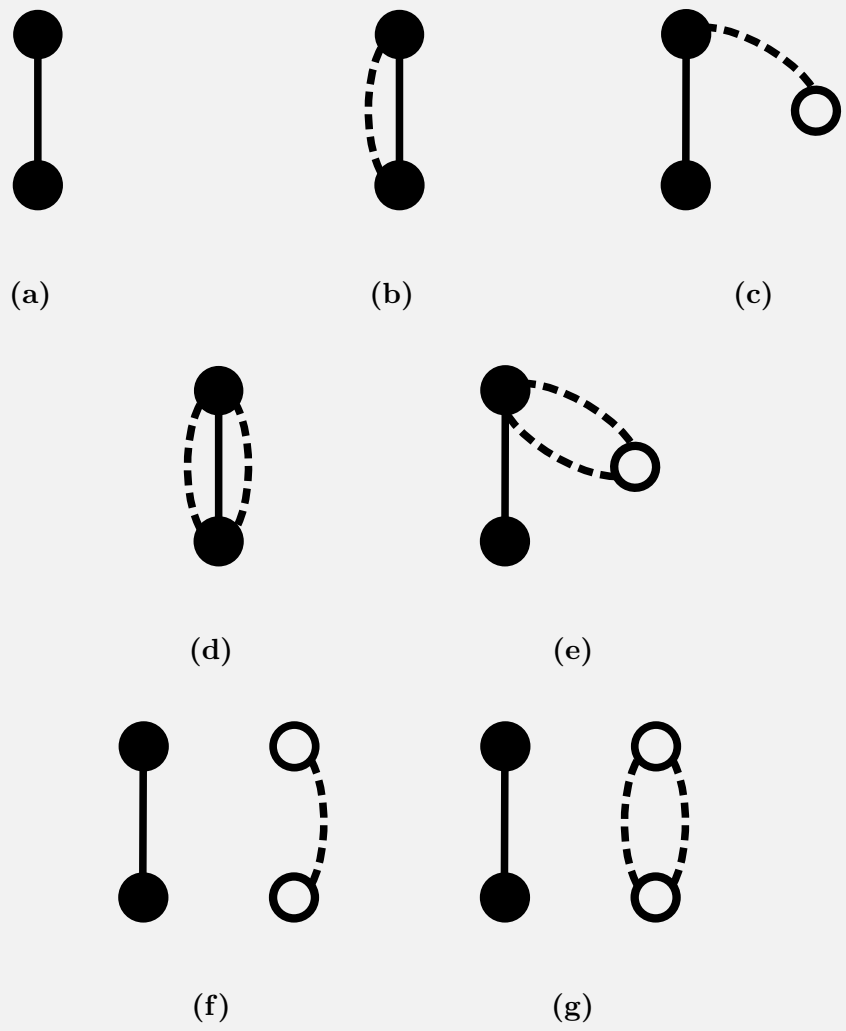

Figure 2.2 – Diagrammatic representation of the LCA expansion of a two-body operator in Eq. (2.41): (a) is the uncorrelated operator $\widehat{\Omega}^{[2]}$, (b) and (c) are the two terms of the linear correlated operator $\widehat{\Omega}^{[2],\mathrm{l}}$ of Eq. (2.43), (d) and (e) are the two terms of the quadratic correlated operator $\widehat{\Omega}^{[2],\mathrm{q}}$ of Eq. (2.45), (f) and (g) are the disconnected terms not considered in the LCA.

In order to preserve the normalization properties, the normalization factor $\mathcal{N}$, is expanded up to the same order as $\widehat{\Omega}^{\mathrm{LCA}}$ in Eq. (2.41). However, one- and two-body operators are expanded differently, and therefore have a different normalization factor, $\mathcal{N}^{[1]}$ and $\mathcal{N}^{[2]}$ respectively,

$$\mathcal{N}^{[1]} = 1 + \frac{2}{A} \sum_{\alpha<\beta}{}_{\mathrm{nas}} \langle \alpha\beta | \, \hat{l}^{\dagger}(1,2) + \hat{l}^{\dagger}(1,2)\hat{l}(1,2) + \hat{l}(1,2) \, |\alpha\beta\rangle_{\mathrm{nas}} \, , \tag{2.50}$$

$$\mathcal{N}^{[2]} = 1 + \frac{2(2A-3)}{A(A-1)} \sum_{\alpha<\beta}{}_{\mathrm{nas}} \langle \alpha\beta | \, \hat{l}^{\dagger}(1,2) + \hat{l}^{\dagger}(1,2)\hat{l}(1,2) + \hat{l}(1,2) \, |\alpha\beta\rangle_{\mathrm{nas}} \, . \tag{2.51}$$

2.3 References

[1] J. Blomqvist and A. Molinari, Nucl. Phys. A **106**, 545 (1968).
[2] M. Moshinsky and Y. Smirnov, *The harmonic oscillator in modern physics* (Harwood Academic Publishers, Amsterdam, 1996).
[3] S. K. Bogner and D. Roscher, Phys. Rev. C **86**, 064304 (2012).
[4] H. Feldmeier, W. Horiuchi, T. Neff, and Y. Suzuki, Phys. Rev. C **84**, 054003 (2011).
[5] C. Ciofi degli Atti and D. Treleani, Phys. Rev. C **60**, 024602 (1999).
[6] S. C. Pieper, R. B. Wiringa, and V. Pandharipande, Phys. Rev. C **46**, 1741 (1992).
[7] O. Benhar, V. R. Pandharipande, and S. C. Pieper, Rev. Mod. Phys. **65**, 817 (1993).
[8] R. Guardiola, P. Moliner, J. Navarro, et al., Nucl. Phys. A **609**, 218 (1996).
[9] M. Alvioli, C. Ciofi degli Atti, and H. Morita, Phys. Rev. C **72**, 054310 (2005).
[10] C. Gearheart, PhD thesis (Washington University, St. Louis, 1994).
[11] S. Janssen, J. Ryckebusch, W. Van Nespen, and D. Debruyne, Nucl. Phys. A **672**, 285 (2000).
[12] K. I. Blomqvist et al., Phys. Lett. B **421**, 71 (1998).
[13] J. Ryckebusch, D. Debruyne, W. Van Nespen, and S. Janssen, Phys. Rev. C **60**, 034604 (1999).
[14] C. J. G. Onderwater, K. Allaart, E. C. Aschenauer, et al., Phys. Rev. Lett. **81**, 2213 (1998).
[15] R. B. Wiringa, R. A. Smith, and T. L. Ainsworth, Phys. Rev. C **29**, 1207 (1984).
[16] R. Schiavilla, V. Pandharipande, and R. Wiringa, Nucl. Phys. A **449**, 219 (1986).

CHAPTER 3

Results

Chapter 1 illustrated the importance of SRC in the nuclear structure. Recent experiments at high-luminosity and high-energy accelerators map out the strength of SRC in nuclei and examine their isospin structure. The purpose of this dissertation is to theoretically quantify the magnitude of SRC in nuclei and study the mass and isospin dependence of the SRC. This chapter presents the numerical calculations which are based on the formalisms introduced in Chapter 2. Sections 3.1 till 3.4 present chronologically the published results by means of the A1 publications in which they were contained [1–4]. The obtained calculations are compared to the experimental observations discussed in Chapter 1.

In sections 3.1 and 3.2, an approximate method to quantify the magnitude of NN and 3N SRC and their mass dependence is proposed. The method is based on the expansion of the low-order correlation operator approximation (LCA) introduced in Section 2.2, which constructs short-ranged correlated wave functions by applying two-body correlations to the mean-field Slater determinant. Due to the local character of the correlations, it is assumed that the correlation operator in the LCA will affect mostly the mean-field nucleons that are "sufficiently close". The two- and three-nucleon transformations discussed in Section 2.1 are used to quantify these nucleon pairs and triples. The scaling factor of inclusive cross section ratios, $a_2(A/^2\mathrm{H})$, introduced in Section 1.3, can be interpreted as a measure for the amount of SRC in the target nucleus A relative to the deuteron. Accordingly, one can link the suggested number of correlated pairs with the $a_2(A/^2\mathrm{H})$ coefficient. However, a direct link is not obvious at all.

The paper in Section 3.3 investigates the factorization properties off the exclusive electro-induced two-nucleon knockout reactions $A(e, e'pN)$. Factorization results in an approximate expression for the cross section which becomes proportional to a specific function of selected dynamic variables. With the use of Monte Carlo simulations, the effect of typically applied kinematic cuts for $A(e, e'pp)$ processes is studied. Also the impact of FSI on the proposed factorization function is considered.

Nuclear SRC typically manifest themselves in the tail part of the nucleon momentum distributions. The LCA is a flexible method for computing the momentum distributions throughout the whole mass range, thereby including the majority of the effects of SRC. Sections 3.4 and 3.6 consider the mass and isospin dependence of respectively the one- and two-nucleon momentum distributions in the LCA. The calculated distributions confirm the assumptions made in Sections 3.1 till 3.3 that the correlations are dominated by nucleon pairs with vanishing relative radial and angular momentum quantum numbers. Of course, the LCA method is only justified if the resulting physical quantities like radii and kinetic energies are in reasonable agreement with data and results from more realistic approaches. The impact of the short-range dynamics on the average nucleon kinetic energies and the root-mean-square radii for symmetric and asymmetric nuclei is also discussed in Section 3.4.

The most important correlation operators concerning correlation over short distances are the central and tensor correlations. Often, the spin-isospin correlations are put forward as another significant contribution. In Section 3.4, spin-isospin correlations are included in the single-nucleon momentum distributions. In Section 3.5, the contribution of the spin-isospin correlations to the single-nucleon momentum distribution is discussed in more detail.

3.1 Counting the number of correlated pairs in a nucleus

Maarten Vanhalst[1], Wim Cosyn[1] and Jan Ryckebusch[1]

[1]Department of Physics and Astronomy, Ghent University,
Proeftuinstraat 86, B-9000 Gent, Belgium

Phys. Rev. C **84**, 031302(R) – Published 21 September 2011

Abstract

We suggest that the number of correlated nucleon pairs in an arbitrary nucleus can be estimated by counting the number of proton-neutron, proton-proton, and neutron-neutron pairs residing in a relative S state. We present numerical calculations of those amounts for the nuclei ^{4}He, ^{9}Be, ^{12}C, ^{27}Al, ^{40}Ca, ^{48}Ca, ^{56}Fe, ^{63}Cu, ^{108}Ag, and ^{197}Au. The results are used to predict the values of the ratios of the per-nucleon electron-nucleus inelastic scattering cross section to the deuteron in the kinematic regime where correlations dominate.

The nucleus is a prototype of a dense quantum liquid with a high packing fraction [1]. Naively one could expect some severe medium effects for the nucleons. Several experimental investigations confirmed the robustness of the nucleons. This is for example reflected in the successful use of the Impulse Approximation (IA) in nuclear reaction theory. In the IA the bound and free nucleon properties (charges, magnetic moments, form factors) are considered identical. A few experiments, however, found indications for medium-modified nuclear properties. Recent $^4\mathrm{He}(\vec{e},e'\vec{p})$ measurements [2], for example, could be described after implementing medium-modified proton form factors. Also in comparing deep inelastic scattering cross sections with those on the deuteron, one finds that under some kinematics conditions the naive scaling ratios do not hold. This observation is known as the EMC (European Muon Collaboration) effect [3] and indicates that under selected kinematics the whole of the nucleus appears to be more than the sum of its constituents.

Recently, it was suggested [4] that the magnitude of the EMC effect can be predicted from the knowledge of the measured $a_2(A/D)$ coefficients. The $a_2(A/D)$ coefficients are defined as

$$a_2(A/D)\left(x_B,Q^2\right)=\frac{2}{A}\frac{\sigma^A\left(x_B,Q^2\right)}{\sigma^D\left(x_B,Q^2\right)}\,, \tag{1}$$

where $\sigma^A\left(x_B,Q^2\right)$ is the inclusive (e,e') cross section for the target nucleus A at a particular four-momentum transfer Q^2 and Bjorken $1.4\leq x_B=\frac{Q^2}{2M\omega}\leq 2$ (M is the nucleon mass, and ω the energy transfer). The observed plateau in the measured x_B dependence of a_2 for $1.4\leq x_B\leq 2$ is a strong indication for scattering from a correlated nucleon pair [5, 6]. As a matter of fact, the a_2 coefficients can be interpreted as a measure for the effect of short-range correlations (SRC) in the target nucleus A relative to deuteron D. In this paper, we suggest

a technique that allows one to estimate the number of nucleon pairs prone to SRC in an arbitrary nucleus $A(N,Z)$. We use these estimates to predict the values of the coefficients $a_2(A/D)$.

A time-honored method to quantify the effect of correlations in classical and quantum systems is the use of correlation functions. The latter encode those portions of the system that depart from mean-field behavior. The realistic (correlated) wave functions $\mid \overline{\Psi}\rangle$ are constructed by applying a many-body correlation operator to the mean-field Slater determinant $\mid \Psi\rangle$ [7, 8]

$$\mid \overline{\Psi} \rangle = \frac{1}{\sqrt{\langle \Psi \mid \widehat{\mathcal{G}}^{\dagger}\widehat{\mathcal{G}} \mid \Psi \rangle}} \, \widehat{\mathcal{G}} \mid \Psi \rangle \, . \tag{2}$$

The $\widehat{\mathcal{G}}$ reflects the full central, spin and isospin dependence of the nucleon-nucleon force but is dominated by the central and tensor correlations

$$\begin{aligned} \widehat{\mathcal{G}} &\approx \widehat{\mathcal{S}} \left[\prod_{i<j=1}^{A} \left(1 - g_c(r_{ij}) + f_{t\tau}(r_{ij}) \widehat{S}_{ij} \vec{\tau}_i . \vec{\tau}_j \right) \right] , \\ &= \widehat{\mathcal{S}} \left[\prod_{i<j=1}^{A} \left(1 - g_c(r_{ij}) + \widehat{t}\,(i,j) \right) \right] , \end{aligned} \tag{3}$$

where $g_c(r_{12})$ and $f_{t\tau}(r_{12})$ are the central and tensor correlation function, $\widehat{S}_{12}$ the tensor operator and $\widehat{\mathcal{S}}$ the symmetrization operator. The correlation functions g_c and $f_{t\tau}$ determine the radial dependence and magnitude of the correlations. Over the last couple of decades, various many-body calculations adopting a plethora of techniques [7–10] have made predictions for the correlation functions g_c and $f_{t\tau}$. These calculations, confirmed the following robust features. First, the two-nucleon correlations represent a local property. This implies that the correlations are universal or only weakly A dependent [11]. This means that g_c and $f_{t\tau}$ are very much confined to the bulk part of the nuclear density and only depend on the inter-nucleon distance. The universality property implies that the $f_{t\tau}\left(r_{ij}\right) \widehat{S}_{ij} \vec{\tau}_i . \vec{\tau}_j$ correlation operator in a nucleus A is not very different from the one that mixes the ${}^3D_1$ and ${}^3S_1$ wave-function components in deuterium [8]. Second, it was observed that for moderate relative pair momenta ($300 \leq k_{12} \leq 600$ MeV), the effect of the tensor correlations is dominant [12, 13]. As the $\widehat{S}_{12}$ exclusively affects nucleon pairs in a spin $S = 1$ state, it makes the proton-neutron (pn) correlations to dominate at moderate values of the relative pair momentum. We stress that the universality property does not imply that the correlation functions g_c and $f_{t\tau}$ are insensitive to model assumptions. The correlation functions depend on the choice of the Hamiltonian, for example. Indeed, a softer Hamiltonian (implying less correlated wave functions) will require other correlation functions than a hard Hamiltonian [14].

Upon computing the response of the nucleus to some one-body operator $\widehat{\Omega} = \sum_{i=1}^{A} \widehat{\Omega}^{[1]}(i)$, into lowest order the effect of the correlations can be implemented by means of an effective transition operator which includes the effect of the correlations [8, 12]

$$\widehat{\Omega}^{eff} = \widehat{\mathcal{G}}^{\dagger} \, \widehat{\Omega} \, \widehat{\mathcal{G}} \approx \widehat{\Omega} + \sum_{i<j=1}^{A} \left(\left[\widehat{\Omega}^{[1]}(i) + \widehat{\Omega}^{[1]}(j) \right] \left[-g_c\left(r_{ij}\right) + \widehat{t}\,(i,j) \right] + h.c. \right) . \tag{4}$$

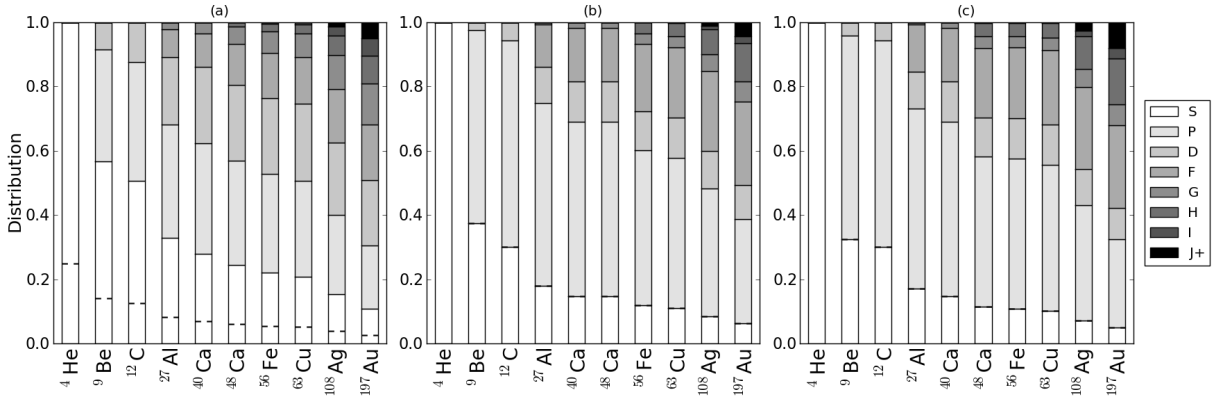

Figure 1 – The distribution of the relative quantum numbers $l = S, P, D, F, G, H, I, \geq J$ for (a) the proton-neutron pairs, (b) the proton-proton pairs, and (c) the neutron-neutron pairs for the various target nuclei. For the proton-neutron pairs there are contributions from ${}^1S_0(T = 1)$ and ${}^3S_1(T = 0)$. The contribution from the ${}^1S_0(T = 1)$ is indicated by the dashed line. Results are obtained in HO basis with $\hbar\omega(\text{MeV}) = 45A^{-\frac{1}{3}} - 25A^{-\frac{2}{3}}$.

Obviously, through the correlations a typical one-body operator (like the γ^* - nucleus interaction in the IA approximation) receives two-nucleon contributions which are completely determined by the product of the correlation functions and the one-body operator. The nucleon-nucleon correlations are very local and will only affect nucleon pairs which are "close". Accordingly, the correlation operators $-g_c\,(r_{ij}) + \widehat{t}\,(i,j)$ act as projection operators and will almost exclusively affect nucleon pairs that reside in a relative S state.

We suggest that the significance of two-nucleons correlations in a certain nucleus $A(N, Z)$ is proportional to the number of relative S states. In order to compute this number, a coordinate transformation from $(\vec{r}_1, \vec{r}_2)$ to $(\vec{r}_{12} = \vec{r}_1 - \vec{r}_2,\ \ \vec{R} = \frac{\vec{r}_1+\vec{r}_2}{2})$ is required. The single-particle states in the Slater determinant $\mid \Psi \rangle$ are denoted by $\alpha_a = (n_a l_a j_a m_a t_a)$, where $t_a = \pm\frac{1}{2}$ is the isospin quantum number. In a harmonic-oscillator (HO) basis the normalized and antisymmetrized two-nucleon wave functions can be written as

$$
\begin{aligned}
|\alpha_a\alpha_b; J_R M_R\rangle = \sum_{LM_L}\sum_{nl}\sum_{N\Lambda}\sum_{SM_S}\sum_{TM_T} & \frac{1}{\sqrt{1+\delta_{\alpha_a\alpha_b}}}\left[1-(-1)^{l+S+T}\right] \\
& \times \mathcal{C}\,(\alpha_a\alpha_b J_R M_R; (nlN\Lambda)LM_L SM_S TM_T) \\
& \times \left|(nl, N\Lambda)LM_L, \left(\frac{1}{2}\frac{1}{2}\right)SM_S, \left(\frac{1}{2}\frac{1}{2}\right)TM_T\right\rangle\ , \qquad (5)
\end{aligned}
$$

where T (S) is the total isospin (spin) of the pair. Further, $|nl\rangle$ ($|N\Lambda\rangle$) is the relative (center of mass, c.m.) pair wave function. The explicit expression for the coefficient $\mathcal{C}$ can be found in Eq. (20) of Ref. [15]. With the aid of the above expression (5) one can project two-nucleon states in $(\vec{r}_1, \vec{r}_2)$ on nucleon states in $\left(\vec{r}_{12}, \vec{R}\right)$ and determine for each pair $(\alpha_a\alpha_b)$ of shell-model states the weight of the various relative (nl) and c.m. $(N\Lambda)$ quantum numbers. For two-nucleon states in a non-HO basis, one can obtain the weights of the various $(nlN\Lambda)$ combinations by expanding the single-particle wave functions in a HO basis.

We have computed the $\mathcal{C}$ coefficients for all target nuclei A either for which the $a_2(A/D)$ coefficient has been published or for which one may expect data in the foreseeable future

[16]. The Slater determinant is constructed by filling the single-particle states as they are determined in the nuclear shell model. We denote the Fermi level for the proton and neutron single-particle states as α_F^p and α_F^n. The quantity

$$\sum_{J_R M_R} \sum_{\alpha_a \leq \alpha_F^p} \sum_{\alpha_b \leq \alpha_F^n} \langle \alpha_a \alpha_b; J_R M_R \, | \alpha_a \alpha_b; J_R M_R \rangle = NZ \ , \tag{6}$$

determines exactly the number of proton-neutron pairs. Similar expressions hold for the number of proton-proton $\left(\frac{Z(Z-1)}{2}\right)$ and neutron-neutron pairs $\left(\frac{N(N-1)}{2}\right)$. After inserting the right-hand side of Eq. (5) in the above expression, one can compute how much of each combination $|(nl, N\Lambda)LM_L, SM_S, TM_T\rangle$ of pair quantum numbers contributes to the total number of pairs. Here, we are particularly interested in the quantum numbers (nl) of the relative wave function. We denote the relative orbital angular momentum $l = 0, 1, 2, \ldots$ as $S, P, D, \ldots$. The numerical calculations get increasingly more time consuming as A increases due to the combinatorics of all possible shell-model pairs. The accuracy of the numerical calculations can be checked against the normalization condition of Eq. (6). In Fig. 1 we display the relative contribution of the various l to the pair wave functions $\left|(nl, N\Lambda)LM_L, \left(\frac{1}{2}\frac{1}{2}\right) SM_S, \left(\frac{1}{2}\frac{1}{2}\right) TM_T\right\rangle$ for the nuclei ^{4}He, ^{9}Be, ^{12}C, ^{27}Al, ^{40}Ca, ^{48}Ca, ^{56}Fe, ^{63}Cu, ^{108}Ag, and ^{197}Au. It is obvious that with increasing A a smaller fraction of the nucleon pairs resides in a relative S state. Whereas, for ^{12}C about 50% of the pn pairs has $l = 0$ for the heaviest nucleus ^{197}Au this is a mere 10%. Accordingly, with increasing A, a smaller and smaller fraction of the nucleon-nucleon pairs will be prone to correlation effects. In addition, there is a strong isospin dependence as the fraction of the proton-neutron pairs residing in a relative S state is substantially larger than for proton-proton and neutron-neutron pairs.

Naively, one could expect that the number of correlated pn (pp) pairs in a nucleus scales like NZ $(\frac{Z(Z-1)}{2}) \sim A^2$. As illustrated in Fig. 2 our calculations rather indicate that the number of pairs that are prone to correlation effects follows a power law $\sim A^{1.44\pm0.01}$. As a matter of fact, we find that the power law is very robust. Calculations with Woods-Saxon (WS) wave functions, for example, result in a computed number of S states that is very close (order of one percent) to the HO predictions. The $N - Z$ asymmetry is reflected in an unequal number of pp, nn, and pn $^1S_0(T = 1)$ pairs. We stress that the ratio of the nn to pp $^1S_0(T = 1)$ pairs can be considerably smaller than predicted by naive $\frac{N(N-1)}{Z(Z-1)}$ combinatorics. For Au, for example, one expects a ratio of 2.24 whereas the data of Fig. 2 lead to 1.77.

Now, we wish to connect the number of pairs with $l = 0$ with the measured values of $a_2(A/D)$. In an inclusive $A(e, e')$ process the correlated part of the electron-nucleus (eA) response (corresponding with the last two terms in Eq. (4)) can be probed by selecting events $1.4 \leq x_B \leq 2$. The magnitude of the response is proportional with a product of two terms. First, the number of pairs that are prone to SRC, and, second, the value of the correlation functions evaluated at the relative momentum of the pair. Indeed, as is pointed out in Refs. [18, 19] in the kinematical regime where correlations are probed, the eA response obeys $\sim F(P)\sigma_{eNN}(k_{12})$, where P is the c.m. momentum of the correlated pair on which the absorption takes place and $F(P)$ is the corresponding c.m. distribution (the combination $F(P)\sigma_{eNN}(k_{12})$ is referred to as the decay function in Ref. [18]). The σ_{eNN} stands for the elementary cross section for electron scattering from a correlated NN pair. The σ_{eNN} contains the Fourier-transformed correlation functions $g_c(k_{12})$ and $f_{t\tau}(k_{12})$ evaluated at the relative momentum k_{12} of the pair. An analytic expression for σ_{epp} can be

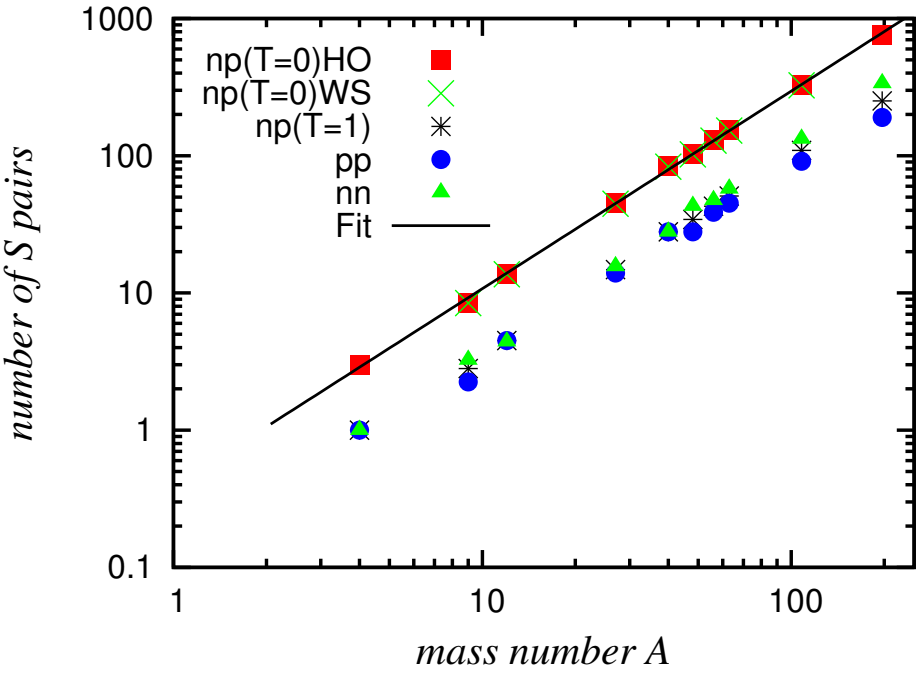

Figure 2 – (Color online) The computed number of pp, nn and pn pairs with $l = 0$. For pn we discriminate between ${}^3S_1(T = 0)$ and ${}^1S_0(T = 1)$. Unless indicated otherwise the results are for a HO basis. For the ${}^3S_1(T = 0)$ pn pairs also the predictions in a WS basis are shown. The parametrizations for the WS potentials are from Ref. [17].

found in Ref. [19]. It is worth stressing that given the kinematics, there are two possible values of k_{12} corresponding with photoabsorption on nucleon "1" and photoabsorption on nucleon "2" of the pair. The dominant contribution to the inclusive $A(e, e')$ cross section for $1.4 \lesssim x_B \lesssim 2$ stems from pairs with $k_F \lesssim k_{12} \lesssim 2k_F$, with k_F the Fermi momentum. In that momentum region, the $g_c(k_{12})$ is substantially smaller than $f_{t\tau}(k_{12})$, which causes the tensor correlated pn pairs to dominate [20] [21] [22].

The universality of the tensor correlations, which translates to the weak A dependence of $f_{t\tau}(k_{12})$, allows one to assume that the cross section σ_{epn} for electron scattering from a correlated proton-neutron pair in the nucleus will almost equal the one for electron scattering from the deuteron, provided that the cross sections are evaluated at equal values of the high relative momentum k_{12} of the pair. In a symbolic way, this feature can be expressed throught the scaling relation $\sigma_{epn}(k_{12}) \approx \sigma_{eD}(k_{12})$. This property is related to the fact that at high momenta the nuclear momentum distributions $n^A(k)$ are very much like scaled deuteron momentum distributions: $n^A(k) \approx C^A n^D(k)$, where C^A is a measure for the amount of pn correlations in A [11] [24].

With the above-mentioned scaling relation $\sigma_{epn}(k_{12}) \approx \sigma_{eD}(k_{12})$ valid at high relative momenta, one can transform the ratio of of Eq. (1) (the per-nucleon electron-nucleus inelastic

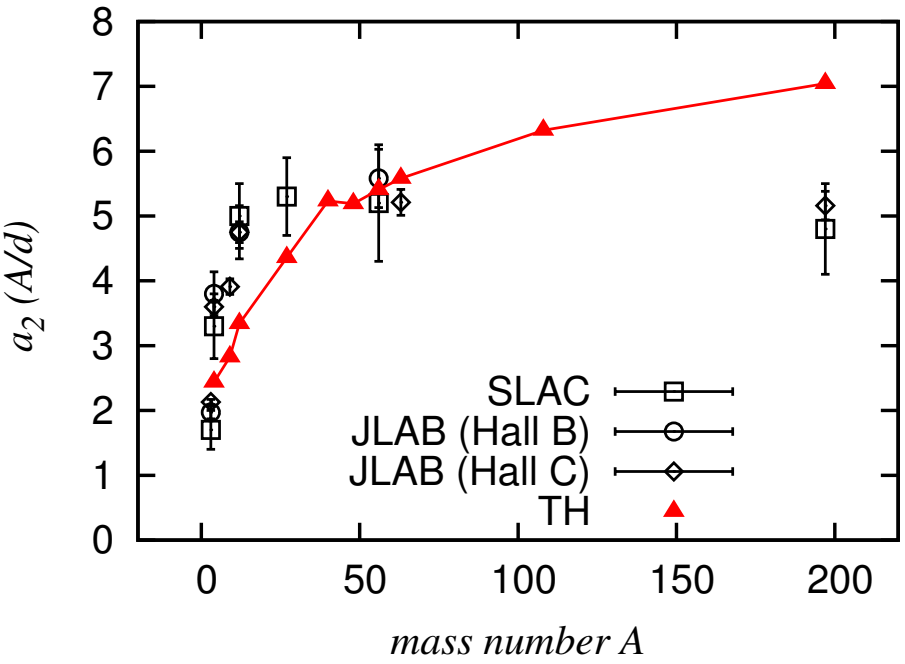

Figure 3 – (Color online) The computed values for the $a_2(A/D)$ for various nuclei. The data are from Refs. [5] (SLAC), [6] (JLAB Hall B) and [23] (JLAB Hall C). The triangles denote the theoretical predictions obtained with the Eq. (7).

Table 1 – The $a_2(A/D)$ values for various nuclei. The data from direct measurements of the nucleus to deuteron cross sections are from Refs. [5] (SLAC), [6] (JLAB Hall B) and [23] (JLAB Hall C). The values of Ref. [4] are phenomenological extractions based on the measured EMC data and the observed linear correlation between the magnitude of the EMC effect and the measured a_2 scaling factor. The quoted values of Ref. [23] are the raw ratios. Ref. [23] also contains corrected values for a_2 which are about 15% smaller.

A	Ref. [5]	Ref. [6]	Ref. [4]	Ref. [23]	Eq. (7)
^{4}He	3.3 ± 0.5	3.80 ± 0.34		3.60 ± 0.10	2.4
^{9}Be			4.08 ± 0.60	3.91 ± 0.12	2.8
^{12}C	5.0 ± 0.5	4.75 ± 0.41		4.75 ± 0.16	3.3
^{27}Al	5.3 ± 0.6		5.13 ± 0.55		4.4
^{40}Ca			5.44 ± 0.70		5.2
^{48}Ca					5.2
^{56}Fe	5.2 ± 0.9	5.58 ± 0.45			5.4
^{63}Cu				5.21 ± 0.20	5.6
^{108}Ag			7.29 ± 0.83		6.3
^{197}Au	4.8 ± 0.7		6.19 ± 0.65	5.16 ± 0.22	7.0

scattering cross section to the deuteron) into the form

$$a_2(A/D) = \frac{2}{A}\frac{\int_{PS} d\vec{k}_{12} d\vec{P} F(P) B^{np}_{l=0}(A) \sigma_{epn}(k_{12})}{\int_{PS} d\vec{k}_{12} \sigma_{eD}(k_{12})} , \approx \frac{2}{A} B^{np}_{l=0}(A) \int_{PS} d\vec{P} F(P) , \quad (7)$$

where the integrations extend over those parts of the phase space (PS) which are compatible with $1.4 \leq x_B \leq 2$. The quantity $B^{np}_{l=0}(A)$ is the number of pn pairs in a relative $|n,l\rangle$ state with the quantum numbers of the deuteron, $^3S_1(T=0)$. One can estimate the $B^{np}_{l=0}(A)$ from Eq. (5) by combining the computed coefficients for all possible $|(n=0\ , l=0, N\Lambda)LM_L, S=1M_S, T=0M_T=0\rangle$ combinations. In Fig. 2 we have summed over all possible n to obtain the total amount of $l=0$ states. For all target nuclei, the $n=0$ contribution dominates, but its relative importance decreases with growing A. The $n=0$ represents 100% of the $l=0$ pn states for ^{4}He, about 80% for the medium-heavy nuclei (Ca, Fe, Cu), 70% for ^{108}Ag, and 62% for ^{197}Au. Pairs residing in a $|n\neq 0, l=0\rangle$ state have a much smaller chance of being "close" than their $|n=0,l=0\rangle$ counterparts and are less prone to SRC effects. We assume that only $|n=0,l=0\rangle$ proton-neutron pairs contribute to $B^{np}_{l=0}(A)$.

The c.m. motion of the pair in finite nuclei (absent in the deuteron) and the imposed conditions in x_B make that a fraction of the correlated proton-neutron pairs are not counted in the $A(e,e')$ signal in the numerator of Eq. (1). The $F(P)$ for a nucleus A can be reliably computed in a mean-field model. Indeed, the ^{12}C$(e,e'pp)$ measurements of Ref. [25] determined $F(P)$ over a large P range and observed it to be compatible with a mean-field prediction. We have performed Monte-Carlo simulations in order to determine the correction factor $\int_{PS} d\vec{P} F(P)$ for all nuclei which are considered here. We find that for $A>4$ about 25% of the correlated pairs are excluded from the experimentally scanned phase space due to the c.m. motion of the correlated pair. From the simulations we observed that the correction factor is only slightly mass number dependent. With this correction factor, the Eq. (7) allows us to make predictions for the $a_2\,(A/D)$. The predictions are contained in Fig. 3 and Table 1 and compared with experimental data. One striking observation from our calculations, is that the predicted $a_2\,(A/D)$ for ^{40}Ca and ^{48}Ca are identical and equal to 5.2. On the basis of naive NZ combinatorics one may have expected a 30% difference between the two. For heavier target nuclei, the data seem to suggest that the $a_2\,(A/D)$ coefficient saturates. Our calculations predict a strong linear rise in the A dependence of the a_2 for $A \lesssim 40$. At higher A one enters a second regime with a much softer linear rise with A. Our calculations increase linearly with $\log(A)$ and tend to underestimate the data at low A and overestimate the data for the heavier nuclei. Final state interactions, for example, which are neglected in this work, may induce some additional A dependence in the a_2 ratio [23]. It is clear that more data are needed to establish the situation at large A. The observed phenomenological linear relationship between the scaling factor a_2 and the magnitude of the EMC effect [4] gives $a_2 = 7.29 \pm 0.83$ for Ag and $a_2 = 6.19 \pm 0.65$ for Au, values that are not inconsistent with our results.

In conclusion, we suggest that the number of correlated pairs in a nucleus is proportional with the number of relative S two-nucleon states. We find this number to obey a power law $dA^{1.44\pm0.01}$ with $d = 0.39 \pm 0.02$ ($d = 0.13 \pm 0.01$) for $T=0$ ($T=1$) proton-neutron

pairs. The power law is robust in that it is independent of the choices made with regard to the single-particle wave functions. We have used the computed amount of $T = 0$ pn pairs to predict the value of the measured $a_2(A/D)$ coefficients, which provide a measure of the number of correlated pairs in the target nucleus A relative to the deuteron. The observed power law in the number of relative S states translates to a linear increase of a_2 with $\log(A)$. We observe that our predictions are not inconsistent with the trend and magnitude of the data, lending support to our suggestion.

This work was supported by the Fund for Scientific Research Flanders. We are grateful to Kris Heyde for useful discussions and comments.

---

[1] S. Wong, *Introductory nuclear physics, second edition* (John Wiley & Sons, 1998).
[2] M. Paolone, S. P. Malace, S. Strauch, et al., Phys. Rev. Lett. **105**, 072001 (2010).
[3] D. F. Geesaman, K. Saito, and A. W. Thomas, Ann. Rev. Nucl. Part. Sci. **45**, 337 (1995).
[4] L. Weinstein, E. Piasetzky, D. Higinbotham, et al., Phys. Rev. Lett. **106**, 052301 (2011).
[5] L. Frankfurt, M. Strikman, D. Day, and M. Sargsian, Phys. Rev. C **48**, 2451 (1993).
[6] K. Egiyan, N. Dashyan, M. Sargsian, et al., Phys. Rev. Lett. **96**, 082501 (2006).
[7] S. C. Pieper, R. B. Wiringa, and V. Pandharipande, Phys. Rev. C **46**, 1741 (1992).
[8] R. Roth, T. Neff, and H. Feldmeier, Prog. Part. Nucl. Phys. **65**, 50 (2010).
[9] M. Alvioli, C. Ciofi degli Atti, and H. Morita, Phys. Rev. Lett. **100**, 162503 (2008).
[10] C. Bisconti, F. A. d. Saavedra, G. Co', and A. Fabrocini, Phys. Rev. C **73**, 054304 (2006).
[11] H. Feldmeier, W. Horiuchi, T. Neff, and Y. Suzuki, Phys. Rev. C **84**, 054003 (2011).
[12] S. Janssen, J. Ryckebusch, W. Van Nespen, and D. Debruyne, Nucl. Phys. A **672**, 285 (2000).
[13] R. Schiavilla, R. B. Wiringa, S. C. Pieper, and J. Carlson, Phys. Rev. Lett. **98**, 132501 (2007).
[14] E. Anderson, S. Bogner, R. Furnstahl, and R. Perry, Phys. Rev. C **82**, 054001 (2010).
[15] J. Ryckebusch, D. Debruyne, and W. Van Nespen, Phys. Rev. C **57**, 1319 (1998).
[16] N. Fomin, Ph.D.Thesis, University of Virginia (2008).
[17] N. Schwierz, I. Wiedenhover, and A. Volya, ArXiv e-prints, 0709.3525 (2007).
[18] L. Frankfurt, M. Sargsian, and M. Strikman, Int. J. Mod. Phys. A **23**, 2991 (2008).
[19] J. Ryckebusch, Phys. Lett. B **383**, 1 (1996).
[20] E. Piasetzky, M. Sargsian, L. Frankfurt, et al., Phys. Rev. Lett. **97**, 162504 (2006).
[21] R. Subedi, R. Shneor, P. Monaghan, et al., Science **320**, 1476 (2008).
[22] H. Baghdasaryan, L. B. Weinstein, J. M. Laget, et al., Phys. Rev. Lett. **105**, 222501 (2010).
[23] N. Fomin, J. Arrington, R. Asaturyan, et al., ArXiv e-prints, 1107.3583 (2011).
[24] C. Ciofi degli Atti and C. B. Mezzetti, Phys. Rev. C **79**, 051302 (2009).
[25] K. I. Blomqvist et al., Phys. Lett. B **421**, 71 (1998).

3.2 Quantifying short-range correlations in nuclei

Maarten Vanhalst[1], Jan Ryckebusch[1] and Wim Cosyn[1]

[1]Department of Physics and Astronomy, Ghent University,
Proeftuinstraat 86, B-9000 Gent, Belgium

Phys. Rev. C **86**, 044619 – Published 17 October 2012

Abstract

Background Short-range correlations (SRC) are an important ingredient of the dynamics of nuclei.

Purpose An approximate method to quantify the magnitude of the two-nucleon (2N) and three-nucleon (3N) short-range correlations (SRC) and their mass dependence is proposed.

Method The proposed method relies on the concept of the "universality" or "local nuclear character" of the SRC. We quantify the SRC by computing the number of independent-particle model (IPM) nucleon pairs and triples which reveal beyond-mean-field behavior. It is argued that those can be identified by counting the number of nucleon pairs and triples in a zero relative orbital momentum state. A method to determine the quantum numbers of pairs and triples in an arbitrary mean-field basis is outlined.

Results The mass dependence of the 2N and 3N SRC is studied. The predictions are compared to measurements. This includes the ratio of the inclusive inelastic electron scattering cross sections of nuclei to ^{2}H and ^{3}He at large values of the Bjorken variable. Corrections stemming from the center-of-mass motion of the pairs are estimated.

Conclusions We find that the relative probability per nucleon for 2N and 3N SRC has a soft dependence with mass number A and that the proton-neutron 2N SRC outnumber the proton-proton (neutron-neutron) 2N SRC. A linear relationship between the magnitude of the EMC effect and the predicted number of proton-neutron SRC pairs is observed. This provides support for the role of local nuclear dynamics on the EMC effect.

1 Introduction

We define the nuclear packing factor (NPF) as the fraction of the nuclear volume that is occupied by nucleons. A rough order of magnitude estimate of the NPF can be arrived at using uniform spheres for the nuclear and nucleon density. The nuclear radius R_A can be reasonably determined from $R_A = 1.2(\text{fm})\ A^{1/3}$. It is not obvious what value of the nucleon radius r_N should be used. In models of relativistic heavy-ion collisions it is customary [1] to use expulsion distances d, which simulate the hard-core NN repulsion, of the order of 1 fm, corresponding with $r_N \approx 0.5$ fm. This leads to NPF=0.07. A recent reanalysis of electron scattering data resulted in a root-mean-square charge radius of the proton $r_p^c = \sqrt{\langle r_p^2 \rangle} = 0.897(18)$ fm [2]. Assuming that the r_p^c is an estimate of the proton and neutron radius one arrives at NPF $= \left(\frac{r_p^c(\text{fm})}{1.2}\right)^3 = 0.42$. It is clear that the computed NPF is very sensitive to the adopted value of the nucleon radius. The estimate of the NPF on the basis of r_p^c should be considered as an upper limit. Indeed, the established value of the nuclear saturation density of 0.17 nucleons/fm^3 corresponds with a mean internucleon distance of 1.8 fm implying that $r_N \leq 0.9$ fm.

From the above, it is clear that one expects that the nucleus is more like a saturated quantum liquid than a gas of freely moving nucleons. Accordingly, the nuclear wave functions receive large corrections from short-range (SRC) and long-range correlations. These days it is common practice to implement the effect of SRC in nuclear computations. Examples include the calculations of matrix elements for double-β decay [3], of event simulations in heavy-ion collisions [4], and of hadron transparencies in nuclei [5].

The EMC effect [6] is the reduction of the cross section for leptonic scattering off a nucleon bound in a nucleus relative to that of a free nucleon (mass M_N). The EMC effect was observed in Deep Inelastic Scattering (DIS) experiments on nuclei at high virtual-photon virtualities $Q^2 = q^2 - \omega^2 \gtrsim 2$ GeV^2 for Bjorken $x_B = \frac{Q^2}{2M_N\omega}$ in the range $0.3 \leq x_B \leq 0.7$. The ratio of per nucleon cross sections is denoted by $R = \frac{2}{A}\frac{\sigma^A}{\sigma^D}$ where σ^A is the cross section for leptonic scattering from the target A. The magnitude of the EMC effect can be quantified by means of the slope $-\frac{dR}{dx_B}$ [7]. Another remarkable feature of the ratio R is that it adopts a constant value (this factor is commonly referred to as the SRC scaling factor $a_2(A/D)$) for $1.5 \lesssim x_B \lesssim 2$ and moderate values of Q^2 [8–10]. It has been suggested [11] that the $a_2(A/D)$ can be related to the high-momentum components of the nuclear wave functions. A phenomenological linear relationship between the $a_2(A/D)$ and the magnitude of the EMC effect expressed as $-\frac{dR}{dx_B}$ has been observed [12–14]. This indicates that the magnitude of the European Muon Collaboration (EMC) effect may be driven by SRC. In this picture the magnitude of the EMC effect is (partly) related to the temporal local density fluctuations which are induced by the high virtualities of the leptonic probe. Recent measurements [7] corroborate this relation between the local nuclear environment and the magnitude of the EMC effect.

Given an arbitrary nucleus $A(N, Z)$ we address the issue of quantifying the number of two-nucleon (2N) pairs prone to SRC and the number of 3N triples prone to SRC. Along the same lines we investigate to what extent the mass dependence of the NN SRC can be captured by some approximate principles. We wish to develop a robust method which is applicable to any nucleus from He to Pb. From this method we expect, for example, that it

allows one to study the mass dependence of the SRC without combining results from various types of calculations.

Momentum distributions contain the information about 1N, 2N, 3N, ... properties of the nuclear ground state. Over the years various methods to compute the nuclear 1N and 2N momentum distributions have been developed. Ab-initio calculations which solve the Schrödinger equation with realistic nucleon-nucleon interactions are available for light nuclei like ^{4}He [15–17]. For medium-weight nuclei ($12 \leq A \leq 40$) truncation schemes based on cluster expansions can be adopted [18]. Correlated-basis function theory has been applied to compute ground-state densities and momentum distributions for doubly-closed-shell nuclei from ^{12}C to ^{208}Pb [19, 20]. Thanks to the enormous progress in theoretical many-body nuclear physics and the availability of nuclear momentum distributions in a broad mass range, times are ripe to learn more about SRC, for example by mapping its A and isospin dependence. It remains notoriously difficult, though, to establish quantitative relationships between observables and the computed momentum distributions [11, 21–25]. Here, we do not attempt a high-precision calculation of momentum distributions. Our goal is to gather insight into the mass and isospin dependence of the SRC from stylized facts of momentum distributions.

In a mean-field model fluctuations are completely ignored. The SRC induce spatio-temporal fluctuations from the mean-field predictions for the nuclear density distributions for example. As a result of SRC, realistic nuclear wave functions reflect the coexistence of single nucleon (mean-field) structures and cluster structures. The clusters account for beyond mean-field behavior. As the nucleon-nucleon interaction is short ranged, the clusters attributed to SRC are predominantly 2N. The central result of this paper asserts that the amount of 2N and 3N SRC in nuclei can be reasonably quantified by counting the number of nucleon pairs and triples in a zero relative orbital state in a mean-field ground-state wave function. In order to quantify the isospin dependence of the 2N and 3N correlations, additional information about the spin dependence of the clusters is necessary.

This paper is organized as follows. Sect. 2 is devoted to a discussion of momentum distributions and of how they can be used to quantify the mass and isospin dependence of SRC. In Sect. 3 we address the issue whether inclusive electron scattering data can be linked to the number of correlated 2N and 3N clusters. Thereby, we deal with both the $a_2(A/D)$ coefficient and the magnitude of the EMC effect.

2 Quantifying nuclear correlations

In this section we start from stylized facts of nuclear momentum distributions in order to arrive at criteria to quantify the 2N and 3N SRC in nuclei. Our focus is on their mass dependence.

2.1 Nuclear momentum distributions

In this subsection we provide the definitions and normalization conventions of the nuclear momentum distributions used here. For the sake of the simplicity of the notations, we will

only consider the positional degrees-of-freedom. Unless stated otherwise the spin - and isospin degrees-of-freedom are not explicitly written in the expressions.

The one-body momentum distribution of nuclei is defined as

$$P_1\left(\vec{k}\right) = \frac{1}{(2\pi)^3}\int d\vec{r}_1 \int d\vec{r}_1{}' e^{i\vec{k}\cdot\left(\vec{r}_1-\vec{r}_1{}'\right)}\rho_1\left(\vec{r}_1,\vec{r}_1{}'\right) \ , \tag{1}$$

where $\rho_1\left(\vec{r}_1,\vec{r}_1{}'\right)$ is the one-body non-diagonal density matrix

$$\rho_1\left(\vec{r}_1,\vec{r}_1{}'\right) = \int \left\{d\vec{r}_{2-N}\right\} \Psi_A^*\left(\vec{r}_1,\vec{r}_2,\vec{r}_3,\ldots,\vec{r}_A\right)\Psi_A\left(\vec{r}_1{}',\vec{r}_2,\vec{r}_3,\ldots,\vec{r}_A\right) \ . \tag{2}$$

Here, Ψ_A is the ground-state wave function of the nucleus A and the notation

$$\left\{d\vec{r}_{i-N}\right\} = d\vec{r}_i d\vec{r}_{i+1}\ldots d\vec{r}_A \ , \tag{3}$$

has been introduced. For $\langle\Psi_A|\ \Psi_A\rangle = 1$, one has that

$$\int d\vec{k} P_1\left(\vec{k}\right) = 1 \ . \tag{4}$$

We introduce relative and center-of-mass (c.m.) coordinates of nucleon pairs in coordinate $\left(\vec{r}_{12},\vec{R}_{12}\right)$ and momentum space $\left(\vec{k}_{12},\vec{P}_{12}\right)$

$$\vec{r}_{12} = \frac{\vec{r}_1-\vec{r}_2}{\sqrt{2}} \qquad \vec{R}_{12} = \frac{\vec{r}_1+\vec{r}_2}{\sqrt{2}} \tag{5}$$

$$\vec{k}_{12} = \frac{\vec{k}_1-\vec{k}_2}{\sqrt{2}} \qquad \vec{P}_{12} = \frac{\vec{k}_1+\vec{k}_2}{\sqrt{2}} \ , \tag{6}$$

and define the two-body momentum distribution in the standard fashion as

$$P_2\left(\vec{k}_{12},\vec{P}_{12}\right) = \frac{1}{(2\pi)^6}\int d\vec{r}_{12}\int d\vec{R}_{12}\int d\vec{r}_{12}{}'\int d\vec{R}_{12}{}' \times e^{i\vec{k}_{12}\cdot\left(\vec{r}_{12}-\vec{r}_{12}{}'\right)}e^{i\vec{P}_{12}\cdot\left(\vec{R}_{12}-\vec{R}_{12}{}'\right)}\rho_2\left(\vec{r}_{12},\vec{R}_{12};\vec{r}_{12}{}',\vec{R}_{12}{}'\right) \ . \tag{7}$$

Here, $\rho_2\left(\vec{r}_{12},\vec{R}_{12};\vec{r}_{12}{}',\vec{R}_{12}{}'\right)$ is the two-body non-diagonal density matrix

$$\begin{aligned}
&\rho_2\left(\vec{r}_{12},\vec{R}_{12};\vec{r}_{12}{}',\vec{R}_{12}{}'\right)\\
&= \rho_2\Big(\vec{r}_1 = \tfrac{+\vec{r}_{12}+\vec{R}_{12}}{\sqrt{2}},\vec{r}_2 = \tfrac{-\vec{r}_{12}+\vec{R}_{12}}{\sqrt{2}};\vec{r}_1{}' = \tfrac{+\vec{r}_{12}{}'+\vec{R}_{12}{}'}{\sqrt{2}},\vec{r}_2{}' = \tfrac{-\vec{r}_{12}{}'+\vec{R}_{12}{}'}{\sqrt{2}}\Big)\\
&= \int \left\{d\vec{r}_{3-N}\right\}\Psi_A^*\left(\vec{r}_1,\vec{r}_2,\vec{r}_3,\ldots,\vec{r}_A\right)\Psi_A\left(\vec{r}_1{}',\vec{r}_2{}',\vec{r}_3,\ldots,\vec{r}_A\right) \ .
\end{aligned} \tag{8}$$

One has the normalization condition

$$\int d\vec{k}_{12}\int d\vec{P}_{12} P_2\left(\vec{k}_{12},\vec{P}_{12}\right) = 1 \ . \tag{9}$$

In a spherically symmetric system, the two-body momentum distribution $P_2\left(\vec{k}_{12},\vec{P}_{12}\right)$ depends on three independent variables. One of the most obvious choices [26] is

$$\left(\mid \vec{k}_{12} \mid, \mid \vec{P}_{12} \mid, \theta_{\vec{k}_{12}\vec{P}_{12}}\right) \ , \tag{10}$$

where $\theta_{\vec{k}_{12}\vec{P}_{12}}$ is the angle between $\vec{P}_{12}$ and $\vec{k}_{12}$.

The distributions $P_1\left(\vec{k}\right)$ and $P_2\left(\vec{k}_{12},\vec{P}_{12}\right)$ reflect all information about one-nucleon and two-nucleon properties contained in the ground-state wave function. Other quantities can be directly related to them. Here, we list some of the most frequently used ones.

The two-body c.m. momentum distribution is defined as $\left(d\vec{P}_{12} = P_{12}^2 dP_{12} d\Omega_{P_{12}}\right)$,

$$P_2(P_{12}) = \int d\vec{k}_{12} \int d\Omega_{P_{12}} P_2\left(\vec{k}_{12},\vec{P}_{12}\right) \ . \tag{11}$$

The quantity $P_{12}^2 P_2\left(P_{12}\right) dP_{12}$ is related to the probability of finding a nucleon pair in A with c.m. momentum $P_{12} =\mid \vec{P}_{12} \mid$ irrespective of the value and direction of the relative momentum $\vec{k}_{12}$ of the pair. The $P_2\left(P_{12}\right)$ receives contributions from the proton-proton, neutron-neutron, and proton-neutron pairs

$$P_2\left(P_{12}\right) = P_2^{pp}\left(P_{12}\right) + P_2^{nn}\left(P_{12}\right) + P_2^{pn}\left(P_{12}\right) \ . \tag{12}$$

In a spherically symmetric nucleus, it is convenient to introduce the quantities

$$n_1\left(k\right) = \int d\Omega_k P_1\left(\vec{k}\right) \ , \tag{13}$$

$$n_2\left(k_{12},P_{12}\right) = \int d\Omega_{k_{12}} \int d\Omega_{P_{12}} P_2\left(\vec{k}_{12},\vec{P}_{12}\right) \ . \tag{14}$$

The quantity $n_1\left(k\right) k^2 dk$ gives the probability of finding a nucleon with a momentum in the interval $[k, k+dk]$. The $n_2\left(k_{12},P_{12}\right) k_{12}^2 dk_{12} P_{12}^2 dP_{12}$ is the combined probability of finding a nucleon pair with a relative momentum in $[k_{12}, k_{12}+dk_{12}]$ and c.m. momentum in $[P_{12}, P_{12}+dP_{12}]$.

2.2 Mean-field approximation and beyond

A time-honored method to account for the effect of correlations in classical and quantum systems is the introduction of correlation functions. Realistic nuclear wave functions $\mid \Psi\rangle$ can be computed after applying a many-body correlation operator to a Slater determinant $\mid \Psi^{MF}\rangle$

$$\mid \Psi_A\rangle = \frac{1}{\sqrt{\langle \ \Psi_A^{MF} \mid \widehat{\mathcal{G}}^\dagger \widehat{\mathcal{G}} \mid \Psi_A^{MF} \ \rangle}} \ \widehat{\mathcal{G}} \mid \Psi_A^{MF} \ \rangle \ . \tag{15}$$

The nuclear correlation operator $\widehat{\mathcal{G}}$ is complicated but as far as the short-range correlations are concerned, it is dominated by the central, tensor and spin correlations [27]

$$\widehat{\mathcal{G}} \approx \widehat{\mathcal{S}}\left[\prod_{i<j=1}^{A}\left(1 - g_c(r_{ij}) + f_{t\tau}(r_{ij}) S_{ij} \vec{\tau}_i \cdot \vec{\tau}_j + f_{s\tau}(r_{ij}) \vec{\sigma}_i \cdot \vec{\sigma}_j \ \ \vec{\tau}_i \cdot \vec{\tau}_j\right)\right] \ , \tag{16}$$

where $g_c(r_{12})$, $f_{t\tau}(r_{12})$, $f_{s\tau}(r_{12})$ are the central, tensor, and spin-isospin correlation function, $\widehat{\mathcal{S}}$ the symmetrization operator and S_{12} the tensor operator

$$\begin{aligned} S_{12} &= \frac{3}{r_{12}^2}\vec{\sigma}_1\cdot\vec{r}_{12}\ \ \vec{\sigma}_2\cdot\vec{r}_{12} - \vec{\sigma}_1\cdot\vec{\sigma}_2 \\ &= \sqrt{\frac{24\pi}{5}}\sum_{M_L}(-1)^{M_L}\,Y_{2M_L}\left(\Omega_{r_{12}}\right)\left[\vec{\sigma}_1\otimes\vec{\sigma}_2\right]_{2-M_L}\ . \end{aligned} \tag{17}$$

The operator S_{12} admixes relative two-nucleon states of different orbital angular momentum, is operative on triplet spin states only, and conserves the total angular momentum of the pair.

We stress that the correlation functions cannot be considered as universal and that in some many-body approaches, particularly for light nuclei, they do not appear. The momentum distributions which result from the calculations depend on the interplay between many factors, including the choices made with regard to the nucleon-nucleon interaction, the single-particle basis (if applicable), the many-body approximation scheme, ... As a matter of fact, different nucleon-nucleon interactions and many-body approaches may produce, particularly in the region of SRC (short distances/high momenta), momentum distributions which are very similar (see, e.g. Refs. [15, 17, 28, 29]).

The $g_c(r_{12})$ quantifies how strongly two point-like nucleons treated as quasi-particles, are spatially correlated when they are a distance r_{12} apart. The $g_c(r_{12})$ gives rise to local density fluctuations about the mean-field predictions from the reference state $\mid \Psi_A^{MF} \rangle$. The GD $g_c(r_{12})$ (computed for nuclear matter) from Fig. 1 is not very different from the one for monoatomic molecules in a liquid. Indeed, for $r_{12} \to 0$ one has that the GD $g_c\left(r_{12}\right) \to 1$ which reflects the fact that nucleons have a finite size (or, in other words they are subject to a nucleon-nucleon interaction with a hard core). For values of r_{12} which are larger than a few times the diameter of a nucleon, the $g_c\left(r_{12}\right) \to 0$. From this we conclude that the fluctuations from the MF densities are confined to short internucleon distances. Therefore, the 2N SRC are a highly local property and are insensitive to the properties of the other surrounding nucleons. This is the fundamental reason why SRC can be considered as "universal" [17]. Whereas a large model dependence for the g_c is observed, the $f_{t\tau}$ seems to be much better constrained. We have added the squared D-wave component of the deuteron wave function $\Psi_D\left(k_{12}\right)$ in Fig. 1. Obviously, the momentum dependence of $\mid f_{t\tau}\left(k_{12}\right)\mid^2$ and the deuteron momentum distribution $n_D \equiv \mid \Psi_D\left(k_{12}\right)\mid^2$ are highly similar.

The effect of the correlation functions on the momentum distributions can be roughly estimated from their squared Fourier transforms. The effect of the tensor correlation function is largest for moderate relative momenta ($100 \lesssim k_{12} \lesssim 500$) MeV. For very large k_{12}, the g_c is the dominant contribution. The harder the $g_c(r_{12})$ the stronger the effect of correlations. We stress that in the plane-wave impulse approximation, the SRC contribution to the $(e, e'pp)$ cross section is proportional to $\left|g_c\left(k_{12}\right)\right|^2$ [25].

After introducing the wave functions of Eq. (15), the one-body and two-body momentum distributions of Eqs. (1) and (7) can be written as

$$P_1\left(\vec{k}\right) = P_1^{(0)}\left(\vec{k}\right) + P_1^{(1)}\left(\vec{k}\right)\ , \tag{18}$$

$$P_2\left(\vec{k}_{12},\vec{P}_{12}\right) = P_2^{(0)}\left(\vec{k}_{12},\vec{P}_{12}\right) + P_2^{(1)}\left(\vec{k}_{12},\vec{P}_{12}\right)\ . \tag{19}$$

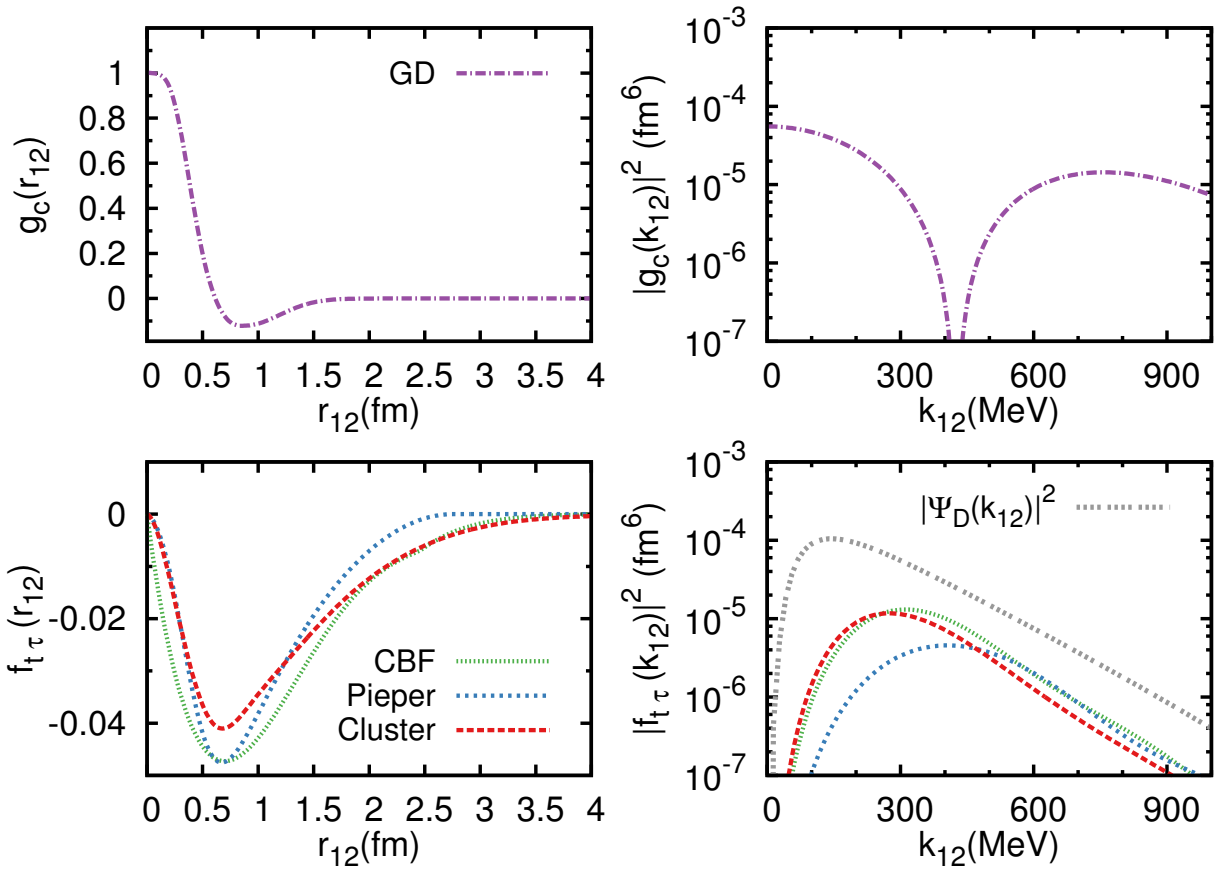

Figure 1 – (color online). The radial and momentum dependence of a central and some tensor correlation functions. The central correlation function "GD" is for nuclear matter and from Ref. [30]. The tensor correlation function "Pieper" is for ^{16}O and from Ref. [28], the "CBF" one is for ^{16}O and from Ref. [29], and the "cluster" one is for ^{16}O and from Ref. [31], $\Psi_D\left(k_{12}\right)$ is the $l=2$ component of the non-relativistic deuteron wave function generated with the Paris potential [32, 33] (not to scale).

The $P_1^{(0)}$ and $P_2^{(0)}$ are the mean-field parts and are fully determined by the Slater determinant $\mid \Psi_A^{MF} \rangle$. After inserting the expressions (1) and (2) into the Eq. (13) one obtains

$$n_1^{(0)}\left(k\right) = \int d\Omega_k P_1^{(0)}\left(\vec{k}\right) = \frac{2}{\pi} \sum_{n_h l_h j_h} \left(2j_h+1\right) S_{n_h l_h j_h} \left(\int dr r^2 j_{l_h}(kr) \psi_{n_h l_h j_h}(r) \right)^2 , \quad (20)$$

where $j_l(r)$ is the spherical Bessel function of the first kind and the sum extends over all occupied single-particle states. The $0 \leq S_{n_h l_h j_h} \leq 1$ is the occupation probability of the corresponding single-particle state. The presence of short-range and long-range correlations leads to occupation probabilities smaller than one. With the adopted normalization convention of Eq. (4) one typically obtains that

$$\int dk k^2 n_1^{(0)}\left(k\right) \approx 0.6 - 0.8 \, , \quad (21)$$

or, about $60-80\%$ of the nucleons are mean-field like. We stress that a considerable fraction of this depletion can be attributed to long-range correlations, an effect which is not considered here.

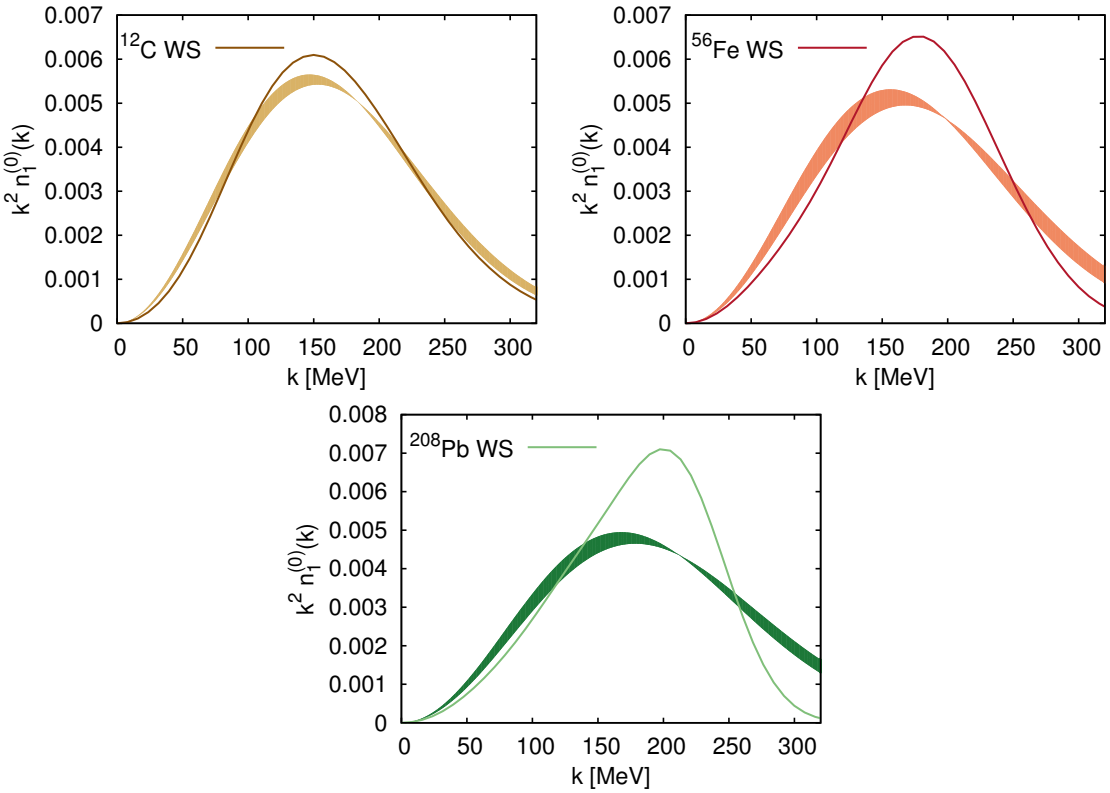

Figure 2 – (color online). The computed $k^2 n_1^{(0)}(k)$ versus k for the nuclei ^{12}C, ^{56}Fe and ^{208}Pb and a Boltzmann fit including the error bars. The extracted values of kT are 12.0±0.5 MeV (C), 14±1 MeV (Fe), and 16±1 MeV (Pb). The calculations are performed with WS single-particle states. The adopted normalization convention is $\int dk\, k^2\, n_1^{(0)}(k) = 1$.

The distribution $k^2 n_1^{(0)}(k)$ as it can be computed from Eq. (20) is reminiscent for a phenomenon which is confined to a certain scale, or, in other words, it is Gaussian like. The typical scale is determined by the Fermi momentum $k_F \approx 250$ MeV. This is illustrated in Fig. 2 where we show the momentum dependence of the $k^2 n_1^{(0)}(k)$ for ^{12}C, ^{56}Fe and ^{208}Pb as computed with Woods-Saxon (WS) wave functions. For the sake of curiosity we have fitted the computed $k^2 n_1^{(0)}(k)$ with a Boltzmann distribution

$$\frac{4\pi}{(2\pi M_N kT)^{3/2}} k^2 \exp -\frac{k^2}{2M_N kT} \,. \tag{22}$$

The results of the one-parameter fit are shown in Fig. 2. The fit is remarkably good for Carbon and gets increasingly inaccurate with increasing mass number. From the fit of the Boltzmann distribution we obtain $kT \approx 12$ MeV (C), $kT \approx 14$ MeV (Fe), $kT \approx 16$ MeV (Pb). Accordingly, for the IPM part of the momentum distribution, the typical energy exchange per momentum degree-of-freedom $\frac{1}{2}kT$ is of the order of 6-8 MeV.

The correlated part $k^2 n_1^{(1)}(k)$, on the other hand, is reminiscent of the nucleus as a system of interdependent nucleons and is obviously non-Gaussian. In contrast to the mean-field part $n_1^{(0)}$, the correlated part $n_1^{(1)}$ extends over "all" momentum scales. Or, in other words the 2N, 3N, ... correlations generate a fat momentum tail to the $n_1(k)$. The high-momentum tails to $n_1(k)$ have a very similar form for all nuclei, including the deuteron, which alludes to some universal character of SRC [17].

It has been theoretically predicted [34–36] and experimentally confirmed in semi-exclusive $A(e,e'p)$ measurements [37] that the major fraction of the $n_1^{(1)}\,(k > k_F)$ strength is contained in very specific parts of the single-nucleon removal energy-momentum phase space, namely those where the ejected nucleon is part of a pair with high relative and small c.m. momentum. This is the so-called ridge in the spectral function [36] which reflects the fact that high-momentum nucleons in the one-body momentum distribution are related to 2N dynamics with two nucleons which are close and move back-to-back with approximately equal and opposite momenta.

From recent calculations [26] of the two-body momentum distributions in ^{3}He and ^{4}He the following conclusions could be drawn. At high relative momenta and small c.m. momenta, the c.m. and relative motion of the pair is decoupled, an effect which is reminiscent of 2N SRC. For the correlated pn pairs the relative motion can be described by the high-momentum part of the deuteron wave function. This suggests the following expression for the correlated part of the pn two-body momentum distribution

$$n_2^{(1)}\left(2k_F \lesssim k_{12}, P_{12} \lesssim 150 \text{ MeV}\right) \approx a_{pn}\left(A,Z\right) n_D\left(k_{12}\right) F^{pn}\left(P_{12}\right) \ , \tag{23}$$

where $a_{pn}\left(A,Z\right)$ is a proportionality factor related to the number of correlated proton-neutron pairs in the nucleus ^AZ relative to the deuteron and $n_D\left(k_{12}\right)$ is the high-k_{12} deuterium momentum distribution. Further, the $F^{pn}\left(P_{12}\right)$ is the c.m. distribution of the correlated pn pairs. It corresponds with that part of $P_2\left(P_{12}\right)$ of Eq. (11) that stems from pn pairs with a zero relative orbital angular momentum $l_{12} = 0$ and a total spin $S = 1$. The proposed scaling behavior (23) can be attributed to the dominance of the tensor correlations at medium relative momenta and the fact that $\mid f_{t\tau}\left(k_{12} > k_F\right) \mid^2 \sim \left|\Psi_D\left(k_{12}\right)\right|^2$, two qualitative observations which can made from Fig. 1.

2.3 Quantifying two-nucleon correlations

We suggest that the significance of 2N correlations in a nucleus $A(N,Z)$ is proportional to the number of relative $l_{12} = 0$ states [21]. There are experimental results supporting this conjecture. First, in high-resolution ^{16}O$(e,e'pp)^{14}$N measurements performed at the electron accelerators in Amsterdam [38] and Mainz [39], the quantum numbers of the target nucleus and the residual nucleus are unambiguously determined. For the transitions to low-lying states in the residual nucleus, the eightfold differential cross section for the exclusive $(e,e'pp)$ reaction has been studied as a function of the initial c.m. momentum P_{12} of the proton-proton pair which is involved in the reaction process. This has provided insight into the quantum numbers of the pairs involved in the reaction process. We denote by $\left|l_{12}\left(\vec{r}_{12}\right), \Lambda_{12}\left(\vec{R}_{12}\right)\right\rangle$ the orbital wave function corresponding with the relative and c.m. motion of a nucleon pair. For the ground-state (g.s.) to g.s. transition, for example,

$$^{16}\text{O}(0^+, g.s.) + e \longrightarrow ^{14}\text{C}(0^+, g.s.) + e' + pp \ , \tag{24}$$

the active diproton resides in a state with quantum numbers $|l_{12} = 0, \Lambda_{12} = 0\rangle$ at lower P_{12} and $|l_{12} = 1, \Lambda_{12} = 1\rangle$ at higher P_{12}. Two independent calculations from the Pavia and Ghent groups have demonstrated that the largest contributions from SRC to the eight-fold cross section are confined to low P_{12} values [39]. This provides

direct evidence of pp correlations being confined to $|l_{12}=0,\Lambda_{12}=0\rangle$ pairs. In that sense, the ^{16}O$(e,e'pp)^{14}$N measurements nicely confirmed the back-to-back picture of SRC: diprotons are subject to SRC whenever they happen to be close (or, in a relative $l_{12}=0$ state) and moving back-back (or, in a state with $P_{12}\approx 0$ which corresponds with $\Lambda_{12}=0$).

High-resolution $(e,e'pn)$ measurements which have the potential to access the pn correlations are very challenging [40]. Theoretical $(e,e'pn)$ calculations [36, 41, 42] have predicted that the tensor parts of the SRC are responsible for the fact that the correlated pn strength is typically a factor of 10 bigger than the correlated pp strength. Calculations indicated that the tensor correlations are strongest for pn pairs pairs with "deuteron-like" $|l_{12}=0,S=1\rangle$ relative states [41, 42]. Recently, the dominance of the pn correlations over pp and nn ones has been experimentally confirmed [43, 44].

Accordingly, a reasonable estimate of the amount of correlated nucleon pairs in $A(N,Z)$ is provided by the number of pairs in a $l_{12}=0$ state. In order to determine that number for a given set of single-particle states, one needs a coordinate transformation from $(\vec{r}_1,\vec{r}_2)$ to $\left(\vec{r}_{12}=\frac{\vec{r}_1-\vec{r}_2}{\sqrt{2}},\vec{R}_{12}=\frac{\vec{r}_1+\vec{r}_2}{\sqrt{2}}\right)$. For a harmonic oscillator (HO) Hamiltonian this transformation can be done with the aid of Moshinsky brackets [45]

$$\begin{aligned}\mid n_1 l_1\left(\vec{r}_1\right) n_2 l_2\left(\vec{r}_2\right); LM_L\rangle = & \sum_{n_{12}l_{12}N_{12}\Lambda_{12}} \langle n_{12}l_{12}N_{12}\Lambda_{12}; L \mid n_1 l_1 n_2 l_2; L\rangle \\ & \times \mid n_{12}l_{12}\left(\vec{r}_{12}\right) N_{12}\Lambda_{12}\left(\vec{R}_{12}\right); LM_L\rangle \ . \end{aligned} \tag{25}$$

We define the interchange operator for the spatial, spin, and isospin coordinate as

$$\mathcal{P}_{12}=\mathcal{P}_{12}\left(\vec{r}_1,\vec{r}_2\right)\mathcal{P}_{12}\left(\vec{\sigma}_1,\vec{\sigma}_2\right)\mathcal{P}_{12}\left(\vec{\tau}_1,\vec{\tau}_2\right) \ . \tag{26}$$

After introducing the spin and isospin degrees-of-freedom, in a HO basis a normalized and antisymmetrized two-nucleon state reads ($\alpha_i\equiv(n_i l_i j_i t_i)$)

$$\begin{aligned}&|\alpha_1\alpha_2; JM\rangle_{na} = \frac{1}{\sqrt{2\left(1+\delta_{\alpha_1\alpha_2}\right)}}\left(1-\mathcal{P}_{12}\right)|\alpha_1\left(\vec{r}_1\right)\alpha_2\left(\vec{r}_2\right); JM\rangle \\ &= \sum_{LM_L}\sum_{n_{12}l_{12}}\sum_{N_{12}\Lambda_{12}}\sum_{SM_S}\sum_{TM_T}\frac{1}{\sqrt{2\left(1+\delta_{\alpha_1\alpha_2}\right)}}\left[1-(-1)^{l_{12}+S+T}\right] \\ &\times\langle n_{12}l_{12}N_{12}\Lambda_{12}; L \mid n_1 l_1 n_2 l_2; L\rangle \hat{j}_1\hat{j}_2\hat{L}\hat{S}\begin{Bmatrix} l_1 & l_2 & L \\ \frac{1}{2} & \frac{1}{2} & S \\ j_1 & j_2 & J\end{Bmatrix}\langle LM_L SM_S \mid JM\rangle \\ &\times\langle\frac{1}{2}t_1\frac{1}{2}t_2 \mid TM_T\rangle\left|\left[n_{12}l_{12}\left(\vec{r}_{12}\right), N_{12}\Lambda_{12}\left(\vec{R}_{12}\right)\right] LM_L, SM_S, TM_T\right\rangle \ , \end{aligned} \tag{27}$$

where we have used the shorthand notation $\hat{j}\equiv\sqrt{2j+1}$.

With the above conventions one has that the total amount of proton-neutron pairs can be obtained from a sum over all pn pairs in the nuclear ground state

$$\sum_{JM}\sum_{\alpha_1\leq\alpha_F^p}\sum_{\alpha_2\leq\alpha_F^n} {}_{na}\langle\alpha_1\alpha_2; JM\ |\alpha_1\alpha_2; JM\rangle_{na} = NZ \ , \tag{28}$$

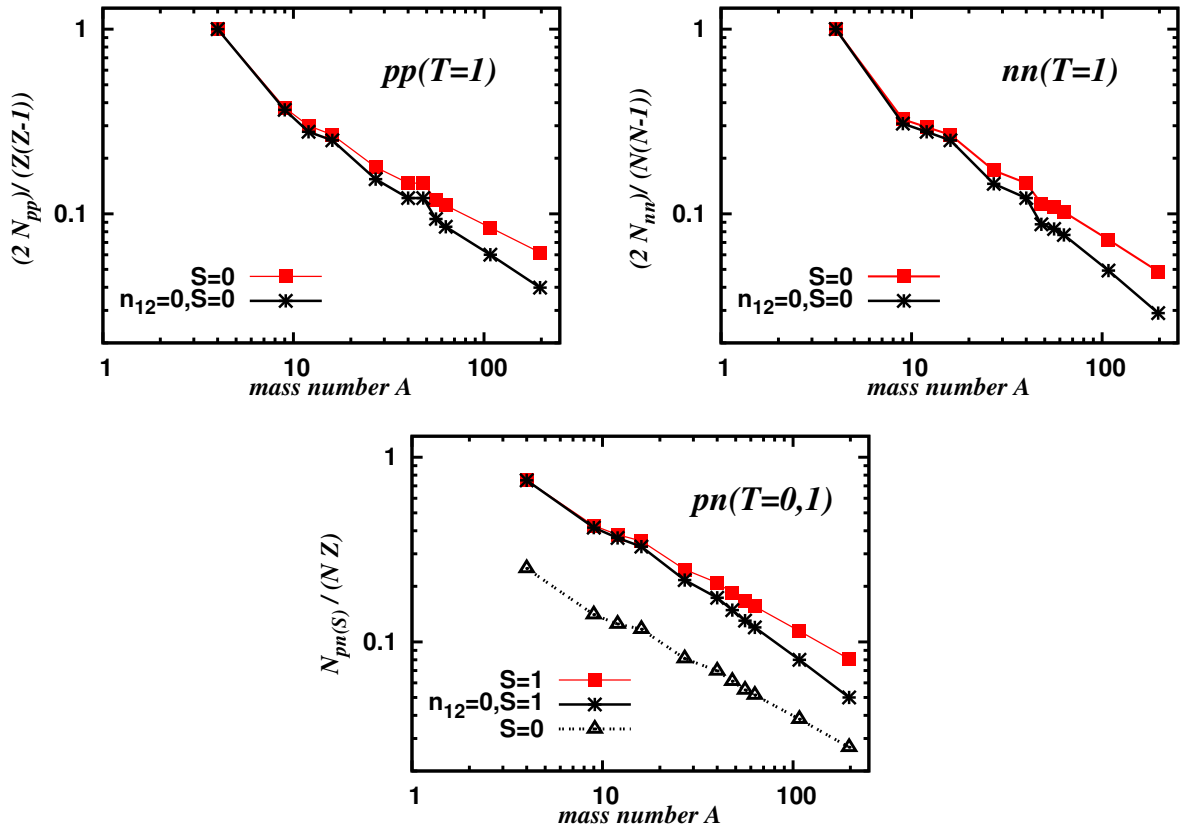

Figure 3 – (color online). The computed values for $\frac{2}{Z(Z-1)}N_{pp}$, $\frac{2}{N(N-1)}N_{nn}$, and $\frac{1}{(NZ)}N_{pn(S)}$ which represent the predicted fraction of the pairs which are prone to SRC. The results are obtained for HO single-particle wave functions with $\hbar\omega(MeV) = 45.A^{-\frac{1}{3}} - 25.A^{-\frac{2}{3}}$ and for the target nuclei ^{4}He, ^{9}Be, ^{12}C, ^{16}O, ^{27}Al, ^{40}Ca, ^{48}Ca, ^{56}Fe, ^{63}Cu, ^{108}Ag, and ^{197}Au.

where α_F^p and α_F^n denote the Fermi level for the proton and neutron. Similar expressions hold for the number of proton-proton and neutron-neutron pairs

$$\frac{Z(Z-1)}{2} = \sum_{JM} \sum_{\alpha_1 \leq \alpha_F^p} \sum_{\alpha_2 \leq \alpha_F^p} {}_{na}\left\langle \alpha_1\alpha_2; JM \,|\alpha_1\alpha_2; JM\right\rangle_{na} \ , \tag{29}$$

$$\frac{N(N-1)}{2} = \sum_{JM} \sum_{\alpha_1 \leq \alpha_F^n} \sum_{\alpha_2 \leq \alpha_F^n} {}_{na}\left\langle \alpha_2\alpha_2; JM \,|\alpha_1\alpha_2; JM\right\rangle_{na} \ . \tag{30}$$

Starting from the Eq. (27) one can compute in a HO single-particle basis how much a pair wave function with quantum numbers

$$\left|\left[n_{12}l_{12}\left(\vec{r}_{12}\right), N_{12}\Lambda_{12}\left(\vec{R}_{12}\right)\right] LM_L, SM_S, TM_T\right\rangle \tag{31}$$

contributes to the sum-rules of Eqs. (28) – 30). This can also be done for any other basis $|nljm\rangle$ of non-relativistic single-particle states. In that case, the adopted procedure involves

an extra expansion of $|nljm\rangle$ in a HO basis

$$|nljm\rangle = \sum_{m_l m_s} \langle l m_l \frac{1}{2} m_s \mid jm\rangle \psi_{nlj}(r) Y_{lm_l}(\Omega)\, \chi_{\frac{1}{2}m_s}$$
$$= \sum_{n_H} \left(\int dr r^2 \phi^*_{n_H l}(r) \psi_{nlj}(r) \right) |n_H l j m\rangle \ , \tag{32}$$

where $\phi_{n_H l}(r)$ are the radial HO wave functions. A two-nucleon state can then be expressed in a HO basis for which the Eq. (27) can be used to determine the weight of the pair wave functions of Eq. (31).

The IPM pp pairs are mainly subject to the central SRC which requires them to be close. This implies that a reasonable estimate of the number of IPM pp pairs which receive substantial corrections from the SRC is given by an expression of the type

$$N_{pp}(A,Z) = \sum_{JM} \sum_{\alpha_1 \le \alpha_F^p} \sum_{\alpha_2 \le \alpha_F^p} {}_{na}\langle \alpha_1 \alpha_2; JM| \, \mathcal{P}^{l_{12}=0}_{\vec{r}_{12}} \, |\alpha_1 \alpha_2; JM\rangle_{na} \ , \tag{33}$$

where $\mathcal{P}^{l_{12}=0}_{\vec{r}_{12}}$ is a projection operator for two-nucleon relative states with $l_{12}=0$. A similar expression to Eq. (33) holds for the nn pairs. For the pn pairs it is important to discriminate between the triplet and singlet spin states

$$N_{pn(S)}(A,Z) = \sum_{JM} \sum_{\alpha_1 \le \alpha_F^p} \sum_{\alpha_2 \le \alpha_F^n} {}_{na}\langle \alpha_1 \alpha_2; JM| \, \mathcal{P}^{l_{12}=0}_{\vec{r}_{12}} \mathcal{P}^{S}_{\vec{\sigma}} \, |\alpha_1 \alpha_2; JM\rangle_{na} \ . \tag{34}$$

In Fig. 3 we display some computed results for the N_{pp}, N_{nn}, and $N_{pn(S)}$ for 11 nuclei. The selection of the nuclei is motivated by the availability of inclusive electron-scattering data and covers the full mass range from Helium to Gold. We have opted to display the results relative to the sum rule values of the Eqs. (28) and (29), which allows one to interpret the results in terms of probabilities: given an arbitrary pair wave function, what is the chance that it has zero orbital relative momentum and a specific spin quantum number. In a naive IPM picture for ^{4}He, the pp pair is in a $|l_{12}=0, S=0, T=1\rangle$ state. As this 2N configuration is prone to central SRC effects, the corresponding probability is 1. The physical interpretation is that for ^{4}He "all" IPM pp-pair wave function combinations receive corrections from SRC. For a medium-heavy nucleus like ^{56}Fe or ^{63}Cu we find $\frac{N_{pp}}{\frac{Z(Z-1)}{2}} \approx 0.1$, which leads one to conclude that about 90% of the IPM pp pair wave functions do not receive corrections from central SRC. For the heaviest nucleus considered here (Au) $\frac{2N_{pp}}{Z(Z-1)} = 0.06$, which means that only about 190 out of the 3081 possible pp pair combinations are subject to SRC.

Comparing the mass dependence of the pp and nn results of Fig. 3 one observes similar trends. For the pn results a softer decrease with increasing A is predicted. There are about three times as many pn($T=0$) states than pn($T=1$) states with $l_{12}=0$. This would be trivial in a system with only spin and isospin degrees of freedom. In a system in which the kinetic energy plays a role and in which there are spin-orbit couplings, we cannot see any trivial reason why this should be the case. In this respect, we wish to stress that for most nuclei discussed $N \neq Z$. A stronger criterion for selecting nucleon pairs at close proximity is imposing $n_{12}=0$ in addition to $l_{12}=0$ and we have added also those results to Fig. 3. We find the results of Fig. 3 robust in that the A dependence and magnitudes are not very

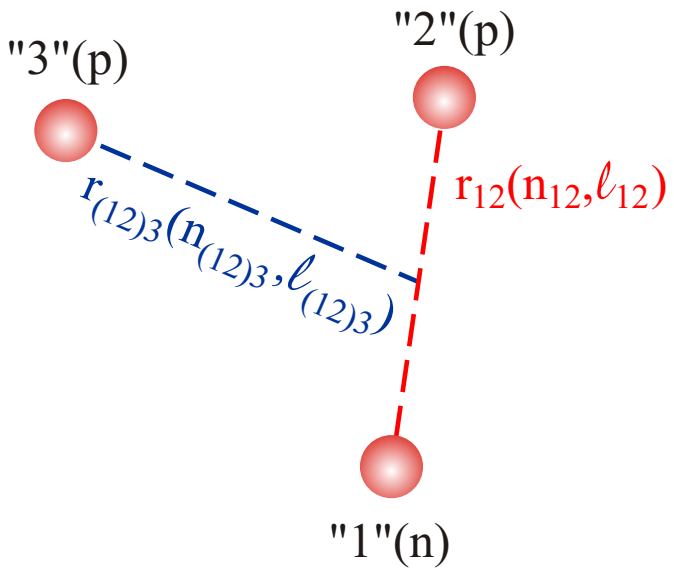

Figure 4 – (color online). Use of Jacobi coordinates in the ppn system.

sensitive to the choices made with regard to the single-particle wave functions. All the results of Fig. 3 are displayed on a log-log plot and can be reasonably fitted with a straight line, pointing towards a power-law mass dependence A^{α} for the N_{pp}, N_{pn} and $N_{pn(S)}$.

2.4 Quantifying three-nucleon correlations

In order to quantify the magnitude of the 3N correlations for an arbitrary $A(N,Z)$, we build on a recent paper by Feldmeier et al. [17]. There, it is pointed out that 3N correlations can be induced without introducing genuine three-body forces. In terms of the correlation operators of Sect. 2.2, three-body correlations will naturally emerge in cluster expansions by means of operators of the type $g_c\,(r_{12})\,g_c\,(r_{13})$, $g_c\,(r_{12})\,f_{t\tau}\,(r_{13})$, ...

The strongest source of three-nucleon correlations is the tensor correlation operator acting on the $(S=1,T=0)$ channel of the pn states of Eq. (27). We consider ppn configurations and explain one possible mechanism to create a correlated state (see also Fig. 4). In the uncorrelated wave function one has a n(1)p(2) pair in a $|l_{12}=0\ \ S_{12}=1\,;T_{12}=0\rangle$ state and a p(2)p(3) pair in a $|l_{23}=0\ \ S_{23}=0\,;T_{23}=1\rangle$ state. Accordingly, both pairs are in relative $l=0$ states. In Ref. [17] it is explained that these two pairs can be brought into a correlated three-nucleon status by flipping the spin of proton 2. In the correlated part of the wave function one has an n(1)p(2) pair in a $|l_{12}=2\ \ S_{12}=1\,;T_{12}=0\rangle$ and an p(2)p(3) pair in a $|l_{23}=1\ \ S_{23}=1\,;T_{23}=1\rangle$ state. This configuration can be energetically favorable through the presence of the strong tensor correlation in the pn pair. Indeed, the energy gain through the tensor induced n(1)p(2) correlation can compensate for the energy loss of breaking the pairing in the p(2)p(3) pair.

Given $A(N,Z)$ we propose to find all the antisymmetrized 3N states with orbital quantum

numbers

$$(n_{12}=0\; l_{12}=0\; n_{(12)3}=0\; l_{(12)3}=0)\;, \tag{35}$$

in the IPM wave function and identify them as the dominant contributors to 3N SRCs. This corresponds with seeking for those 3N wave-function components where all three nucleons are "close". This can be technically achieved by constructing antisymmetrized 3N states starting from a MF Slater determinant, and performing a transformation from the particle coordinates $(\vec{r}_1,\vec{r}_2,\vec{r}_3)$ to the internal Jacobi coordinates $\left(\vec{r}_{12},\vec{r}_{(12)3},\vec{R}_{123}\right)$

$$\vec{r}_{(12)3}=\frac{\vec{R}_{12}-\sqrt{2}\vec{r}_3}{\sqrt{3}},\qquad\qquad \vec{R}_{123}=\frac{\sqrt{2}\vec{R}_{12}+\vec{r}_3}{\sqrt{3}}\;. \tag{36}$$

One readily finds for uncoupled three-nucleon states in a HO basis [45]

$$\begin{aligned}
&|n_1l_1m_{l_1}(\vec{r}_1),n_2l_2m_{l_2}(\vec{r}_2),n_3l_3m_{l_3}(\vec{r}_3)\rangle=\sum_{LM_L}\sum_{n_{12}l_{12}}\sum_{N_{12}\Lambda_{12}}\sum_{L_1M_{L_1}}\\
&\times\sum_{n_{(12)3}l_{(12)3}}\sum_{N_{123}\Lambda_{123}}\sum_{m_{l_{12}}m_{\Lambda_{12}}}\sum_{m_{l_{(12)3}}m_{\Lambda_{123}}}\langle l_1m_{l_1}l_2m_{l_2}\mid LM_L\rangle\\
&\times\langle l_{12}m_{l_{12}}\Lambda_{12}M_{\Lambda_{12}}\mid LM_L\rangle\;\;\langle\Lambda_{12}M_{\Lambda_{12}}l_cm_{l_c}\mid L_1M_{L_1}\rangle\\
&\times\langle l_{(12)3}m_{l_{(12)3}}\Lambda_{123}M_{\Lambda_{123}}\mid L_1M_{L_1}\rangle\;\;\langle n_{12}l_{12}N_{12}\Lambda_{12};L\mid n_1l_1n_2l_2;L\rangle\\
&\times\langle n_{(12)3}l_{(12)3}N_{123}\Lambda_{123};L_1\mid N_{12}\Lambda_{12}n_3l_3;L_1\rangle_\beta\\
&\times|n_{12}l_{12}m_{l_{12}}(\vec{r}_{12})\rangle\quad\left|n_{(12)3}l_{(12)3}m_{l_{(12)3}}\left(\vec{r}_{(12)3}\right)\right\rangle\\
&\times\left|N_{123}\Lambda_{123}M_{\Lambda_{123}}\left(\vec{R}_{123}\right)\right\rangle\;,
\end{aligned} \tag{37}$$

where we have adopted the notation $\langle\ldots\mid\ldots\rangle_\beta$ for the Standard Transformation Brackets (STB) [45].

Antisymmetrized (a) uncoupled three-nucleon states can be obtained from the three-nucleon wave functions of Eq. (37) using the interchange operator of Eq. (26)

$$\begin{aligned}
|\alpha_am_a,\alpha_bm_b,\alpha_cm_c\rangle_a=\;&[1-\mathcal{P}_{12}]\,|\alpha_am_a(\vec{r}_1),\alpha_bm_b(\vec{r}_2),\alpha_cm_c(\vec{r}_3)\rangle\\
&+[1-\mathcal{P}_{12}]\,|\alpha_bm_b(\vec{r}_1),\alpha_cm_c(\vec{r}_2),\alpha_am_a(\vec{r}_3)\rangle\\
&+[1-\mathcal{P}_{12}]\,|\alpha_cm_c(\vec{r}_1),\alpha_am_a(\vec{r}_2),\alpha_bm_b(\vec{r}_3)\rangle\;.
\end{aligned} \tag{38}$$

The total number of ppn triples can now be expressed as

$$N\frac{Z(Z-1)}{2}=\sum_{\alpha_a,\alpha_b\le\alpha_F^p}\sum_{\alpha_c\le\alpha_F^n}\sum_{m_am_bm_c}{}_{na}\langle\alpha_am_a,\alpha_bm_b,\alpha_cm_c\,|\alpha_am_a\alpha_bm_b\alpha_cm_c\rangle_{na}\;, \tag{39}$$

which allows for a stringent test of the analytical derivations and their numerical implementation. Along similar lines to those used to derive the number of correlated 2N clusters in Eq. (33), the number of ppn triples with the orbital quantum numbers of Eq. (35) can be obtained from

$$\begin{aligned}
N_{ppn}(A,Z)=\sum_{\alpha_a,\alpha_b\le\alpha_F^p}\sum_{\alpha_c\le\alpha_F^n}\sum_{m_am_bm_c}{}_{na}\langle\alpha_am_a,\alpha_bm_b,\alpha_cm_c|\,\mathcal{P}_{\vec{r}_{12}}^{n_{12}=0,l_{12}=0}\\
\times\mathcal{P}_{\vec{r}_{(12)3}}^{n_{(12)3}=0,l_{(12)3}=0}\,|\alpha_am_a,\alpha_bm_b,\alpha_cm_c\rangle_{na}\;.
\end{aligned} \tag{40}$$

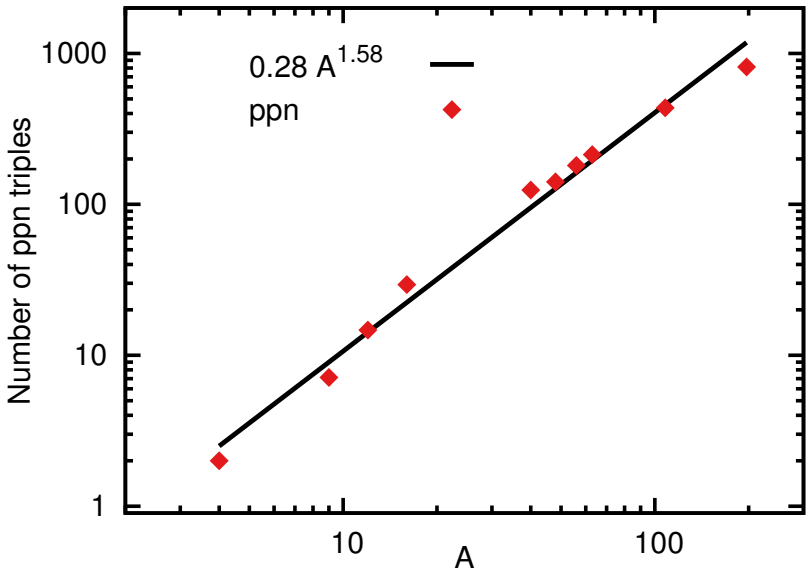

Figure 5 – (color online). The mass dependence of the amount of ppn triples with quantum numbers $\left|n_{12}=0\ l_{12}=0, n_{(12)3}=0\ l_{(12)3}=0\right\rangle$. The results can be reasonably fitted with a power law $0.28A^{1.58\pm0.20}$. The results are obtained for HO single-particle wave functions with $\hbar\omega(MeV) = 45.A^{-\frac{1}{3}} - 25.A^{-\frac{2}{3}}$ and for the nuclei ^{4}He, ^{9}Be, ^{12}C, ^{16}O, ^{40}Ca, ^{48}Ca, ^{56}Fe, ^{63}Cu, ^{108}Ag, and ^{197}Au.

We associate the $N_{ppn}(A,Z)$ with the number of ppn SRC triples. The A dependence of $N_{ppn}(A,Z)$ is displayed in Fig. 5. There is striking linear correlation between the logarithm of the mass number and the logarithm of the number ppn triples which are close in the MF ground-state wave function.

3 Results

In this section we discuss how our predictions for the number of correlated 2N pairs and correlated 3N triples can be connected with experimental results from inclusive electron scattering.

3.1 Separation of the correlation and mean-field contributions

We start with illustrating that the separation of the mean-field and correlated contributions to the inclusive $A(e,e')$ cross sections is feasible. In order to achieve this, we use stylized features of the $n_1(k)$ in Monte-Carlo (MC) simulations to illustrate that a separation between the mean-field $n_1^{(0)}(k)$ and the correlated $n_1^{(1)}(k)$ part can be made in the $A(e,e')$ signal.

We assume that quasi-elastic single-nucleon knockout $e+A \to e'+(A-1)+N$ is the major source of $A(e,e')$ strength. With $q(\omega,\vec{q})$, $p_A(M_A,\vec{0})$, $p_{A-1}(E_{A-1},\vec{p}_{A-1})$, $p_f(E_N,\vec{p}_f)$ we denote the four-momenta of the virtual photon, of the target nucleus, of the residual $A-1$ system, and of the ejected nucleon. From energy-momentum conservation

$$q + p_A - p_{A-1} = p_f, \tag{41}$$

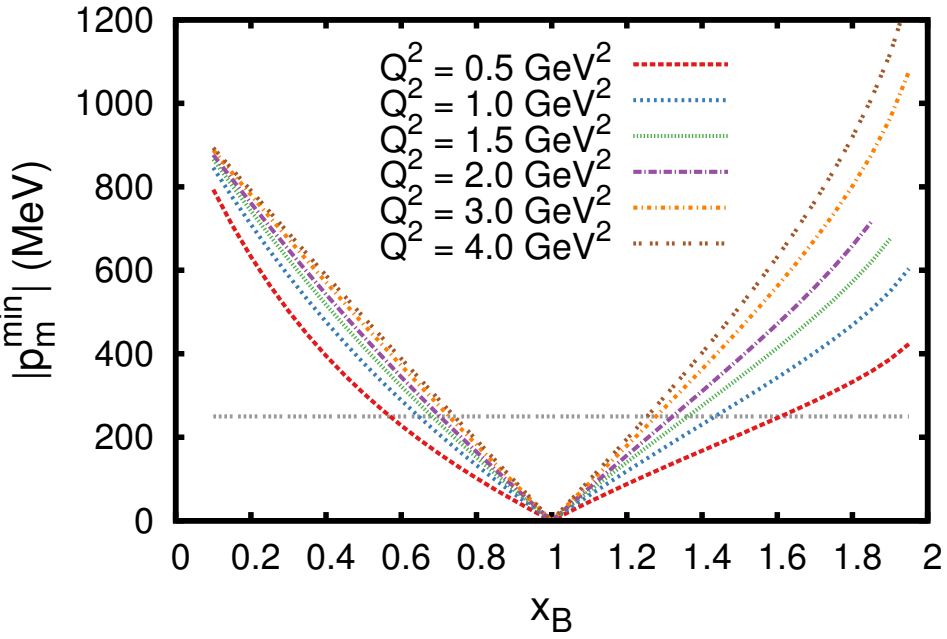

Figure 6 – (Color online). Relation between the minimum of the missing momentum $|p_m^{min}|$ for the deuteron and x_B at various values of the four-momentum transfer Q^2.

one can deduce for $A = 2$ a relation between the minimum of the missing momentum $\vec{p}_m = \vec{p}_f - \vec{q}$ and the Bjorken scaling variable x_B for fixed Q^2 [46]. The results are shown in Fig. 6. Obviously, for $Q^2 \geq 1.5$ GeV^2 and $x_B > 1.5$ one mainly probes nucleons with a momentum well above the Fermi momentum for the deuteron. For finite nuclei the situation is more involving as $A - 1$ represents an additional degree of freedom which can carry a fraction of the transferred four-momentum. We have performed MC simulations for a fixed energy of the impinging electron beam ϵ_i and a fixed electron scattering angle θ_e. The p_m for a mean-field nucleon is drawn from the MF part $n_1^{(0)}(k)$ of $n_1(k)$. For a correlated nucleon the p_m is drawn from $n_1^{(1)}(k)$. Parameterizations for $n_1^{(0)}(k)$ and $n_1^{(1)}(k)$ are obtained from [35]

$$n_1^{(0)}(k) = A^{(0)} e^{-B^{(0)}k^2}[1 + \mathcal{O}(k^2)], \quad (42)$$

$$n_1^{(1)}(k) = A^{(1)} e^{-B^{(1)}k^2} + C^{(1)} e^{-D^{(1)}k^2}, \quad (43)$$

where $A^{(0)}$, $B^{(0)}$, $A^{(1)}$, $B^{(1)}$, $C^{(1)}$ and $D^{(1)}$ depend on A.

In Fig. 7 we compare the x_B distribution of simulations for the mean-field and correlated part of one nucleon knockout in ^{12}C. As stated in Eq. (21), the number of events is normalized as $\int \mathrm{d}k\, k^2 n_1^{(0)}(k) = 0.7$. For $x_B > 1.5$, the events originate almost uniquely from $n_1^{(1)}(k)$.

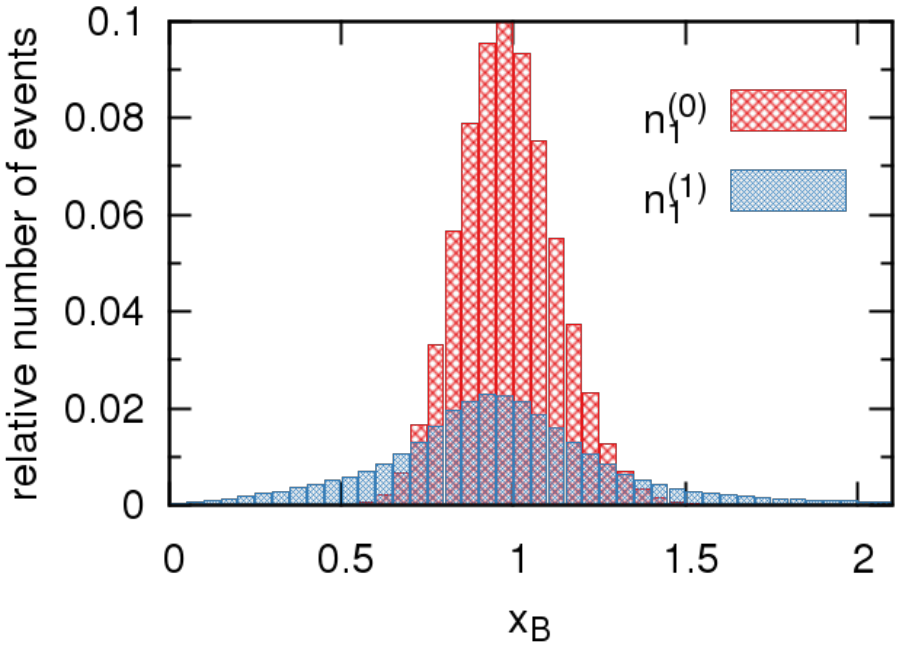

Figure 7 – (Color online). Simulation of one-nucleon knockout in ^{12}C with separated mean field and correlated momentum distribution. The number of events is normalized as in Eq. (21). The electron kinematics is determined by $\epsilon_i = 5.766\,\text{GeV}$ and $\theta_e = 18°$.

3.2 Two-body correlations

Following the experimental observation [9, 10, 47] that the ratio of the inclusive electron scattering cross sections from a target nucleus A and from the deuteron D

$$\frac{\sigma^A\left(x_B, Q^2\right)}{\sigma^D\left(x_B, Q^2\right)}\,, \tag{44}$$

scales for $1.5 \lesssim x_B \lesssim 2$ and moderate Q^2, it has been suggested [47] to parameterize the σ^A in the following form

$$\sigma^A\left(1.5 \lesssim x_B \lesssim 2, Q^2\right) = \frac{A}{2} a_2\left(A/D\right) \sigma_2\left(A, x_B, Q^2\right)\,, \tag{45}$$

where $\sigma_2\left(A, x_B, Q^2\right)$ is the effective cross section for scattering from a correlated 2N cluster in nucleus A. Assuming that σ_2 is some local function which does not depend on the target nucleus A

$$\sigma_2\left(A, x_B, Q^2\right) \approx \sigma_2\left(A = 2, x_B, Q^2\right) \approx \sigma^D\left(x_B, Q^2\right), \tag{46}$$

one can rewrite Eq. (45) as

$$a_2\left(A/D\right) = \frac{2}{A}\frac{\sigma^A\left(x_B, Q^2\right)}{\sigma^D\left(x_B, Q^2\right)} \quad \left(1.5 \lesssim x_B \lesssim 2\right)\,. \tag{47}$$

In this simplified reaction-model picture, which ignores amongst other things the c.m. motion of pairs in finite nuclei, the quantity $\frac{A}{2} a_2\left(A/D\right)$ can be connected with the number of correlated pairs in the nucleus A. Assuming that all pn pairs contribute one would expect

that for the relative amount of correlated two-nucleon clusters $a_2\,(A/D) \sim A$. Based on the observed dominance of correlated pn pairs over pp and nn pairs [43], and the universality of the deuteron-like high-momentum tail of the correlated two-body momentum distribution (23), we suggest that the correlated pn pairs contributing to the $a_2(A/D)$, are predominantly $(T = 0, S = 1)$ pairs and that $a_2(A/D)$ is proportional to the quantity $N_{pn(S=1)}(A, Z)$ defined in Eq. (34).

In Ref. [48] the ratio of Eq. (44) has been calculated with spectral functions obtained from state-of-the-art nuclear matter calculations in the local density approximation for the correlated part and $A(e, e'p)$ scattering data for the mean-field part [49, 50]. The calculations suggested large FSI effects, whilst the plane-wave calculations did not exhibit the scaling present in the data at $1.5 \lesssim x_B$. In Refs. [11, 22] it is argued that a complete treatment of FSI in this kinematics needs to include inelastic channels in the rescattering and that this cancels part of the elastic FSI contribution included in Ref. [48]. The results in Ref. [48] seem to refute the validity of Eq. (45), which hinges on the assumption that the FSI effects on correlated pairs in a nucleus are almost identical to those in the deuteron in a high-momentum state. This requires that for $1.5 \lesssim x_B$ the FSI is primarily in the correlated pair and that the remaining $A - 2$ nucleons act as spectators. Such a behavior is suggested by the calculation of the quasi-elastic cross sections in Ref. [51] and by a space-time analysis of the nuclear FSI at $x_B > 1$ carried out in Ref. [11] where it is stressed that the reinteraction distances are $\lesssim 1$ fm, supporting the idea that the first rescattering should be very similar to FSI in the deuteron (see a recent discussion in Ref. [22]). Therefore the assumption of Eq. (45) seems a reasonable one for light nuclei where the amount of rescatterings is of the order of 1. For medium-heavy and heavy nuclei, the average amount of rescatterings is larger than 1 and it has to be verified if the assumption still holds. The settlement and clarification of all the cited issues related to the role of FSI in inclusive reactions requires further studies with a full reaction model.

In a finite nucleus correlated pairs can have a non-zero c.m. momentum. This c.m. motion is a correction factor when connecting the measured $a_2(A/D)$ to the number of correlated pn pairs $N_{pn(S=1)}(A, Z)$. We aim to provide an estimate for this correction factor. Therefore, we consider the two-nucleon knockout reaction $e + A \to e' + (A - 2) + N + N$ following the break-up of a correlated 2N cluster. For an inclusive cross section, the tensor correlated pn$(S = 1)$ pairs dominate the signal [43, 44, 52].

As pointed out in Refs. [11, 25], the cross section for the exclusive $(e, e'NN)$ reaction can be written in a factorized form as

$$\sigma^A(e, e'NN) = KF^{NN}(P_{12})\sigma_{eNN}(k_{12})\,, \tag{48}$$

where $P_{12}(k_{12})$ is the c.m. (relative) momentum of the correlated pair on which the photoabsorption takes place and K is a kinematic factor. The above expression is valid in the plane-wave and spectator approximation for electron scattering on a pair with zero relative orbital momentum. The σ_{eNN} stands for the elementary cross section for electron scattering from a correlated 2N pair with relative momentum k_{12}. The σ_{eNN} contains the Fourier-transformed correlation functions $g_c(k_{12})$ and $f_{t\tau}(k_{12})$. An analytic expression for σ_{epp} is contained in Ref. [25] and has been tested against data in Ref. [53].

As argued above, in order to link the exclusive cross section of Eq. (48) to the inclusive ones contained in the Eq. (45) one assumes that $\sigma_{epn} \approx \sigma_{eD}$ and one introduces a proportionality

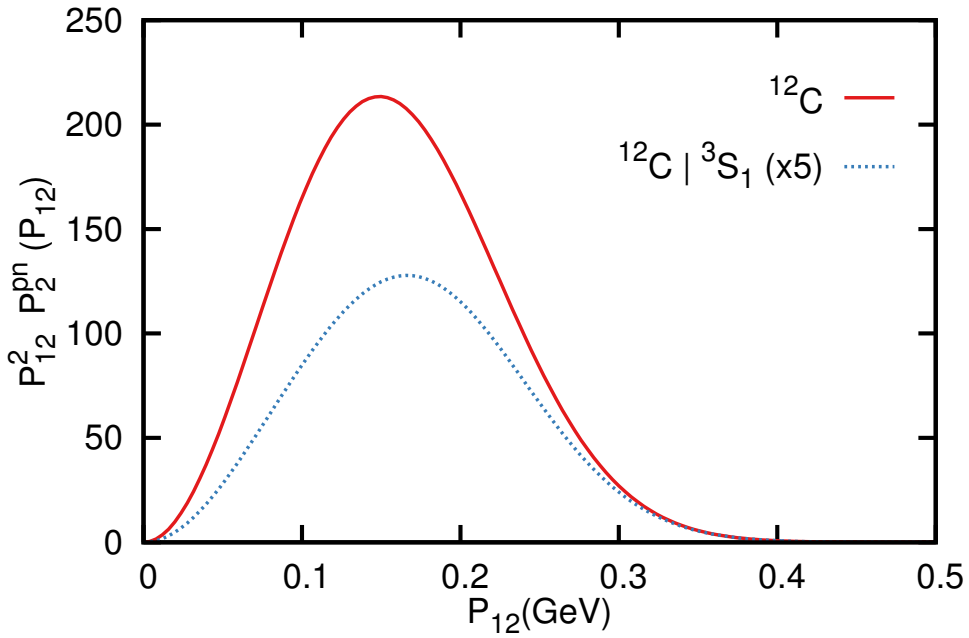

Figure 8 – (Color online) The pn c.m. distribution $P_{12}^2 P_2^{pn}(P_{12})$ and $P_{12}^2 P_2^{pn}\left(P_{12}|^3S_1\right) = P_{12}^2 F^{pn}(P_{12})$ for ^{12}C. The calculations are performed with HO single-particle states and adopt the normalization convention $\int dP_{12}\ P_{12}^2 P_2^{pn}(P_{12}) = NZ$.

factor $N_{pn(S=1)}(A,Z)$ which counts the number of correlated pn pairs in A. With the scaling relation of Eq. (48) for the $(e,e'pn)$ reaction, one can transform the ratio of Eq. (47) into a form which accounts for the c.m. motion of the pair

$$a_2(A/D) = \frac{2}{A}\frac{\int_{PS} \mathrm{d}\vec{k}_{12}\mathrm{d}\vec{P}_{12} N_{pn(S=1)}(A,Z) F^{pn}(P_{12})\sigma_{eD}(k_{12})}{\int_{PS} d\vec{k}_{12}\sigma_{eD}(k_{12})} ,$$
$$\approx \frac{2}{A} N_{pn(S=1)}(A,Z)\int_{PS} d\vec{P}_{12} F^{pn}(P_{12}) , \qquad (49)$$

where the integrations extend over those part of the c.m. momentum phase (PS) included in the data. A basic assumption underlying the above equation is that the factorization of Eq. (23) approximately holds. The computed widths of the c.m. momentum distributions for the correlated pn pairs contained in Table 1 indicate that the major fraction of the pn pairs has $P_{12} \lesssim 150$ MeV which is within the ranges for the validity of Eq. (23).

In line with our assumption that the correlated pairs are dominated by pn in a relative $^3S_1$ state, $F^{pn}(P_{12})$ can be expressed as the conditional two-body c.m. momentum distribution

$$F^{pn}(P_{12}) = P_2^{pn}\left(P_{12}|^3S_1\right) . \qquad (50)$$

Figure 8 shows calculations for the $P_2^{pn}(P)$ and $P_2^{pn}(P|^3S_1)$ for ^{12}C. The c.m. distribution of correlated pn pairs ($F^{pn}(P_{12})$) can be well parameterized in terms of a Gaussian distribution. The widths $\sigma_{c.m.}$ obtained from a Gaussian fit to $P_2^{pn}(P_{12}|^3S_1)$ are given in Table 1.

To estimate the c.m. correction factor we have performed MC simulations of pn knockout with and without inclusion of the c.m. motion. This amounts to drawing the c.m. momentum

	A	$\sigma_{c.m.}$	c.m. correction factor
	^{12}C	115 MeV	1.64 ± 0.23
	^{56}Fe	128 MeV	1.70 ± 0.27
	^{208}Pb	141 MeV	1.71 ± 0.29

Table 1 – The second column gives the width of the c.m. distribution of correlated pn pairs. The third column provides the computed c.m. correction factor. The errors represent the dependence on the choice of correlation function.

from $F^{pn}(P_{12}) = \delta(P_{12})$ and $F^{pn}(P_{12}) \sim e^{-\frac{P_{12}^2}{2\sigma_{c.m.}^2}}$, where $\sigma_{c.m.}$ is the A dependent width. For $1.5 \leq x_B \leq 2$, the initial momentum distribution of the correlated pair is given by correlated part of the two-body momentum distribution $n_2^{(1)}(k_{12}, P_{12})$. The Eq. (23) states that the $n_2^{(1)}(k_{12}, P_{12})$ can be considered universal. As illustrated in Fig. 1 one has $n_D(k_{12}) \sim |f_{t\tau}(k_{12})|^2$. As the relative momentum distribution is approximately proportional to the tensor correlation function, we draw k_{12} from the distribution $k_{12}^2 |f_{t\tau}(k_{12})|^2$. Energy conservation reads

$$(q + p_A - p_{A-2} - p_s)^2 = p_f^2 = m_N^2, \tag{51}$$

where $q(\omega, \vec{q})$, $p_A(M_A, \vec{0})$ and $p_{A-2}(E_{A-2}, -(\vec{p}_s + \vec{p}_m))$ are the four-momenta of the virtual photon, target nucleus and residual $A-2$ system, respectively. The virtual photon interacts with one of the nucleons, resulting in a fast nucleon $p_f(E_f, \vec{p}_f)$ with $\vec{p}_f = \vec{p}_m + \vec{q}$ and a slow nucleon $p_s(E_s, \vec{p}_s)$. With the aid of Eq. (51), one can calculate the x_B-distribution of the simulated events. We apply the kinematics of the Jefferson Lab (JLab) experiment E02-019 [10]: $\epsilon_i = 5.766\,\text{GeV}$ and $\theta_e = 18^\circ$. The average $< Q^2 >$ of the generated events (including c.m. motion) in the x_B region of interest is 2.7 GeV^2. This value, which is A-independent, agrees with the one quoted in Ref. [10].

The results of our simulations are summarized in Figs. 9 and 10. Fig. 9 shows the $x_B - k_{12}$ scatter plot of 10^6 simulated events with and without inclusion of c.m. motion for ^{12}C. In both situations the mass difference between inital and final state causes a small shift to lower x_B compared to the deuteron case. Second, we observe considerable shifts in the distribution of the events in the (k_{12}, x_B) plane due to c.m. motion. In Fig. 10, one can observe how c.m. motion considerably increases the number of events with $1.5 \leq x_B \leq 2$. The impact of the c.m. corrections increases with growing x_B. Experimentally, the $a_2(A/D)$ coefficient is determined by integrating data for $1.5 \leq x_B \leq 1.85$. We estimate the c.m. correction factor by the ratio

$$\frac{\#\text{ simulated events with inclusion of c.m. motion}}{\#\text{ simulated events without inclusion of c.m. motion}}\,. \tag{52}$$

in this x_B region. The resulting correction factor for several nuclei is contained in Table 1. We performed the simulations with the three different correlation functions $f_{t\tau}$ in Fig. 1. The dependence of the result on the choice of correlation function is represented by the error of the c.m. correction factor.

Fig. 3 quantifies the fraction of all possible pn pairs which are prone to SRC relative to the total amount of possible pn pair combinations. In our picture one has $N_{pn(S=1)} = 1$ for D. This means that we do interpret the $l_{12} = 0$ component of the deuteron wave function as the IPM part which receives large corrections from tensor SRC. The per nucleon probability for

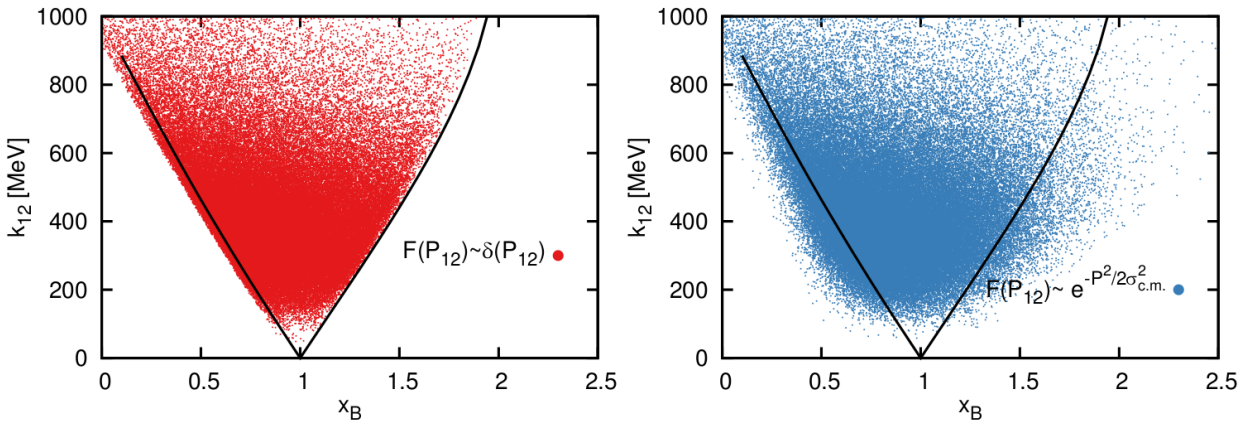

Figure 9 – (Color online) The $k_{12} - x_B$ scatter plot of $^{12}\mathrm{C}(e, e'pn)$ MC simulations with ($F(P_{12}) \sim e^{-\frac{P_{12}^2}{2\sigma_{c.m.}^2}}$) and without ($F(P_{12}) \sim \delta(P_{12})$) inclusion of c.m. motion. For the sake of comparison the solid line shows the minimum relative momentum k_{12}^{min} for $Q^2 = 2.7\,\mathrm{GeV}^2$ in the deuteron.

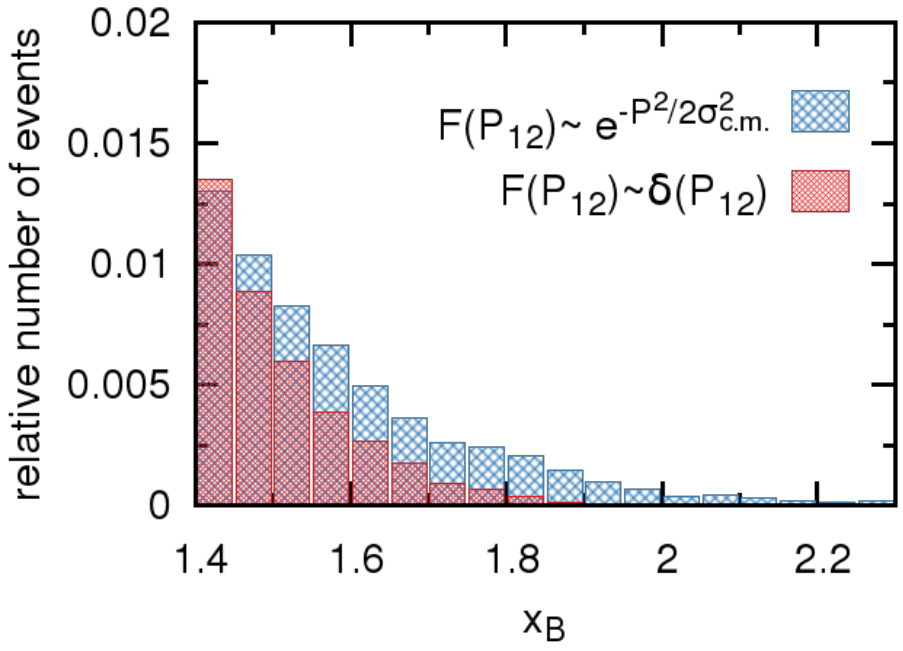

Figure 10 – (Color online) Histogram of the x_B distribution of $^{12}\mathrm{C}(e, e'pn)$ MC simulations with ($F(P_{12}) \sim e^{-\frac{P_{12}^2}{2\sigma_{c.m.}^2}}$) and without ($F(P_{12}) \sim \delta(P_{12})$) inclusion of c.m. motion. The kinematics is the one of the JLab experiment E02-019 [10]: $\epsilon_i = 5.766\,\mathrm{GeV}$ and $\theta_e = 18°$.

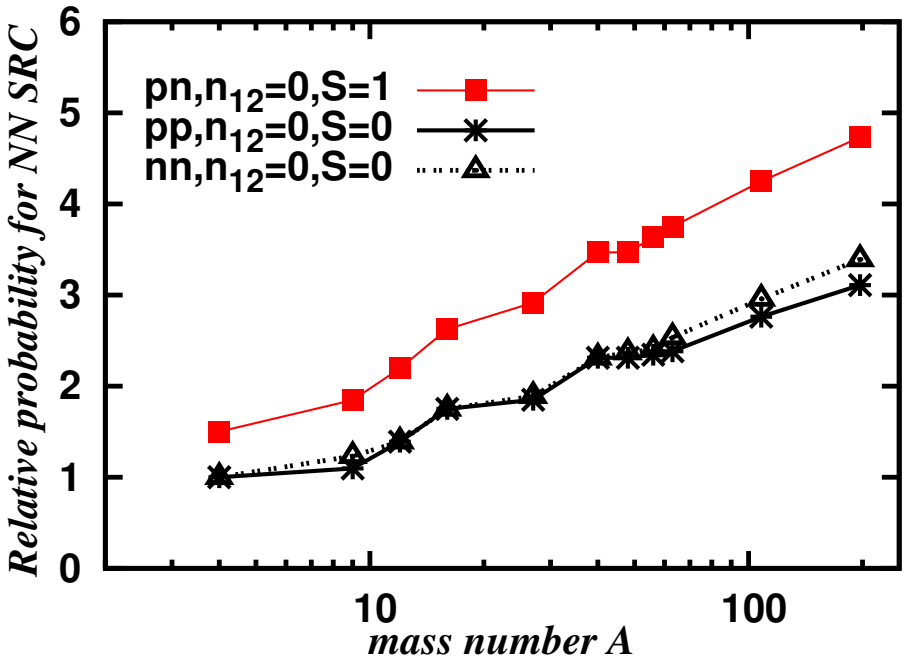

Figure 11 – The mass dependence of the per nucleon probability for pn SRC relative to the deuterium.

a pn SRC relative to the deuterium can be defined as

$$\frac{2}{N+Z}\frac{N_{pn(S=1)}(A,Z)}{N_{pn(S=1)}(A=2,Z=1)} = \frac{2}{A}N_{pn(S=1)}(A,Z)\ . \tag{53}$$

Similar expressions hold for the per nucleon pp SRC and the per nucleon nn SRC

$$\frac{2}{Z}N_{pp(S=0)}(A,Z) \qquad \frac{2}{N}N_{nn(S=0)}(A,Z)\ . \tag{54}$$

The results of the per nucleon probabilities are collected in Fig. 11. Relative to ^{2}H, the per nucleon probability of pn SRC are 2.20, 3.63, 4.73 times larger for Carbon, Iron, Gold. Along similar lines, relative to the "free" pp system the per nucleon probability of pp SRC are 1.39, 2.34, 3.11 times larger for Carbon, Iron, Gold.

In Fig. 12 we compare our predictions computed with the aid of the Eq. (49) with the extracted values of $a_2(A/D)$. We have opted to correct the predicted a_2 coefficients and not the data for c.m. motion. We stress that the c.m. correction factor cannot be computed in a model-independent fashion. For light nuclei our predictions tend to underestimate the measured a_2. This could be attributed to the lack of long-range clustering effects in the adopted wave functions. Indeed, it was pointed out in Ref. [54] that the high-density cluster components in the wave functions are an important source of correlation effects beyond the mean-field approach. For heavy nuclei our predictions for the relative SRC probability per nucleon do not saturate as much as the data seem to indicate. In Ref. [11] the authors estimated the mass dependence of a_2 by means of an expression of the type $a_2 \sim \int d^3\vec{r}\rho^2_{\rm MF}(\vec{r})$. Using Skyrme Hartree-Fock densities $\rho_{\rm MF}(\vec{r})$ a power-law of $A^{0.12}$ emerged. After normalizing to the measured value for $a_2(^{12}{\rm C}/D)$ the predicted power-low dependence agrees nicely with the data.

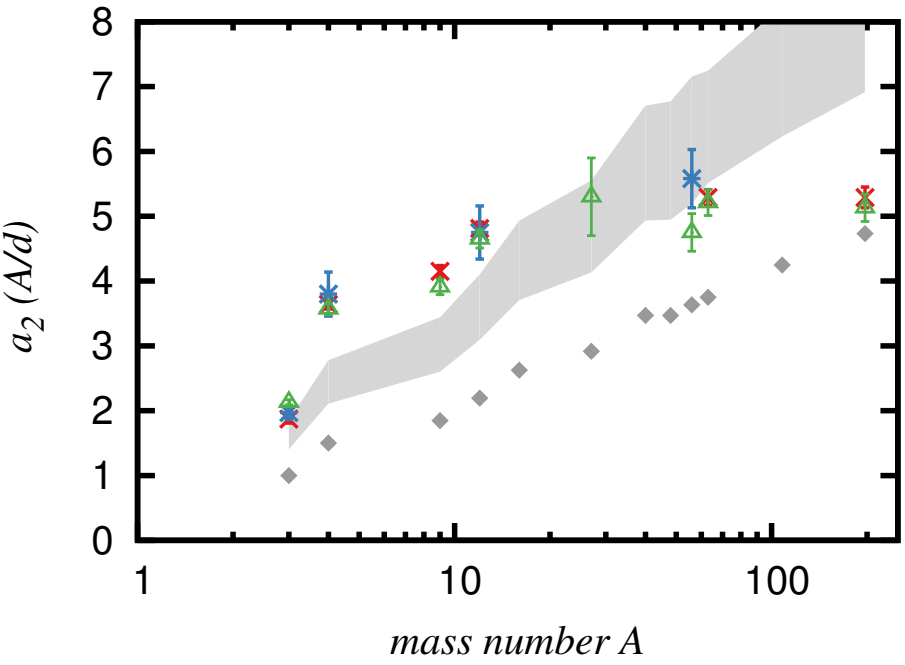

Figure 12 – (Color online) The computed values for the $a_2(A/D)$ for various nuclei. The data are from Refs. [9, 10, 14]. The shaded region is the prediction after correcting the computed values of $a_2(A/D)$ for the c.m. motion of the pair. The correction factor are determined by linear interpolation of the factors listed in Table 1. The width of the shaded area is determined by the error of the c.m. correction factors.

We stress that final-state interactions (FSI) represent another source of corrections which may induce an additional A-dependent correction to the data. FSI of the outgoing nucleons with the residual spectator nucleons, could shift part of the signal strength out of the cuts applied to the experimental phase space (or likewise move strength in) and decrease (or increase) the measured cross section and the corresponding a_2 coefficient.

In Fig. 13 we display the magnitude of the EMC effect, quantified by means of $-\frac{dR}{dx_B}$ versus our predictions for the quantity $\frac{2}{A}N_{pn(S=1)}$ or, the "per nucleon probability for pn SRC relative to the deuteron". We stress that the numbers which one finds on the x-axis are the results of parameter-free calculations. We consider the "per nucleon probability for pn SRC relative to the deuteron" as a measure for the magnitude of the proton-neutron SRC in a given nucleus. Obviously, there is a nice linear relationship between the quantity which we propose as a per nucleon measure for the magnitude of the SRC and the magnitude of the EMC effect.

3.3 Three-body correlations

The measurements of Refs. [9, 10] indicate that the ratio of the inclusive cross sections

$$\frac{\sigma^A\left(x_B, Q^2\right)}{\sigma^{^3\mathrm{He}}\left(x_B, Q^2\right)}\,, \tag{55}$$

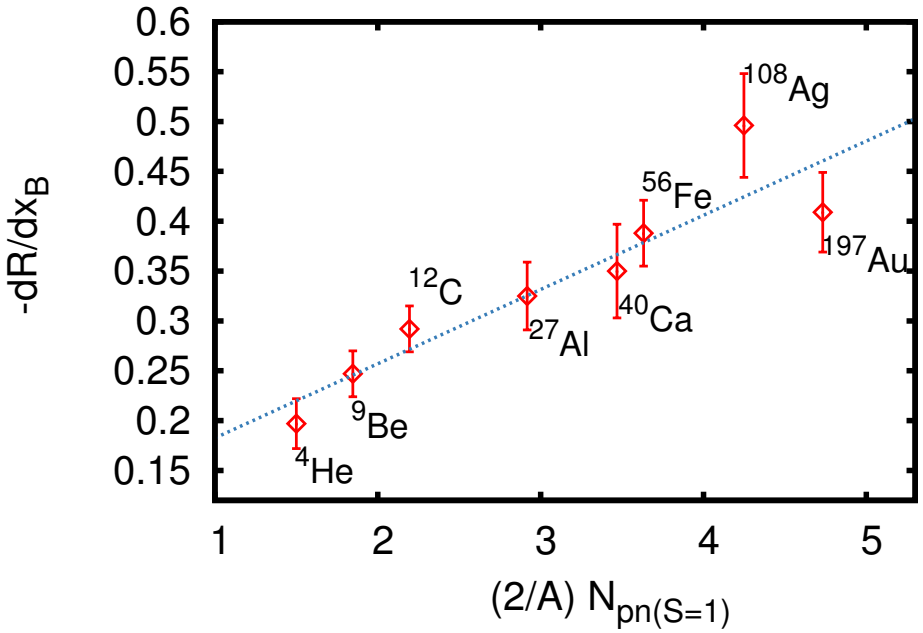

Figure 13 – The magnitude of the EMC effect versus the computed per nucleon number of correlated pn pairs. The data are from the analysis presented in Refs. [7, 14, 55]. The fitted line obeys the equation $-\frac{dR}{dx_B} = (0.108 \pm 0.028) + \frac{2}{A} N_{pn(S=1)} \cdot (0.074 \pm 0.010)$.

approximately scales for $2.25 \lesssim x_B \lesssim 3.0$. Along similar lines as those used in quantifying the 2N SRC in Sec. 3.2, it has been suggested [9] to parameterize the inclusive $A(e,e')$ cross section in the following form

$$\sigma^A \left(2.25 \lesssim x_B \lesssim 3, Q^2\right) = \frac{A}{3} a_3 \left(A/^3\mathrm{He}\right) \sigma_3 \left(x_B, Q^2\right) , \tag{56}$$

where $\sigma_3 \left(x_B, Q^2\right)$ is the cross section for scattering from a correlated 3N cluster which is once again assumed to be A independent. Inserting Eq. (56) into Eq. (55), one obtains

$$a_3 \left(A/^3\mathrm{He}\right) = \frac{3}{A} \frac{\sigma^A \left(x_B, Q^2\right)}{\sigma^{^3\mathrm{He}} \left(x_B, Q^2\right)} \quad \left(2.25 \lesssim x_B \lesssim 3.0\right) \ . \tag{57}$$

Notice that in the kinematic regime where 3N correlations are expected to dominate $(2.25 \lesssim x_B)$ the experimental situation is unsettled. For example, the recently measured $a_3(^4\mathrm{He}/^3\mathrm{He})$ ratios [10] are significantly larger than those reported in Ref. [9].

Similar to the per nucleon pn SRC of Eq. (53) we define the per nucleon probability for a ppn SRC relative to ^{3}He as

$$\frac{3}{A} \frac{N_{ppn}\left(A,Z\right)}{N_{ppn}\left(A=3,Z=2\right)} = \frac{3}{A} N_{ppn}\left(A,Z\right) , \tag{58}$$

where we used the fact that $N_{ppn}\left(A=3,Z=2\right) = 1$ in our framework. The results of the per nucleon probability of ppn SRC are collected in Figure 14.

The quantity of Eq. (58) can be linked to $a_3(A/^3\mathrm{He})$ under the condition that corrections stemming from c.m. motion of the correlated ppn triples, FSI effects, ... are small. Under

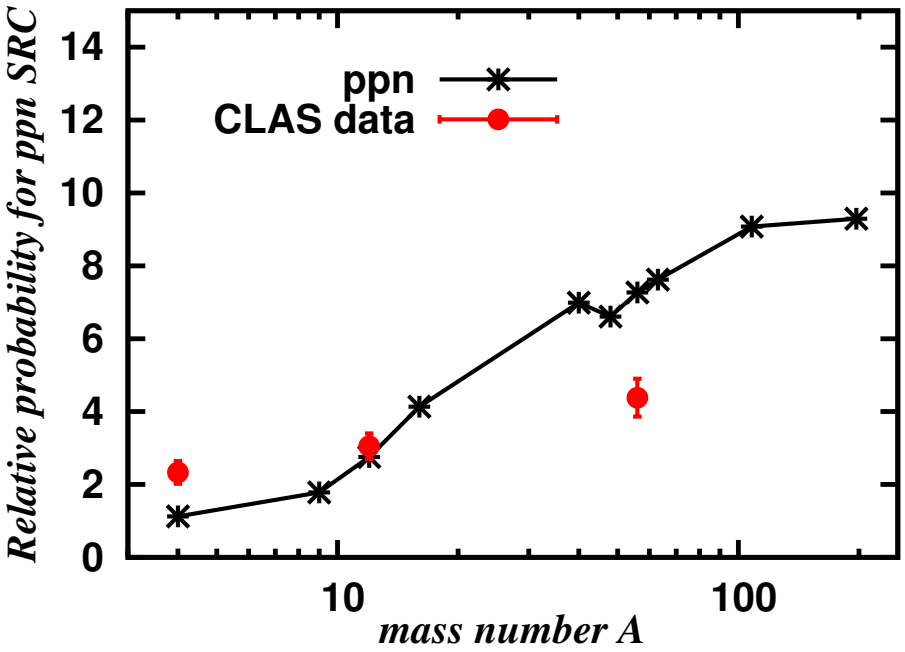

Figure 14 – The mass dependence of the per nucleon probability for ppn SRC relative to ^{3}He. We stress that neither the data nor the theoretical calculations have been corrected for c.m. motion and FSI effects. The data are from Ref. [9].

those idealized conditions one would have

$$a_3(A,^3\mathrm{He}) \approx \frac{3}{A} N_{ppn}(A,Z)\ . \tag{59}$$

In the naive assumption that all 3N pairs contribute to the $a_3(A/^3\mathrm{He})$ ratio, one expects an A^2 dependency. We suggest that only ppn triples in a "close" configuration contribute and we count the number of SRC triples with the aid of the Eq. (40). The ppn contributions will be larger than the pnn ones due to the magnitude of the electromagnetic coupling. Correlated triples should have at least one pn pair due to the dominant character of the tensor component. In Fig. 14 we show the predictions for the $a_3(A/^3\mathrm{He})$ coefficient as computed with the Eq. (59) and compare it to the data. We stress that the experimental situation is largely unsettled and that neither the data nor the theoretical calculations have been corrected for c.m. motion and FSI effects. For Helium and Carbon our predictions are in line with the experimental value. For Iron the prediction is about a factor of two larger than the experimentally determined ratio of cross sections. Our parameter-free calculations reproduce the fact that the mass dependence is much softer than the A^2 dependence that one would expect on naive grounds.

4 Conclusion

We have provided arguments that the mass dependence of the magnitude of the NN and NNN correlations can be captured by some approximate principles. Our method is based on the assumption that correlation operators generate the correlated part of the nuclear wave

function from that part of the mean-field wave function where two nucleons are "sufficiently close". This translates to computing those parts of the two-nucleon and three-nucleon wave functions with zero relative orbital momentum in order to identify short-range correlated pairs and triples.

We have calculated the number of pn, pp and nn $l_{12} = 0$ SRC pairs and studied their mass and isospin dependence. The A dependence of the magnitude of the pp, nn, and pn SRC manifests itself in a power-law dependence. We found a significant higher per nucleon SRC probability for pn pairs than for pp and for nn. To connect the computed number of SRC pairs to the measured $a_2\,(A/\mathrm{D})$ corrections are in order. Published experimental data include the radiation and Coulomb corrections. The correction factor stemming from final-state interactions and from the c.m. motion of the correlated pair, however, is far from established. We proposed a method to estimate the c.m. correction factor based on general properties of nucleon momentum distributions. Using Monte Carlo simulation we find a correction factor of about 1.7 ± 0.3. Our model calculations for a_2 are of the right order of magnitude and capture the A-dependence qualitatively. For small A our predictions underestimate the data, while we do not find the same degree of saturation for high A that the (scarce) data seem to suggest.

To compute the number of 3N SRC in a nucleus, we count the ppn states with three nucleons which are close. We have quantified the number of 3N SRC and provided predictions for the measured $a_3\,(A/^3\mathrm{He})$ coefficients. Our model calculations for the a_3 are of the same order of magnitude as the (scarce) data but overestimate the ^{56}Fe data point. In this comparison no corrections for c.m. motion and FSI effects have been made and it remains to be studied in how far they can blur the connection between inclusive electron-scattering data and the SRC information. We find a linear relationship between the magnitude of the EMC effect and the computed per nucleon number of SRC pn pairs. This may indicate that the EMC effect is (partly) driven by local nuclear dynamics (fluctuations in the nuclear densities), and that the number of pn SRC pairs serves as a measure for the magnitude of this effect.

Acknowledgments

The computational resources (Stevin Supercomputer Infrastructure) and services used in this work were provided by Ghent University, the Hercules Foundation and the Flemish Government – department EWI. This work is supported by the Research Foundation Flanders.

---

[1] W. Broniowski and M. Rybczynski, Phys. Rev. C **81**, 064909 (2010).
[2] P. G. Blunden and I. Sick, Phys. Rev. C **72**, 057601 (2005).
[3] J. Engel, J. Carlson, and R. Wiringa, Phys. Rev. C **83**, 034317 (2011).
[4] M. Alvioli and M. Strikman, Phys. Rev. C **83**, 044905 (2011).
[5] W. Cosyn, M. C. Martinez, and J. Ryckebusch, Phys. Rev. C **77**, 034602 (2008).
[6] J. Aubert et al., Phys. Lett. B **123**, 275 (1983).
[7] J. Seely, A. Daniel, D. Gaskell, et al., Phys. Rev. Lett. **103**, 202301 (2009).
[8] D. Day, J. Mccarthy, Z. Meziani, et al., Phys. Rev. Lett. **59**, 427 (1987).
[9] K. Egiyan, N. Dashyan, M. Sargsian, et al., Phys. Rev. Lett. **96**, 082501 (2006).
[10] N. Fomin, J. Arrington, R. Asaturyan, et al., Phys. Rev. Lett. **108**, 092502 (2012).

[11] L. Frankfurt, M. Sargsian, and M. Strikman, Int. J. Mod. Phys. A **23**, 2991 (2008).
[12] L. Weinstein, E. Piasetzky, D. Higinbotham, et al., Phys. Rev. Lett. **106**, 052301 (2011).
[13] O. Hen, E. Piasetzky, and L. Weinstein, Phys. Rev. C **85**, 047301 (2012).
[14] J. Arrington, A. Daniel, D. Day, et al., ArXiv e-prints, 1206.6343 (2012).
[15] R. Schiavilla, R. B. Wiringa, S. C. Pieper, and J. Carlson, Phys. Rev. Lett. **98**, 132501 (2007).
[16] R. Wiringa, R. Schiavilla, S. C. Pieper, and J. Carlson, Phys. Rev. C **78**, 021001 (2008).
[17] H. Feldmeier, W. Horiuchi, T. Neff, and Y. Suzuki, Phys. Rev. C **84**, 054003 (2011).
[18] M. Alvioli, C. Ciofi degli Atti, and H. Morita, Phys. Rev. Lett. **100**, 162503 (2008).
[19] C. Bisconti, F. A. d. Saavedra, G. Co', and A. Fabrocini, Phys. Rev. C **73**, 054304 (2006).
[20] C. Bisconti, F. Arias de Saavedra, and G. Co, Phys. Rev. C **75**, 054302 (2007).
[21] M. Vanhalst, W. Cosyn, and J. Ryckebusch, Phys. Rev. C **84**, 031302 (2011).
[22] J. Arrington, D. Higinbotham, G. Rosner, and M. Sargsian, Prog. Part. Nucl. Phys. **67**, 898 (2012).
[23] R. Shneor, P. Monaghan, R. Subedi, et al., Phys. Rev. Lett. **99**, 072501 (2007).
[24] J. Ryckebusch, Phys. Rev. C **64**, 044607 (2001).
[25] J. Ryckebusch, Phys. Lett. B **383**, 1 (1996).
[26] M. Alvioli, C. Ciofi degli Atti, L. P. Kaptari, et al., Phys. Rev. C **85**, 021001 (2012).
[27] R. Roth, T. Neff, and H. Feldmeier, Prog. Part. Nucl. Phys. **65**, 50 (2010).
[28] S. C. Pieper, R. B. Wiringa, and V. Pandharipande, Phys. Rev. C **46**, 1741 (1992).
[29] F. Arias de Saavedra, G. Co', A. Fabrocini, and S. Fantoni, Nucl. Phys. A **605**, 359 (1996).
[30] C. Gearheart, PhD thesis (Washington University, St. Louis, 1994).
[31] M. Alvioli, C. Ciofi degli Atti, and H. Morita, Phys. Rev. C **72**, 054310 (2005).
[32] M. Lacombe, B. Loiseau, J. M. Richard, et al., Phys. Rev. C **21**, 861 (1980).
[33] M. Lacombe, B. Loiseau, R. Mau, et al., Physics Letters B **101**, 139 (1981).
[34] L. Frankfurt and M. Strikman, Phys. Rep. **160**, 235 (1988).
[35] C. Ciofi degli Atti and S. Simula, Phys. Rev. C **53**, 1689 (1996).
[36] S. Janssen, J. Ryckebusch, W. Van Nespen, and D. Debruyne, Nucl. Phys. A **672**, 285 (2000).
[37] M. Iodice, E. Cisbani, R. De Leo, et al., Phys. Lett. B **653**, 392 (2007).
[38] R. Starink, M. van Batenburg, E. Cisbani, et al., Phys. Lett. B **474**, 33 (2000).
[39] J. Ryckebusch and W. Van Nespen, Eur. Phys. J. A **20**, 435 (2004).
[40] D. Middleton, J. Annand, C. Barbieri, et al., Eur. Phys. J. A **29**, 261 (2007).
[41] J. Ryckebusch, S. Janssen, W. Van Nespen, and D. Debruyne, Phys. Rev. C **61**, 021603R (2000).
[42] C. Barbieri, C. Giusti, F. Pacati, and W. Dickhoff, Phys. Rev. C **70**, 014606 (2004).
[43] R. Subedi, R. Shneor, P. Monaghan, et al., Science **320**, 1476 (2008).
[44] H. Baghdasaryan, L. B. Weinstein, J. M. Laget, et al., Phys. Rev. Lett. **105**, 222501 (2010).
[45] M. Moshinsky and Y. Smirnov, *The harmonic oscillator in modern physics* (Harwood Academic Publishers, Amsterdam, 1996).
[46] M. Sargsian, Int. J. Mod. Phys. E **10**, 405 (2001).
[47] L. Frankfurt, M. Strikman, D. Day, and M. Sargsian, Phys. Rev. C **48**, 2451 (1993).
[48] O. Benhar, A. Fabrocini, S. Fantoni, and I. Sick, Phys. Lett. B **343**, 47 (1995).

[49] O. Benhar, A. Fabrocini, S. Fantoni, and I. Sick, Nucl. Phys. A **579**, 493 (1994).
[50] I. Sick, S. Fantoni, A. Fabrocini, and O. Benhar, Phys. Lett. B **323**, 267 (1994).
[51] C. Ciofi degli Atti and S. Simula, Phys. Lett. B **325**, 276 (1994).
[52] E. Piasetzky, M. Sargsian, L. Frankfurt, et al., Phys. Rev. Lett. **97**, 162504 (2006).
[53] K. I. Blomqvist et al., Phys. Lett. B **421**, 71 (1998).
[54] M. Hirai, S. Kumano, K. Saito, and T. Watanabe, Phys. Rev. C **83**, 035202 (2011).
[55] J. Gomez, R. G. Arnold, P. E. Bosted, et al., Phys. Rev. D **49**, 4348 (1994).

3.3 Factorization of exclusive electroinduced two-nucleon knockout

Camille Colle[1], Wim Cosyn[1], Jan Ryckebusch[1] and Maarten Vanhalst[1]

[1]Department of Physics and Astronomy, Ghent University, Proeftuinstraat 86, B-9000 Gent, Belgium

Phys. Rev. C **89**, 024603 – Published 10 February 2014

Abstract

We investigate the factorization properties of the exclusive electroinduced two-nucleon knockout reaction $A(e, e'pN)$. A factorized expression for the cross section is derived and the conditions for factorization are studied. The $A(e, e'pN)$ cross section is shown to be proportional to the conditional center-of-mass (c.m.) momentum distribution for close-proximity pairs in a state with zero relative orbital momentum and zero radial quantum number. The width of this conditional c.m. momentum distribution is larger than the one corresponding with the full c.m. momentum distribution. It is shown that the final-state interactions (FSIs) only moderately affect the shape of the factorization function for the $A(e, e'pN)$ cross sections. Another prediction of the proposed factorization is that the mass dependence of the $A(e, e'pp)$ $[A(e, e'pn)]$ cross sections is much softer than $\frac{Z(Z-1)}{2}$ $[NZ]$.

1 Introduction

In recent years, substantial progress has been made in exploring the dynamics of short-range correlations (SRCs) in nuclei. On the experimental side, exclusive $A(p, 2p + n)$ [1] and $A(e, e'pN)$ [2–4] measurements have probed correlated pairs in nuclei and identified proton-neutron (pn) pairs as the dominant contribution. Inclusive $A(e, e')$ [5–7] measurements in kinematics favoring correlated pair knockout, have provided access to the mass dependence of the amount of correlated pairs relative to the deuteron. On the theoretical side, *ab initio* [8–11], cluster expansion [12–14], correlated basis function theory [15, 16], and low-momentum effective theory [17], calculations have provided insight in the fat high-momentum tails of the momentum distributions attributable to multinucleon correlations. Tensor correlations have been identified as the driving mechanism for the fat tails just above the Fermi momentum. The highest momenta in the tail of the momentum distribution are associated with the short-distance repulsive part of the nucleon-nucleon force and $N \geq 3$ correlations. Recent reviews of nuclear SRC can be found in Refs. [18, 19].

We have proposed a method to quantify the amount of correlated pairs in an arbitrary nucleus [20–22]. Thereby, we start from a picture of a correlated nuclear wave function as a product

of a correlation operator acting on an independent-particle model (IPM) Slater determinant $\Psi_A^{\rm IPM}$ [17]. The SRC-susceptible pairs are identified by selecting those parts of $\Psi_A^{\rm IPM}$ that provide the largest contribution when subjected to typical nuclear correlation operators. It is found that IPM nucleon-nucleon pairs with vanishing relative orbital momentum and vanishing relative radial quantum numbers, receive the largest corrections from the correlation operators. This can be readily understood by realizing that IPM close-proximity pairs are highly susceptible to SRC corrections. This imposes constraints on the relative orbital and radial quantum numbers of the two-nucleon cluster components in the IPM wave functions which receive SRC corrections.

With the proposed method of quantifying SRC we can reasonably account for the mass dependence of the $\frac{A(e,e')}{d(e,e')}$ ratio under conditions of suppressed one-body contributions (Bjorken $x_B \gtrsim 1.2$) [21] and the mass dependence of the magnitude of the EMC effect [22, 23]. In connecting the SRC information to inclusive electron-scattering data at Bjorken $x_B \gtrsim 1.2$, there are complicating issues like the role of c.m. motion [21, 24] and final-state interactions (FSIs) [25]. More quantitative information on SRC and their mass and isospin dependence, is expected to come from exclusive electroinduced two-nucleon knockout which is the real fingerprint of nuclear SRC [26]. Reactions of this type are under investigation at Jefferson Laboratory (JLab) and results for ^{12}C$(e,e'pN)$ have been published [3, 4].

In this paper, we investigate the factorization properties of the exclusive $A(e,e'pN)$ reaction. Factorization is a particular result that emerges only under specific assumptions in the description of the scattering process. It results in an approximate expression for the cross section which becomes proportional to a specific function of selected dynamic variables. For exclusive quasielastic $A(e,e'p)$ processes, for example, the factorization function is the one-nucleon momentum distribution evaluated at the initial nucleon's momentum. It will be shown that for exclusive $A(e,e'pN)$ these roles are respectively played by the c.m. momentum distribution for close-proximity pairs and the c.m. momentum of the initial pair.

In Sec. 2 we present calculations for the pair c.m. momentum distribution in the IPM. It is shown that the correlation-susceptible IPM pairs have a broader c.m. width than those that are less prone to SRC corrections. In Sec. 3, we show that after making a number of reasonable assumptions, the eightfold $A(e,e'pN)$ cross section factorizes with the conditional pair c.m. momentum distribution as the factorization function. In Sec. 4 we report on results of Monte Carlo simulations for $A(e,e'pp)$ processes in kinematics corresponding to those accessible in the JLab Hall A and Hall B detectors. We study the effect of typically applied cuts on several quantities. In Sec. 5 it is investigated to what extent FSIs affect the factorization function of the exclusive $A(e,e'pN)$ process. Finally, our conclusions are stated in Sec. 6.

2 Pair Center-of-mass momentum distributions

In this section we study the pp and pn pair c.m. momentum distribution for ^{12}C, ^{27}Al, ^{56}Fe and ^{208}Pb which we deem representative for the full mass range of stable nuclei. We

introduce the relative and c.m. coordinates and momenta

$$\vec{r}_{12} = \vec{r}_1 - \vec{r}_2, \qquad \vec{R}_{12} = \frac{\vec{r}_1 + \vec{r}_2}{2} \ , \tag{1}$$

$$\vec{k}_{12} = \frac{\vec{k}_1 - \vec{k}_2}{2}, \qquad \vec{P}_{12} = \vec{k}_1 + \vec{k}_2 \ . \tag{2}$$

The corresponding two-body momentum density reads

$$P_2\left(\vec{k}_{12}, \vec{P}_{12}\right) = \frac{1}{(2\pi)^6} \int d\vec{r}_{12} \int d\vec{r}\,'_{12} \int d\vec{R}_{12} \int d\vec{R}\,'_{12} \times e^{\imath \vec{k}_{12}\cdot\left(\vec{r}\,'_{12}-\vec{r}_{12}\right)} e^{\imath \vec{P}_{12}\cdot\left(\vec{R}\,'_{12}-\vec{R}_{12}\right)} \rho_2(\vec{r}\,'_{12}, \vec{R}\,'_{12}; \vec{r}_{12}, \vec{R}_{12}), \tag{3}$$

where $\rho_2(\vec{r}\,'_{12}, \vec{R}\,'_{12}; \vec{r}_{12}, \vec{R}_{12})$ is the non-diagonal two-body density (TBD) matrix

$$\rho_2(\vec{r}\,'_{12}, \vec{R}\,'_{12}; \vec{r}_{12}, \vec{R}_{12}) = \int \{d\vec{r}_{3-A}\} \Psi^*_A(\vec{r}\,'_1, \vec{r}\,'_2, \vec{r}_3, \ldots, \vec{r}_A) \Psi_A(\vec{r}_1, \vec{r}_2, \vec{r}_3, \ldots, \vec{r}_A). \tag{4}$$

Here, Ψ_A is the normalized ground-state wave function of the nucleus A and $\{d\vec{r}_{i-A}\} \equiv d\vec{r}_i d\vec{r}_{i+1} \ldots d\vec{r}_A$. For a spherically symmetric system, $P_2\left(\vec{k}_{12}, \vec{P}_{12}\right)$ depends on three independent variables, for example the magnitudes $\left|\vec{k}_{12}\right|$ and $\left|\vec{P}_{12}\right|$ and the angle between $\vec{k}_{12}$ and $\vec{P}_{12}$. In Ref. [13] two-body momentum distributions for ^{3}He and ^{4}He are shown to be largely independent of the angle between $\vec{k}_{12}$ and $\vec{P}_{12}$ for $P_{12} \lesssim 200$ MeV. Integrating over the directional dependence of Eq. (3), the quantity

$$n_2(k_{12}, P_{12}) k_{12}^2 dk_{12} P_{12}^2 dP_{12} = k_{12}^2 dk_{12} P_{12}^2 dP_{12} \int d\Omega_{k_{12}} \int d\Omega_{P_{12}} P_2(\vec{k}_{12}, \vec{P}_{12}) \ , \tag{5}$$

is connected to the probability of finding a nucleon pair with relative and c.m. momentum in $[k_{12}, k_{12} + dk_{12}]$ and $[P_{12}, P_{12} + dP_{12}]$. With the spherical-wave expansion for the two vector plane waves in Eq. (3) one obtains

$$n_2(k_{12}, P_{12}) = \frac{4}{\pi^2} \sum_{lm_l} \sum_{\Lambda M_\Lambda} n_2^{lm_l \Lambda M_\Lambda}(k_{12}, P_{12}), \tag{6}$$

with

$$n_2^{lm_l \Lambda M_\Lambda}(k_{12}, P_{12}) = \int dr\,'_{12}\ {r\,'_{12}}^2 \int dR\,'_{12}\ {R\,'_{12}}^2 \int dr_{12}\ r_{12}^2 \int dR_{12}\ R_{12}^2 \times j_l(k_{12} r_{12}) j_l(k_{12} r\,'_{12}) j_\Lambda(P_{12} R_{12}) j_\Lambda(P_{12} R\,'_{12}) \rho_2^{lm_l \Lambda M_\Lambda}(r\,'_{12}, R\,'_{12}; r_{12}, R_{12}). \tag{7}$$

Here, $\rho_2^{lm_l \Lambda M_\Lambda}(r\,'_{12}, R\,'_{12}; r_{12}, R_{12})$ is the projection of the TBD matrix on relative and c.m. orbital angular-momentum states $|lm_l\rangle$ and $|\Lambda M_\Lambda\rangle$.

The pair c.m. momentum distribution is defined by

$$P_2(P_{12}) = \int d\Omega_{P_{12}} \int d\vec{k}_{12} P_2(\vec{k}_{12}, \vec{P}_{12}) = \int dk_{12} k_{12}^2 n_2(k_{12}, P_{12}), \tag{8}$$

and the quantity $P_2(P_{12})\ P_{12}^2\ dP_{12}$ is related to the probability of finding a nucleon pair with $\left|\vec{P}_{12}\right|$ in $[P_{12}, P_{12}+dP_{12}]$ irrespective of the magnitude and direction of $\vec{k}_{12}$. Similarly, the pair relative momentum distribution is defined as

$$n_2(k_{12}) = \int d\Omega_{k_{12}} \int d\vec{P}_{12} P_2(\vec{k}_{12}, \vec{P}_{12})\ . \tag{9}$$

In the IPM, the ground-state wave function can be expanded in terms of single-particle wave functions ϕ_{α_i}

$$\Psi_A^{\rm IPM} = (A!\,)^{-1/2} {\rm det}\Big[\phi_{\alpha_i}(\vec{x}_j)\Big], \tag{10}$$

and the TBD matrix is given by

$$\begin{aligned}\rho_2^{\rm IPM}(\vec{r}\,'_{12}, \vec{R}\,'_{12}; \vec{r}_{12}, \vec{R}_{12}) &= \frac{2}{A(A-1)} \sum_{\alpha<\beta} \frac{1}{2} \\ &\times \left[\phi_\alpha^*(\vec{x}_1\,')\phi_\beta^*(\vec{x}_2\,') - \phi_\beta^*(\vec{x}_1\,')\phi_\alpha^*(\vec{x}_2\,')\right] \left[\phi_\alpha(\vec{x}_1)\phi_\beta(\vec{x}_2) - \phi_\beta(\vec{x}_1)\phi_\alpha(\vec{x}_2)\right]. \end{aligned} \tag{11}$$

Here, $\vec{x} \equiv (\vec{r}, \vec{\sigma}, \vec{\tau})$ is a shorthand notation for the spatial, spin, and isospin coordinates. The summation $\sum_{\alpha<\beta}$ extends over all occupied single-particle levels and implicitly includes an integration over the spin and isospin degrees of freedom (d.o.f.).

In a HO basis the uncoupled single-particle states read

$$\phi_\alpha(\vec{x}) \equiv \psi_{n_\alpha l_\alpha m_{l_\alpha}}(\vec{r}) \chi_{\sigma_\alpha}(\vec{\sigma})\, \xi_{\tau_\alpha}(\vec{\tau})\,. \tag{12}$$

The A dependence can be taken care of by means of the parameterization $\hbar\omega({\rm MeV}) = 45\ A^{-\frac{1}{3}} - 25\ A^{-\frac{2}{3}}$. A transformation from $(\vec{r}_1, \vec{r}_2)$ to $(\vec{r}_{12}, \vec{R}_{12})$ for the uncoupled normalized-and-antisymmetrized (nas) two-nucleon states can be readily performed in a HO basis [20, 21]

$$\begin{aligned} \mid \alpha\beta\rangle_{\rm nas} &= \sum_{\substack{nlm_l N\Lambda M_\Lambda \\ SM_S TM_T}} \langle nlm_l N\Lambda M_\Lambda SM_S TM_T \mid \alpha\beta\rangle \mid nlm_l N\Lambda M_\Lambda SM_S TM_T\rangle \\ &= \sum_{A=\{\substack{nlm_l N\Lambda M_\Lambda \\ SM_S TM_T\}}} C^A_{\alpha\beta} \mid A\rangle, \end{aligned} \tag{13}$$

with the transformation coefficient $C_{\alpha\beta}^{nlm_l N\Lambda M_\Lambda SM_S TM_T}$ given by

$$\begin{aligned} C_{\alpha\beta}^{nlm_l N\Lambda M_\Lambda SM_S TM_T} &= \frac{1}{\sqrt{2}} \left[1 - (-1)^{l+S+T}\right] \langle \frac{1}{2}\tau_\alpha \frac{1}{2}\tau_\beta \mid TM_T\rangle \langle \frac{1}{2}\sigma_\alpha \frac{1}{2}\sigma_\beta \mid SM_S\rangle \\ &\times \sum_{LM_L} \langle l_\alpha m_{l_\alpha} l_\beta m_{l_\beta} \mid LM_L\rangle \langle nlN\Lambda; L \mid n_\alpha l_\alpha n_\beta l_\beta; L\rangle_{\rm SMB} \langle LM_L \mid lm_l \Lambda M_\Lambda\rangle\,, \end{aligned} \tag{14}$$

where we use the Talmi-Moshinsky brackets $\langle|\rangle_{\rm SMB}$ [27] to separate out the relative and c.m. coordinates in the products of single-particle wave functions.

After performing the transformation of Eq. (13) for the TBD matrix of Eq. (11), $P_2(P_{12})$ can be written as

$$P_2(P_{12}) = \frac{2}{\pi} \sum_{nlm_l} \sum_{\Lambda M_\Lambda} P_2^{nlm_l \Lambda M_\Lambda}(P_{12}), \tag{15}$$

with

$$P_2^{nlm_l\Lambda M_\Lambda}(P_{12}) = \frac{2}{A(A-1)} \sum_{\alpha<\beta} \sum_{NN'} \sum_{SM_STM_T} (C_{\alpha\beta}^{nlm_lN'\Lambda M_\Lambda SM_STM_T})^\dagger C_{\alpha\beta}^{nlm_lN\Lambda M_\Lambda SM_STM_T} \times \int dR'_{12}\ {R'_{12}}^2 \int dR_{12}\ R_{12}^2\ \ j_\Lambda(P_{12}R'_{12}) j_\Lambda(P_{12}R_{12}) R_{N'\Lambda}(\sqrt{2}R'_{12}) R_{N\Lambda}(\sqrt{2}R_{12}) \tag{16}$$

A Woods-Saxon basis, for example, first needs to be expanded in a HO basis before a projection of the type (16) can be made. Using Eqs. (15) and (16), the conditional pair c.m. momentum distribution for a given relative radial quantum number n and relative orbital momentum l, can be defined as

$$P_2(P_{12}|nl = \nu\lambda) = \frac{2}{\pi} \sum_{m_l} \sum_{\Lambda M_\Lambda} P_2^{\nu\lambda m_l\Lambda M_\Lambda}(P_{12})\ . \tag{17}$$

Obviously, one has

$$P_2(P_{12}) = \sum_{\nu\lambda} P_2(P_{12}|nl = \nu\lambda) = \sum_{\lambda} P_2(P_{12}|l = \lambda), \tag{18}$$

where $P_2(P_{12}|l = \lambda)$ is the conditional pair c.m. momentum distribution for $l = \lambda$.

A symmetric correlation operator $\widehat{\mathcal{G}}$ can be applied to the IPM wave function of Eq. (10) in order to obtain a realistic ground-state wave function [15, 28–30]

$$\mid \Psi_A\rangle = \frac{1}{\sqrt{\langle\ \Psi_A^{\rm IPM} \mid \widehat{\mathcal{G}}^\dagger\widehat{\mathcal{G}} \mid \Psi_A^{\rm IPM}\ \rangle}}\ \widehat{\mathcal{G}} \mid \Psi_A^{\rm IPM}\ \rangle\ . \tag{19}$$

The operator $\widehat{\mathcal{G}}$ is complicated but as far as the SRC are concerned, it is dominated by the central, tensor and spin-isospin correlations [31, 32]

$$\widehat{\mathcal{G}} \approx \widehat{\mathcal{S}}\Big[\prod_{i<j=1}^{A}\Big(1 + \hat{\wr}\,(\vec{x}_i, \vec{x}_j)\Big)\Big]\ , \tag{20}$$

with $\widehat{\mathcal{S}}$ the symmetrization operator and

$$\hat{\wr}\,(\vec{x}_1, \vec{x}_2) = -g_c(r_{12}) + f_{t\tau}(r_{12}) S_{12}\vec{\tau}_1\cdot\vec{\tau}_2 + f_{\sigma\tau}(r_{12})\vec{\sigma}_1\cdot\vec{\sigma}_2\vec{\tau}_1\cdot\vec{\tau}_2\,, \tag{21}$$

where $g_c(r_{12})$, $f_{t\tau}(r_{12})$, $f_{\sigma\tau}(r_{12})$ are the central, tensor, and spin-isospin correlation functions, and S_{12} the tensor operator. The sign convention of $-g_c(r_{12})$ in Eq. (21) implies that $\lim\limits_{r_{12}\to 0} g_c(r_{12}) = g_0$ $(0 < g_0 \leq 1)$). We stress that the correlation functions cannot be considered as universal [29]. They depend for example on the choices made with regard to the nucleon-nucleon interaction, the single-particle basis and the many-body approximation scheme.

With Eq. (19), the intrinsic complexity stemming from the nuclear correlations is shifted from the wave functions to the transition operators. For example, the ground-state matrix element with a two-body operator $\hat{\mathcal{O}}^{[2]}$ adopts the form

$$\langle\Psi_A \mid \hat{\mathcal{O}}^{[2]} \mid \Psi_A\rangle = \frac{1}{\langle\ \Psi_A^{\rm IPM} \mid \widehat{\mathcal{G}}^\dagger\widehat{\mathcal{G}} \mid \Psi_A^{\rm IPM}\ \rangle} \langle\ \Psi_A^{\rm IPM} \mid \widehat{\mathcal{G}}^\dagger\hat{\mathcal{O}}^{[2]}\widehat{\mathcal{G}} \mid \Psi_A^{\rm IPM}\ \rangle\ , \tag{22}$$

whereby high-order many-body operators are generated. Throughout this work we adopt the two-body cluster (TBC) approximation, which amounts to discarding all terms in $\widehat{\mathcal{G}}^{\dagger}\hat{\mathcal{O}}^{[2]}\widehat{\mathcal{G}}$ except those in which the transition operator and the correlators act on the same pair of particles. In this lowest-order cluster expansion the matrix element of Eq. (22) becomes with the aid of Eq. (20)

$$\begin{aligned}
&\langle \Psi_A \mid \hat{\mathcal{O}}^{[2]} \mid \Psi_A \rangle \approx \frac{1}{\langle\ \Psi_A \mid \Psi_A\ \rangle} \\
&\times \langle\ \Psi_A^{\rm IPM} \mid \sum_{i<j=1}^{A} \left(1+\hat{\imath}\left(\vec{x}_i,\vec{x}_j\right)\right)^{\dagger} \hat{\mathcal{O}}^{[2]}\left(i,j\right) \left(1+\hat{\imath}\left(\vec{x}_i,\vec{x}_j\right)\right) \mid \Psi_A^{\rm IPM}\rangle \\
&= \frac{1}{\langle \Psi_A \mid \Psi_A\ \rangle} \Big[\langle\ \Psi_A^{\rm IPM} \mid \hat{\mathcal{O}}^{[2]} \mid \Psi_A^{\rm IPM}\ \rangle + \text{TBC corrections}\Big]. \qquad (23)
\end{aligned}$$

In this expansion, the matrix element is written as the sum of the bare (or IPM) contribution and the TBC corrections to it. The $P_2(P_{12})$ and $n_2(k_{12})$ of Eqs. (8-9) can be computed with the aid of the Eq. (23) using the transition operators $\delta\left(\vec{P}_{ij}-(\vec{k}_i+\vec{k}_j)\right)$ and $\delta\left(\vec{k}_{ij}-\frac{\vec{k}_i-\vec{k}_j}{2}\right)$. As the $\hat{\imath}$ involves only relative coordinates, the $P_2(P_{12})$ is not affected by the SRC corrections in the TBC approximation. We define $n_2^{\rm IPM}(k_{12})$ as the IPM contribution of $n_2(k_{12})$ and $n_2^{\rm TBC}(k_{12})$ the result obtained with Eq. (23). Accordingly, $n_2^{\rm TBC}(k_{12}) = n_2^{\rm IPM}(k_{12}) + \text{TBC corrections}$. For $n_2^{\rm TBC}(k_{12})$ the denominator $\langle\ \Psi_A \mid \Psi_A\ \rangle$ in Eq. (23) can be numerically computed by imposing the normalization conditions: $\int dk_{12} n_2^{\rm TBC}(k_{12}) k_{12}^2 = 1$. As in Eqs. (7) and (17), one can introduce projection operators, and select the contributions to $n_2^{\rm TBC}(k_{12})$ stemming from particular quantum numbers (nl) of the relative two-nucleon wave functions in $\Psi_A^{\rm IPM}$. We define $n_2^{2n+l}(k_{12})$ as the contribution to $n_2^{\rm TBC}$ considering only (nl) configurations in $\Psi_A^{\rm IPM}$ with constant $2n+l$. Obviously, one has

$$\sum_{2n+l} n_2^{2n+l}(k_{12}) = n_2^{\rm TBC}(k_{12}). \qquad (24)$$

The computed n_2^{2n+l}, $n_2^{\rm TBC}$ and $n_2^{\rm IPM}$ for ^{56}Fe are shown in Fig. 1. Below the Fermi momentum k_F, the effect of the correlation operator is negligible and $n_2^{\rm IPM}(k_{12}) \approx n_2^{\rm TBC}(k_{12})$. For $k_{12} > k_F$, $n_2^{\rm IPM}(k_{12})$ drops rapidly while $n_2^{\rm TBC}(k_{12})$ exhibits the SRC related high momentum tail. The tail is dominated by the $2n+l=0$ configurations. This indicates that most of the SRC are dynamically generated through the operation of the correlation operators on $nl = 00$ IPM pairs.

In Sec. 3, it is shown that in the limit of vanishing FSIs the factorization function of the exclusive $A(e,e'pN)$ cross section is $P_2(P_{12}|nl=00)$. In Figs. 2 and 3, we display the computed $P_2(P_{12})$ and $P_2(P_{12}|nl=00)$ for the pp and pn pairs in ^{12}C, ^{27}Al, ^{56}Fe and ^{208}Pb. The relative weight of the $(nl=00)$ in the total c.m. distribution decreases spectacularly with increasing mass number A. This will reflect itself in the mass dependence of the $A(e,e'NN)$ cross sections which are predicted to scale much softer than A^2. The $(nl=00)$ pairs are strongly localized in space which enlarges the $P_2(P_{12}|nl=00)$ width relative to the $P_2(P_{12})$ one. The mass dependence of the normalized $P_2(P_{12})$ reflects itself in a modest growth of the width of the distribution. For the light nuclei ^{12}C and ^{27}Al, the pp and pn c.m. distributions look very similar.

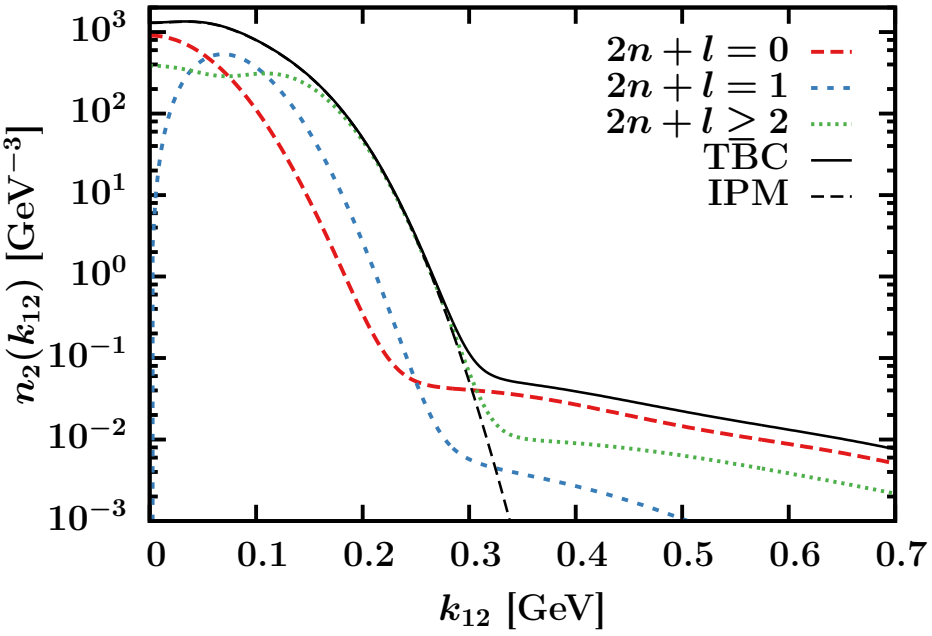

Figure 1 – (Color online) The momentum dependence of the computed $n_2^{2n+l}(k_{12})$, $n_2^{\rm TBC}(k_{12})$ and $n_2^{\rm IPM}(k_{12})$ for ^{56}Fe in a HO basis. In order to quantify the effect of SRC we have used the $g_c\,(r_{12})$ of Ref. [33] and the $f_{t\tau}\,(r_{12})$, $f_{\sigma\tau}(r_{12})$ of Ref. [28].

At first sight the computed $P_2(P_{12})$ for the pp and pn pairs in Figs. 2 and 3 look very Gaussian. In what follows, we use the moments to quantify the non-Gaussianity of the P_2. The first moment, or mean, of a distribution $F(x)$ is defined as

$$\mu_1 = \mu = \frac{\int_D xF(x)\mathrm{d}x}{\int_D F(x)\mathrm{d}x}, \tag{25}$$

where D is the domain of the distribution. For $m > 1$, we define the central moments as

$$\mu_m = \frac{\int_D (x-\mu)^m F(x)\mathrm{d}x}{\int_D F(x)\mathrm{d}x}\,. \tag{26}$$

The width is defined as $\sigma = \sqrt{\mu_2}$. With regard to μ_3 and μ_4, it is common practice to describe a distribution with the skewness γ_1 and excess kurtosis κ

$$\gamma_1 \equiv \frac{\mu_3}{\sigma^3} \tag{27}$$

$$\kappa \equiv \frac{\mu_4}{\sigma^4} - 3, \tag{28}$$

which are both vanishing for a Gaussian distribution.

For a spherically symmetric distribution, one can derive the distributions $P_{2,i}\,(P_{12,i})$ $(i = x, y, z)$ along the axes from

$$P_{12}^2 P_2\left(P_{12} = \sqrt{P_{12,x}^2 + P_{12,y}^2 + P_{12,z}^2}\right). \tag{29}$$

Gaussian $P_{2,i}$ give rise to a $P_{12}^2 P_2\,(P_{12,i})$ of the Maxwell-Boltzmann type.

		HO			WS		
		σ (MeV)	γ_1 [Eq. (27)]	κ [Eq. (28)]	σ (MeV)	γ_1 [Eq. (27)]	κ [Eq. (28)]
^{12}C	$P_{2,x}(P_{12,x}\|nl=00)$	156	0.00	−0.25	158	0.00	−0.28
^{12}C	$P_{2,x}(P_{12,x})$	140	−0.01	−0.12	142	−0.01	−0.05
^{27}Al	$P_{2,x}(P_{12,x}\|nl=00)$	164	0.00	−0.45	168	0.00	−0.45
^{27}Al	$P_{2,x}(P_{12,x})$	144	−0.01	−0.20	148	−0.01	−0.20
^{56}Fe	$P_{2,x}(P_{12,x}\|nl=00)$	172	0.00	−0.54	174	0.00	−0.54
^{56}Fe	$P_{2,x}(P_x)$	146	−0.01	−0.27	149	0.00	−0.26
^{208}Pb	$P_{2,x}(P_{12,x}\|nl=00)$	178	0.00	−0.58	177	0.00	−0.63
^{208}Pb	$P_{2,x}(P_{12,x})$	145	0.00	−0.31	146	0.00	−0.31

Table 1 – The moments of the $P_{2,x}\,(P_{12,x})$ and the $P_{2,x}\,(P_{12,x}|nl=00)$ distributions for pp pairs as computed in a HO and WS single-particle basis for various nuclei.

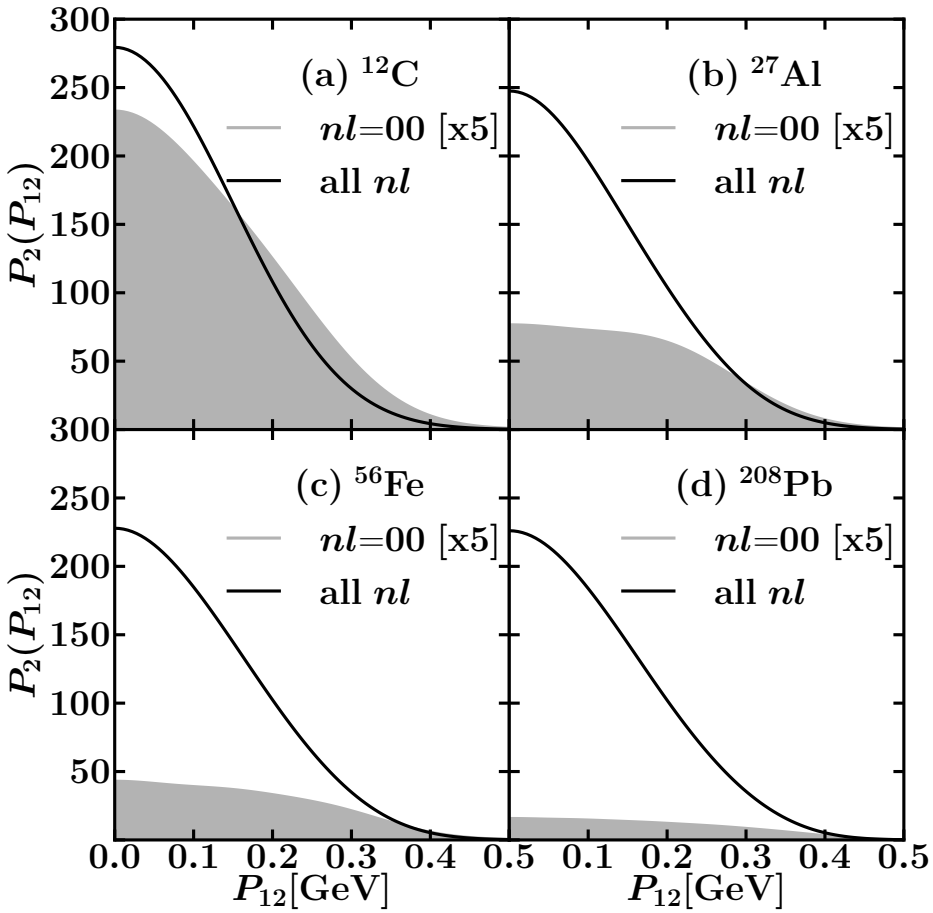

Figure 2 – The momentum dependence of $P_2(P_{12})$ and the $P_2\,(P_{12}|nl = 00)$ for pp pairs in different nuclei. The adopted normalization convention is that $\int_0^\infty \mathrm{d}P_{12}\; P_{12}^2 P_2(P_{12}) = 1$. Note that only the pp contributions to $P_2(P_{12})$ are considered when performing the integral. The results are obtained in a HO basis.

Table 1 shows the computed moments of the $P_{2,x}(P_{12,x}|nl = 00)$ and $P_{2,x}(P_{12,x})$ distributions for pp pairs. These results are obtained with HO and Woods-Saxon (WS) single-particle wave functions. We find that the c.m. distributions are not perfectly Gaussian and that the non-Gaussianity grows with A. The values of the widths are only moderately sensitive to the single-particle basis used. The WS widths are larger by a few percent than the HO ones.

In Fig. 4, the calculated widths of the $P_{2,x}(P_{12,x})$ and $P_{2,x}(P_{12,x}|l)$ are shown for pp, nn and np pairs. For the np pairs we discriminate between singlet ($S = 0$) and triplet ($S = 1$) spin states. From Fig. 4 we draw the following conclusions. The width of the $P_{2,x}(P_{12}|l)$ depends on l. For $l = 0$ and np pairs, the width of $P_{2,x}(P|l)$ is almost independent of S. For heavy nuclei there is a substantial difference in the width of the $P_{2,x}(P|l = 0)$ for pp, nn and np pairs but for light nuclei this is not the case. A similar but smaller dependence on the width is found for n at fixed l, the width of $P_2(P_{12}|nl)$ decreases for increasing n. We conclude that from the width of the c.m. distribution of the pairs one can infer information about their relative orbital momentum.

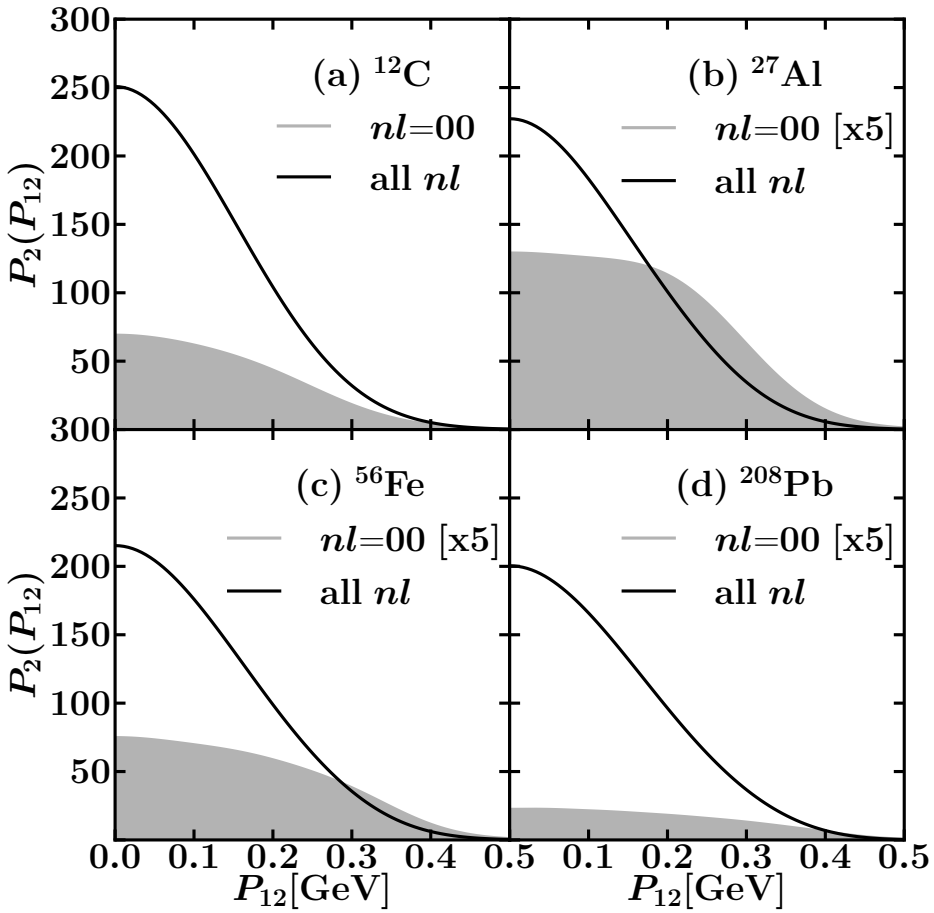

Figure 3 – As in Fig. 2 but for pn pairs.

3 Factorization of the two-nucleon knockout cross section

It is well known that the fivefold differential cross section for the exclusive $A(e,e'p)A-1$ reaction under quasifree kinematics with $A-1$ spectators

$$\gamma^*\,(q) + A-1\,(p_{A-1}) + N\,(k_1) \longrightarrow A-1\,(p_{A-1}) + N\,(p_1)\ , \tag{30}$$

factorizes as

$$d^5\sigma(e,e'p) = K_{ep}\sigma_{ep}P_1(\vec{k}_m, E_m)\ . \tag{31}$$

Here, K_{ep} is a kinematical factor and σ_{ep} the off-shell electron-proton cross section. Further, $\vec{k}_m = -\vec{p}_{A-1} = \vec{k}_1$ is the missing momentum and $E_m = q^0 - T_{p_1} - T_{A-1}$ the missing energy, whereby T_{A-1} and T_{p_1} are the kinetic energy of the recoiling nucleus and ejected nucleon. The $P_1(\vec{k}, E)$ is the one-body spectral function and is associated with the combined probability of removing a proton with momentum $\vec{k}$ from the ground-state of A and of finding the residual $A-1$ nucleus at excitation energy E (measured relative to the ground-state of the target nucleus). The factorization is exact in a non-relativistic reaction model with $A-1$ spectators and vanishing FSIs [34]. The validity of the spectator approximation requires that the E_m is confined to low values, corresponding to states with a predominant one-hole character relative to the ground state of the target nucleus A.

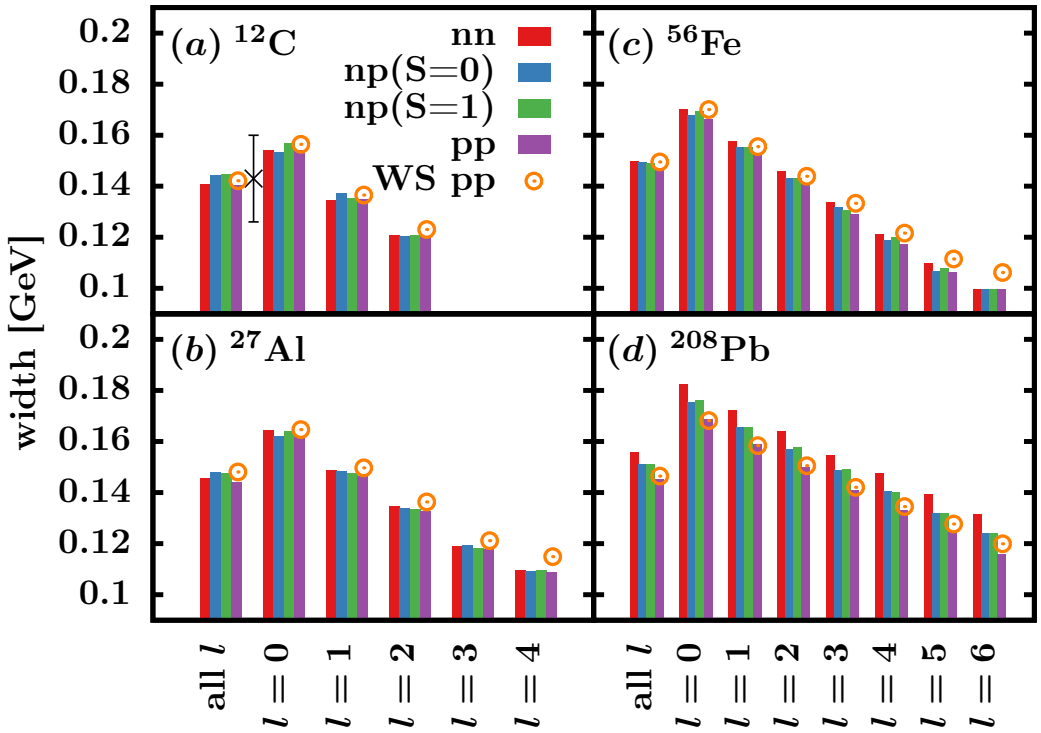

Figure 4 – (Color online) Computed widths of the $P_{2,x}$ ($P_{12,x}$) (denoted as "all l") and $P_{2,x}$ ($P_{12,x}|l$) distributions for pp, nn, np($S=0$) and np($S=1$) pairs in ^{12}C, ^{27}Al, ^{56}Fe, ^{208}Pb. Unless stated otherwise the results are obtained in a HO basis. For pp pairs we also display results for a WS basis (denoted as "WS pp"). The black cross is the experimental result from Ref. [1].

Below, it is shown that also the $A(e,e'pN)$ differential cross section factorizes under certain assumptions. The factorization function is connected to the c.m. motion of close-proximity pairs. In Ref. [35] the factorization function is introduced as the so-called *decay function*. In Ref. [36] a factorized expression for the $A(e,e'pp)$ cross section has been derived. Thereby, in computing the matrix elements, all FSI effects have been neglected and the zero-range approximation ($\lim_{r_{12}\to 0}$) has been adopted. A ^{12}C$(e,e'pp)$ experiment conducted at the Mainz Microtron (MAMI) [37] showed very good quantitative agreement with the predicted diproton pair c.m. momentum factorization up to momenta of about 500 MeV. Here, the formalism of Ref. [36] is extended to include the effect of FSIs and to soften the zero-range approximation. Note that the limit $\lim_{r_{12}\to 0}$ effectively amounts to projecting on states with vanishing relative orbital momentum.

We consider exclusive $A(e,e'NN)$ reactions in the spectator approximation with a virtual photon coupling to a correlated pair $N\,(k_1)\,N\,(k_2)$

$$\gamma^*\,(q) + A-2\,(p_{A-2}) + N\,(k_1)\,N\,(k_2) \longrightarrow A-2\,(p_{A-2}) + N\,(p_1) + N\,(p_2)\ . \tag{32}$$

In a non-relativistic treatment, the corresponding matrix element is given by

$$\begin{aligned}\mathcal{M}^{\mu} = \int d\vec{x}_1 \int d\vec{x}_2 \Big[\chi^{\dagger}_{s_1}(\vec{\sigma}_1)\xi^{\dagger}_{t_1}(\vec{\tau}_1)\,\chi^{\dagger}_{s_2}(\vec{\sigma}_2)\xi^{\dagger}_{t_2}(\vec{\tau}_2)\,e^{-i\vec{p}_1\cdot\vec{r}_1}e^{-i\vec{p}_2\cdot\vec{r}_2} - (1\leftrightarrow 2)\Big] \\ \times\,\mathcal{F}^{\dagger}_{\rm FSI}(\vec{r}_1,\vec{r}_2)\hat{\mathcal{O}}^{\mu}(\vec{x}_1,\vec{x}_2)\phi_{\alpha_1}(\vec{x}_1)\phi_{\alpha_2}(\vec{x}_2)\,.\end{aligned} \tag{33}$$

Here, $s_i(t_i)$ are the spin (isospin) projection of the outgoing nucleons. Further, $\mathcal{F}_{\rm FSI}(\vec{r}_1,\vec{r}_2)$

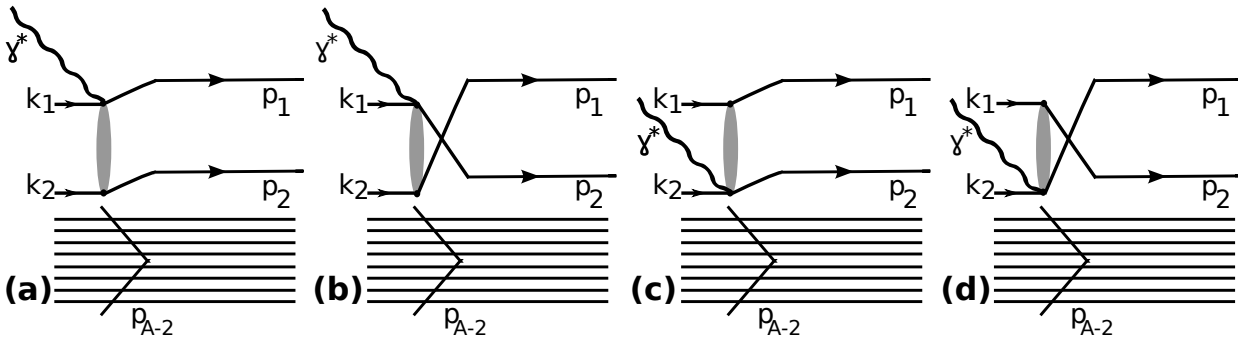

Figure 5 – The four contributions to the $A(e,e'NN)$ amplitude of Eq. (33).

is an operator encoding the FSIs for a reaction where two nucleons are brought into the continuum at the spatial localizations $\vec{r}_1$ and $\vec{r}_2$ respectively. We assume that $\mathcal{F}_{\rm FSI}$ does not depend on the spin and isospin d.o.f, which is a fair approximation at higher energies. The amplitude of Eq. (33) refers to the physical situation whereby, as a result of virtual-photon excitation, two nucleons are excited from bound states $\alpha_1\alpha_2$ into continuum states.

In Eq. (33), the effect of the correlations is implemented in the TBC approximation by means of a symmetric two-body operator [29, 31]

$$\hat{\mathcal{O}}^{\mu}(\vec{x}_1,\vec{x}_2) = \left[e^{i\vec{q}\cdot\vec{r}_1}\Gamma^{\mu}_{\gamma^\star N}(\vec{x}_1) + e^{i\vec{q}\cdot\vec{r}_2}\Gamma^{\mu}_{\gamma^\star N}(\vec{x}_2)\right]\hat{\wr}\,(\vec{x}_1,\vec{x}_2)\ , \tag{34}$$

where the operator $\hat{\wr}\,(\vec{x}_1,\vec{x}_2)$ has been defined in Eq. (21) and $\vec{q}$ is the three-momentum of the virtual photon. The $\Gamma^{\mu}_{\gamma^\star N}(\vec{x}_i)$ denotes the one-body virtual photon coupling to a bound nucleon with coordinate $\vec{x}_i$ (includes the spatial, spin, and isospin d.o.f.). The Eq. (34) can be interpreted as the SRC-corrected photo-nucleon coupling which operates on IPM many-body wave functions.

The amplitude of Eq. (33) involves four contributions schematically shown in Fig. 5. For the sake of brevity, in the following we consider the term of Fig. 5(a) with a photon-nucleon coupling on coordinate $\vec{r}_1$ and the outgoing nucleon with momentum $\vec{p}_1$ directly attached to this vertex. The corresponding amplitude is denoted by $\mathcal{M}^{\mu}_{a}$. The other three terms in Fig. 5 follow a similar derivation.

In a HO single-particle basis, one can write

$$\begin{aligned}\mathcal{M}^{\mu}_{a} = &\int d\vec{r}_1 \int d\vec{r}_2 e^{-i(\vec{p}_1-\vec{q})\cdot\vec{r}_1} e^{-i\vec{p}_2\cdot\vec{r}_2}\mathcal{F}^{\dagger}_{\rm FSI}(\vec{r}_1,\vec{r}_2)\psi_{n_1l_1m_{l_1}}(\vec{r}_1)\psi_{n_2l_2m_{l_2}}(\vec{r}_2)\,,\\ &\times\langle s_1t_1, s_2t_2 \mid \Gamma^{\mu}_{\gamma^\star N}(\vec{x}_1)\,\hat{\wr}\,(\vec{x}_1,\vec{x}_2) \mid \sigma_1\tau_1,\sigma_2\tau_2\rangle\end{aligned} \tag{35}$$

where σ_i (τ_i) are the spin (isospin) quantum numbers of the bound states. Further, $\psi_{n_1l_1m_{l_1}}$ and $\psi_{n_2l_2m_{l_2}}$ are the radial HO wave functions as introduced in Eq. (12).

Similar to the Eq. (13), we apply the Talmi-Moshinsky brackets $\langle|\rangle_{\rm SMB}$ [27] to transform

Eq. (35) to relative and c.m. radial coordinates to obtain

$$\mathcal{M}_a^\mu = \sum_{LM_L} \sum_{\substack{nlm_l \\ N\Lambda M_\Lambda}} \int d\vec{r}_{12} \int d\vec{R}_{12} e^{-i\vec{P}_{12}\cdot\vec{R}_{12}} e^{-i\vec{k}^-\cdot\vec{r}_{12}} \mathcal{F}^\dagger_{\rm FSI}(\vec{R}_{12}+\frac{\vec{r}_{12}}{2}, \vec{R}_{12}-\frac{\vec{r}_{12}}{2})$$
$$\times \psi_{nlm_l}(\frac{\vec{r}_{12}}{\sqrt{2}}) \psi_{N\Lambda M_\Lambda}(\sqrt{2}\vec{R}_{12}) \langle l_1 m_{l_1} l_2 m_{l_2} \mid LM_L\rangle \langle l m_l \Lambda M_\Lambda \mid LM_L\rangle$$
$$\times \langle nlN\Lambda; L \mid n_1 l_1 n_2 l_2; L\rangle_{\rm SMB} \langle s_1 t_1, s_2 t_2 \mid \Gamma^\mu_{\gamma^\star N}(\vec{x}_1)\,\hat{\imath}\,(\vec{x}_1,\vec{x}_2) \mid \sigma_1\tau_1, \sigma_2\tau_2\rangle\ , \qquad (36)$$

where $\vec{P}_{12} = \vec{p}_1 + \vec{p}_2 - \vec{q}$, $\vec{k}^\mp = \frac{\vec{p}_1 - \vec{p}_2}{2} \mp \frac{\vec{q}}{2}$.

In Eq. (36) the sum over the relative quantum numbers is dominated by ($nl = 00$). This is based on the observation that typical correlation operators act over relatively short internucleon distances and mostly affect the ($nl = 00$) components of the ψ_{nlm_l} wave functions. For a more detailed explanation we refer to the discussion of Fig. 1 in Sect. 2 and Refs. [20, 21].

For close-proximity nucleons one can set $\vec{r}_{12} \approx \vec{0}$ in the FSI operator:

$$\begin{aligned} \mathcal{F}_{\rm FSI}(\vec{r}_1, \vec{r}_2) &= \mathcal{F}_{\rm FSI}(\vec{R}_{12}+\frac{\vec{r}_{12}}{2}, \vec{R}_{12}-\frac{\vec{r}_{12}}{2}) \\ &\approx \mathcal{F}_{\rm FSI}(\vec{R}_{12}, \vec{R}_{12})\,. \end{aligned} \qquad (37)$$

This approximation amounts to computing the effect of FSIs as if the the two nucleons are brought into the continuum at the same spatial point (determined by the c.m. coordinate of the pair), which is very reasonable for close-proximity nucleons. With the above assumptions one arrives at the expression for the matrix element

$$\mathcal{M}_a^\mu \approx \langle s_1 t_1, s_2 t_2 \mid \widehat{\Gamma}^\mu_{\gamma^\star N}(\vec{k}^-) \mid \sigma_1\tau_1, \sigma_2\tau_2\rangle$$
$$\times \sum_{N\Lambda M_\Lambda} \langle l_1 m_{l_1} l_2 m_{l_2} \mid \Lambda M_\Lambda\rangle \langle 00 N\Lambda; \Lambda \mid n_1 l_1 n_2 l_2; \Lambda\rangle_{\rm SMB}$$
$$\times \int d\vec{R}_{12} e^{-i\vec{P}_{12}\cdot\vec{R}_{12}} \mathcal{F}^\dagger_{\rm FSI}(\vec{R}_{12}, \vec{R}_{12}) \psi_{N\Lambda M_\Lambda}(\sqrt{2}\vec{R}_{12})\,, \qquad (38)$$

with

$$\widehat{\Gamma}^\mu_{\gamma^\star N}(\vec{p}) \equiv \int d\vec{r}_{12} e^{-i\vec{p}\cdot\vec{r}_{12}} \psi_{000}(\frac{\vec{r}_{12}}{\sqrt{2}}) \Gamma^\mu_{\gamma^\star N}(\vec{x}_1) \hat{\imath}(\vec{x}_1, \vec{x}_2)\,. \qquad (39)$$

In deriving the Eq. (38), we have separated the integration over the spatial and spin-isospin d.o.f.. In addition, use has been made of the fact that the operator $\hat{\imath}(\vec{x}_1, \vec{x}_2)$ of Eq. (21) does not depend on the c.m. coordinate $\vec{R}_{12}$. The most striking feature of Eq. (38) is the factorization of the amplitude in a term connected to the c.m. motion of the initial pair and a term which contains the full complexity of the photon-nucleon coupling to a correlated pair.

After summing the four terms that contribute to Eq. (33) and squaring the matrix element, the eightfold differential cross section factorizes according to

$$d^8\sigma(e, e' NN) = K_{eNN} \sigma_{e2N} F^D_{n_1 l_1, n_2 l_2}(\vec{P}_{12}), \qquad (40)$$

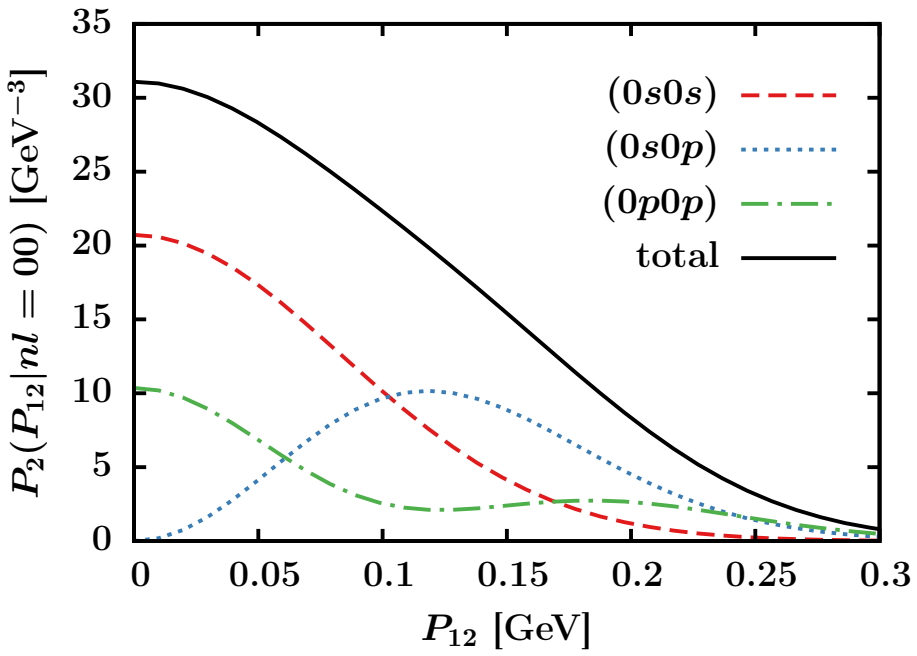

Figure 6 – (Color online) The contribution of the different shell-model pair combinations to the $P_2\,(P_{12}|nl=00)$ for pp pairs in ^{12}C.

with K_{eNN} a kinematic factor. Further, the off-shell electron-two-nucleon cross section is given by

$$\sigma_{e2N} \propto L_{\mu\nu} \sum_{\substack{s_1 s_2 \sigma_1 \sigma_2 \\ \tau_1 \tau_2}} J^\mu \left(J^\nu\right)^\dagger \,, \tag{41}$$

with $L_{\mu\nu}$ the leptonic tensor and J^μ the hadronic current given by

$$\begin{aligned} J^\mu = &\langle s_1 t_1, s_2 t_2 \mid \widehat{\Gamma}^\mu_{\gamma^\star N}(\vec{k}^-) \mid \sigma_1\tau_1, \sigma_2\tau_2\rangle - \langle s_2 t_2, s_1 t_1 \mid \widehat{\Gamma}^\mu_{\gamma^\star N}(\vec{k}^+) \mid \sigma_1\tau_1, \sigma_2\tau_2\rangle \\ &+ \langle s_1 t_1, s_2 t_2 \mid \widehat{\Gamma}^\mu_{\gamma^\star N}(\vec{k}^+) \mid \sigma_1\tau_1, \sigma_2\tau_2\rangle - \langle s_2 t_2, s_1 t_1 \mid \widehat{\Gamma}^\mu_{\gamma^\star N}(\vec{k}^-) \mid \sigma_1\tau_1, \sigma_2\tau_2\rangle \,. \end{aligned} \tag{42}$$

The factorization function $F^D_{n_1 l_1, n_2 l_2}(\vec{P}_{12})$ in Eq. (40) can be associated with the distorted c.m. momentum distribution of pairs in a relative $(nl = 00)$ state of the nucleus A

$$\begin{aligned} F^D_{n_1 l_1, n_2 l_2}(\vec{P}_{12}) = 4 \sum_{m_{l_1} m_{l_2}} \Bigg| \sum_{N\Lambda M_\Lambda} \int d\vec{R}_{12} e^{-i\vec{P}_{12}\cdot\vec{R}_{12}} \langle l_1 m_{l_1} l_2 m_{l_2} \mid \Lambda M_\Lambda\rangle \\ \times \langle n_1 l_1 n_2 l_2; \Lambda \mid 00 N\Lambda; \Lambda\rangle_{\rm SMB} \mathcal{F}^\dagger_{\rm FSI}(\vec{R}_{12}, \vec{R}_{12}) \psi_{N\Lambda M_\Lambda}(\sqrt{2}\vec{R}_{12}) \Bigg|^2 \,, \end{aligned} \tag{43}$$

where the factor 4 accounts for the spin degeneracy of the HO states.

In the limit of vanishing FSIs ($\mathcal{F}_{\rm FSI} \equiv 1$), one has

$$P_2(P_{12}|nl=00) = \frac{1}{A(A-1)} \frac{3}{(2\pi)^3} \sum_{n_\alpha l_\alpha n_\beta l_\beta} \int d\Omega_{P_{12}} F^D_{n_\alpha l_\alpha, n_\beta l_\beta}(\vec{P}_{12}) \,. \tag{44}$$

This establishes a connection between the $A(e,e'NN)$ factorization function and the contribution of pairs with quantum numbers $(n_1 l_1 n_2 l_2)$ to $P_2(P_{12}|nl=00)$, illustrated for pp pairs in ^{12}C in Fig. 6.

In the naive IPM, each two-hole (2h) state $(n_1l_1)^{-1}(n_2l_2)^{-1}$ can be associated with a sharp excitation energy in the $A-2$ system. In reality, the 2h strength corresponding with $(n_1l_1)^{-1}(n_2l_2)^{-1}$ extends over a wide energy range [38]. Current $A(e,e'pN)$ measurements are performed at Q^2-values of the order of GeV^2 not allowing one to measure cross sections for real exclusive processes as could be done at lower Q^2 values [26, 39, 40]. Accordingly, rather than probing the individual 2h contributions to P_2, the measured semi-inclusive $A(e,e'pN)$ cross sections can be linked to the $P_2(P_{12} \mid nl = 00)$ which involves a summation over the 2h states. From Fig. 6 it can be appreciated that in high-resolution $A(e,e'pN)$ measurements the c.m. distribution depends on the two-hole structure of the discrete final A-2 state [38, 39].

The $A(e,e'p)$ reaction allows one to access the $P_1(\vec{k}_m, E_m)$ modulo corrections from FSIs. It is worth stressing that there is no simple analogy for the $A(e,e'pN)$ reaction and that a direct connection with the two-body spectral function $P_2(\vec{P}_{12}, \vec{k}_{12}, E_{2m})$ is by no means evident, if not impossible.

4 Monte Carlo simulations

In this section, we investigate the implications of the proposed factorization of Eq. (40) for the $A(e,e'pp)$ opening-angle and c.m. distributions accessible in typical measurements. We present Monte Carlo simulations for $A(e,e'pp)$ building on the expression (40) suggesting that the magnitude of the cross section is proportional to $P_2(P_{12}|nl = 00)$. In this section the effects of FSIs are neglected. Its impact will be the subject of Sect. 5.

The data-mining effort at CLAS in Jlab [41, 42] is analyzing exclusive $(e,e'pN)$ for ^{12}C, ^{27}Al, ^{56}Fe, and ^{208}Pb for a 5.014 GeV unpolarized electron beam [41]. In order to guarantee the exclusive character of the events, cuts are applied to the leading proton: $0.62 < \frac{|\vec{p}_1|}{|\vec{q}|} < 0.96$, $\theta_{\vec{p}_1,\vec{q}} < 25^\circ$ and $k_1 > 300\,\mathrm{MeV}$. To increase the sensitivity to SRC-driven processes one imposes the kinematic constraints $x_B = \frac{Q^2}{2M_N\omega} > 1.2$ and $Q^2 > 1.4$ GeV^2. We have performed $(e,e'pp)$ simulations for all 4 target nuclei. The electron kinematics are drawn from the measured $x_B - Q^2$ distributions. We then generate two protons from the phase space by adoping a reaction picture of the type (32) whereby we assume that one nucleon absorbs the virtual photon. This results in a fast leading proton $p_1(E_1, \vec{p}_1 = \vec{k}_1 + \vec{q})$ and a recoil proton $p_2(E_2, \vec{p}_2 = \vec{k}_2)$, where $\vec{k}_1$ and $\vec{k}_2$ are the initial proton momenta. The initial c.m. momentum $\vec{P}_{12} = \vec{k}_1 + \vec{k}_2$ is drawn from the computed HO pp pair c.m. momentum distribution $P_2(P_{12}|nl = 00)$ of Table 1. We choose $\vec{k}_1$ along the z-axis and $\vec{q}$ in the xz plane. The recoil $A-2$ nucleus can have excitation energies between 0 and 80 MeV. All $A(e,e'pp)$ results of this section are obtained for 10^5 events which comply with the kinematic cuts.

First, we investigate in how far the factorization function can be addressed after applying kinematic cuts. This can be done by comparing the input and extracted pp c.m. distributions. Fig. 7 shows the extracted c.m. distribution from the simulated ^{12}C$(e,e'pp)$ events. The kinematic cuts have a narrowing effect (less than 10 %) on the distributions along the x- and y-axis. In addition, one observes a shift of roughly 100 MeV and an increase in the non-Gaussianity of the c.m. distribution along the z-axis. Similar observations have been made for the other three target nuclei.

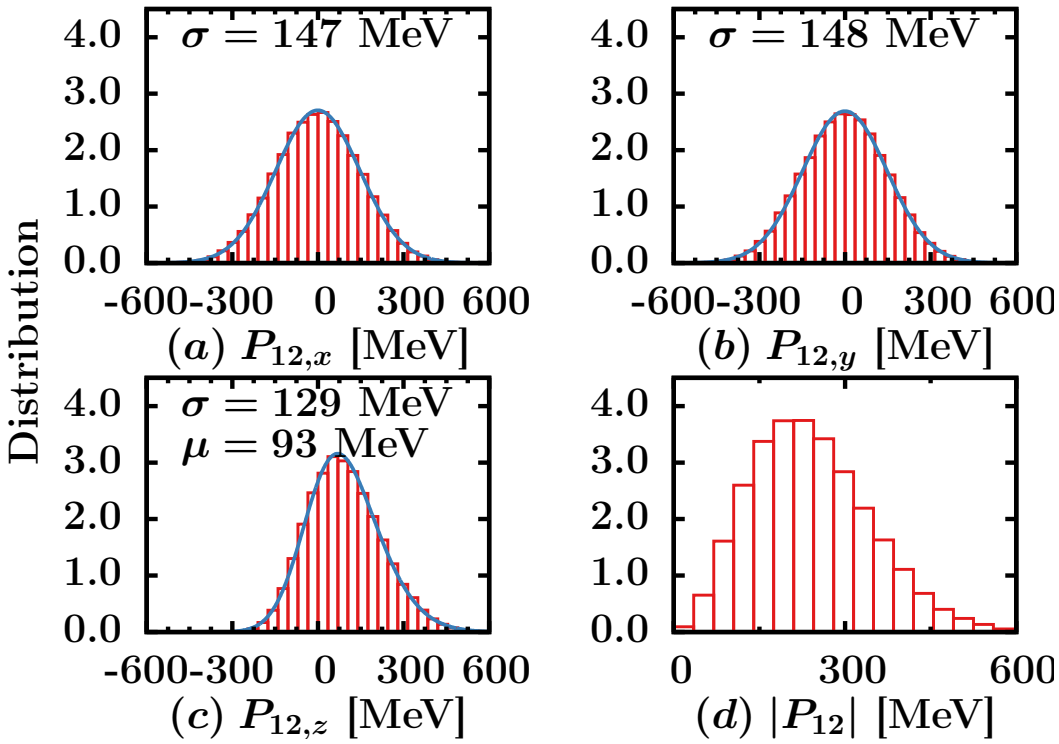

Figure 7 – (Color online) Total (bottom right) and directional pp c.m. distributions extracted from the ^{12}C$(e, e'pp)$ simulations in the CLAS kinematics described in the text. The blue solid line is a fit with a skew normal distribution.

We now address the issue whether the extracted c.m. distributions can provide information about the relative quantum numbers of the pairs. To this end, we have performed simulations starting from the assumption that the $(e, e'pp)$ cross section factorizes with $P_2(P_{12}|nl)$ for various nl combinations. The results of the simulations are summarized in Table 2. The narrowing effect attributed to the kinematic cuts is less significant for $l > 0$ pairs. Photon absorption on $l = 0$ and $l = 1$ pairs leads to differences in the extracted widths of the c.m. momentum distributions of the order of 20 MeV, which leads us to conclude that high-accuracy $A(e, e'pp)$ experiments could indeed provide information about the relative orbital angular momentum of the correlated pairs.

Fig. 8 shows the simulated opening-angle (γ) distributions of the initial-state protons for all four target nuclei considered. The A$(e, e'pp)$ simulations starting from the computed $P_2(P_{12}|nl = 00)$ and $P_2(P_{12})$ provide very similar backwardly peaked $\cos\gamma$ distributions. The peak is not due to the kinematic cuts as a uniform c.m. momentum distributions gives rise to a flat $\cos\gamma$ distribution. The shape of the simulated $\cos\gamma$ distributions is hardly target-mass dependent. The peak at 180 degrees in the $\cos\gamma$ distributions conforms with the picture of correlated nucleons moving back to back with high relative and low c.m. momentum.

We now turn our attention to an ^{12}C$(e, e'pp)$ measurement probing a restricted part of phase space. The JLab Hall-A ^{12}C$(e, e'pp)$ experiment of Refs. [3, 4], used an incident electron beam of 4.672 GeV and three spectrometers. We consider the kinematic settings with $\omega = 0.865$ GeV, $Q^2 = 2$ GeV^2, $x_B = 1.2$ and a median missing momentum $p_m = 0.55$ GeV. Figure 9 shows the shapes of the simulated and measured $\cos\gamma$ simulations. The proposed factorization for the $A(e, e'pp)$ cross section accounts for the shape of the measured $\cos\gamma$

	$nl = 00$	$l = 0$	$l = 1$	$l = 2$	all l
$\sigma_x^i(MeV)$	156	154	135	121	140
$\sigma_x^f(MeV)$	147	145	130	118	134

Table 2 – The width of the c.m. distribution along the x-axis for pp pairs with different relative orbital momentum l. σ_x^i is the width used as input parameter in the ^{12}C$(e, e'pp)$ simulations. The σ_x^f is the width extracted after the simulation.

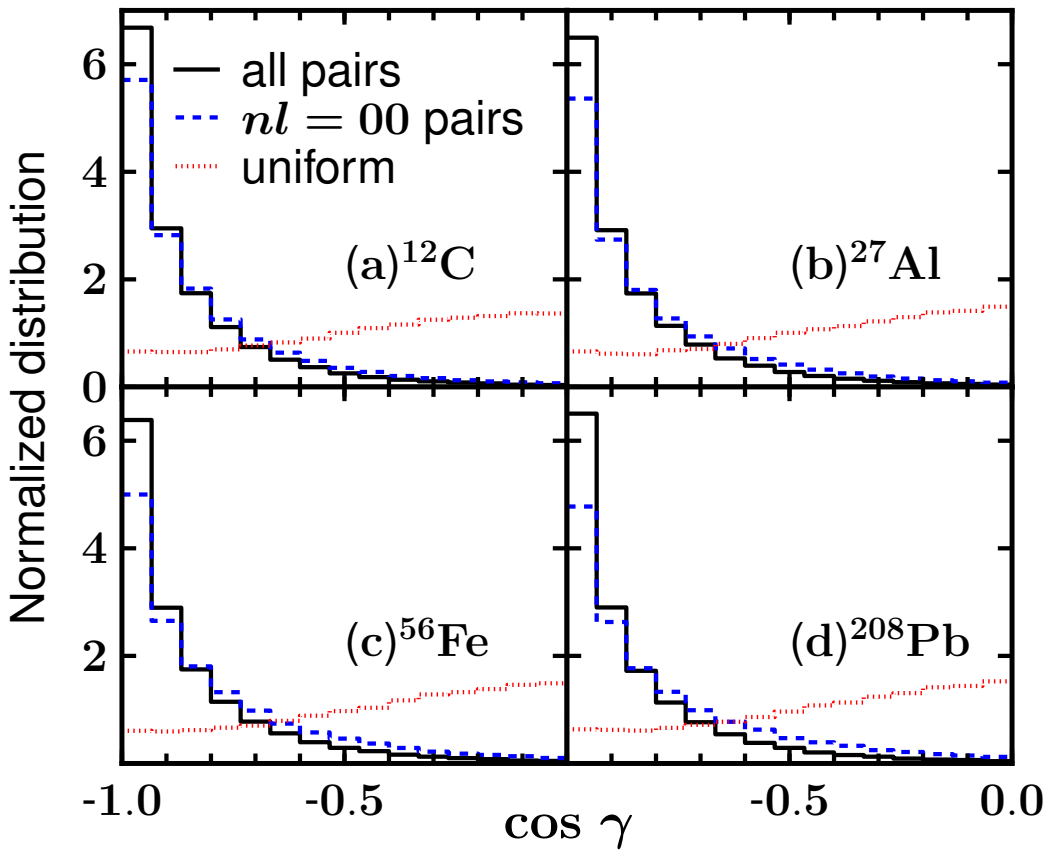

Figure 8 – (Color online) The opening angle distribution of the simulated A$(e, e'pp)$ events in the kinematics described in the text. The black solid, blue dashed and red dotted line is for a reaction picture with an $(e, e'pp)$ cross section proportional to $P_2(P_{12})$, to $P_2(P_{12}|nl = 00)$, and to a uniform pair c.m. distribution.

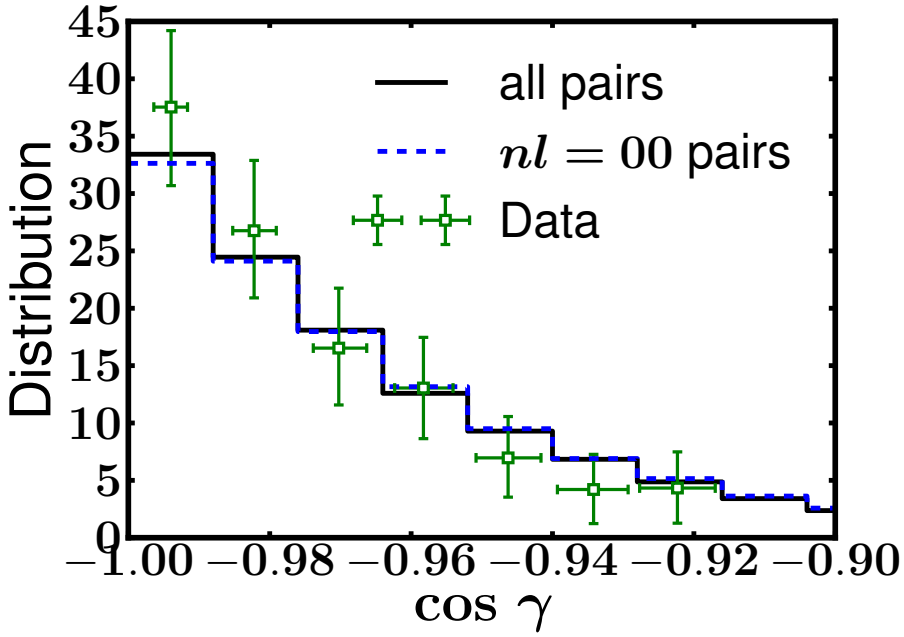

Figure 9 – (Color online) The opening angle distribution of the $^{12}\mathrm{C}(e,e'pp)$ reaction in the kinematics of Ref. [3]. Curve notations of Fig. 8 are used.

distribution. We stress that the computed pair c.m. distributions (Table 1) are the sole input to the simulations.

5 Final state interactions

In this section the impact of FSIs on the proposed factorization function of Eq. (40) is investigated. In order to keep computing times reasonable we limit ourselves to some particular kinematic cases and introduce an additional approximation. We start from Eq. (43) for the distorted momentum distribution $F^D_{n_1l_1,n_2l_2}(\vec{P}_{12})$ and apply the zero-range approximation [36, 43] which amounts to setting $\psi_{\alpha_1}(\vec{r}_1)\psi_{\alpha_2}(\vec{r}_2) \approx \psi_{\alpha_1}(\vec{R}_{12})\psi_{\alpha_2}(\vec{R}_{12})$ in Eq. (35). Consequently, we can write

$$F^D_{n_1l_1,n_2l_2}(\vec{P}_{12}) = 4 \sum_{m_{l_1}m_{l_2}} \left| \int d\vec{R}_{12} e^{-i\vec{P}_{12}\cdot\vec{R}_{12}} \mathcal{F}^\dagger_{\mathrm{FSI}}(\vec{R}_{12},\vec{R}_{12}) \psi_{n_1l_1m_{l_1}}(\vec{R}_{12}) \psi_{n_2l_2m_{l_2}}(\vec{R}_{12}) \right|^2 . \quad (45)$$

It is possible to derive a relativized version of this expression [43]

$$F^D_{n_1\kappa_1,n_2\kappa_2}(\vec{P}_{12}) = \sum_{s_1,s_2,m_1,m_2} \left| \int d\vec{R}_{12}\, e^{i\vec{P}_{12}\cdot\vec{R}_{12}} \bar{u}(\vec{k}_1,s_1)\psi_{n_1\kappa_1m_1}(\vec{R}_{12}) \right.$$
$$\left. \times\, \bar{u}(\vec{k}_2,s_2)\psi_{n_2\kappa_2m_2}(\vec{R}_{12})\mathcal{F}_{\mathrm{FSI}}(\vec{R}_{12},\vec{R}_{12}) \right|^2 . \quad (46)$$

Here, $u(\vec{k},s)$ are positive-energy Dirac spinors and $\psi_{n\kappa m}$ are relativistic mean-field wave functions [44] with quantum numbers $(n, j = |\kappa|/2, m)$. We neglect the projections on the

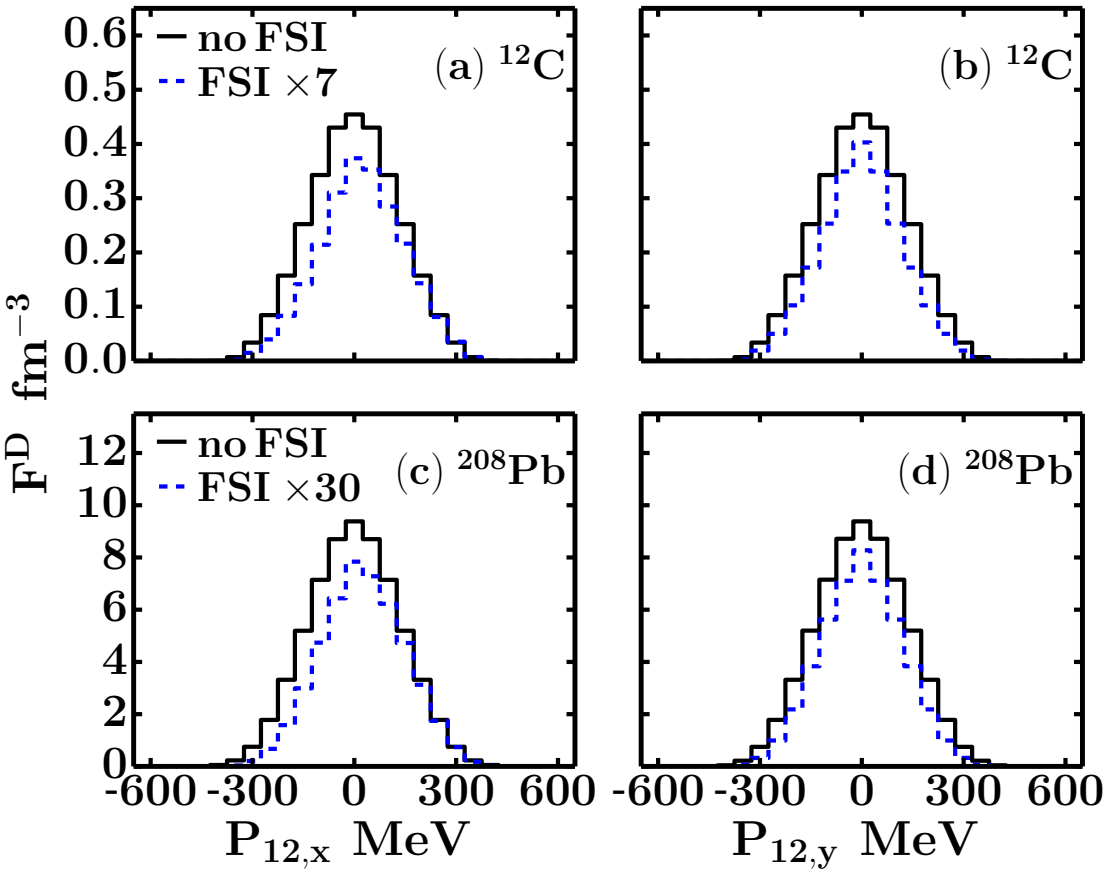

Figure 10 – (Color online) The two-body c.m. momentum distribution for ^{12}C$(e,e'pp)$ (top) and ^{208}Pb$(e,e'pp)$ (bottom) with (RMSGA) and without (no-FSI) inclusion of FSIs. We consider the kinematics $|\vec{q}|$= 1.4 GeV, $|\vec{p}_1|$= 0.82$|\vec{q}|$ and $\theta_{\vec{p}_1,\vec{q}} = 10°$. The FSI results have been multiplied by a factor of 7 for ^{12}C$(e,e'pp)$ and by a factor of 30 for ^{208}Pb$(e,e'pp)$.

lower components of the plane-wave Dirac spinors. The FSIs of the ejected pair with the remaining $A-2$ spectators, encoded in $\mathcal{F}_{\rm FSI}$, can be computed in a relativistic multiple-scattering Glauber approximation (RMSGA) [45, 46]. As the c.m. momentum is conserved in interactions among the two ejected nucleons, we discard those. This approximation does not affect the shape of $F^D_{n_1\kappa_1,n_2\kappa_2}(\vec{P}_{12})$.

We include FSIs for the JLab data mining kinematics considered in Sec. 4. We have computed the distorted c.m. momentum distribution of Eq. (46) for the kinematics that yields the most events in the simulations of Sec. 4: $|\vec{q}|$= 1.4 GeV, $|\vec{p}_1|$= 0.82$|\vec{q}|$, $\theta_{\vec{p}_1,\vec{q}} = 10°$. As in Sec. 4, $\vec{k}_1$ lies along the z-axis and the $\vec{q}$ is located in the xz plane. The results of the FSI calculations are summarized in Figs. 10 and 11.

In Fig. 10 we compare the RMSGA c.m. momentum distributions $F^D(\vec{P}_{12,x}) = \sum_{n_1\kappa_1,n_2\kappa_2}$ $F^D_{n_1\kappa_1,n_2\kappa_2}(\vec{P}_{12,x})$ and $F^D(\vec{P}_{12,y})$ with their respective plane-wave (no-FSI) limit. First, the FSIs are responsible for a substantial reduction of the cross sections: a factor of about 7 for carbon and about 30 in lead. The effects of FSIs on the shape of $F^D(\vec{P}_{12})$, however, are rather modest. Gaussian fits to the $F^D(\vec{P}_{12,i=x,y})$ result in widths which are less than 10% smaller than in the plane-wave limit. The effects of FSIs on the shape of the c.m. distributions

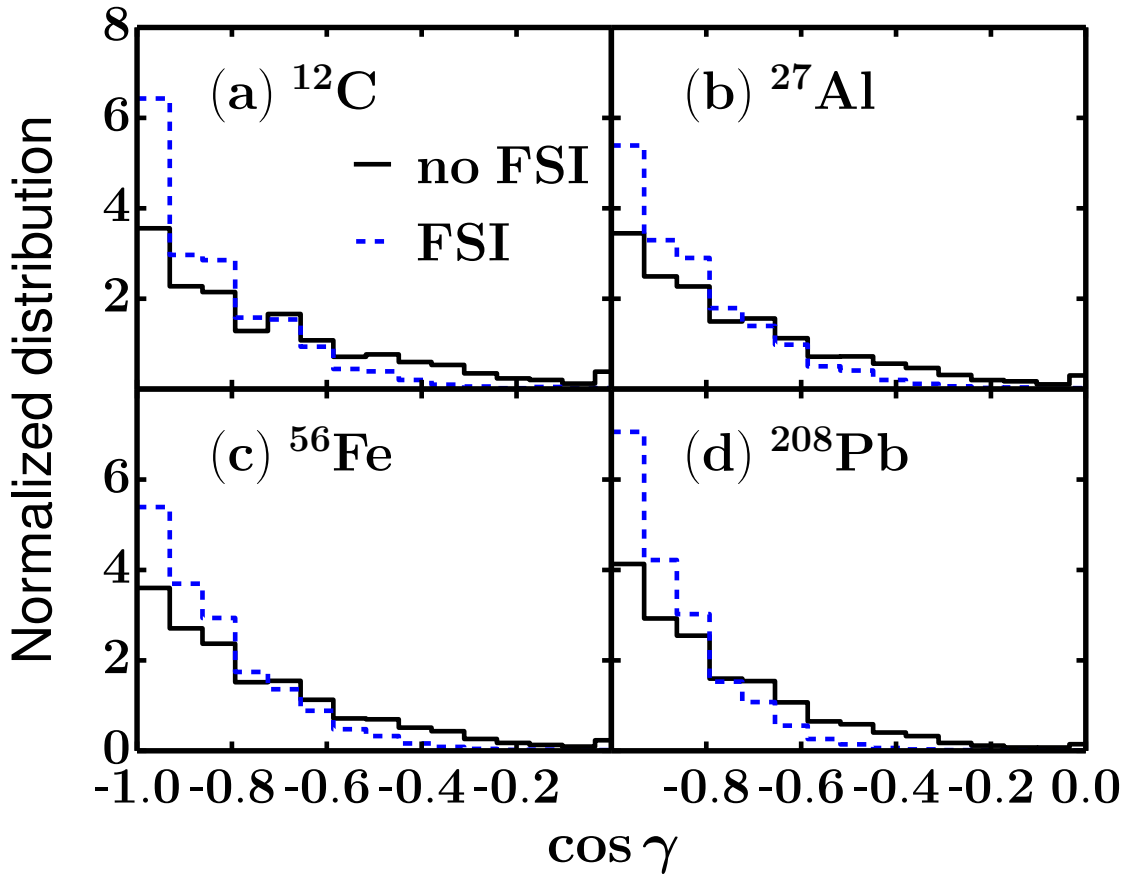

Figure 11 – (Color online) The normalized opening angle distributions for A$(e, e'pp)$ for ^{12}C, ^{27}Al, ^{56}Fe and ^{208}Pb in the kinematics of Fig. 10.

in Fig. 10 can be qualitatively understood considering that the nucleons undergoing FSIs are slowed down on average: $(\vec{p}_1, \vec{p}_2) \xrightarrow{\text{FSI}} \zeta\,(\vec{p}_1, \vec{p}_2)$ with $0 < \zeta \leq 1$. It is straightforward to show that for the adopted conventions this results in $P_{12,x} \to \zeta P_{12,x} - (1-\zeta)p_{1,x}$, and $P_{12,y} \to \zeta P_{12,y}$. This explains the observed contraction and shift to the right in the $P_{12,x}$ distribution, and the contraction of the $P_{12,y}$ distributions.

The effect of FSIs on the shape of the normalized opening angle distributions is studied in Fig. 11 for four target nuclei. It is clear that they become even more forwardly peaked after including FSIs.

6 Summary

Summarizing, we have shown that in the plane-wave limit the factorization function for the exclusive SRC-driven $A(e, e'pN)$ reaction is the conditional c.m. distribution $P_2(P_{12}|nl = 00)$ for pN pairs in a nodeless relative state with a vanishing orbital momentum. We have illustrated that in a two-body cluster expansion the correlated part of the momentum distribution originates mainly from correlation operators acting on IPM pairs with $(nl = 00)$ quantum numbers, supporting the assumptions underlying the proposed factorization of the

$A(e,e'pN)$ reaction. Numerical calculations indicate that the $P_2(P_{12}|nl=00)$ has a wider distribution than the unconditional $P_2(P_{12})$ one. An important implication of the proposed factorization is that the mass dependence of the $A(e,e'pp)$ and $A(e,e'pn)$ cross section is predicted to be much softer than $\frac{Z(Z-1)}{2}$ and NZ respectively.

We have examined the robustness of the proposed factorization of the two-nucleon knockout cross sections against kinematic cuts and FSIs. Both mechanisms modestly affect the shape of the c.m. distributions which leads us to conclude that they can be accessed in $A(e,e'pN)$ measurements. The FSIs bring about a mass-dependent reduction of the cross sections which is of the order of 10 for carbon and 30 for lead.

ACKNOWLEDGMENTS

The authors wish to thank Or Hen, Eli Piasetzky, and Larry Weinstein for stimulating discussions and suggestions. This work is supported by the Research Foundation Flanders (FWO-Flanders) and by the Interuniversity Attraction Poles Programme P7/12 initiated by the Belgian Science Policy Office. The computational resources (Stevin Supercomputer Infrastructure) and services used in this work were provided by Ghent University, the Hercules Foundation and the Flemish Government.

---

[1] A. Tang, J. W. Watson, J. Aclander, et al., Phys. Rev. Lett. **90**, 042301 (2003).
[2] R. A. Niyazov, L. B. Weinstein, G. Adams, et al., Phys. Rev. Lett. **92**, 052303 (2004).
[3] R. Shneor, P. Monaghan, R. Subedi, et al., Phys. Rev. Lett. **99**, 072501 (2007).
[4] R. Subedi, R. Shneor, P. Monaghan, et al., Science **320**, 1476 (2008).
[5] K. Egiyan, N. Dashyan, M. Sargsian, et al., Phys. Rev. C **68**, 014313 (2003).
[6] K. Egiyan, N. Dashyan, M. Sargsian, et al., Phys. Rev. Lett. **96**, 082501 (2006).
[7] N. Fomin, J. Arrington, R. Asaturyan, et al., ArXiv e-prints, 1107.3583 (2011).
[8] R. Schiavilla, R. B. Wiringa, S. C. Pieper, and J. Carlson, Phys. Rev. Lett. **98**, 132501 (2007).
[9] R. B. Wiringa, R. Schiavilla, S. C. Pieper, and J. Carlson, Phys. Rev. C **78**, 021001 (2008).
[10] H. Feldmeier, W. Horiuchi, T. Neff, and Y. Suzuki, Phys. Rev. C **84**, 054003 (2011).
[11] R. B. Wiringa, R. Schiavilla, S. C. Pieper, and J. Carlson, Phys. Rev. C **89**, 024305 (2014).
[12] M. Alvioli, C. Ciofi degli Atti, and H. Morita, Phys. Rev. Lett. **100**, 162503 (2008).
[13] M. Alvioli, C. Ciofi degli Atti, L. P. Kaptari, et al., Phys. Rev. C **85**, 021001 (2012).
[14] M. Alvioli, C. Ciofi degli Atti, L. P. Kaptari, et al., Phys. Rev. C **87**, 034603 (2013).
[15] F. Arias de Saavedra, C. Bisconti, G. Co', and A. Fabrocini, Phys. Rept. **450**, 1 (2007).
[16] C. Bisconti, F. A. d. Saavedra, and G. Co', Phys. Rev. C **75**, 054302 (2007).
[17] S. Bogner and D. Roscher, Phys. Rev. C **86**, 064304 (2012).
[18] J. Arrington, D. Higinbotham, G. Rosner, and M. Sargsian, Prog. Part. Nucl. Phys. **67**, 898 (2012).
[19] L. Frankfurt, M. Sargsian, and M. Strikman, Int. J. Mod. Phys. A **23**, 2991 (2008).
[20] M. Vanhalst, W. Cosyn, and J. Ryckebusch, Phys. Rev. C **84**, 031302 (2011).
[21] M. Vanhalst, J. Ryckebusch, and W. Cosyn, Phys. Rev. C **86**, 044619 (2012).
[22] M. Vanhalst, J. Ryckebusch, and W. Cosyn, ArXiv e-prints, 1210.6175 (2012).

[23] W. Cosyn, M. Vanhalst, and J. Ryckebusch, ArXiv e-prints, 1308.5583 (2013).
[24] J. Arrington, A. Daniel, D. Day, et al., ArXiv e-prints, 1206.6343 (2012).
[25] O. Benhar, Phys. Rev. C **87**, 024606 (2013).
[26] R Starink, M. van Batenburg, E Cisbani, et al., Phys. Lett. B **474**, 33 (2000).
[27] M. Moshinsky and Y. Smirnov, *The harmonic oscillator in modern physics* (Harwood Academic Publishers, Amsterdam, 1996).
[28] S. C. Pieper, R. B. Wiringa, and V. Pandharipande, Phys. Rev. C **46**, 1741 (1992).
[29] J. Engel, J. Carlson, and R. Wiringa, Phys. Rev. C **83**, 034317 (2011).
[30] R. Roth, T. Neff, and H. Feldmeier, Prog. Part. Nucl. Phys. **65**, 50 (2010).
[31] S. Janssen, J. Ryckebusch, W. Van Nespen, and D. Debruyne, Nucl. Phys. A **672**, 285 (2000).
[32] J. Ryckebusch, V. Van der Sluys, K. Heyde, et al., Nucl. Phys. A **624**, 581 (1997).
[33] C. Gearheart, PhD thesis (Washington University, St. Louis, 1994).
[34] J. Caballero, T. Donnelly, E. Moya de Guerra, and J. Udias, Nucl. Phys. A **632**, 323 (1998).
[35] L. L. Frankfurt and M. I. Strikman, Phys. Rept. **160**, 235 (1988).
[36] J. Ryckebusch, Phys. Lett. B **383**, 1 (1996).
[37] K. I. Blomqvist et al., Phys. Lett. B **421**, 71 (1998).
[38] C. Barbieri, C. Giusti, F. Pacati, and W. Dickhoff, Phys. Rev. C **70**, 014606 (2004).
[39] J. Ryckebusch and W. Van Nespen, Eur. Phys. J. A **20**, 435 (2004).
[40] D. Middleton, J. Annand, C. Barbieri, et al., Eur. Phys. J. A **43**, 137 (2010).
[41] L. Weinstein and S. Kuhn, Short distance structure of nuclei: Mining the wealth of existing jefferson lab data, DOE Grant DE-SC0006801.
[42] O. Hen, H. Hakobyan, R. Shneor, et al., Phys. Lett. B **722**, 63 (2013).
[43] W. Cosyn and J. Ryckebusch, Phys. Rev. C **80**, 011602 (2009).
[44] R. J. Furnstahl, B. D. Serot, and H.-B. Tang, Nucl. Phys. A **615**, 441 (1997).
[45] J. Ryckebusch, D. Debruyne, P. Lava, et al., Nucl. Phys. A **728**, 226 (2003).
[46] W. Cosyn and J. Ryckebusch, Phys. Rev. C **87,** 064608 (2013).

3.4 Stylized features of single-nucleon momentum distributions

Maarten Vanhalst[1], Jan Ryckebusch[1] and Wim Cosyn[1]

[1]Department of Physics and Astronomy, Ghent University, Proeftuinstraat 86, B-9000 Gent, Belgium

Submitted for publication

Abstract

Background Nuclear short-range correlations (SRC) typically manifest themselves in the tail parts of the single-nucleon momentum distributions.

Purpose To develop an approximate flexible method for computing the single-nucleon momentum distributions throughout the whole mass table, thereby including the majority of the effects of SRC. To use this method to study the mass and isospin dependence of SRC.

Method The framework adopted in this work, corrects mean-field models for central, spin-isospin and tensor correlations by shifting the complexity induced by the SRC from the wave functions to the operators. It is argued that the expansion of these modified operators can be truncated to a low order.

Results The proposed model can generate the SRC-related high-momentum tail of the single-nucleon momentum distribution. These are dominated by correlations operating on mean-field pairs with vanishing relative radial and angular-momentum quantum numbers. In asymmetric nuclei, the correlations make the average kinetic energy for the minority nucleons larger than for the majority nucleons.

Conclusions The proposed method explains the dominant role of proton-neutron pairs in generating the SRC and accounts for the magnitude and mass dependence of SRC as probed in inclusive electron scattering. It also provides predictions for the ratio of the amount of correlated proton-proton to proton-neutron pairs which are in line with the observations.

1 Introduction

One of the most elusive properties of nuclei is that nucleons forcefully repel each other as they get close. Since the early days of nuclear physics, it has been recognized that this repulsion is an important ingredient of the dynamics of nuclei, and induces pair, triple, ... correlations in the wave functions for atomic nuclei. This calls for a more sophisticated approach to the quantum mechanical structure of nuclei and the nuclear response to external probes.

Momentum distributions contain all the information about the momentum decomposition of the nuclear motion. The computation of single-nucleon momentum distributions has reached a very high level of sophistication. Ab-initio methods with variational wave functions can be used to compute the momentum distributions for nuclei up to $A = 12$ [1–5]. Also for atomic mass number infinity, or nuclear matter, exact calculations with realistic nucleon-nucleon interactions can be performed [6, 7]. Momentum distributions for mid-heavy and heavy nuclei cannot be computed with exact methods to date. Advanced approximate schemes like cluster expansions [5, 8, 9] and correlated basis function theory [10, 11] are able to provide momentum distributions for heavier nuclei.

We wish to develop an approximate practical way of computing the short-range contributions to momentum distributions for stable nuclei over the entire mass range. Thereby, we start from wave functions that can be written as correlation operators acting on a single Slater determinant. The computation of expectation values of one-body and two-body operators for those wave functions involves multi-body effective operators and a truncation scheme is in order. We propose a low-order correlation operator approximation, dubbed LCA, that truncates the modified correlated operator corresponding with an one-body operator to the level of two-body operators. For the computation of the single-nucleon momentum distribution, the LCA model developed in Sec. 2, preserves some fundamental properties like the normalization conditions.

In Sec. 3, we illustrate that the LCA method is a practical approximate way of computing the effect of SRC on single-nucleon momentum distributions for nuclei over the entire mass range. It will be shown that after inclusion of central, spin-isospin and tensor correlations, it can capture some stylized features of nuclear momentum distributions. Due to its wide range of applicability, the LCA framework allows one to study the mass and isospin dependence of SRC and to arrive at a comprehensive picture of the impact of SRC throughout the mass table. To assess how realistic the LCA method is, we compare its one-body momentum distributions for ^{4}He, ^{9}Be and ^{12}C with those from ab-initio calculations.

Of course, the LCA approximate method is only justified if the resulting physical quantities like radii and kinetic energies are in reasonable agreement with data and results from more realistic approaches. The impact of short-range dynamics on the average nucleon kinetic energies and the rms radii for symmetric and asymmetric nuclei is discussed in Sec. 4. As the correlations induce high-momentum components, they increase the average kinetic energies. The isospin dependence of the SRC is at the origin of some interesting features which depend on the asymmetry of nuclei [7, 12]. Also these asymmetry effects will be discussed in Sec. 4.

2 Formalism

A time-honored method to account for correlations in independent particle models (IPM) is to shift the complexity induced by the correlations from the wave functions to the operators [3, 13]. The correlated wave functions $\mid \Psi\rangle$ are constructed by applying a many-body correlation operator $\widehat{\mathcal{G}}$ to the uncorrelated wave functions $\mid \Phi\rangle$. The operator $\widehat{\mathcal{G}}$ corrects the IPM Slater determinant $\mid \Phi\rangle$ for short-range and other correlations:

$$\mid \Psi\rangle = \frac{1}{\sqrt{\mathcal{N}}}\widehat{\mathcal{G}} \mid \Phi\rangle, \tag{1}$$

with the normalization factor $\mathcal{N} \equiv \langle \Phi \mid \widehat{\mathcal{G}}^{\dagger}\widehat{\mathcal{G}} \mid \Phi\rangle$. Determining the operator $\widehat{\mathcal{G}}$ represents a major challenge [14]. One can be guided, however, by the knowledge of the basic features of the nucleon-nucleon force. As far as the short-range nucleon-nucleon (NN) correlations are concerned, $\widehat{\mathcal{G}}$ is dominated by the central, spin-isospin and tensor correlations [4, 15, 16]

$$\widehat{\mathcal{G}} \approx \widehat{\mathcal{S}} \left(\prod_{i<j=1}^{A} \Big[1 + \hat{l}\,(i,j) \Big] \right) , \tag{2}$$

with $\widehat{\mathcal{S}}$ the symmetrization operator and

$$\begin{aligned} \hat{l}\,(i,j) &= -\hat{g}(i,j) + \hat{s}(i,j) + \hat{t}(i,j) \\ &= -g_c(r_{ij}) + f_{\sigma\tau}(r_{ij})\vec{\sigma}_i \cdot \vec{\sigma}_j \vec{\tau}_i \cdot \vec{\tau}_j + f_{t\tau}(r_{ij})\widehat{S}_{ij}\vec{\tau}_i \cdot \vec{\tau}_j \ . \end{aligned} \tag{3}$$

Here, $\widehat{S}_{ij}$ is the tensor operator and $r_{ij} = |\vec{r}_i - \vec{r}_j|$. Further, $g_c(r_{12})$, $f_{\sigma\tau}(r_{12})$ and $f_{t\tau}(r_{12})$ are the central, spin-isospin and tensor correlation functions. This paper uses the central correlation function by Gearhart [17]. For the spin-isospin and tensor correlation functions we use those by Pieper et al. [18]. In Refs. [15, 19] we provided arguments and evidence to support our claim that these correlation functions can be considered realistic.

Evaluating the expectation value of an operator $\widehat{\Omega}$ between correlated states is far from trivial. The procedure detailed in Ref. [13] for example, amounts to rewriting the matrix element between correlated states

$$\langle \Psi \mid \widehat{\Omega} \mid \Psi\rangle, \tag{4}$$

as a matrix element between uncorrelated states

$$\frac{1}{\mathcal{N}}\langle \Phi \mid \widehat{\Omega}^{\rm eff} \mid \Phi\rangle \ . \tag{5}$$

Hereby, the impact of the correlations is implemented in an effective transition operator $\widehat{\Omega}^{\rm eff}$ that corrects the operator $\widehat{\Omega}$ for the effect of NN correlations

$$\widehat{\Omega}^{\rm eff} = \widehat{\mathcal{G}}^{\dagger}\ \widehat{\Omega}\ \widehat{\mathcal{G}} = \Big(\prod_{i<j=1}^{A} [1 + \hat{l}(i,j)] \Big)^{\dagger}\ \widehat{\Omega}\ \Big(\prod_{k<l=1}^{A} [1 + \hat{l}(k,l)] \Big) \ . \tag{6}$$

For the sake of computing single-nucleon momentum distributions, it suffices to consider one-body operators

$$\widehat{\Omega} \equiv \sum_{i=1}^{A} \widehat{\Omega}^{[1]}(i) \ . \tag{7}$$

The universal character of SRC hints at a local dynamical origin, which naturally truncates a perturbation expansion like the one of Eq. (6). Further, studies of the single-nucleon spectral function in nuclear matter [6] reveal that the correlated part is mainly furnished by three-body breakup processes. For a finite nucleus A this translates into processes with two close-proximity correlated nucleons and a spectator residual $A-2$ core. This picture has been confirmed in semi-exclusive $A(e,e'p)$ measurements [20, 21]. These observations allow one to treat the SRC as pair correlations to a good approximation. It also justifies a pertubation expansion of the Eq. (6) that truncates the effective operators corresponding with a one-body operator $\widehat{\Omega}^{[1]}$ to the level of two-body operators.

In the LCA framework used in this work, one adopts a perturbation expansion for the Eq. (6). For an effective operator corresponding with a one-body operator, we truncate the $\widehat{\Omega}^{\rm eff}$ to the level of two-body operators and retain the terms that are linear and quadratic in the correlation operator $\hat{l}$. The quadratic terms contain terms with both correlation operators acting on the same particle pair. This results in the following effective operator

$$\widehat{\Omega}^{\rm eff} \approx \widehat{\Omega}^{\rm LCA} = \sum_{i=1}^{A} \widehat{\Omega}^{[1]}(i) + \sum_{i<j=1}^{A} \left\{ \widehat{\Omega}^{[1],{\rm l}}(i,j) + \left[\widehat{\Omega}^{[1],{\rm l}}(i,j)\right]^{\dagger} + \widehat{\Omega}^{[1],{\rm q}}(i,j) \right\}. \tag{8}$$

Here, the linear (l) and quadratic (q) terms read

$$\widehat{\Omega}^{[1],{\rm l}}(i,j) = \left[\Omega^{[1]}(i) + \Omega^{[1]}(j)\right] \hat{l}(i,j), \tag{9}$$

$$\widehat{\Omega}^{[1],{\rm q}}(i,j) = \hat{l}^{\dagger}(i,j)[\widehat{\Omega}^{[1]}(i) + \widehat{\Omega}^{[1]}(j)]\hat{l}(i,j). \tag{10}$$

The LCA effective operator of Eq. (8) has one- and two-body terms, and can be conveniently rewritten as $\widehat{\Omega}^{\rm LCA} = \sum_{i<j}^{A} \widehat{\Omega}^{\rm LCA}(i,j)$ with

$$\widehat{\Omega}^{\rm LCA}(i,j) = \frac{1}{A-1}\left[\widehat{\Omega}^{[1]}(i) + \widehat{\Omega}^{[1]}(j)\right] + \widehat{\Omega}^{[1],{\rm corr}}(i,j)\ , \tag{11}$$

whereby we have introduced a short-hand notation for that part of the operator associated with the correlations

$$\widehat{\Omega}^{[1],{\rm corr}}(i,j) \;\; = \;\; \widehat{\Omega}^{[1],{\rm l}}(i,j) + \left[\widehat{\Omega}^{[1],{\rm l}}(i,j)\right]^{\dagger} + \widehat{\Omega}^{[1],{\rm q}}(i,j)\ . \tag{12}$$

In the absence of correlations only the first term in the expansion of Eq. (8) does not vanish. At medium internucleon distances ($r_{ij} \gtrsim 3$ fm) one has that $\hat{l}(i,j) \to 0$ and the effective operator $\widehat{\Omega}^{\rm LCA}$ equals the uncorrelated operator $\widehat{\Omega}$.

The single-nucleon momentum distribution $n^{[1]}(p)$ is defined as $\left(d^{3(A-1)}\{\vec{r}_{2-A}\} \equiv \prod_{i=2}^{i=A} d^3\vec{r}_i\right)$

$$n^{[1]}(p) = \int \frac{d^2\Omega_p}{(2\pi)^3} \int d^3\vec{r}_1\ d^3\vec{r}_1'\ d^{3(A-1)}\{\vec{r}_{2-A}\} e^{-i\vec{p}\cdot(\vec{r}_1'-\vec{r}_1)} \Psi^*(\vec{r}_1,\vec{r}_{2-A})\Psi(\vec{r}_1',\vec{r}_{2-A}). \tag{13}$$

The corresponding single-nucleon operator $\hat{n}_p$ reads

$$\hat{n}_p = \frac{1}{A}\sum_{i=1}^{A} \int \frac{d^2\Omega_p}{(2\pi)^3} e^{-i\vec{p}\cdot(\vec{r}_i'-\vec{r}_i)} = \sum_{i=1}^{A} \hat{n}_p^{[1]}(i). \tag{14}$$

Table 1 – The norm $\mathcal{N}$ of Eq. (15) for a wide range of nuclei.

^{2}H	1.128	^{40}Ca	1.637
^{4}He	1.327	^{48}Ca	1.629
^{9}Be	1.384	^{56}Fe	1.638
^{12}C	1.435	^{108}Ag	1.704
^{16}O	1.527	^{197}Ag	1.745
^{27}Al	1.545	^{208}Pb	1.741

This operator and the expansion of Eq. (11) determine an effective two-body operator $\hat{n}_p^{\rm LCA}$ from which the correlated single-nucleon momentum distributions at momentum p can be computed.

In order to preserve the normalization properties $\int dp\ p^2 n^{[1]}(p) = 1$ in the LCA, the normalization factor $\mathcal{N}$ of Eq. (1) is expanded up to the same order as the operator of Eq. (11),

$$\mathcal{N} = 1 + \frac{2}{A} \sum_{\alpha<\beta} {}_{\rm nas}\langle \alpha\beta \mid \hat{l}^\dagger(1,2) + \hat{l}^\dagger(1,2)\hat{l}(1,2) + \hat{l}(1,2) \mid \alpha\beta\rangle_{\rm nas}. \tag{15}$$

Here, $\mid \alpha\beta\rangle_{\rm nas}$ is the uncoupled normalized and anti-symmetrized (nas) two-nucleon state. The summation $\sum_{\alpha<\beta}$ extends over all occupied single-nucleon states. Those states are identified by the quantum numbers $\alpha \equiv n_\alpha l_\alpha j_\alpha m_{j_\alpha} t_\alpha$, whereby t_α denotes the isospin projection.

In order to construct the IPM single-particle wave functions we adopt a harmonic oscillator (HO) basis with a global mass-dependent parameterization

$$\hbar\omega = 45A^{-1/3} - 25A^{-2/3}. \tag{16}$$

In a HO basis, a transformation from $(\vec{r}_1, \vec{r}_2)$ to $(\vec{r}_{12} = \vec{r}_1 - \vec{r}_2, \vec{R}_{12} = \frac{\vec{r}_1+\vec{r}_2}{2})$ for the nas two-nucleon state can be readily performed [19, 22]

$$\mid \alpha\beta\rangle_{\rm nas} = \sum_A C^A_{\alpha\beta} \mid A\rangle, \tag{17}$$

with $A \equiv \{nlSjm_jNLM_LTM_T\}$ and $C^A_{\alpha\beta} \equiv \langle A \mid \alpha\beta\rangle_{\rm nas}$. Here, n and l are the radial and orbital angular-momentum quantum numbers corresponding with the relative motion of the pair. The jm_j are the quantum numbers of the total angular momentum of the pair. The TM_T (S) determine the isospin (spin) quantum numbers of the pair. The c.m. wave function is described by the quantum numbers NLM_L.

Table 1 lists the computed values of the normalization factors of Eq. (15) for a range of nuclei from ^{2}H to ^{208}Pb. The model dependence of the computed $\mathcal{N}$ is related to the choices made with regard to the IPM basis and the correlation functions. The deviation of $\mathcal{N}$ from 1 can be interpreted as a quantitative measure for the total effect of the SRC operators on the IPM ground-state wave function. For the deuteron, the tensor correlation operator acting on the relative S-wave of the IPM nucleon pair wave function is responsible for the D-wave component. The LCA is a crude approximation for the proton-neutron deuteron system. Nevertheless, the tail part of the LCA deuteron momentum one-body momentum

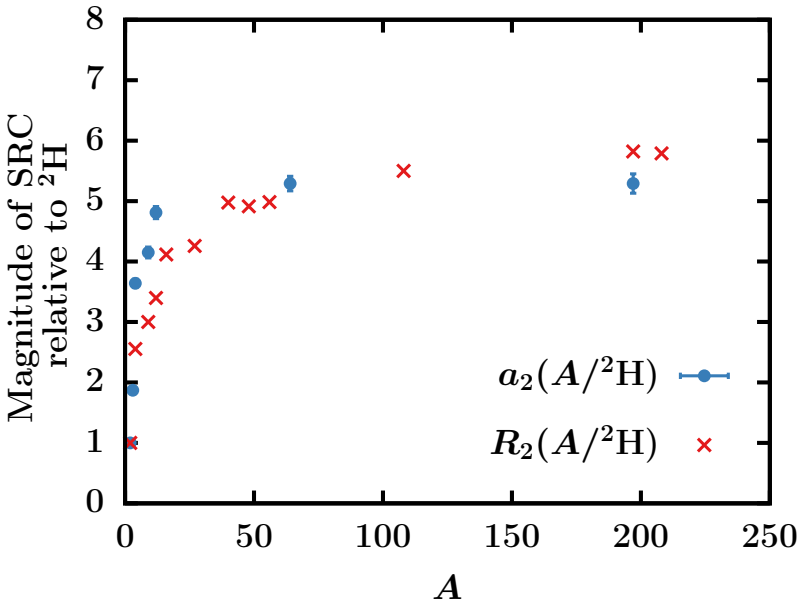

Figure 1 – (Color online) The mass dependence of the computed ratios $R_2(A/^2\mathrm{H})$ defined in Eq. (18) and of the experimentally extracted $a_2(A/^2\mathrm{H})$ coefficients from Ref. [23].

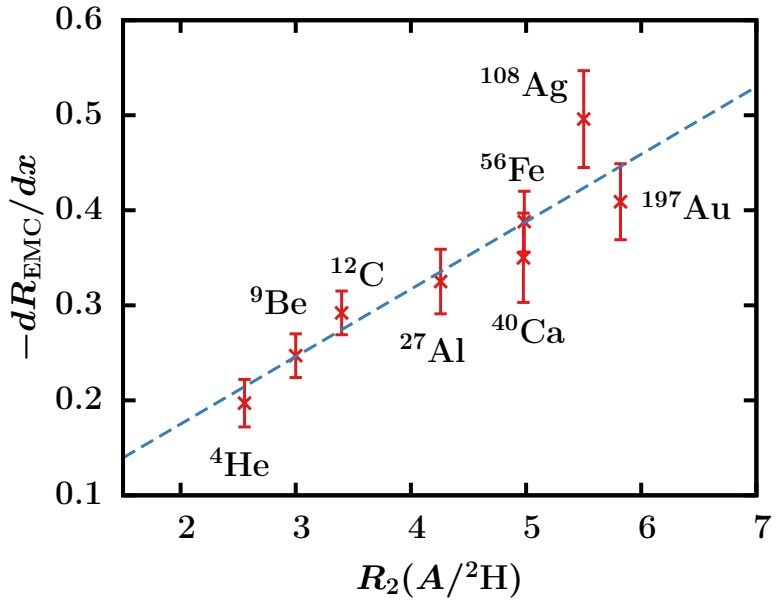

Figure 2 – The measured magnitude of the EMC effect, $-\frac{dR_{EMC}}{dx}$ is plotted as a function of the computed $R_2(A/^2\mathrm{H})$ ratios defined in Eq. (18). The values of the EMC magnitude are from the analysis presented in Ref. [24]. The fitted dashed line obeys the equation $-\frac{dR_{EMC}}{dx} = (0.033 \pm 0.035) + (0.071 \pm 0.009) \cdot R_2(A/^2\mathrm{H})$.

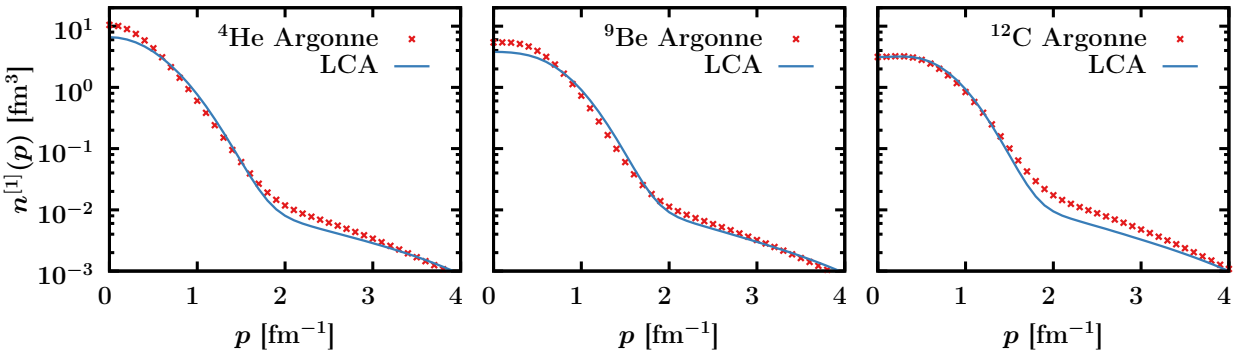

Figure 3 – (Color online) The momentum dependence of the $n^{[1]}(p)$ for ^{4}He, ^{9}Be and ^{12}C. The red crosses are the QMC results of Ref. [4] obtained with the Argonne v_{18} two-nucleon and Urbana X three-nucleon potentials.

distribution is in fair agreement with the realistic WCJ1 one [25], which has a 7.3% D-wave admixture. The $a_2(A/^2\mathrm{H})$ coefficient is an experimentally determined quantity which is connected with the magnitude of SRC in nucleus A relative to ^{2}H [26, 27]. It is extracted from the scaling behavior of the measured $A(e,e')/^2\mathrm{H}(e,e')$ cross-section ratio in selected kinematics favoring virtual-photon scattering from correlated pairs. In Fig. 1, the ratios of the computed norms for A relative to ^{2}H

$$R_2(A/^2\mathrm{H}) = \frac{\mathcal{N}(A) - 1}{\mathcal{N}(^2\mathrm{H}) - 1} \,, \tag{18}$$

are compared to the measured a_2 coefficients of Ref. [23]. In the framework developed in this work, the $R_2(A/^2\mathrm{H})$ are a measure of the magnitude of the aggregated effect of SRC in nucleus A relative to their magnitude in ^{2}H. As can be appreciated from Fig. 1, the mass dependence of the measured a_2 and computed $R_2(A/^2\mathrm{H})$ ratios is roughly the same. For $A \lesssim 40$, $R_2(A/^2\mathrm{H})$ increases strongly with mass number A which hints at a strong mass dependence of the quantitiative effect of SRC. For $A > 40$, the predicted mass dependence of the magnitude of the SRC is soft.

Recently, it has been suggested that the magnitude of the European Muon Collaboration (EMC) effect in a specific nucleus A is connected with the magnitude of the SRC in A [28]. Consequently, one can expect a linear relation between the R_2 of Eq. (18) and the magnitude $-\frac{dR_{EMC}}{dx}$ of the EMC effect. This suggestion is clearly confirmed in Fig. 2 which provides additional support for the proposed LCA method for implementing SRC.

3 Single-nucleon momentum distribution

In order to test the realistic character of the LCA method, in Fig. 3 we compare the LCA results for the $n^{[1]}(p)$ with those obtained with quantum Monte-Carlo (QMC) methods using realistic two-nucleon and three-nucleon Hamiltonians [4]. To facilitate the comparison over the various nuclei we adopt the normalization $1 = \int dp\ p^2 n^{[1]}(p)$. Clearly, the predicted momentum dependence of the QMC and LCA methods is qualitatively comparable. Up to the characteristic nuclear Fermi momentum $p_F = 1.25$ fm^{-1}, the shape of $n^{[1]}(p)$ is very Gaussian in both approaches. For $p > p_F$ the distribution is heavy-tailed. The QMC and the

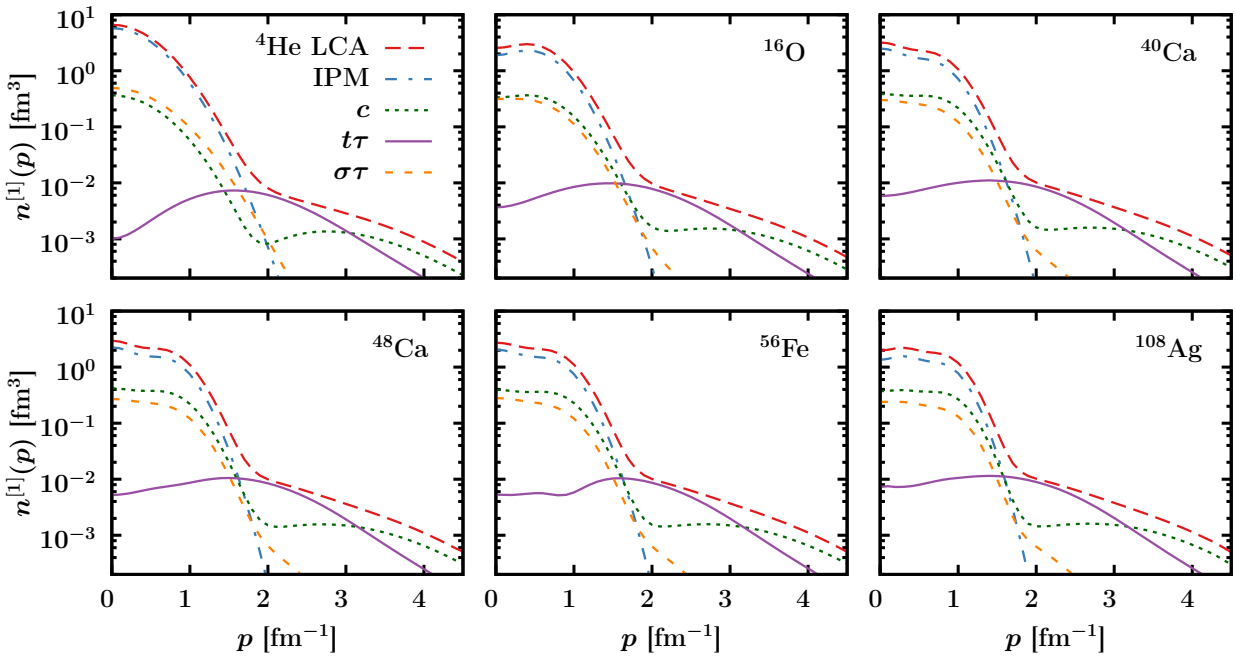

Figure 4 – (Color online) The single-nucleon momentum distribution $n^{[1]}(p)$ for six nuclei. The long dashed line is the full LCA result. The dashed-dotted line is the IPM contribution to the LCA result. Also shown are the results of a calculation that only includes the two-body central (green dotted line), tensor (purple solid line) and spin-isospin (orange short dashed line) correlation contribution. The LCA result includes the interference between all contributions.

LCA method predict a comparable exponential-like fat tail, which is very remarkable given the very different frameworks in which the results are obtained. It is not surprising that for ^{4}He and ^{9}Be the LCA and QMC display some differences at low p, given that LCA does not account for the complicated long-range cluster structures of those nuclei. For ^{12}C, the LCA and QMC results are in reasonable agreement. In this context, it is worth mentioning that the nuclear-matter studies of Ref. [7] have clearly illustrated that the fat tails of the single-nucleon distributions are sensitive to the adopted realistic nucleon-nucleon interaction. This is related to the fact that the short-range part of the NN force is not well constrained by a fit to scattering data.

The computed momentum dependence of the $n^{[1]}(p)$ are displayed in Fig. 4 for a range of nuclei from He to Ag. Some stylized features which apply to all studied nuclei are emerging from the LCA calculations. For $p \lesssim 1.5$ fm^{-1} the distribution is dominated by the IPM contribution. The fat tails are induced by the correlations whereby one distinguishes two regions. For $1.5 \lesssim p \lesssim 3$ fm^{-1} the tensor correlations dominate. The effect of the central correlations extends over a large momentum range and for $p > 3.5$ fm^{-1}, it represents the dominant contribution to $n^{[1]}(p)$ (with the tensor part gradually losing in importance). For all nuclei the crossover between the tensor and the central correlated part of the tail of $n^{[1]}(p)$ occurs at a momentum slightly larger than 3 fm^{-1}. At momenta approaching 4 fm^{-1} the central correlations provide about half of the the $n^{[1]}(p)$. A major source of strength to the other half is due to the interference between the central and spin-isospin correlations (not shown separately in Fig. 4). This qualitative behavior is in line with the ab-initio ^{4}He results of Ref. [4] (see Figure 3 of that reference). The abovementioned conclusions which apply to the correlated part of the one-body momentum distributions of all nuclei studied here, are

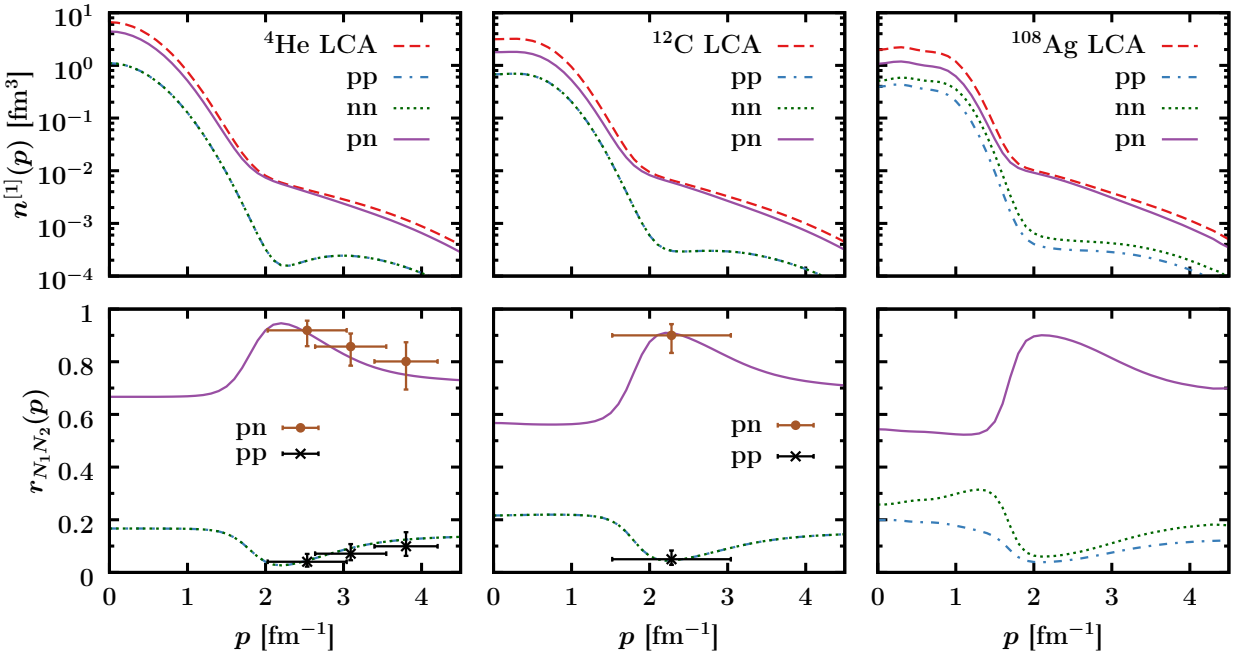

Figure 5 – (Color online) The top panels show the LCA results for the momentum dependence of the contribution of pp pairs ($n^{[1]}_{pp}(p)$), nn pairs ($n^{[1]}_{nn}(p)$), and pn pairs ($n^{[1]}_{pn}(p)$) to the $n^{[1]}(p)$ of ^{4}He, ^{12}C and ^{108}Ag. The bottom panels show the momentum dependence of the ratios $r_{N_1N_2} = n^{[1]}_{N_1N_2}(p)/n^{[1]}(p)$ for $N_1N_2 = pp, nn, pn$. The data points for ^{4}He are extracted from the bottom panel of Fig. 2 in Ref. [29]. The data points for ^{12}C are extracted from Ref. [30]. For ^{4}He and ^{12}C the theoretical results for pp overlap almost perfectly with those for nn.

qualitatively in line with the nuclear-matter results of Ref. [7]. This illustrates that the effect of SRC on single-nucleon momentum distributions can be summarized in some universally applicable principles.

The dominant role of the tensor correlations for intermediate nucleon momenta $1.5 \lesssim p \lesssim 3$ fm^{-1}, has some important implications for the isospin dependence of the effect of short-range correlations. With the aid of Eq. (11) one can write

$$n^{[1]}(p) = n^{[1]}_{pp}(p) + n^{[1]}_{nn}(p) + n^{[1]}_{pn}(p), \tag{19}$$

with

$$n^{[1]}_{N_1N_2}(p) = \frac{1}{\mathcal{N}} \sum_{\alpha<\beta} \delta_{t_\alpha,N_1}\delta_{t_\beta,N_2} \times {}_{\rm nas}\langle \alpha\beta \mid \hat{n}^{\rm LCA}_p(1,2) \mid \alpha\beta\rangle_{\rm nas}. \tag{20}$$

The LCA results for $n^{[1]}_{N_1N_2}(p)$ are shown in Fig. 5. The ratio $r_{N_1N_2}(p) \equiv n^{[1]}_{N_1N_2}(p)/n^{[1]}(p)$ quantifies the relative contribution of N_1N_2 pairs to $n^{[1]}(p)$ at given momentum p. In a naive IPM one expects momentum-independent values of $r_{pp} = \frac{Z(Z-1)}{A(A-1)}$, $r_{nn} = \frac{N(N-1)}{A(A-1)}$ and $r_{pn} = \frac{2NZ}{A(A-1)}$. For $p < p_F$ the plotted ratios in the bottom panel of Fig. 5 very much follow these naive expectations. The tensor dominated momentum range is characterized by an increase of the pn contribution to $n^{[1]}(p)$.

The above discussion provides a natural explanation for the observation that SRC-sensitive reactions like two-nucleon knockout ($A(e,e'pN)$ and $A(p,ppN)$ reactions for example) are very much dominated by the pn channel in the tensor-dominated region which roughly

corresponds with $1.5 \lesssim p \lesssim 3$ fm^{-1}. The bottom panels of Fig. 5 suggest that under those conditions the pn channel can represent 90% of the correlated strength, leaving a mere 5% for the pp channel. This prediction seems to be in line with the experimental observations.

Indeed, the small ratio of pp-to-np pairs above the Fermi momentum was experimentally verified in ^{12}C$(e, e'p(p))$ measured at Jefferson Lab [30]. The quoted pp to pn ratio of $\frac{1\pm0.3\%}{18\pm5\%}$, displayed in Fig. 5 is compatible with the LCA predictions thereby assuming that the pp and nn contributions are equal for $N = Z$ nuclei. From an analysis of the ratio $\frac{^{12}\mathrm{C}(p,ppn)}{^{12}\mathrm{C}(p,pp)}$ it could be inferred that the removal of a proton from the nucleus with initial momentum 275–550 MeV/c is 92^{+8}_{-18}% of the time accompanied by a neutron [31]. Also this result is in line with the LCA predictions for ^{12}C contained in Fig. 5. Our results indicate that similar anomalously large r_{pn}/r_{pp} ratios may be found for heavier nuclei when probing the tensor-dominated tail of the single-nucleon momentum distribution.

Another interesting feature of the results of Fig. 5 is that the $r_{pp}(p)$ $[r_{pn}(p)]$ reaches its minimum (maximum) at $p \approx 2$ fm^{-1}. For $p > 2$ fm^{-1} the $r_{pp}(p)$ grows and the $r_{pn}(p)$ decreases. Experimental evidence supporting this prediction has been recently obtained in the simultaneous measurement of exclusive ^{4}He$(e, e'pp)$ and ^{4}He$(e, e'pn)$ at $(e, e'p)$ missing momenta from 2 to 4.3 fm^{-1} [29]. In those measurements, the kinematics is tuned to probe a nucleon at a given momentum $p > p_F$ in conjunction with its correlated partner. These are precisely the SRC induced two-nucleon processes which systematically dominate the LCA $n^{[1]}(p)$ above the Fermi momentum. One may be tempted to connect A$(e, e'pN)$ cross sections to two-nucleon momentum distributions (TNMD). First, even after cross-section factorization no direct connection between the cross sections and TNMD can be established [32]. Second, as has been pointed out in Ref. [3], a nice pictorial description is given in Figure 12 of that reference, the correlated part of the TNMD receives large SRC contributions from three-nucleon configurations. Thereby the correlation is mediated through a third nucleon. The exclusive A$(e, e'pN)$ measurements are not kinematically optimized to probe those three-nucleon configurations. The A$(e, e'pN)$ kinematical settings are optimized to probe SRC-related two-nucleon configurations, and it is precisely those configurations which are the source of strength of the tails of the single-nucleon momentum distributions.

The ^{4}He data points shown in Fig. 5 are extracted from the ^{4}He$(e, e'pp)/^4$He$(e, e'pn)$ cross-section ratios of Ref. [29], whereby we have assumed that $r_{nn} = r_{pp}$. The r_{np} and r_{pp} cannot be directly connected to the ^{4}He$(e, e'pp)/^4$He$(e, e'p)$ and ^{4}He$(e, e'pn)/^4$He$(e, e'p)$ cros-section ratios also shown in Fig. 2 of Ref. [29]. Indeed, for $p > p_F$ the $r_{N_1N_2}(p)$ encodes information about correlated pairs, whereas the ^{4}He$(e, e'p)$ cross sections also contain contributions from other sources like final-state interactions and triple correlations.

As the central correlations, which are blind for the isospin of the interacting pairs, gain in importance with increasing p one observes that the $r_{N_1N_2}(p)$ ratios gradually approach a limiting value which is different from the IPM values, in particular for heavier nuclei.

The above discussions indicate that the LCA framework in combination with central and tensor correlations, captures the stylized features of the SRC including its mass and isospin dependence. We now wish to shed light on the underlying physics mechanics of the correlated part of the momentum distribution. More in particular we address the question: "What are the quantum numbers of the IPM pairs which are most affected by the correlations?" This discussion will lead to an understanding of the high p limits in the bottom panels of Fig. 5.

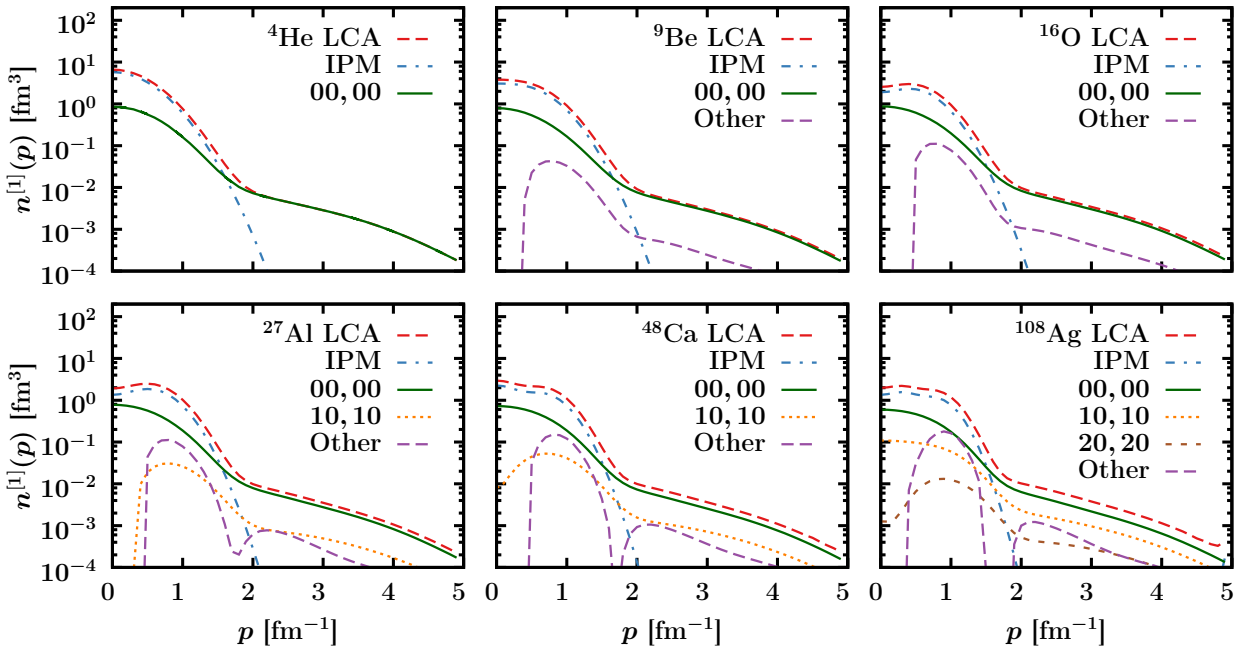

Figure 6 – (Color online) The momentum dependence of the $n^{[1]}(p)$ for six nuclei. The red dashed line is the LCA result. The blue dashed-dotted line is the IPM contribution to the LCA result. Also shown are the $n^{[1],\mathrm{corr}}_{nl,n'l'}(p)$ that dominate the high momentum tail. The purple dashed line is the summed contribution of the the $n^{[1],\mathrm{corr}}_{nl,n'l'}(p)$ which are not shown separately.

One can determine the contributions from the relative quantum numbers nl of the IPM pairs to the correlated part of $n^{[1]}(p)$ (denoted by $n^{[1],\mathrm{corr}}(p)$) by means of the expansion of Eq. (17). One finds,

$$\hat{n}^{[1],\mathrm{corr}}_{nl,n'l'}(p) = \sum_{\alpha<\beta}\sum_{A,B} \left(C^A_{\alpha\beta}\right)^\dagger C^B_{\alpha\beta}\, \delta_{nn_A}\delta_{ll_A}\delta_{n'n_B}\delta_{l'l_B} \langle A \mid \hat{n}^{[1],\mathrm{corr}}_p(1,2) \mid B\rangle \ , \tag{21}$$

where the operator $\hat{n}^{[1],\mathrm{corr}}_p(1,2)$ has been defined as in Eq. (12). Obviously, one has

$$\sum_{nl}\sum_{n'l'} n^{[1],\mathrm{corr}}_{nl,n'l'}(p) = n^{[1],\mathrm{corr}}(p) \ . \tag{22}$$

The $n^{[1],\mathrm{corr}}_{nl,n'l'}(p)$ that provide the largest contribution to $n^{[1]}(p)$ are shown in Fig. 6. It is clear that correlation operators acting on $nl = 00$ IPM pairs are responsible for the major fraction of the $n^{[1]}(p)$ for $p \gtrsim 2$ fm^{-1}. For heavier nuclei, the contributions from pairs with $n > 0$, $l = 0$ gain in importance. Non-diagonal $\hat{n}^{[1],\mathrm{corr}}_{nl,n'l'}(p)$ represent a small fraction of the high-momentum tail.

We wish to stress that correlation operators acting on IPM pairs can change the quantum numbers. For example, the tensor operator acting on the deuteron's $l = 0$ IPM pair generates the correlated $l = 2$ state. The dominant role of $nl = 00$ IPM pairs in the creation of high-momentum components, provides support for our proposed method to quantify the SRC by counting the number of $nl = 00$ IPM pairs [19, 22, 32]. Consequently, for high p the central correlations dominate and the $r_{N_1N_2}(p)$ ratios of Fig. 5 are connected with the amount of N_1N_2 IPM pairs with $nl = 00$. Using the computed number of of $nl = 00$ pairs

Table 2 – Results from the IPM and LCA framework for the kinetic energy per proton and neutron ($\langle T_p\rangle$ and $\langle T_n\rangle$) for a variety of nuclei. We compare to values obtained for the average correlated kinetic energy per nucleon $\langle T_N\rangle$ from alternate calculations [33, 34].

A	x_p	$\langle T_N\rangle$ (MeV)						$\langle T_p\rangle / \langle T_n\rangle$	
		IPM (p)	IPM (n)	LCA (p)	LCA(n)	[33]	[34]	IPM	LCA
^{2}H	0.500	14.95	14.93	20.95	20.91			1.00	1.00
^{4}He	0.500	13.80	13.78	25.28	25.23		19.63	1.00	1.00
^{9}Be	0.444	15.81	16.58	28.91	27.33			0.95	1.06
^{12}C	0.500	16.08	16.06	28.96	28.92	32.4	22.38	1.00	1.00
^{16}O	0.500	15.61	15.59	29.48	29.43	30.9	23.81	1.00	1.00
^{27}Al	0.481	16.61	16.92	30.93	30.26		25.12	0.98	1.02
^{40}Ca	0.500	16.44	16.42	31.23	31.18	33.8	27.72	1.00	1.00
^{48}Ca	0.417	15.64	17.84	33.04	30.06		27.05	0.88	1.10
^{56}Fe	0.464	16.71	17.45	32.33	31.13	32.7		0.96	1.04
^{108}Ag	0.435	16.48	17.81	33.55	31.16			0.93	1.08

in ^{12}C we find $r_{pp} = r_{nn} = 0.16$ and $r_{pn} = 0.68$. For ^{108}Ag, a similar calculation leads to $r_{pp} = 0.14$, $r_{nn} = 0.20$ and $r_{pn} = 0.66$. For high p these numbers are fair predictions for the computed ratios $r_{N_1N_2}(p)$ in Fig 5.

4 Single-nucleon kinetic energies and rms radii

In a non-relativistic framework, the diagonal single-nucleon kinetic energy operator $\widehat{T}^{[1]}$ can be written as

$$\widehat{T}^{[1]} = \sum_{i=1}^{A} \widehat{T}^{[1]}(i) = \sum_{i=1}^{A} \frac{-\hbar^2}{2M_i}\nabla_i^2, \tag{23}$$

where M_i is the nucleon mass. In the IPM, the average kinetic energy $\langle T_p\rangle$ per proton is given by

$$\left\langle T_p^{IPM}\right\rangle = \frac{1}{Z}\sum_{\alpha} \delta_{t_\alpha,p}\langle\alpha \mid \widehat{T}^{[1]}(1) \mid \alpha\rangle \ . \tag{24}$$

A similar definition is adopted for the average kinetic energy per neutron $\langle T_n\rangle$. In the LCA framework developed in Sec. 2 one has

$$\left\langle T_p^{\rm LCA}\right\rangle = \frac{1}{\mathcal{N}}\frac{1}{Z}\sum_{\alpha<\beta} {}_{\rm nas}\langle\alpha\beta \mid \widehat{T}_p^{\rm LCA}(1,2) \mid \alpha\beta\rangle_{\rm nas}, \tag{25}$$

where the operator $\widehat{T}_p^{\rm LCA}$ can be obtained from Eq. (11). Since we work in a non-relativistic framework, we have adopted a hard cutoff of 4.5 fm^{-1} for the maximum nucleon momentum in the calculations of the kinetic energy.

Table 2 compares the IPM and LCA predictions for the kinetic energies per proton and neutron. Obviously, as the kinetic energies can be associated with the fourth moments of the $n^{[1]}(p)$, they are highly sensitive to its fat tails. Indeed, inclusion of the correlations increases the $\langle T_p\rangle$ and $\langle T_n\rangle$ by a factor of about two. For the sake of reference, the average kinetic

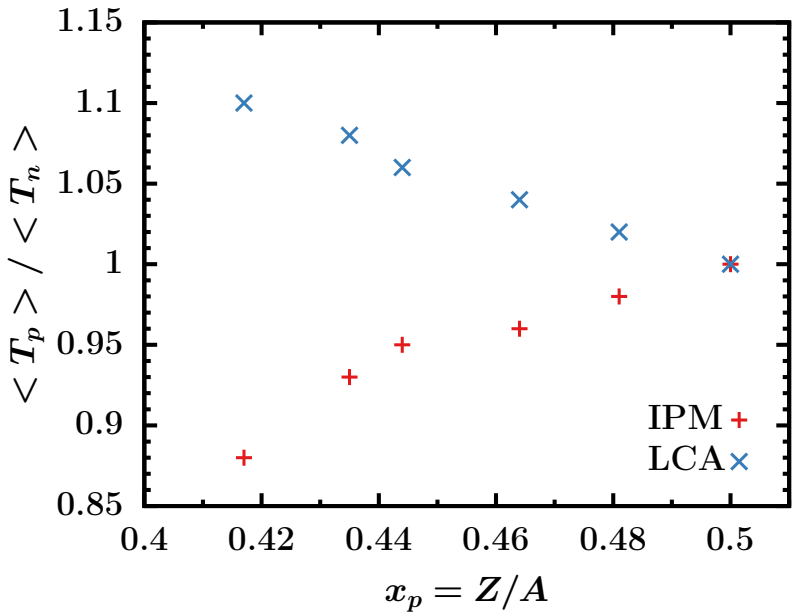

Figure 7 – The IPM and LCA predictions for the $\langle T_p \rangle / \langle T_n \rangle$ as a function of the proton fraction x_p.

energy of a one-component nuclear Fermi gas is 21 MeV. For the heaviest nuclei studied in this work we find values which are about 50% larger. The LCA results for the average kinetic energies for ^{9}Be are comparable those of realistic calculations quoted in Table 1 of Ref. [35] — $\langle T_p \rangle = 29.82$ MeV and $\langle T_n \rangle$=27.09 MeV. As can be appreciated from Table 2, the LCA predictions for the correlated kinetic energies $\langle T_N \rangle$ are comparable with those of the realistic model of Ref. [33]. The predictions for $\langle T_N \rangle$ from the variational calculations of Ref. [34] are systematically smaller.

The parameter $x_p = \frac{Z}{A}$ is the proton fraction and is a measure for the asymmetry of nuclei. As expected for a non-interacting two-component Fermi system, is $\langle T_p \rangle < \langle T_n \rangle$ for asymmetric nuclei ($x_p < 0.5$) in the IPM. As can be appreciated from Fig. 7 after inclusion of the correlations, the situation is reversed with the minority component having a larger average kinetic energy. This can be attributed to the tensor correlations, which are stronger between pn than between pp and nn pairs. The difference between $\langle T_p \rangle$ and $\langle T_n \rangle$ increases roughly linearly with decreasing proton fraction x_p. For the most asymmetric nucleus considered here, ^{48}Ca, $\langle T_p \rangle$ is about 10% larger than $\langle T_n \rangle$.

We now discuss the effect of the correlations on the root-mean-square (rms) radii of the nuclear matter distribution. The rms radii can be computed with an operator of the form

$$\widehat{r^2} = \frac{1}{A} \sum_i \left(\vec{r}_i - \vec{R}_{cm} \right)^2 , \tag{26}$$

with $\vec{R}_{cm} = \frac{1}{A} \sum_i \vec{r}_i$. Using a procedure which is completely similar to the one used for the kinetic energy, in the LCA the operator $\widehat{r^2}$ becomes a correlated operator with a one-body and a two-body part. Table 3 compares the IPM and the LCA predictions for the rms radii. The IPM predictions which are obtained with the global parameterization of Eq. (16) tend to overestimate the measured radii for light and heavy nuclei, and underestimate them for mid-heavy nucleus. All in all, the effect of the correlations on the computed rms radii is

Table 3 – Results from the IPM and LCA framework for the rms radii for a variety of nuclei. The results are compared with those from the Unitary Correlation Operator Method (UCOM) [34] and experimental values (Expt) [36]. All radii are in fm.

A	IPM	LCA	UCOM [34]	Expt [36]
^{4}He	1.84	1.70	1.35	1.6755 ± 0.0028
^{9}Be	2.32	2.13		2.5190 ± 0.0120
^{12}C	2.46	2.23	2.36	2.4702 ± 0.0022
^{16}O	2.59	2.32	2.28	2.6991 ± 0.0052
^{27}Al	3.06	2.72	2.82	3.0610 ± 0:0031
^{40}Ca	3.21	2.84	2.93	3.4776 ± 0.0019
^{48}Ca	3.47	3.05	3.20	3.4771 ± 0.0020
^{56}Fe	3.63	3.20		3.7377 ± 0:0016
^{108}Ag	4.50	3.94		4.6538 ± 0.0025
^{197}Au	5.73	5.21		5.4371 ± 0.0038
^{208}Pb	5.83	5.28		5.5012 ± 0.0013

rather modest. The LCA predictions are in acceptable agreement with the experimental values and the predictions from the UCOM framework of Ref. [34]. We stress that our IPM results are obtained with a single Slater determinant with HO wave functions from the global parameterization of Eq. (16). It is likely that one can find a slightly modified parametrization that brings the LCA rms radii closer to the data.

5 Summary

We have introduced an approximate flexible method, dubbed LCA, for the computation of the SRC contributions to the single-nucleon momentum distributions $n^{[1]}(p)$ throughout the whole mass table. A basis of single-particle wave functions and a set of correlation functions serves as an input to LCA. For the numerical calculations presented here, we have included the central, spin-isospin and tensor correlations and mass-independent correlation functions. The approximate LCA method predicts the characteristic high-momentum part of the single-nucleon momentum distribution for a wide range of nuclei. For the light nuclei ^{4}He, ^{9}Be and ^{12}C, the LCA predictions for the tails of the single-nucleon momentum distributions are in line with those of sophisticated QMC calculations with realistic Hamiltonians. The predicted aggregated effect of SRC and its mass dependence closely matches the observations from inclusive electron scattering (a_2 coefficients and the magnitude of the EMC effect).

In the LCA, one can separate contributions of the central, spin-isospin and tensor correlations and study how these affect the relative strength of nn, pp and pn pairs in the high-momentum tail of $n^{[1]}(p)$. For $1.5 \lesssim p \lesssim 3$ fm^{-1} the $n^{[1]}(p)$ is dominated by tensor-induced pn correlations. Our prediction for the relative strength of pp and pn pairs in the tail part of $n^{[1]}(p)$ is in line with observations in exclusive two-nucleon knockout studies. We have shown that the high-momentum tail of $n^{[1]}(p)$ is dominated by the correlation operators acting on mean-field pairs with vanishing relative radial quantum number and vanishing orbital angular momentum, i.e. IPM pairs in a close-proximity configuration. Another prediction of the LCA

is that in asymmetric nuclei, the correlations are responsible for the fact that the average kinetic energy of the minority nucleons is larger than for the majority nucleons. The LCA method provides results for the correlated average kinetic energies and nuclear radii which are in line with those of alternate many-body approaches.

Acknowledgment

We thank O. Hen and E. Piasetzky for many fruitful discussions. This work is supported by the Research Foundation Flanders (FWO-Flanders) and by the Interuniversity Attraction Poles Programme P7/12 initiated by the Belgian Science Policy Office. The computational resources (Stevin Supercomputer Infrastructure) and services used in this work were provided by Ghent University, the Hercules Foundation and the Flemish Government.

---

[1] R. Schiavilla, R. B. Wiringa, S. C. Pieper, and J. Carlson, Phys. Rev. Lett. **98**, 132501 (2007).
[2] R. B. Wiringa, R. Schiavilla, S. C. Pieper, and J. Carlson, Phys. Rev. C **78**, 021001 (2008).
[3] H. Feldmeier, W. Horiuchi, T. Neff, and Y. Suzuki, Phys. Rev. C **84**, 054003 (2011).
[4] R. B. Wiringa, R. Schiavilla, S. C. Pieper, and J. Carlson, Phys. Rev. C **89**, 024305 (2014).
[5] M. Alvioli, C. Ciofi degli Atti, L. P. Kaptari, et al., Phys. Rev. C **87**, 034603 (2013).
[6] O. Benhar, A. Fabrocini, and S. Fantoni, Nucl. Phys. A **505**, 267 (1989).
[7] A. Rios, A. Polls, and W. H. Dickhoff, Phys. Rev. C **89**, 044303 (2014).
[8] M. Alvioli, C. Ciofi degli Atti, and H. Morita, Phys. Rev. Lett. **100**, 162503 (2008).
[9] M. Alvioli, C. Ciofi degli Atti, L. P. Kaptari, et al., Phys. Rev. C **85**, 021001 (2012).
[10] F. Arias de Saavedra, C. Bisconti, G. Co', and A. Fabrocini, Phys. Rept. **450**, 1 (2007).
[11] C. Bisconti, F. A. d. Saavedra, and G. Co', Phys. Rev. C **75**, 054302 (2007).
[12] M. M. Sargsian, Phys. Rev. C **89**, 034305 (2014).
[13] S. K. Bogner and D. Roscher, Phys. Rev. C **86**, 064304 (2012).
[14] T. Neff and H. Feldmeier, Nucl. Phys. A **713**, 311 (2003).
[15] S. Janssen, J. Ryckebusch, W. Van Nespen, and D. Debruyne, Nucl. Phys. A **672**, 285 (2000).
[16] J. Ryckebusch, V. Van der Sluys, K. Heyde, et al., Nucl. Phys. A **624**, 581 (1997).
[17] C. Gearheart, PhD thesis (Washington University, St. Louis, 1994).
[18] S. C. Pieper, R. B. Wiringa, and V. Pandharipande, Phys. Rev. C **46**, 1741 (1992).
[19] M. Vanhalst, J. Ryckebusch, and W. Cosyn, Phys. Rev. C **86**, 044619 (2012).
[20] K. G. Fissum, M. Liang, B. D. Anderson, et al., Phys. Rev. C **70**, 034606 (2004).
[21] M. Iodice, E. Cisbani, R. De Leo, et al., Phys. Lett. B **653**, 392 (2007).
[22] M. Vanhalst, W. Cosyn, and J. Ryckebusch, Phys. Rev. C **84**, 031302 (2011).
[23] O. Hen, E. Piasetzky, and L. B. Weinstein, Phys. Rev. C **85**, 047301 (2012).
[24] J. Arrington, A. Daniel, D. B. Day, et al., Phys. Rev. C **86**, 065204 (2012).
[25] F. Gross and A. Stadler, Phys. Rev. C **82**, 034004 (2010).
[26] N. Fomin, J. Arrington, R. Asaturyan, et al., Phys. Rev. Lett. **108**, 092502 (2012).
[27] L. Frankfurt, M. Strikman, D. Day, and M. Sargsian, Phys. Rev. C **48**, 2451 (1993).

[28] L. Weinstein, E. Piasetzky, D. Higinbotham, et al., Phys. Rev. Lett. **106**, 052301 (2011).
[29] I. Korover, N. Muangma, O. Hen, et al., ArXiv e-prints, 1401.6138 (2014).
[30] R. Subedi, R. Shneor, P. Monaghan, et al., Science **320**, 1476 (2008).
[31] E. Piasetzky, M. Sargsian, L. Frankfurt, et al., Phys. Rev. Lett. **97**, 162504 (2006).
[32] C. Colle, W. Cosyn, J. Ryckebusch, and M. Vanhalst, Phys. Rev. C **89**, 024603 (2014).
[33] C. Ciofi degli Atti and S. Simula, Phys. Rev. C **53**, 1689 (1996).
[34] H. Feldmeier, T. Neff, R. Roth, and J. Schnack, Nucl. Phys. A **632**, 61 (1998).
[35] M. M. Sargsian, J. Phys. Conf. Ser. **496**, 012007 (2014).
[36] I. Angeli and K. Marinova, Atomic Data and Nuclear Data Tables **99**, 69 (2013).

3.5 Spin-isospin correlations

The most important correlation operators concerning correlation over short distances are the central and tensor correlations. Often, the spin-isospin correlations are put forward as another significant contribution. In section 3.4, the single-nucleon momentum distribution is calculated including the spin-isospin correlations. In this section we take a more detailed look at the effect of the spin-isospin correlations on the single-nucleon momentum distributions obtained by the LCA.

Table 3.1 lists the normalization factors of Eq. (2.50) with and without the spin-isospin correlations for a range of nuclei from ^{2}H to ^{208}Pb. The inclusion of an extra correlation increases the normalization factor with 5% for ^{2}H and approximately 12% for the other nuclei. The results seem to suggest that spin-isospin correlations are an important ingredient of SRC.

As is proposed in Section 3.4, the deviation of $\mathcal{N}^{[1]}_{\sigma\tau}$ from 1 can be interpreted as a quantitative measure for the total effect of the SRC on the ground-state wave function. In Figure 3.1, the ratios of the computed norms relative to ^{2}H,

$$R_2^{\sigma\tau}(A/^2\mathrm{H}) = \frac{\mathcal{N}^{[1]}_{\sigma\tau}(A) - 1}{\mathcal{N}^{[1]}_{\sigma\tau}(^2\mathrm{H}) - 1}, \tag{3.1}$$

are compared to the measured $a_2(A/^2\mathrm{H})$ coefficients and the R_2 ratios without spin-isospin correlation. The inclusion of the spin-isospin correlations reduce the ratios significantly. Both the a_2 coefficient and the ratios R_2 or $R_2^{\sigma\tau}$ are a measure for the amount of SRC for a nucleus A relative to the deuteron. Remember, the a_2 coefficient is obtained in kinematic conditions that probe nucleons with a momentum higher than the Fermi momentum. In contrast, the R_2 ratios also include effect from correlations below the Fermi momentum. Therefore, there is no direct relation between the values of the a_2 coefficient and the values of the ratios R_2 or $R_2^{\sigma\tau}$. Although there is no direct relation, a similar mass dependence can still be expected. Indeed, both the ratios (R_2 and $R_2^{\sigma\tau}$) and the a_2 coefficient increase strongly with mass number A for light nuclei, and show a soft A dependence for heavier nuclei.

Figure 3.2 compares single-nucleon momentum distributions $n^{[1]}(p)$ with and without spin-isospin correlations. The effect of the spin-isospin correlations on the shape of the total single-nucleon momentum distribution is limited. The amount of nucleon pairs in the high-momentum tail is slightly reduced, and accordingly the amount of nucleons with a momentum lower than the Fermi momentum k_F is increased.

Figure 3.3 shows the separate contribution of the different correlations to $n^{[1]}(p)$. The contribution of the spin-isospin correlations is mainly concentrated below the Fermi momentum with a heavy tail up to 3 fm^{-1}. This explains reduction of the nucleon pairs in the high-momentum tail observed in Figure 3.2. Furthermore, the interplay with the central correlations creates some negative interference around the Fermi momentum and a slight positive interference at $p > 3$ fm^{-1}.

One can conclude that spin-isospin correlations are an important ingredient of SRC. Concerning single-nucleon momentum distributions, however, the effect is concentrated in the

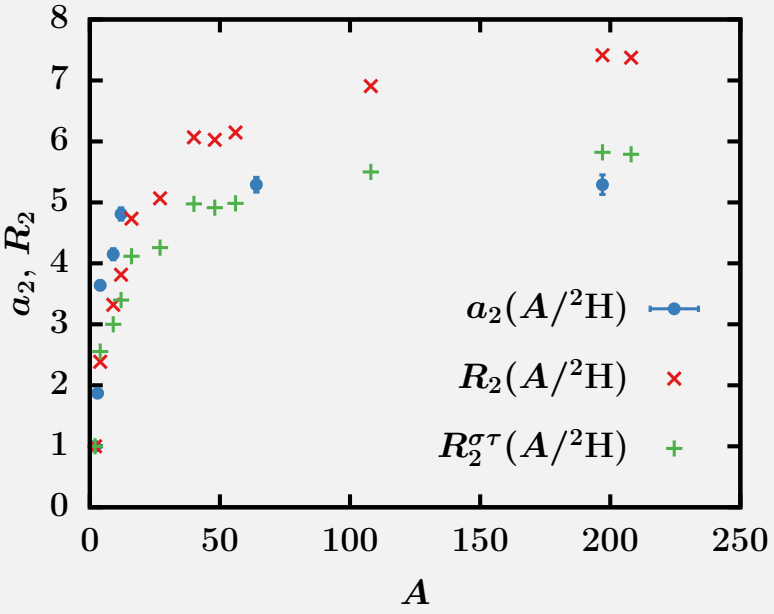

Figure 3.1 – The mass dependence of the computed $R_2(A/^2\mathrm{H})$ and the experimental extracted $a_2(A/^2\mathrm{H})$ coefficients from Ref. [5].

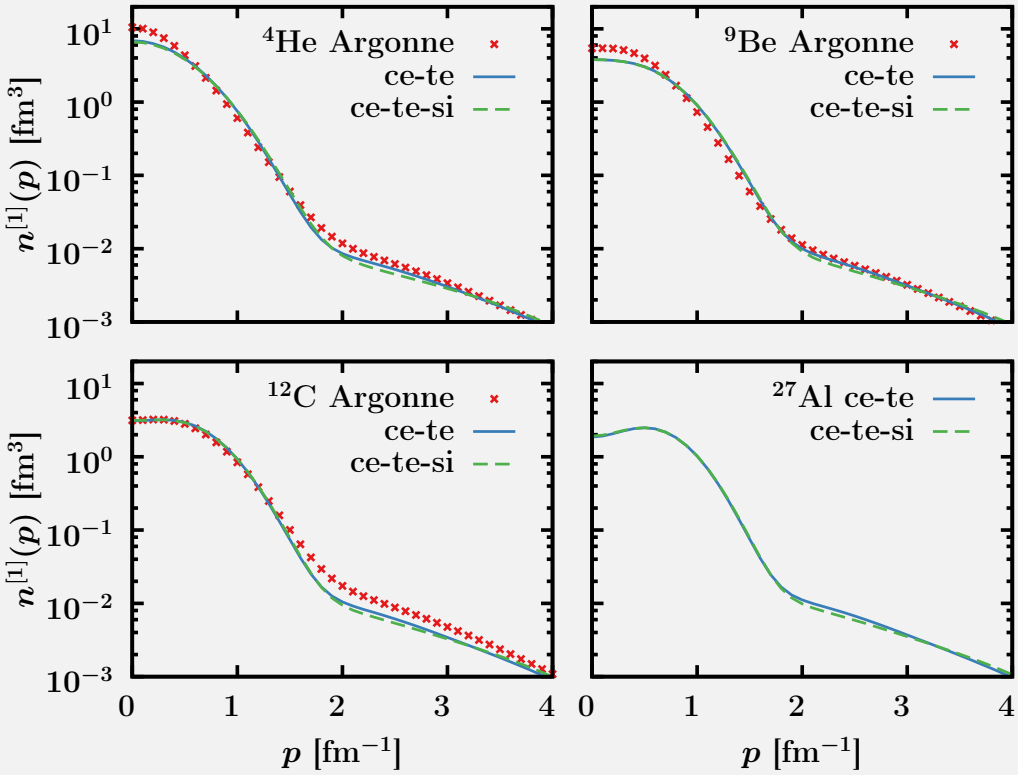

Figure 3.2 – The momentum dependence of the $n^{[1]}(p)$ for ^{4}He, ^{9}Be, ^{12}C and ^{27}Al with central and tensor correlations (ce-te) and with central, tensor and spin-isospin correlations (ce-te-si). The red crosses are the QMC results of Ref. [6] with the Argonne v_{18} and Urbana X three-nucleon potential.

Table 3.1 – The norms $\mathcal{N}^{[1]}$ and $\mathcal{N}^{[1]}_{\sigma\tau}$, respectively with and without the inclusion of the spin-isospin correlations.

el	$\mathcal{N}^{[1]}$	$\mathcal{N}^{[1]}_{\sigma\tau}$	el	$\mathcal{N}^{[1]}$	$\mathcal{N}^{[1]}_{\sigma\tau}$
^{2}H	1.075	1.128	^{40}Ca	1.455	1.637
^{4}He	1.179	1.327	^{48}Ca	1.452	1.629
^{9}Be	1.249	1.384	^{56}Fe	1.461	1.638
^{12}C	1.286	1.435	^{108}Ag	1.518	1.704
^{16}O	1.355	1.527	^{197}Au	1.556	1.745
^{27}Al	1.380	1.545	^{208}Pb	1.553	1.741

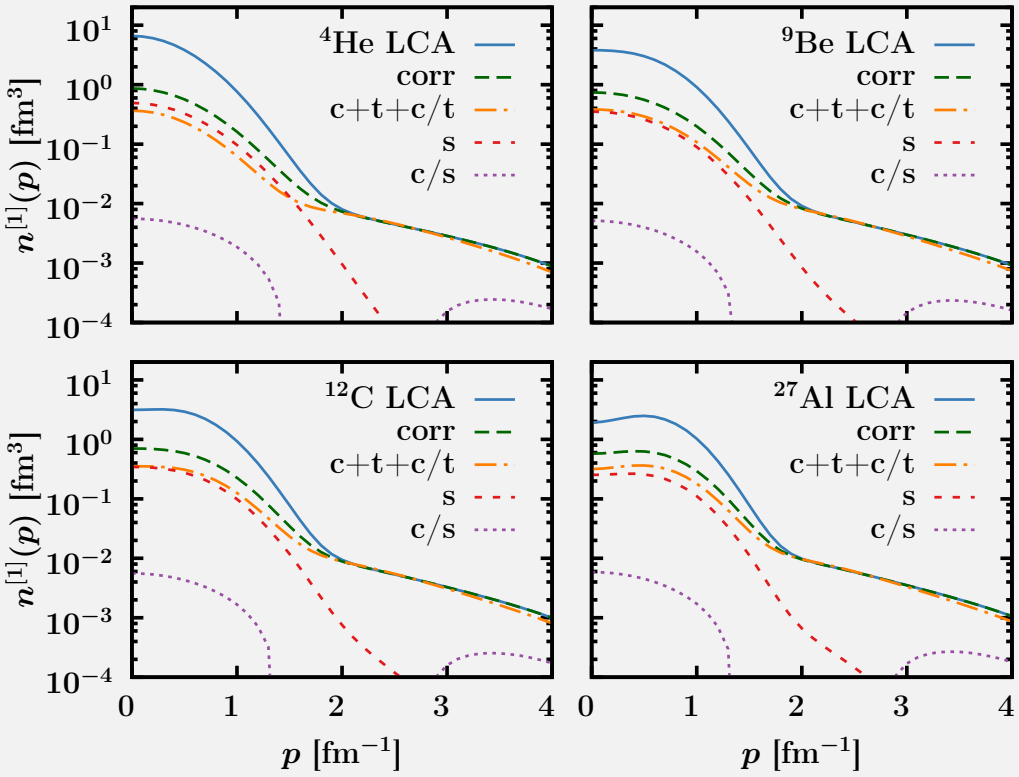

Figure 3.3 – The momentum dependence of the single-nucleon momentum distributions $n^{[1]}(p)$ for ^{4}He, ^{9}Be, ^{12}C and ^{27}Al. The full line is the full LCA result. The orange dashed-dot line is the contribution of the central, the tensor and the interference between central and tensor contributions. The red dashed (purple dotted) line is the contribution of the spin-isospin correlation (interference between central and spin-isospin contributions). The dashed green line is the total correlated part of the LCA result. The interference between tensor and spin-isospin contributions is so small that it falls outside the scales of the figure.

area below k_F and its contribution to the total distribution is less notable than the contribution of the central and tensor component. Experimental measurements which probe SRC are performed for kinematics that select high-momentum nucleons. Although the total effect demonstrated by the normalization factor is significant, the effect of the spin-isospin correlation function on these experimental observables is expected to be less distinct. This does not exclude a significant effect on two-nucleon momentum distributions discussed in the next section or other SRC-related features.

3.6 The two-nucleon momentum distribution

The paper in Section 3.4 studied the single-nucleon momentum distribution in the LCA framework. It was illustrated that SRC manifest themselves in the tail part of the momentum distribution. Furthermore, the LCA method was able to explain stylized features of the single-nucleon momentum distribution such as the dominant role of the proton-neutron pairs and the ratio of correlated proton-proton to proton-neutron pairs. This section considers the two-nucleon momentum distribution. In line with the results for the single-nucleon distribution, one expects to see signature of SRC in the two-nucleon momentum distribution.

The two-nucleon momentum distribution $n^{[2]}(\vec{k}_{12}, \vec{P}_{12})$ is defined as

$$n^{[2]}(\vec{k}_{12}, \vec{P}_{12}) = \frac{2}{A(A-1)} \frac{1}{(2\pi)^6} \int d^{3A}\{\vec{r}_{1-A}\} d^{3A}\{\vec{r}\,'_{1-A}\} \times \sum_{i<j=1}^{A} e^{-\imath \vec{k}_{12}\cdot(\vec{r}\,'_{ij}-\vec{r}_{ij})} e^{-\imath \vec{P}_{12}\cdot(\vec{R}'_{ij}-\vec{R}_{ij})} \prod_{k\neq\{i,j\}} \delta^3\left(\vec{r}_k - \vec{r}\,'_k\right) \Psi^*(\vec{r}_{1-A}) \Psi(\vec{r}\,'_{1-A}). \quad (3.2)$$

The corresponding two-body operator is

$$\hat{n}_{\vec{k}_{12},\vec{P}_{12}} = \frac{2}{A(A-1)} \sum_{i<j=1}^{A} \frac{1}{(2\pi)^6} e^{-\imath \vec{k}_{12}\cdot(\vec{r}\,'_{ij}-\vec{r}_{ij})} e^{-\imath \vec{P}_{12}\cdot(\vec{R}'_{ij}-\vec{R}_{ij})} = \sum_{i<j=1}^{A} \hat{n}^{[2]}_{\vec{k}_{12},\vec{P}_{12}}(i,j). \quad (3.3)$$

3.6.1 The relative two-nucleon momentum distribution

The radial relative two-nucleon momentum distribution $n^{[2]}(k_{12})$ is defined by

$$n^{[2]}(k_{12}) = \int d^2\Omega_k \int d^3\vec{P}_{12} n^{[2]}(\vec{k}_{12}, \vec{P}_{12}). \quad (3.4)$$

The corresponding two-body operator is then

$$\hat{n}_{k_{12}} = \int d^2\Omega_k \int d^3\vec{P}_{12} \hat{n}_{\vec{k}_{12},\vec{P}_{12}} = \sum_{i<j=1}^{A} \hat{n}^{[2]}_{k_{12}}(i,j). \quad (3.5)$$

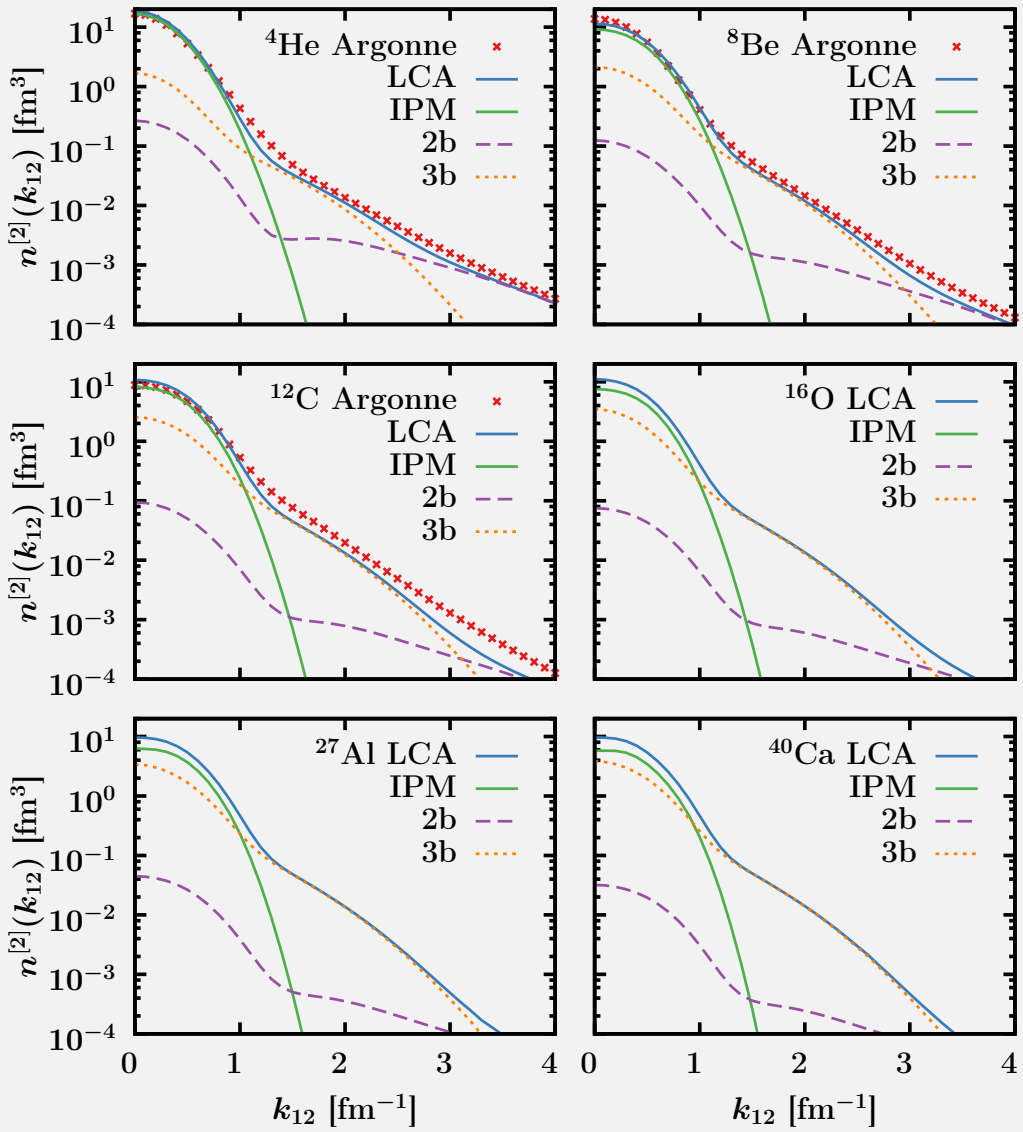

Figure 3.4 – The momentum dependence of $n^{[2]}(k_{12})$ for ^{4}He, ^{8}Be, ^{12}C, ^{16}O, ^{27}Al and ^{40}Ca. The red crosses are the QMC results of Ref. [6] with the Argonne v_{18} and Urbana X three-nucleon potential. The blue line is the full LCA result. The green line is the IPM contribution to the LCA result. The purple dashed (orange dotted) line is the two-body (three-body) contribution $n^{\mathrm{corr},[2]}(k_{12})$ ($n^{\mathrm{corr},[3]}(k_{12})$), to the correlated part, $n^{\mathrm{corr}}(k_{12})$, defined in Eq. (3.8).

This operator and the LCA determine an effective operator $\hat{n}^{\mathrm{LCA}}_{k_{12}}$ from which the correlated relative momentum distribution at k_{12} can be computed,

$$n^{[2]}(k_{12}) = \frac{1}{\mathcal{N}^{[2]}} \langle \Phi | \, \hat{n}^{\mathrm{LCA}}_{k_{12}} \, | \Phi \rangle \,, \tag{3.6}$$

where $\mathcal{N}^{[2]}$ is the two-body normalization factor, defined in Eq. (2.51). More detailed expressions for the matrix elements of $n^{[2]}(k_{12})$ are given in appendix D.4.

In this section, the correlation are limited to the central and tensor correlations. In order to test the realistic character of the LCA method, Figure 3.4 compares the LCA results for the $n^{[2]}(k_{12})$ with those obtained with quantum Monte-Carlo (QMC) methods using realistic

two-nucleon and three-nucleon Hamiltonians [6]. To facilitate the comparison over the various nuclei, the normalization $\int dk_{12}\, k_{12}^2 n^{[2]}(k_{12}) = 1$ is adopted. Clearly the predicted momentum dependence of the QMC and LCA methods are quantitatively comparable. There is some discrepancy in the strength of the high-momentum tail of ^{12}C. In the LCA, the distribution has less strength above the Fermi momentum, $k_{12} > k_F \approx 1.25$ fm^{-1}, and consequently more below the Fermi momentum, than the Argonne result. In other words, there are less nucleon pairs in ^{12}C with high relative momentum in the LCA than in the Argonne results. However, the difference is only small.

According to Eq. (2.48), the correlated part $\hat{n}_{k_{12}}^{\rm corr}$ of the operator $\hat{n}_{k_{12}}^{\rm LCA}$, is a sum of two- and three-body operators,

$$\hat{n}_{k_{12}}^{\rm corr} = \sum_{i<j}^{A} \hat{n}_{k_{12}}^{\rm corr,[2]}(i,j) + \sum_{i<j<k}^{A} \hat{n}_{k_{12}}^{\rm corr,[3]}(i,j,k). \tag{3.7}$$

Accordingly, the correlated part of $n^{[2]}(k_{12})$ (denoted by $n^{[2],{\rm corr}}(k_{12})$) can be split into a part generated by the two-body operators and a part generated by the three-body operators,

$$n^{[2],{\rm corr}}(k_{12}) = n^{{\rm corr},[2]}(k_{12}) + n^{{\rm corr},[3]}(k_{12}). \tag{3.8}$$

The two-body part contains the terms that are represented in Figure 2.2 by the diagrams (b) and (d). In these terms, the operator $\hat{n}_{k_{12}}^{[2]}(i,j)$ and the correlation operator $\hat{l}(i,j)$ act on the same two nucleons. Hence, the two-body part, $n^{{\rm corr},[2]}(k_{12})$, can be interpreted as the relative momentum distribution of correlated nucleon pairs. The terms of the three-body parts are represented by (c) and (e) in Figure 2.2. In these terms, the operator $\hat{n}_{k_{12}}^{[2]}(i,j)$ and the correlation operator $\hat{l}(i,k)$ or $\hat{l}(j,k)$ have one common nucleon. The three-body part, $n^{{\rm corr},[3]}(k_{12})$, can be identified as the relative momentum distribution of two nucleons of which one is part of a correlated pair. The correlated nucleon can have a high-momentum and the two nucleons can have a relative momentum higher than the Fermi momentum, k_F.

There are about A time more terms contributing to $n^{{\rm corr},[3]}(k_{12})$ than terms contributing to $n^{{\rm corr},[2]}(k_{12})$. Consequently, the relative contribution of the three-body terms in Eq. (3.8) increases with increasing number of nucleons A. Figure 3.4 shows that for heavy nuclei and $k_{12} > k_F$, the $n^{[2]}(k_{12})$ is dominated by the three-body contribution. For high momenta — $k_{12} > 2.5$ fm^{-1} for ^{4}He, and $k_{12} > 3$ fm^{-1} for ^{8}Be and heavier nuclei — the two-body contribution dominates. In other words, for high momenta, one probes really small distance scales and the distribution is dominated by correlated pairs. Summarized, the high-momentum tail of the relative two-nucleon momentum distribution is not the relative momentum distribution of correlated nucleon pairs, but mainly the distribution of two nucleons of which one is strongly correlated with a third nucleon.

Figure 3.5 illustrates some stylized features of the two-nucleon momentum distribution emerging from the LCA calculations which apply to all studied nuclei. For $k_{12} \lesssim k_F$, the $n^{[2]}(k_{12})$ distributions are dominated by the IPM contributions. The fat high-momentum tails are induced by the correlations. Although less distinct than in the single-nucleon distribution, one can distinguish two regions: for $1.25 \lesssim k_{12} \lesssim 1.75$ fm^{-1}, the tensor correlations dominate and for $k_{12} > 1.75$ fm^{-1}, the central correlations dominate. An exception is ^{4}He; where the strength of the central and tensor correlations are equal in size.

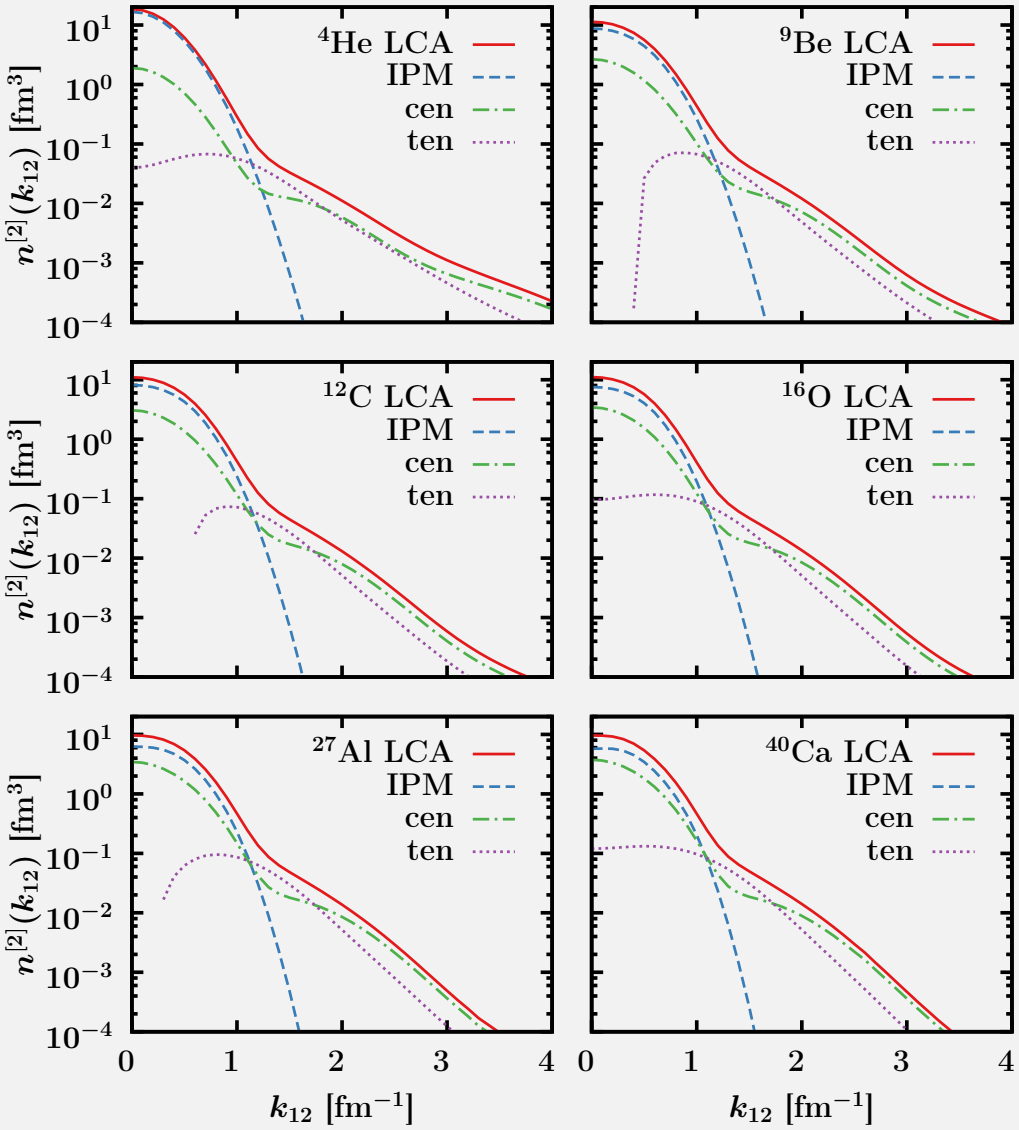

Figure 3.5 – The two-nucleon momentum distribution $n^{[2]}(k_{12})$ for six nuclei. The full line is the LCA result. The dashed line is the IPM contribution to the LCA result. The dashed-dotted (dotted) line only includes the contribution form the central (tensor) correlations. The LCA result includes the central and tensor contribution and their interference.

The spin-isospin structure of SRC is a fundamental quantity because it reflects details of the NN interaction in the medium. It is therefore interesting to investigate the spin-isospin structure in quantities related to SRC, such as the nucleon momentum distributions. The contribution of various ST states to the relative two-nucleon momentum distribution can be achieved with the operator $\hat{n}^{ST}_{k_{12}} = \sum_{i<j} \hat{n}^{[2],ST}_{k_{12}}(i,j)$. The two-body operator $\hat{n}^{[2],ST}_{k_{12}}(i,j)$ is defined as

$$\hat{n}^{[2],ST}_{k_{12}}(i,j) = \mathcal{P}^{\dagger}_{ST}(i,j)\hat{n}^{[2]}_{k_{12}}(i,j)\mathcal{P}_{ST}(i,j), \tag{3.9}$$

where $\mathcal{P}_{ST}(i,j)$ is the projection operator of the total spin and isospin,

$$\mathcal{P}_{ST}(1,2)\,|\alpha\beta\rangle_{\rm nas} = \sum_{A} \delta_{SS_A}\delta_{TT_A} C^{A}_{\alpha\beta}\,|A \equiv n_A(l_A S_A) j_A m_{j_A} N_A L_A M_{L_A} T_A M_{T_A}\rangle\,. \tag{3.10}$$

The correlated ST dependent two-nucleon momentum distribution in the LCA,

$$n^{[2]}_{ST}(k_{12}) = \frac{1}{\mathcal{N}^{[2]}}\,\langle\Phi|\,\hat{n}^{ST,\rm LCA}_{k_{12}}\,|\Phi\rangle\,, \tag{3.11}$$

can be interpreted as the momentum distribution of a nucleon pair with total spin S and total isospin T. The pair is not necessarily correlated. Similar to Eq. (3.8), the correlated part $n^{[2],\rm corr}_{ST}(k_{12})$ of $n^{[2]}_{ST}(k_{12})$ is as sum of two-body and a three-body operators,

$$n^{[2],\rm corr}_{ST}(k_{12}) = n^{\rm corr,[2]}_{ST}(k_{12}) + n^{\rm corr,[3]}_{ST}(k_{12}). \tag{3.12}$$

In the two-body terms the tagged pair, i.e. the pair subjected to $\hat{n}^{[2],ST}_{k_{12}}(i,j)$, is a correlated pair. Hence, the ST quantum numbers of the tagged pair are the quantum numbers of a correlated pair. In the three-body terms, the tagged pair cannot be associated with the quantum numbers of the correlated pair, but the quantum numbers of the two nucleons of which one is correlated by the operator $\hat{l}(i,k)$ or $\hat{l}(j,k)$. The two-body terms and three-body terms are respectively represented by diagrams (b) and (d), and diagrams (c) and (e) in Figure 2.2.

Results are shown in Figure 3.6, where the different ST components are plotted. In the absence of correlations, s-shell nuclei like ^{4}He consist of only $ST = (10)$ and (01) combinations. Nuclei heavier than ^{4}He also contain $ST = (00)$ and (11) combinations. For heavier nuclei, the most numerous nucleon pairs are of the $ST = (11)$ type. In the nuclear matter limit one expects the ratio $1:3:3:9$ for $ST = (00):(10):(01):(11)$.

Introduction of the correlations transmute $ST = (10)$ and (01) pairs into $ST = (00)$ and (11) pairs. This transmutation comes about in the three-body terms of Eq. (3.12) because tensor correlations can flip the spin of a nucleon [7, 8]; e.g. if a pair of nucleons is in a $ST = (01)$ combination, a tensor correlation of one of the nucleons in the pair to a third nucleon can flip the spin of that nucleon and change the pair to $ST = (11)$. The transmutations create the $ST = (00)$ and (11) combinations in ^{4}He. The S-dependence of the tensor correlation seperates the high-momentum tails of the $ST = (01)$ and (10) combinations.

The Argonne and LCA results are quantitatively comparable. A notable difference is the very small $ST = (00)$ contribution of the LCA in ^{4}He. Furthermore, as discussed previously, the strength of the high-momentum tail in ^{12}C is smaller in the LCA calculations than the Argonne calculations. However, the general behavior is similar. For all nuclei, in both the Argonne and the LCA calculations, there is a strong reduction of the $ST = (11)$ combinations for high momenta, $k_{12} > 2$ fm^{-1}.

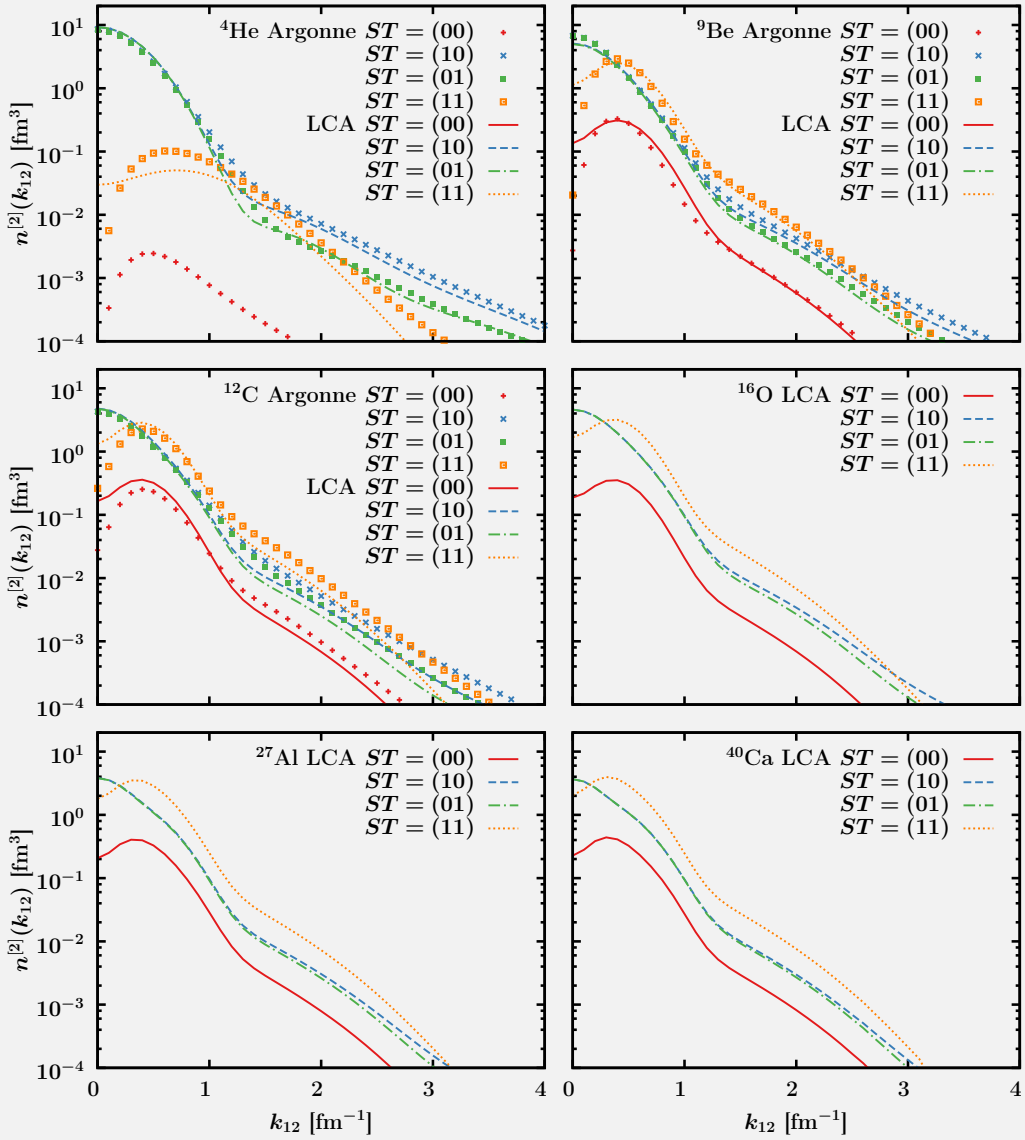

Figure 3.6 – The momentum dependence of the spin-isospin (ST) dependent two-nucleon momentum distribution $n^{[2]}_{ST}(k_{12})$ for ^{4}He, ^{9}Be, ^{12}C, ^{16}O, ^{27}Al and ^{40}Ca. The data points are the QMC results of Ref. [6] with the Argonne v_{18} and Urbana X three-nucleon potential. The $ST = (11)$ contribution for ^{4}He is so small that is falls outside the scales in the figure.

One can determine the effect of the correlation operator on IPM pairs with relative quantum numbers nl in the correlated part of the momentum distribution, $n^{[2],\mathrm{corr}}(k_{12})$ by replacing the correlation operators $\widehat{\mathcal{G}}$ with a projected correlation operator,

$$\widehat{\mathcal{G}}_{nl} = \widehat{\mathcal{S}}\left(\prod_{i<j=1}^{A}\left[1+\hat{l}(i,j)\right]\mathcal{P}_{nl}(i,j)\right) \tag{3.13}$$

where $\mathcal{P}_{nl}$ projects on given relative radial and angular quantum numbers. For the nas two-nucleon state, one has

$$\mathcal{P}_{nl}(1,2)\,|\alpha\beta\rangle_{\mathrm{nas}} = \sum_{A}\delta_{nn_A}\delta_{ll_A}C^{A}_{\alpha\beta}\,|A\equiv n_A(l_AS_A)j_Am_{j_A}N_AL_AM_{L_A}T_AM_{T_A}\rangle\,. \tag{3.14}$$

For the three-nucleon state of Eq. (2.17), the projection operator acting on the first term gives

$$\begin{aligned}\mathcal{P}_{nl}(1,2)\,|\alpha_1\alpha_2\rangle_{\mathrm{nas}}\,|\alpha_3\rangle &= \sum_{A} D^{A}_{(\alpha_1\alpha_2)\alpha_3}\delta_{nn_{12}}\delta_{ll_{12}} \\ &\times\left|A\equiv n_{12}(l_{12}S_{12})j_{12}m_{j_{12}}T_{12}M_{T_{12}}N_{123}L_{123}M_{L_{123}}n_{(12)3}l_{(12)3}m_{l_{(12)3}}m_{s_3}m_{t_3}\right\rangle, \end{aligned}\tag{3.15}$$

where $D^{A}_{(\alpha_1\alpha_2)\alpha_3}$ is a shorthand notation for the transformation coefficient from $|\alpha_1\alpha_2\rangle_{\mathrm{nas}}\,|\alpha_3\rangle$ to $|A\rangle$, discussed in Section 2.1.2.

The correlated part of the relative two-nucleon momentum distribution in the LCA generated with projected correlation operators $\widehat{\mathcal{G}}^{\dagger}_{nl}$ and $\widehat{\mathcal{G}}_{n'l'}$, is denoted by $n^{[2],\mathrm{corr}}_{nl,n'l'}(k_{12})$ and can be obtained after combining Eqs. (2.43), (2.45) and (2.46). Obviously, one has

$$\sum_{nl}\sum_{n'l'} n^{[2],\mathrm{corr}}_{nl,n'l'}(k_{12}) = n^{[2],\mathrm{corr}}(k_{12}). \tag{3.16}$$

The contribution of the different $n^{[2],\mathrm{corr}}_{nl,n'l'}(k_{12})$ are shown in Figure 3.7. The correlation operators acting on the IPM pairs with $nl = 00$ are responsible for the major fraction of the $n^{[2]}(k_{12})$ for $k_{12} > 1.5$ fm^{-1}.

3.6.2 The two-dimensional two-nucleon momentum distribution

The two-dimensional radial two-nucleon momentum distribution $n^{[2]}(k_{12}, P_{12})$ is defined by

$$n^{[2]}(k_{12},P_{12}) = \int d^2\Omega_k \int d^2\Omega_P n^{[2]}(\vec{k}_{12},\vec{P}_{12}). \tag{3.17}$$

The corresponding two-body operator is then

$$\hat{n}_{k_{12},P_{12}} = \int d^2\Omega_k \int d^2\Omega_P \hat{n}_{\vec{k}_{12},\vec{P}_{12}} = \sum_{i<j=1}^{A}\hat{n}^{[2]}_{k_{12},P_{12}}(i,j). \tag{3.18}$$

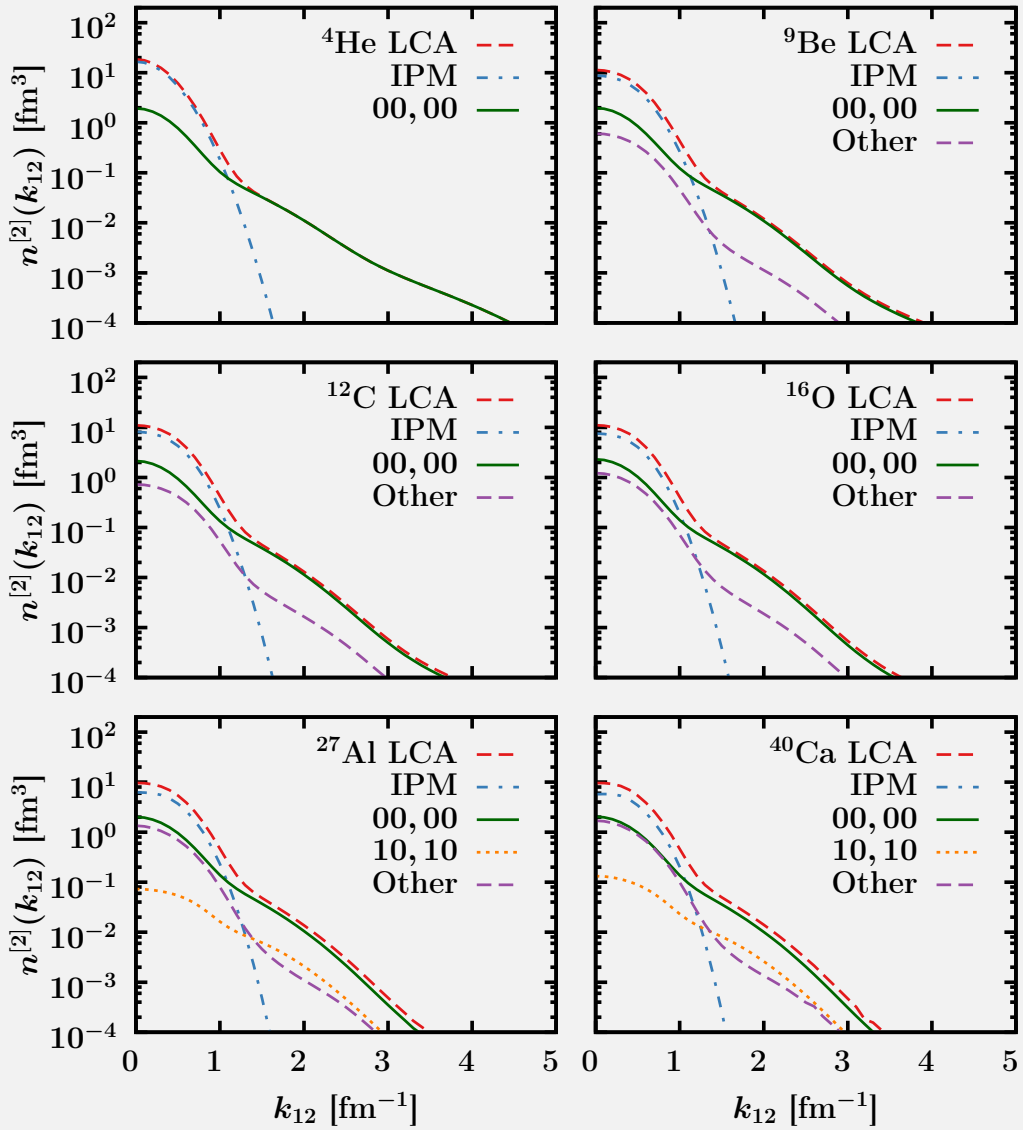

Figure 3.7 – The momentum dependence of the relative two-nucleon momentum distribution $n^{[2]}(k_{12})$ for ^{4}He, ^{9}Be, ^{12}C and ^{16}O. The red dashed line is the full LCA calculations. The blue dashed-dotted line the IPM part. The green line is the $n^{[2],\mathrm{corr}}_{00,00}(k_{12})$ part of the correlated part $n^{[2],\mathrm{corr}}(k_{12})$. The purple dashed line is the sum of all the other $n^{[2],\mathrm{corr}}_{nl,n'l'}(k_{12})$ contributions.

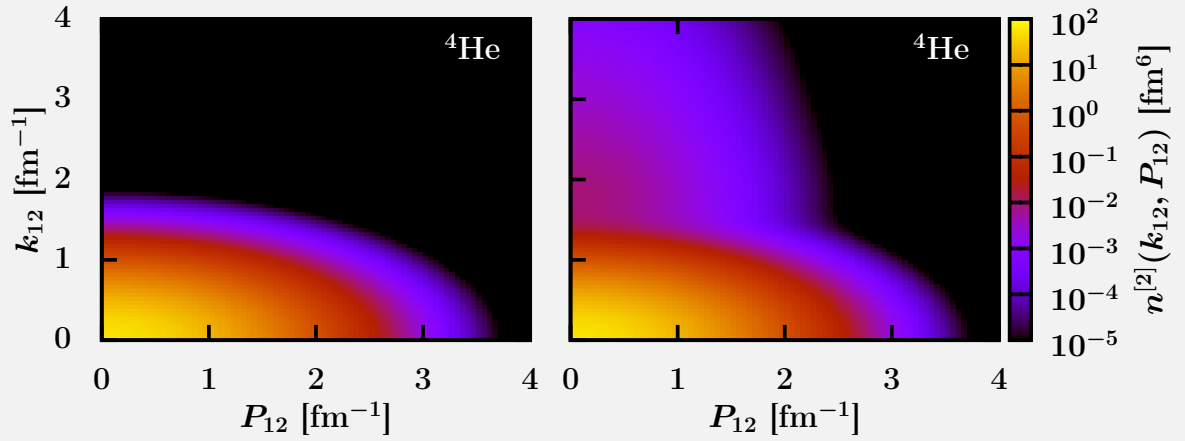

Figure 3.8 – The two-dimensional two-nucleon momentum distribution $n^{[2]}(k_{12}, P_{12})$ for ^{4}He. The left figure is without correlations, the right figure is the LCA. Both figures have the normalization $\int dk_{12}\, k_{12}^2 \int dP_{12}\, P_{12}^2 n^{[2]}(k_{12}, P_{12}) = 1$.

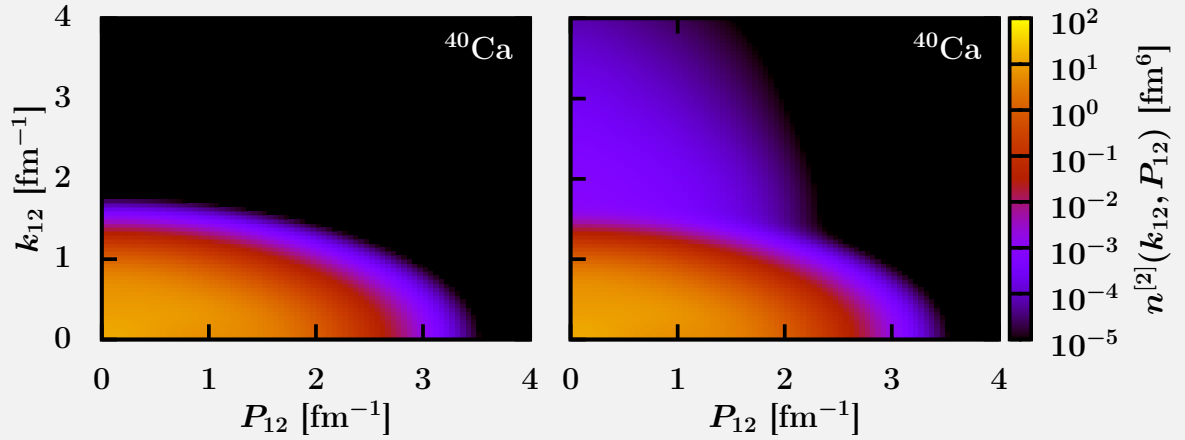

Figure 3.9 – Same as Figure 3.8, but for ^{40}Ca.

In this subsection, the correlated operator $\hat{n}^{\rm corr}_{k_{12},P_{12}}$, defined in Eq. (2.48), is considered to contain only two-body terms,

$$\hat{n}^{\rm corr}_{k_{12},P_{12}} = \sum_{i<j} \hat{n}^{{\rm corr},[2]}_{k_{12},P_{12}}(i,j). \tag{3.19}$$

The expansion of the LCA and the above assumption determine an effective operator $\hat{n}^{\rm eff}_{k_{12},P_{12}}$ from which the correlated relative momentum distribution at relative momentum k_{12} and cm momentum P_{12} can be computed,

$$n^{[2]}(k_{12}, P_{12}) = \frac{1}{\mathcal{N}^{[2]}} \langle \Phi | \, \hat{n}^{\rm eff}_{k_{12},P_{12}} \, | \Phi \rangle \,, \tag{3.20}$$

where $\mathcal{N}^{[2]}$ is the two-body normalization factor, defined in Eq. (2.51).

Figures 3.8 and 3.9 show the $n^{[2]}(k_{12}, P_{12})$ for ^{4}He and ^{40}Ca respectively. It is clearly illustrated how the correlations shift a substantial fraction of the strength to large relative momenta k_{12}. The inclusion of the three-body terms in Eq. (3.19) is expected to shift even more strength to large k_{12}.

3.7 References

[1] M. Vanhalst, W. Cosyn, and J. Ryckebusch, Phys. Rev. C **84**, 031302 (2011).
[2] M. Vanhalst, J. Ryckebusch, and W. Cosyn, Phys. Rev. C **86**, 044619 (2012).
[3] C. Colle, W. Cosyn, J. Ryckebusch, and M. Vanhalst, Phys. Rev. C **89**, 024603 (2014).
[4] M. Vanhalst, W. Cosyn, and J. Ryckebusch, ArXiv e-prints, 1405.3814 (2014).
[5] O. Hen, E. Piasetzky, and L. B. Weinstein, Phys. Rev. C **85**, 047301 (2012).
[6] R. B. Wiringa, R. Schiavilla, S. C. Pieper, and J. Carlson, Phys. Rev. C **89**, 024305 (2014).
[7] H. Feldmeier, W. Horiuchi, T. Neff, and Y. Suzuki, Phys. Rev. C **84**, 054003 (2011).
[8] J. L. Forest, V. R. Pandharipande, S. C. Pieper, et al., Phys. Rev. C **54**, 646 (1996).

CHAPTER 4

Summary and outlook

One of the goals of nuclear physics is providing a complete picture of the structure of nuclei. Mean-field calculations can provide detailed information on the shell structure for a wide range of nuclei. It can provide a natural explanation for many nuclear properties, including the enhanced stability of closed-shell nuclei, the mass evolution of nucleon binding energies, and the spin and parity of odd-mass nuclei.

Mean-field calculations, however, do not capture the impact of correlations on the nuclear structure. These correlations can be classified into two categories. The long-range correlations (LRC) and short-range correlations (SRC). The LRC induce correlations between nucleons at distances of several femtometers, and are connected with the long-range attractive part of the NN interaction. The correction to the mean-field model related to LRC can be physically captured by coupling the single-particle degrees-of-freedom to low-lying collective surface modes and higher-lying giant resonances. The SRC are mainly due to the repulsive core and tensor component of the NN interaction at short distances. The short-range part of the NN interaction leads to strong local fluctuations, and can temporarily excite nucleons from the low-lying shells to higher energies and momenta, where neither the mean-field picture nor models including LRC predict substantial strength. The SRC deplete all single-particle levels and have a significant impact on the nuclear dynamics.

Whereas the existence of SRC was proposed in the early days of nuclear physics, finding direct experimental evidence has been notoriously difficult. In the last two decades of previous century, major breakthroughs have been realized with studies of electroinduced nucleon knockout reactions. In the last decade, major progress has been made in that experimental information about SRC has become more quantitative. Mapping spin, isospin and mass dependence are issues which can be addressed. Ratios of cross sections of inclusive $A(e, e')$ electron scattering reactions show a scaling in the region were NN and 3N SRC are probed. This scaling confirms the suspected universality of the SRC and provides an indication of the relative strength of SRC with mass number A. Resolving the nature and detailed structure of SRC involves nucleon knockout measurements in which two outgoing nucleons are detected

such as exclusive electron scattering $A(e, e'NN)$ reactions. Triple-coincidence measurements where both protons and neutrons are detected reveal a dominance of proton-neutron (pn) pairs over proton-proton (pp) and neutron-neutron (nn) pairs.

Quantifying short-range correlations in nuclei

This dissertation focuses on quantifying the number of SRC in nuclei and on studying their mass and isospin dependence. A method to quantify SRC in an arbitrary nucleus was proposed. Thereby, it was primarily proposed that the short-range correlated part of the nuclear wave function can be generated with correlation operators acting on an IPM (Independent Particle Model) Slater determinant. The SRC-susceptible pairs were identified by selecting those parts of the Slater determinant that provide the largest contribution when subjected to typical nuclear correlation operators. It was argued that IPM NN pairs with vanishing relative orbital momentum and vanishing relative radial quantum numbers, receive the largest corrections from the correlation operators. This can be readily understood by realizing that the IPM two-particle states which are most likely to be correlated at short distances are the states which reflect a substantial likelihood to find a nucleon pair at small internucleon distances. Calculation of the one- and two-nucleon momentum distributions confirmed the dominance of the SRC-susceptible high-momentum tail by correlations operating on mean-field pairs with vanishing relative radial and angular momenta.

Counting the number of nucleon pairs and triples with these quantum numbers provides a method to quantify the NN and 3N SRC. This method is robust in that it is independent of the choices made with regard to the single-particle wave functions. It is applicable to any nucleus from He to Pb and allowed the investigation of the mass dependence, and spin and isospin dependence of the SRC.

The a_2 scaling coefficient obtained in inclusive electron scattering $A(e, e')$ can be interpreted as a measure for the effect of SRC in the target nucleus A relative to the deuteron ^{2}H. However, to connect measured $a_2(A/^2\mathrm{H})$ coefficients to the number of SRC pairs, corrections are in order. Published experimental data include the radiation and Coulomb corrections. On the other hand, the correction factors stemming from final-state interactions and from the center-of-mass motion of the correlated pair are far from established. A Monte Carlo simulation which is able to estimate the A-dependent center-of-mass correction factors, was developed. The simulations are based on general properties of the nucleon momentum distributions. Introducing the correction factors, the model calculations for a_2 were of the right order of magnitude and captured the A-dependence qualitatively. It was found that the relative probability per nucleon for NN and 3N SRC have a soft dependence with mass number A and that the pn NN SRC outnumber the pp (nn) NN SRC. The number of $3N$ SRC was also quantified and a prediction for the measured $a_3(A/^3\mathrm{He})$ was provided. The model predictions for the a_3 are in line with the magnitude extracted from recent measurements. It should be stressed, however, that the current experimental information about a_3 is rather meager. In this comparison, no corrections for cm motion and final state interactions (FSI) effects have been made and it remains to be studied in how far they can blur the connection between inclusive electron-scattering data and the SRC information. A linear relationship between the magnitude of the EMC effect and the calculated number of pn SRC pairs is predicted. This provides additional theoretical support for the role of local nuclear dynamics

on the EMC effect.

A factorized expression for the cross section of the exclusive $A(e, e'pN)$ reactions was derived and the conditions for the factorization were studied. The $A(e, e'pN)$ cross section was shown to be proportional to the conditional center-of-mass momentum distribution for close-proximity pairs in a state with zero relative orbital momentum and zero radial quantum number. The width of this conditional cm momentum distribution is larger than the one corresponding with the full cm momentum distribution. It was shown that the FSI only moderately affect the shape of the factorization function for the $A(e, e'pN)$ cross sections. The proposed factorization predicts a soft mass dependence for the $A(e, e'pN)$ cross section. The robustness of the proposed factorization of the two-nucleon knockout cross sections against kinematic cuts and FSI was examined. Both mechanisms modestly affect the shape of the cm distributions which lead to the conclusion that they can be accessed in $A(e, e'pN)$ measurements. The FSI bring about a controllable mass-dependent reduction of the cross sections.

The low-order correlation operator approximation

SRC typically manifest themselves in the tail parts of the momentum distributions. An approximate flexible method for computing single- and two-nucleon momentum distributions throughout the whole mass table was developed. The low-order correlation operator approximation (LCA) proposed in this work, corrects mean-field models for correlations by shifting the complexity induced by the SRC from the wave functions to the operators. Due to the local character of the SRC, it was argued that the expansion of these operators can be truncated to a low order. In the LCA, both linear terms and quadratic terms in the correlation operator are retained.

After inclusion of the central and tensor correlations, the LCA can generate the SRC-related features of the single- and two-nucleon momentum distribution (like the high-momentum tail). These are dominated by correlation operators acting on mean-field pairs with vanishing relative radial and angular-momentum quantum numbers. The LCA method for single-nucleon momentum distribution explains the dominant role of pn pairs in generating the SRC and provides predictions for the ratio of the amount of correlated pp to pn pairs which are in line with the observations. In the high-momentum tail of the two-nucleon momentum distribution, the LCA distinguishes between the direct contribution of correlated pairs and the contribution of correlations through a third mediator. Consequently, pairs with a high relative momentum often involve the mediation of a third particle. This was illustrated by the spin and isospin dependence of the two-nucleon momentum distribution.

The LCA has also been applied to calculate the effect of SRC on other observables. In the LCA, the SRC have a large impact on the average nucleon kinetic energy. Inclusion of the correlations increases the average kinetic energy by a factor of two to three. It is predicted that in asymmetric nuclei, the SRC are responsible for the fact that the average kinetic energy of the minority nucleons is larger than for the majority nucleons. It is also shown that the SRC have a rather modest A-dependent influence on the nuclear rms radius.

Outlook

In the near future, the data mining initiative at Jefferson Lab [1] will have data available for $A(e, e'pp)$ cross section ratios on several nuclei, giving us access to the mass dependence of this reaction. Our model predicts that the number of correlated pairs over the nuclear mass range has a much softer A-dependence than suggested by naive $\frac{A(A-1)}{2}$ counting. This should also be reflected in the mass dependence of the new $A(e, e'pp)$ data. The derived factorized expression for $A(e, e'pp)$ can be used to study the cross section ratios. In these analysis, one should also account for the effect of final state interactions for the kinematics accessible in the JLab CLAS detector.

For now, the focus has been on electro-induced interactions. Recent results from the ArgoNeuT detector [2] reports the detection of back-to-back proton pairs in charged-current neutrino interactions. These events suggest that mechanisms involving NN SRC pairs in the nucleus are active. In analogy with electron- and hadron-scattering experiments, a neutrino charged-current quasi-elastic interaction on a neutron in a SRC pair is expected to produce back-to-back protons. The realization of consistent models including SRC-related nuclear effects is now being actively pursued, as well as their implementations in Monte Carlo generators (e.g. Refs. [3–5]). In many neutrino experiments, the initial neutrino energy is reconstructed based on the knowledge of the muon energy. It is clear that correlations can introduce a bias [6] and should be considered in the initial neutrino energy reconstruction and the reaction mechanisms.

In this work, the relative two-body momentum distribution $n^{[2]}(k_{12})$ has been computed in the LCA. In computing the two-dimensional distribution $n^{[2]}(k_{12}, P_{12})$, the used cluster expansion is truncated to operators of the two-body type. An extension to operators of the three-body type is feasible. The LCA can also be used to calculate the center-of-mass two-nucleon momentum distributions $n^{[2]}(P_{12})$ and the angular dependent two-nucleon momentum distribution $n^{[2]}(P_{12}, k_{12}, \Theta_{12})$, where Θ_{12} is the angle between the cm and relative momentum. These two-nucleon momentum distributions will reveal more details of the impact of the SRC on nuclear dynamics.

In this work, the central correlation function by Gearheart and the tensor and isospin correlation function of S. Pieper et al. have been used. These correlation functions are model dependent. Whereas there is some agreement between different models concerning the shape of the tensor correlation function, the shape of the central correlation function is far from established. Therefore, the dependence of the momentum distribution on the model for the correlation functions should be considered. Finally, the LCA can also be used to calculate the effect of SRC on other SRC-susceptible observables, like (p, ppN) reactions on unstable nuclei [7].

References

[1] L. Weinstein et al., Short distance structure of nuclei: Mining the wealth of existing jefferson lab data, DOE Grant DE-SC0006801.
[2] R. Acciarri, C. Adams, J. Asaadi, et al., Phys. Rev. D **90**, 012008 (2014).
[3] J. T. Sobczyk, Phys. Rev. C **86**, 015504 (2012).
[4] O. Benhar, A. Lovato, and N. Rocco, ArXiv e-prints, 1312.1210 (2013).

[5] R. Gran, J. Nieves, F. Sanchez, and M. J. V. Vacas, Phys. Rev. D **88**, 113007 (2013).
[6] B. G. Tice, M. Datta, J. Mousseau, et al., Phys. Rev. Lett. **112**, 231801 (2014).
[7] T. Aumann, C. A. Bertulani, and J. Ryckebusch, Phys. Rev. C **88**, 064610 (2013).

APPENDIX A

Moshinsky's transformation brackets

A.1 Moshinsky brackets

Two particles moving in a harmonic oscillator (HO) potential can be described either by using the center-of-well (cw) coordinates $\vec{r}_1$ and $\vec{r}_2$ or the relative and center-of-mass (rcm) coordinates $\vec{r}$ and $\vec{R}$, respectively, which are related to each other by

$$\vec{r} = \frac{1}{\sqrt{2}}(\vec{r}_1 - \vec{r}_2) \qquad \vec{R} = \frac{1}{\sqrt{2}}(\vec{r}_1 + \vec{r}_2) \tag{A.1}$$

and similarly for the momenta

$$\vec{k} = \frac{1}{\sqrt{2}}(\vec{p}_1 - \vec{p}_2) \qquad \vec{P} = \frac{1}{\sqrt{2}}(\vec{p}_1 + \vec{p}_2) \tag{A.2}$$

The Hamiltonian describing the unperturbed motion of two nucleons in a harmonic oscillator is

$$\hat{H} = \frac{1}{2\mu}(\vec{p}_1^{\,2} + \vec{p}_2^{\,2}) + \frac{1}{2}\mu\omega^2(\vec{r}_1^{\,2} + \vec{r}_2^{\,2}) \tag{A.3}$$

$$= \frac{1}{2\mu}(\vec{k}^2 + \vec{P}^2) + \frac{1}{2}\mu\omega^2(\vec{r}^{\,2} + \vec{R}^{\,2}) \tag{A.4}$$

The wave function of the unperturbed motion of the two nucleons is

$$\langle \vec{r}_1 | n_1 l_1 m_1 \rangle \langle \vec{r}_2 | n_2 l_2 m_2 \rangle. \tag{A.5}$$

The form of the Hamiltonian expressed in rcm coordinates is the same, hence, the two-particle wave function can also be written as

$$\langle \vec{r}\,|nlm\rangle \langle \vec{R}\,|NLM\rangle, \tag{A.6}$$

where nlm and NLM describe the quantum numbers of the relative and cm wave function. For the unperturbed two-particle system, the total energy of the system is simply the sum of the one-particle energies. The energy index $\mathcal{E}$ of the two-particle system must be the same in the different coordinates systems due to the conservation of energy:

$$\mathcal{E} = 2n_1 + l_1 + 2n_2 + l_2 = 2n + l + 2N + L. \tag{A.7}$$

The orbital angular momenta of the two subsystems can be coupled to a total angular momentum Λ which must obey the usual coupling conditions

$$|l_1 - l_2| \leq \Lambda \leq l_1 + l_2, \qquad |l - L| \leq \Lambda \leq l + L \tag{A.8}$$

The coupled two-particle states are rotationally invariant, i.e. one-particle states $|n_1 l_1\rangle$ and $|n_2 l_2\rangle$, and $|nl\rangle$ and $|NL\rangle$, are coupled to a well-defined total orbital momentum Λ with projection M_Λ:

$$|n_1 l_1 n_2 l_2; \Lambda M_\Lambda\rangle = \sum_{m_1 m_2} |n_1 l_1 m_1 n_2 l_2 m_2\rangle \langle l_1 m_1 l_2 m_2 | \Lambda M_\Lambda\rangle, \tag{A.9}$$

$$|nlNL; \Lambda M_\Lambda\rangle = \sum_{m_l M_L} |nl m_l NL M_L\rangle \langle l m_l L M_L | \Lambda M_\Lambda\rangle. \tag{A.10}$$

A.1.1 Transformation brackets and coefficients

For any two-body wave function which has the total angular momentum Λ and projection M_Λ, there is a simple (and orthogonal) transformation between the cw and rcm coordinates

$$|n_1 l_1 n_2 l_2; \Lambda M_\Lambda\rangle = \sum_{nl,NL} |nlNL; \Lambda M_\Lambda\rangle \langle nlNL; \Lambda | n_1 l_1 n_2 l_2; \Lambda\rangle, \tag{A.11}$$

where the transformation coefficients $\langle nlNL; \Lambda | n_1 l_1 n_2 l_2; \Lambda\rangle$ are independent of M_Λ and are known in literature as the Moshinsky brackets [1]. Owing to the conservation of energy, moreover, these brackets are zero for all pairs of two-particle states which do not have the same energy index $\mathcal{E}$. In practice, the Moshinsky brackets are calculated recursively, by starting from expressions for $n_1 = n_2 = 0$.

A.1.2 Recursive relations

The transformation brackets $\langle (nl, NL)\Lambda | (n_1 l_1, n_2 l_2)\Lambda\rangle$ between the nuclear two-particle states in the cw and rcm coordinates are generated recursively, starting from an expression for $n_1 = n_2 = 0$ [2],

$$\begin{aligned}\langle (nl, NL)\Lambda | (0l_1, 0l_2)\Lambda\rangle \\ = \Big[\frac{l_1!\, l_2!}{(2l_1)!\,(2l_2)!} \frac{(2l+1)(2L+1)!}{2^{l+L}} \frac{(n+l)!}{n!\,(2n+2l+1)!} \frac{(N+L)!}{N!\,(2N+2L+1)!}\Big] \\ \times (-1)^{n+l+L-\Lambda} \sum_x (2x+1) A(l_1 l, l_2 L, x) W(l L l_1 l_2; \Lambda x),\end{aligned} \tag{A.12}$$

where $W(lLl_1l_2;\Lambda x)$ are the Racah's W coefficients which are related to Wigner's $6j$ symbols

$$W(j_1j_2Jj_3;J_{12}J_{23}) = (-1)^{j_1+j_2+j_3+J}\begin{Bmatrix} j_1 & j_2 & J_{12} \\ j_3 & J & J_{23} \end{Bmatrix}, \tag{A.13}$$

and the coefficient A is given by

$$\begin{aligned} A(l_1l,l_2L,x) = &\Big[\frac{(l_1+l+x+1)!\,(l_1+l-x)!\,(l_1+x-l)!}{(l+x-l_1)!}\Big]^{1/2} \\ &\times\Big[\frac{(l_2+L+x+1)!\,(l_2+L-x)!\,(l_2+x-L)!}{(L+x-l_2)!}\Big]^{1/2}\sum_q(-1)^{\frac{l+q-l_1}{2}} \\ &\times\frac{(l+q-l_1)!}{(\frac{l+q-l_1}{2})!\,(\frac{l+l_1-q}{2})!}\frac{1}{(q-x)!\,(q+x+1)!}\frac{(L+q-l_2)!}{(\frac{L+q-l_2}{2})!\,(\frac{L+l_2-q}{2})!}. \end{aligned} \tag{A.14}$$

The ranges of summation over x and q in the expressions (A.12) and (A.14) are given by the angular momentum coupling rules and the fact that q must not be negative.

From Eq. (A.12) for the case $n_1 = n_2 = 0$, the transformation brackets for arbitrary n_1 and n_2 are obtained with the recursion relations

$$\begin{aligned} \langle nlNL;\Lambda|n_1+1l_1n_2l_2;\Lambda\rangle = &[(n_1+1)(n_1+l_1+\frac{3}{2})]^{-1/2} \\ &\times\sum_{n'l'N'L'}\langle nlNl;\Lambda|-r_1^2\,|n'l'N'L';\Lambda\rangle\,\langle n'l'N'L';\Lambda|n_1l_1n_2l_2;\Lambda\rangle, \end{aligned} \tag{A.15}$$

where all two-particle states involved must belong to the same energy shell: $2n+l+2N+L = 2(n_1+1)+l_1+2n_2+l_2$.

Due to energy conservation and properties of the radial wave functions are the matrix elements of $-r_1^2$ non-zero for just six two-particle states $|n'l'N'L';\Lambda\rangle$. These non-zero matrix elements are given in Table A.1. A similar expression as Eq. (A.15) can be applied if instead of index n_1 the value of n_2 is increased by 1. In this case, the last four expressions of Table A.1 must be taken with a minus sign.

A.1.3 Orthogonality and symmetry relations

There are two orthogonality relations known for the Moshinsky brackets [1]:

$$\sum_{n_1l_2,n_2l_2}\langle nlNL;\Lambda|n_1l_1n_2l_2;\Lambda\rangle\langle n'l'N'L';\Lambda|n_1l_1n_2l_2;\Lambda\rangle = \delta_{nn'}\delta_{ll'}\delta_{NN'}\delta_{LL'}, \tag{A.16}$$

$$\sum_{nl,NL}\langle nlNL;\Lambda|n_1l_1n_2l_2;\Lambda\rangle\langle nlNL;\Lambda|n_1'l_1'n_2'l_2';\Lambda\rangle = \delta_{n_1n_1'}\delta_{l_1l_1'}\delta_{n_2n_2'}\delta_{l_2l_2'}, \tag{A.17}$$

and the following symmetry relations:

$$\langle nlNL;\Lambda|n_1l_1n_2l_2;\Lambda\rangle = (-1)^{L-\Lambda}\langle nlNL;\Lambda|n_2l_2n_1l_1;\Lambda\rangle \tag{A.18}$$

$$= (-1)^{l_1-\Lambda}\langle NLnl;\Lambda|n_1l_1n_2l_2;\Lambda\rangle \tag{A.19}$$

$$= (-1)^{l_1+l}\langle NLnl;\Lambda|n_2l_2n_1l_1;\Lambda\rangle \tag{A.20}$$

$$= (-1)^{l_2+L}\langle n_1l_1n_2l_2;\Lambda|NLnl;\Lambda\rangle \tag{A.21}$$

Table A.1 – The matrix elements of $-r_1^2$ [1].

n'	l'	N'	L'	$\langle nlNl;\Lambda\vert -r_1^2\vert n'l'N'L';\Lambda\rangle$
$n-1$	l	N	L	$\frac{1}{2}[n(n+l+\frac{1}{2})]^{1/2}$
n	l	$N-1$	L	$\frac{1}{2}[N(N+L+\frac{1}{2})]^{1/2}$
$n-1$	$l+1$	$N-1$	$L+1$	$[nN(l+1)(L+1)]^{1/2}(-1)^{\Lambda+L+l}W(l\,l+1\,L\,L+1;1\,\Lambda)$
$n-1$	$l+1$	N	$L-1$	$[n(N+L+\frac{1}{2})(l+1)L]^{1/2}(-1)^{\Lambda+L+l}W(l\,l+1\,L\,L-1;1\,\Lambda)$
n	$l-1$	$N-1$	$L+1$	$[(n+l+\frac{1}{2})Nl(L+1)]^{1/2}(-1)^{\Lambda+L+l}W(l\,l-1\,L\,L+1;1\,\Lambda)$
n	$l-1$	N	$L-1$	$[(n+l+\frac{1}{2})(N+L-\frac{1}{2})lL]^{1/2}(-1)^{\Lambda+L+l}W(l\,l-1\,L\,L-1;1\,\Lambda)$

A.2 Standard transformation brackets

Section A.1 introduces the transformation brackets from two-particle states in terms of coordinates $(\vec{r}_1, \vec{r}_2)$ to those in terms of $(\vec{r}\,, \vec{R}\,)$ related to the first by

$$\begin{pmatrix} \vec{r} \\ \vec{R} \end{pmatrix} = \begin{pmatrix} \frac{1}{\sqrt{2}} & -\frac{1}{\sqrt{2}} \\ \frac{1}{\sqrt{2}} & \frac{1}{\sqrt{2}} \end{pmatrix} \begin{pmatrix} \vec{r}_1 \\ \vec{r}_2 \end{pmatrix} \tag{A.22}$$

This equation shows that in the two-dimensional space of the particle coordinates, we made a rotation by $\pi/4$. This section discusses the transformation brackets when relation between coordinates is given by the general orthogonal matrix

$$\begin{pmatrix} \vec{r} \\ \vec{R} \end{pmatrix} = \begin{pmatrix} \cos\frac{1}{2}\beta & -\sin\frac{1}{2}\beta \\ \sin\frac{1}{2}\beta & \cos\frac{1}{2}\beta \end{pmatrix} \begin{pmatrix} \vec{r}_1 \\ \vec{r}_2 \end{pmatrix}, \tag{A.23}$$

where the angle of rotation is now $\beta/2$.

The transformation bracket for rotations by an angle $\beta/2$ will be designated by

$$\langle nlNL;\Lambda|n_1l_1n_2l_2;\Lambda\rangle_\beta, \tag{A.24}$$

and are generally called the standard transformation brackets (STB). These STB are related to the Moshinsky brackets,

$$\begin{aligned}\langle nlNL;\Lambda|n_1l_1n_2l_2;\Lambda\rangle_\beta = \imath^{2N+L-2n_2-l_2} \sum_{n_1'l_1'n_2'l_2'} \exp[\frac{1}{2}\imath\beta(2n_2'+l_2'-2n_1'-l_1)](-1)^{l_2+L} \\ \times \langle n_1'l_1'n_2'l_2';\Lambda|nlNL;\Lambda\rangle\langle n_1'l_1'n_2'l_2';\Lambda|n_1l_1n_2l_2;\Lambda\rangle. \end{aligned} \tag{A.25}$$

The STB are always real.

A.3 References

[1] M. Moshinsky and Y. Smirnov, *The harmonic oscillator in modern physics* (Harwood Academic Publishers, Amsterdam, 1996).

[2] D. Ursescu, M. Tomaselli, T. Kuehl, and S. Fritzsche, Computer Physics Communications **173**, 140 (2005).

APPENDIX B

Woods-Saxon Potential

B.1 Woods-Saxon Hamiltonian

The Woods-Saxon potential is a mean-field potential between a nucleon and a core. The nucleon and core form a nucleus with mass number $A = Z + N$ containing N neutrons and Z protons. Consequently, the core has $A' = A - 1$ nucleons. In the following, the prime is used to denote quantum numbers of the core. The interaction potential is assumed to be scalar and a sum of different parts; in this case a central, a Coulomb and a spin-orbit part. Woods and Saxon suggested to model the nuclear mean-field, i.e. the nucleon-core interaction, with a spherical symmetric potential that has a Fermi function shape [1],

$$f(r, R, a) = \Big[1 + \exp\Big(\frac{r - R}{a}\Big)\Big]^{-1}, \tag{B.1}$$

where the size R and diffuseness of the surface a are fixed parameters of the same units of length as r. The nuclear central potential is defined as

$$V(r) = -V f(r, R, a), \tag{B.2}$$

where V represents total strength and the minus sign is introduced to represent the attractive nature of the interaction. In addition to the central term of Woods and Saxon, an electromagnetic term, the Coulomb potential, is included to the nuclear proton-core interaction. The following form is adopted for the Coulomb potential $V_C(r)$,

$$V_C(r) = Z' e^2 \begin{cases} (3R^2 - r^2)/(2R^3), & r \leq R_c \\ 1/r, & r > R_c \end{cases}, \tag{B.3}$$

which corresponds to a uniformly charged sphere of radius R_c. The assumption $R_c = R$ has been made, which removes an extra parameter that has little influence on the outcome. The

understanding of the Woods-Saxon potential as a two-body problem (nucleon and core) lead to introduction of a reduced mass μ,

$$\mu = \Big(\frac{1}{m_{n/p}} + \frac{1}{M'}\Big)^{-1}, \tag{B.4}$$

where $m_{n/p}$ is the neutron/proton mass and M' is the mass of the $A-1$ core. Finally, a nuclear spin-orbit contribution is included so that the total effective Hamiltonian is

$$\widehat{H} = -\frac{\hbar^2}{2\mu}\nabla^2 + V(r) + V_C(r) + \frac{1}{2\mu^2 r}\Big(\frac{\partial}{\partial r}\tilde{V}(r)\Big)\vec{l}\cdot\vec{s}. \tag{B.5}$$

The shape of the potential $\tilde{V}(r)$ is also assumed to be a Fermi function,

$$\tilde{V}(r) = \tilde{V} f(r, R_{SO}, a_{SO}), \tag{B.6}$$

where R_{SO} and a_{SO} are the radius and diffuseness parameters of the spin-orbit term.

B.2 Woods-Saxon parametrization

The Hamiltonian of the Woods-Saxon model defined in Eq. (B.5), consists of a central potential defined in Eq. (B.2), a Coulomb potential in Eq. (B.3) and a spin-orbit one defined in Eq. (B.6). Both the central and spin-orbit parts have the Woods-Saxon shape defined in Eq. (B.1). Both of them give 3 parameters: V, R, a and $\tilde{V}$, R_{SO}, a_{SO}. The Coulomb parts has one parameter R_c, but it has little influence on the outcome, so the assumption $R_c = R$ was made. The parameters of the potential change as one goes over the nuclear chart. The dependence of the 7 parameters (the above 6 and the reduced mass μ) on the mass number A defines the structure of parametrization.

It is convenient to parametrize the size of nuclear potentials in terms of the parameters R_0 and $R_{0,SO}$, which are constant over the nuclear chart,

$$R = R_C = R_0 A^{1/3}, \tag{B.7}$$
$$R_{SO} = R_{0,SO} A^{1/3}. \tag{B.8}$$

The surface diffuseness for both the central and spin-orbit potential is assumed to be constant,

$$a = a_{SO} = const. \tag{B.9}$$

The central potential strength depends on the isospin of the nucleon $\vec{t}$ and the core $\vec{T}'$,

$$V = V_0\Big(1 - \frac{4\kappa}{A}\langle\vec{t}\cdot\vec{T}'\rangle\Big). \tag{B.10}$$

For the ground-state of the nucleus, the isospin quantum number is $T = \frac{|N-Z|}{2}$, which together with the relation $\vec{t} + \vec{T}' = \vec{T}$ leads to

$$-4\langle\vec{t}\cdot\vec{T}'\rangle = \begin{cases} 3 & N = Z \\ \pm(N-Z+1)+2 & N > Z \\ \pm(N-Z-1)+2 & N < Z \end{cases}, \tag{B.11}$$

Table B.1 – Woods-Saxon potential parameter set, taken from Ref. [2].

$V_0[MeV]$	κ	$R_0[fm]$	$a = a_{SO}$	λ	$R_{0,SO}[fm]$
52.06	0.639	1.260	0.662	24.1	1.16

where the upper sign is used for the proton and the lower sign for the neutron.

The spin-orbit strength is determined by

$$\tilde{V} = \lambda V_0, \tag{B.12}$$

using a proportionality constant λ which is a constant, making $\tilde{V}$ a constant. The reduced mass μ is given by Eq. (B.4) where the core mass is parametrized as $M' = (A-1)u$.

Thus the Woods-Saxon Hamiltonian for nuclei over the whole nuclear chart can be parametrized by 6 constants V_0, R_0, $R_{0,SO}$, $a = a_{SO}$, λ and κ. The values for these parameters used in this thesis are given in Table B.1.

B.3 References

[1] R. D. Woods and D. S. Saxon, Phys. Rev. **95**, 577 (1954).
[2] N. Schwierz, I. Wiedenhover, and A. Volya, ArXiv e-prints, 0709.3525 (2007).

APPENDIX C

Correlation functions and correlated wave functions

C.1 Correlation functions

As discussed in section 2.2, the correlation operator $\widehat{\mathcal{G}}$ has a complicated structure, but as far as the SRC are concerned, it is dominated by central, tensor and spin-isospin correlations [1],

$$\widehat{\mathcal{G}} \approx \widehat{\mathcal{S}}\Big[\prod_{i<j=1}^{A}\Big(1 - g(r_{ij}) + t(r_{ij})\widehat{S}_{ij}\vec{\tau}_i \cdot \vec{\tau}_j + s(r_{ij})\vec{\sigma}_i \cdot \vec{\sigma}_j \;\; \vec{\tau}_i \cdot \vec{\tau}_j\Big)\Big] , \tag{C.1}$$

where $g(r_{12})$, $t(r_{12})$, $s(r_{12})$ are the central, tensor, and spin-isospin correlation function.

In all of the calculations in this thesis, the central correlation function by Gearheart [2] has been used. This correlation function is shown in Fig. C.1 and heals to zero at $r_{12} \geq 2.5$ fm. It has a hard core at short internucleon distances r_{12}, guaranteeing that the nucleons repel each other strongly when they come close.

For the tensor and spin-isospin correlation functions, the ones by S. Pieper et al. [3] have been used. These are obtained in a variational calculation for the ground state of ^{16}O with the Argonne v_{12} NN potential.

It is worth stressing that the correlation functions are conceived to constitute a general feature of atomic nuclei and that the correlation functions are predicted to exhibit a very small A dependence.

For some calculations the correlation functions are fitted to the function

$$f(r) = \sum_{\lambda=0}^{\lambda_{max}} a_\lambda r^\lambda e^{-br^2} \tag{C.2}$$

Table C.1 – Parameters for the fit of the different correlation function to Eq. (C.2).

	a_0	a_1	a_2	a_3
	a_4	a_5	a_6	a_7
	a_8	a_9	a_{10}	b
g	1.	0.2426	−5.660	125.5
	−791.1	2320.	−3917.	4029.
	−2494.	847.2	−121.8	3.871
t	0.	−0.0143	−0.1400	−0.4110
	−0.1863	2.703	−3.940	2.120
	−0.3311	−0.0541		1.893
s	0.01037	−0.01501	0.4028	−6.268
	38.91	−147.1	309.7	−371.0
	236.6	−64.17		4.926

The parameters for this fit are given in Table C.1. Figures C.1, C.2 and C.3 show respectively the central, tensor and spin-isospin correlation function and their fits.

C.2 Fourier transform of correlated wave functions

The Fourier transformation of the correlated radial HO wave function is defined as

$$\phi^X_{nl,k}(p) = \sqrt{\frac{2}{\pi}} \int dr\; r^2 j_k(pr) f(r) R_{nl}(r) \tag{C.3}$$

where $f(r)$ is the central, tensor or spin-isospin correlation function and $R_{nl}(r)$ the radial HO wave function defined in Eq. (2.3),

$$R_{nl}(r) = \left[\frac{2n!}{\Gamma(n+l+\frac{3}{2})}\nu^{l+3/2}\right]^{1/2} r^l e^{-\frac{\nu r^2}{2}} L_n^{l+\frac{1}{2}}(\nu r^2). \tag{C.4}$$

The generalized Laguerre polynomials $L_n^{l+\frac{1}{2}}(r)$ can be written in a closed form as

$$L_n^{l+\frac{1}{2}}(r) = \sum_{j=0}^{n} (-1)^j \binom{n+l+\frac{1}{2}}{n-j} \frac{r^j}{j!} = \sum_{j=0}^{n} a_{nl,j} r^j. \tag{C.5}$$

Using the fit for the correlation function in Eq. (C.2), Eq. (C.3) becomes

$$\begin{aligned}\phi^X_{nl,k}(p) =& \left[\frac{2n!}{\Gamma(n+l+\frac{3}{2})}\right]^{1/2} \sum_{\lambda=0}^{\lambda_{max}} a_\lambda \sum_{j=0}^{n} a_{nl,j}\, 2^{\frac{1}{2}(2j+l+\lambda-k)} \nu^{-\frac{3}{4}-\frac{\lambda}{2}-\frac{k}{2}} \\ & \times \left(1+2\frac{b}{\nu}\right)^{\frac{1}{2}(-3-2j-l-\lambda-k)} \frac{\Gamma\left[\frac{1}{2}(3+2i+l+\lambda+k)\right]}{\Gamma\left(\frac{3}{2}+k\right)} \\ & \times p^k\, {}_1F_1\left[\frac{1}{2}(3+2i+l+\lambda+k), \frac{3}{2}+k; -\frac{p^2}{2\nu+4b}\right].\end{aligned} \tag{C.6}$$

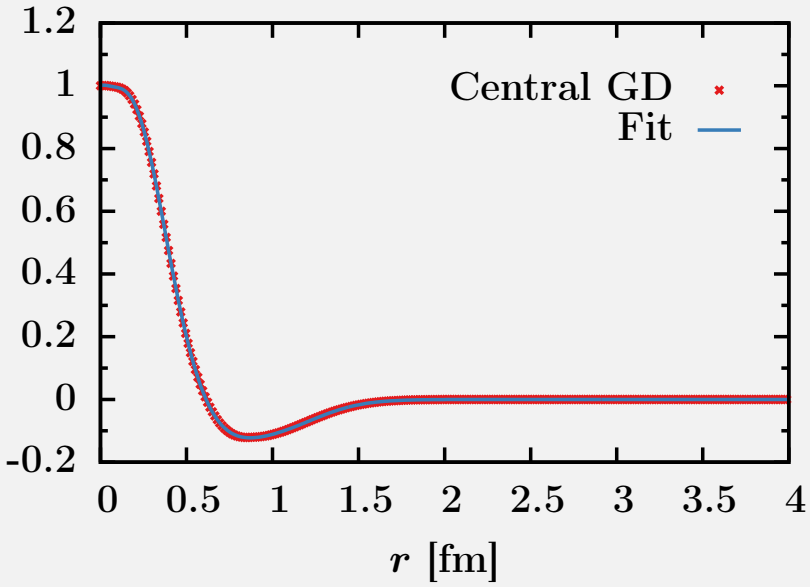

Figure C.1 – Fit of the Gearheart central correlation function $g(r)$ and the fit of Eq. (C.2) with parameters from Table C.1.

The confluent hypergeometric function ${}_1F_1$ is defined as

$$ {}_1F_1(a;b;z) = \sum_{n=0}^{\infty} \frac{a^{(n)} z^n}{b^{(n)} n!} \tag{C.7} $$

where

$$ a^{(0)} = 1, \tag{C.8} $$

$$ a^{(n)} = a(a+1)(a+2)\dots(a+n-1) \tag{C.9} $$

is the rising factorial or Pochhammer function. The uncorrelated radial wave function

$$ \phi_{nl}(p) = \sqrt{\frac{2}{\pi}} \int dr\, r^2 j_l(rp) R_{nl}(R), \tag{C.10} $$

is a special case of $\phi^X_{nl,k}(p)$ with $f(r) \equiv 1$ and $l = k$,

$$ \begin{aligned} \phi_{nl}(p) = &\left[\frac{2n!}{\Gamma(n+l+\frac{3}{2})}\right]^{1/2} \sum_{j=0}^{n} a_{nl,j}\, 2^j \nu^{-\frac{3}{4}-\frac{l}{2}} \frac{\Gamma\left(\frac{3}{2}+i+l\right)}{\Gamma\left(\frac{3}{2}+l\right)} \\ &\times\ p^l\ {}_1F_1\left[\frac{3}{2}+i+l, \frac{3}{2}+l; -\frac{p^2}{2\nu}\right]. \end{aligned} \tag{C.11} $$

C.3 References

[1] R. Roth, T. Neff, and H. Feldmeier, Prog. Part. Nucl. Phys. **65**, 50 (2010).
[2] C. Gearheart, PhD thesis (Washington University, St. Louis, 1994).
[3] S. C. Pieper, R. B. Wiringa, and V. Pandharipande, Phys. Rev. C **46**, 1741 (1992).

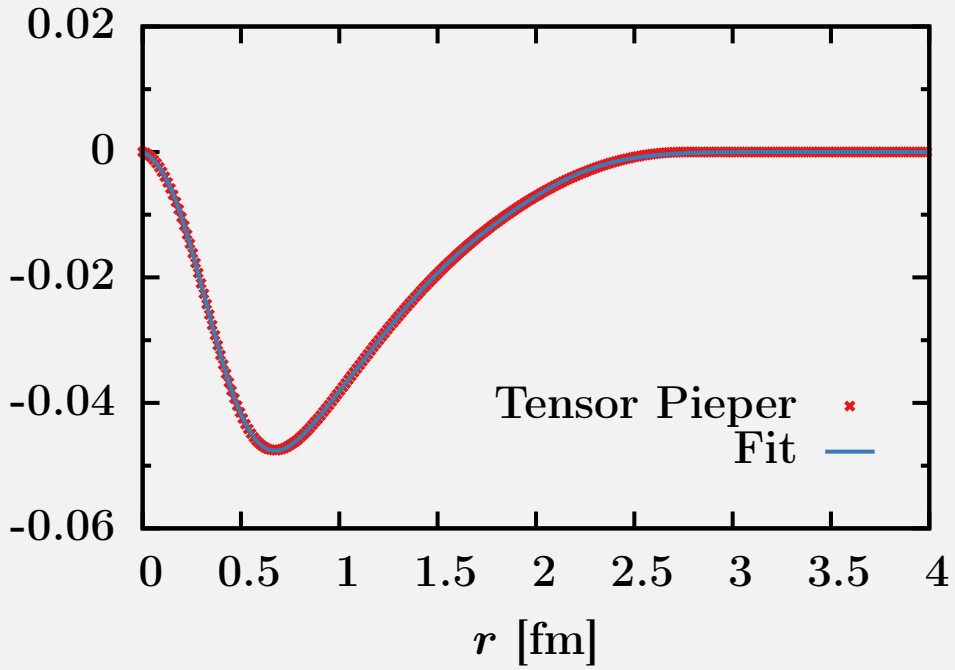

Figure C.2 – Fit of the Pieper et. al. tensor correlation function $t(r)$ and the fit of Eq. (C.2) with parameters from Table C.1.

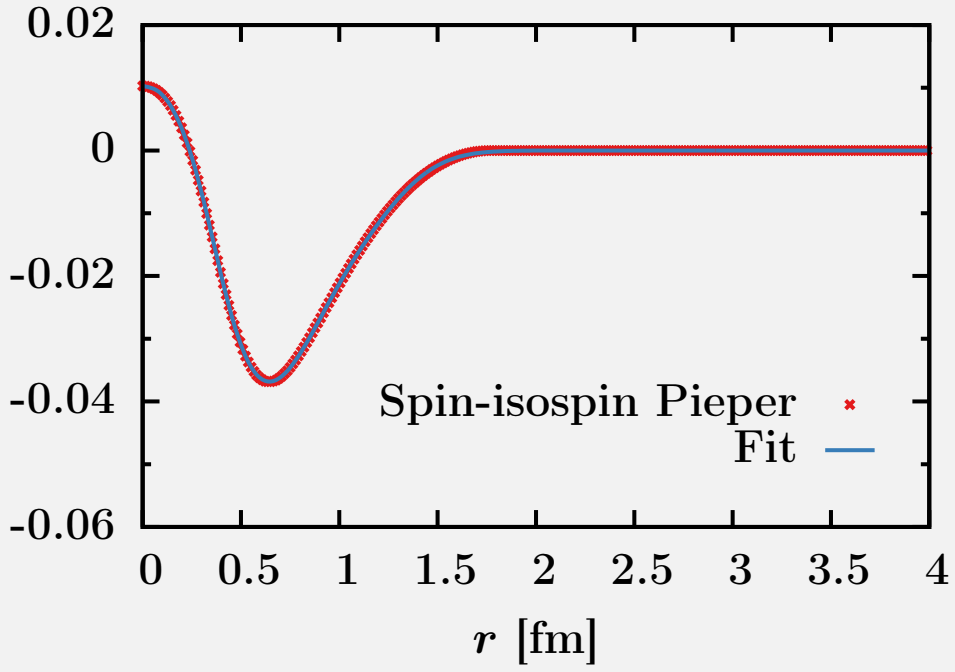

Figure C.3 – Fit of the Pieper et. al. spin-isospin correlation function $s(r)$ and the fit of Eq. (C.2) with parameters from Table C.1.

APPENDIX D

Matrix Elements

In this appendix, more detailed expressions for the matrix elements used in this thesis are derived. It is implicitly assumed that the considered basis is a HO basis.

D.1 Tensor Operator $\hat{S}_{ij}$

The tensor operator is generally defined as

$$\hat{S}_{ij} = \frac{3\vec{\sigma}_i \cdot \vec{r}_{ij}\vec{\sigma}_j \cdot \vec{r}_{ij}}{r_{ij}^2} - \vec{\sigma}_i \cdot \vec{\sigma}_j, \tag{D.1}$$

where $\vec{\sigma}_i$ is the spin operator with

$$\left\langle \frac{1}{2} \middle\| \vec{\sigma} \middle\| \frac{1}{2} \right\rangle = \sqrt{6}. \tag{D.2}$$

The total spin $\vec{S}$ is

$$\vec{S} = \frac{\vec{\sigma}_i + \vec{\sigma}_j}{2}, \tag{D.3}$$

and the tensor operator becomes

$$\hat{S}_{ij} = 2\Big[3\frac{(\vec{S} \cdot \vec{r}_{ij})^2}{r_{ij}^2} - S^2\Big]. \tag{D.4}$$

The product $\vec{S} \cdot \vec{r}_{ij}$ can be written as $S^{(1)} \cdot {r_{ij}}^{(1)}$, where $S^{(1)}$ and ${r_{ij}}^{(1)}$ are spherical tensors of the first order. For the relative distance tensor, one has

$$\frac{{r_{ij}}_m^{(1)}}{r_{ij}} = \sqrt{\frac{4\pi}{3}} Y_m^{(1)}(\Omega_{ij}), \tag{D.5}$$

Table D.1 – Matrix elements of $\langle (l1)jm_j| \hat{S}_{ij} |(l'1)jm_j\rangle$.

	$l' = j-1$	$l' = j$	$l' = j+1$
$l = j-1$	$-\frac{2(j-1)}{2j+1}$	0	$\frac{6\sqrt{j(j+1)}}{2j+1}$
$l = j$	0	2	0
$l = j+1$	$\frac{6\sqrt{j(j+1)}}{2j+1}$	0	$-\frac{2(j+2)}{2j+1}$

where $Y_m^{(1)}(\Omega_{ij}) \equiv Y_{1m}(\Omega_{ij})$ are the spherical harmonics of first order. Thus, the tensor operator can be rewritten as

$$\begin{aligned}\hat{S}_{ij} &= 2\frac{3\pi}{3}\left[3(S^{(1)}\cdot Y^{(1)})^2 - (S^{(1)})^2(Y^{(1)})^2\right] \\ &= \sqrt{\frac{96\pi}{5}}\left[S^{(2)}\cdot Y^{(2)}\right]\end{aligned} \tag{D.6}$$

where $S^{(2)} = [S^{(1)}\otimes S^{(1)}]^{(2)}$ and $Y^{(2)} = \sqrt{\frac{10\pi}{3}}[Y^{(1)}\otimes Y^{(1)}]^{(2)}$.

The matrix elements of the tensor operator are then

$$\begin{aligned}&\langle (lS)jm_j| \sqrt{\frac{96\pi}{5}}\left[S^{(2)}\cdot Y^{(2)}\right] \left|(l'S')j'm'_j\right\rangle \\ &= \sqrt{\frac{96\pi}{5}}\delta_{jj'}\delta_{m_jm'_j}(-1)^{l'+S+J}\begin{Bmatrix} l & l' & 2 \\ S' & S & j\end{Bmatrix}\langle l\|\, Y^{(2)}\,\|l'\rangle\,\langle S\|\, S^{(2)}\,\|S'\rangle\,.\end{aligned} \tag{D.7}$$

The reduced matrix elements are

$$\langle l\|\, Y^{(2)}\,\|l'\rangle = (-1)^l\sqrt{\frac{5(2l+1)(2l'+1)}{4\pi}}\begin{pmatrix} l' & l & 2 \\ 0 & 0 & 0\end{pmatrix}, \tag{D.8}$$

$$\langle S\|\, S^{(2)}\,\|S'\rangle = \delta_{SS'}\delta_{S1}\sqrt{5}. \tag{D.9}$$

So,

$$\begin{aligned}&\langle (lS)jm_j|\, \hat{S}_{ij}\, \left|(l'S')j'm'_j\right\rangle \\ &= (-1)^{S+j}\sqrt{120}\,\hat{l}\hat{l}'\begin{pmatrix} l & l' & 2 \\ 0 & 0 & 0\end{pmatrix}\begin{Bmatrix} l & l' & 2 \\ S' & S & j\end{Bmatrix}\delta_{jj'}\delta_{m_jm'_j}\delta_{SS'}\delta_{S1}.\end{aligned} \tag{D.10}$$

Table D.1 lists all values of Eq. (D.10).

D.2 Norm $\mathcal{N}$

The norm $\mathcal{N}$ is defined as

$$\mathcal{N} \equiv \langle\Phi|\, \widehat{\mathcal{G}}^\dagger\widehat{\mathcal{G}}\,|\Phi\rangle\,. \tag{D.11}$$

The norm in the LCA for a one-body operator $\mathcal{N}^{[1]}$, and for a two-body operator $\mathcal{N}^{[2]}$, are respectively defined in Eq. (2.50) and Eq. (2.51) as

$$\mathcal{N}^{[1]} = 1 + \frac{2}{A}\sum_{\alpha<\beta} \text{nas}\,\langle\alpha\beta|\,\hat{l}(1,2) + \hat{l}^{\dagger}(1,2) + \hat{l}^{\dagger}(1,2)\hat{l}(1,2)\,|\alpha\beta\rangle_{\text{nas}}\,, \tag{D.12}$$

$$\mathcal{N}^{[2]} = 1 + \frac{2(2A-3)}{A(A-1)}\sum_{\alpha<\beta} \text{nas}\,\langle\alpha\beta|\,\hat{l}(1,2) + \hat{l}^{\dagger}(1,2) + \hat{l}^{\dagger}(1,2)\hat{l}(1,2)\,|\alpha\beta\rangle_{\text{nas}}\,, \tag{D.13}$$

After performing transformation from the uncoupled two-particle basis $|\alpha\beta\rangle_{\text{nas}}$ to the relative and c.m. two-particle basis $|n(lS)jm_j\rangle\,|NLM_LTM_T\rangle$, a general matrix element of the norm has the shape

$$\langle n(lS)jm_jNLM_LTM_T|\,[f_1(r)\mathcal{O}^p(1,2)]^{\dagger}\,f_2(r)\mathcal{O}^q(1,2)\,\left|n'(l'S')j'm'_jN'L'M'_LT'M'_T\right\rangle\,, \tag{D.14}$$

where $\mathcal{O}^p(1,2)$ and $\mathcal{O}^q(1,2)$ are the unity operator $\mathbb{1}$ or the central, tensor or spin-isospin operator of Eq. (2.32), and $f_1(r)$ and $f_2(r)$ are 1 or the corresponding central, tensor or spin-isospin correlation function. Using the expansion of the correlation function introduced in Eq. (C.2), a general matrix element reads

$$\langle n(lS)jm_jNLM_LTM_T|\,\mathcal{O}^{p\dagger}(1,2)r^{i+i'}e^{-(b+b')r^2}\mathcal{O}^q(1,2)\,\left|n'(l'S')j'm'_jN'L'M'_LT'M'_T\right\rangle\,. \tag{D.15}$$

Evaluation of the c.m. part gives $\delta_{NN'}\delta_{LL'}\delta_{M_LM'_L}$. The remainder of the matrix element becomes

$$\begin{aligned}\int dr\; R_{nl}(r)r^{i+i'+2}e^{-(b+b')r^2}R_{n'l'}(r)\;&\delta_{SS'}\delta_{jj'}\delta_{m_jm'_j}\delta_{TT'}\delta_{M_TM'_T}\\ &\times\sum_k\langle(lS)jm_jTM_T|\,\mathcal{O}^{p\dagger}(1,2)\,|(kS)jm_jTM_T\rangle\\ &\times\left\langle(kS')j'm'_jT'M'_T\right|\mathcal{O}^q(1,2)\left|(l'S')j'm'_jT'M'_T\right\rangle\,.\end{aligned} \tag{D.16}$$

The Kronecker deltas are general for the considered operators, but the sum over k is operator dependent. The matrix elements of the central and spin-isospin correlation operator are straightforward. The matrix elements of the tensor operator are given in Table D.1. The $R_{nl}(r)$ are the radial wave functions of the spherically-symmetric three-dimension harmonic oscillator of Eq. (2.3),

$$R_{nl}(r) = \Big[\frac{2n!}{\Gamma(n+l+\frac{3}{2})}\nu^{l+3/2}\Big]^{1/2}r^l e^{-\frac{\nu r^2}{2}}L_n^{l+\frac{1}{2}}(\nu r^2). \tag{D.17}$$

A closed form of the generalized Laguerre polynomials $L_n^{l+\frac{1}{2}}(r)$ is

$$L_n^{l+\frac{1}{2}}(r) = \sum_{j=0}^{n}(-1)^j\binom{n+l+\frac{1}{2}}{n-j}\frac{r^j}{j!} = \sum_{j=0}^{n}a_{nl,j}r^j. \tag{D.18}$$

Using Eqs. (D.17) and (D.18), the calculation of the integral in Eq. (D.16) equates to the calculation of integrals of the shape

$$\int dx e^{-x^2}x^N e^{-(B+B')x^2} = \frac{1}{2}(1+B+B')^{-\frac{N+1}{2}}\Gamma(\frac{N+1}{2}), \tag{D.19}$$

where $x \equiv \sqrt{\nu}r$, $B = b/\sqrt{\nu}$, $B' = b'/\sqrt{\nu}$ and $N = i+i'+l+l'+2j+2j'+2$.

D.3 One-nucleon momentum distribution $n^{[1]}(p)$

The one-nucleon momentum distribution $n^{[1]}(p)$ is defined as

$$n^{[1]}(p) = \frac{1}{A}\int \frac{d^2\Omega_p}{(2\pi)^3}\int d^{3A}\{\vec{r}_{1-A}\}d^{3A}\{\vec{r}\,'_{1-A}\} \times \sum_{i=1}^{A} e^{-i\vec{p}\cdot(\vec{r}\,'_i-\vec{r}_i)}\prod_{j\neq i}\delta(\vec{r}_j-\vec{r}\,'_j)\Psi^*(\vec{r}_{1-A})\Psi(\vec{r}\,'_{1-A}), \tag{D.20}$$

where $d^{3A}\{\vec{r}_{1-A}\} = \prod_{i=1}^{i=A} d^3\vec{r}_i$. The corresponding one-body operator, written in the shape of the general operator introduced in Eq. (2.40), is

$$\hat{n}_p = \frac{1}{A}\int \frac{d^2\Omega_p}{(2\pi)^3}\sum_{i=1}^{A} e^{-i\vec{p}\cdot(\vec{r}\,'_i-\vec{r}_i)} = \sum_{i=1}^{A}\hat{n}_p^{[1]}(i), \tag{D.21}$$

This operator and the expansion of Eq. (2.49), determines an effective operator $\hat{n}_p^{\rm LCA}$ from which the correlated one-nucleon momentum distribution at momentum p can be computed,

$$\begin{aligned} n^{[1],\rm LCA}(p) &= \frac{1}{\mathcal{N}^{[1]}}\langle\Phi|\,\hat{n}_p^{[1],\rm LCA}\,|\Phi\rangle \\ &= \frac{1}{\mathcal{N}^{[1]}}\sum_{\alpha}\langle\alpha|\,\hat{n}_p^{[1]}(1)\,|\alpha\rangle + \frac{1}{\mathcal{N}^{[1]}}\sum_{\alpha<\beta}{\rm nas}\,\langle\alpha\beta|\,\Big[\hat{n}_p^{[1],l}(1,2) \\ &\quad + \big[\hat{n}_p^{[1],l}(1,2)\big]^\dagger + \hat{n}_p^{[1],q}(1,2)\Big]\,|\alpha\beta\rangle_{\rm nas}\,. \end{aligned} \tag{D.22}$$

Here $\hat{n}_p^{[1],l}$ and $\hat{n}_p^{[1],q}$ are the linear and quadratic correlation operators defined in Eqs. (2.42) and (2.44), and $\mathcal{N}^{[1]}$ is the one-body normalization factor defined in Eq. (2.50) and discussed in appendix D.2.

The calculation of the uncorrelated matrix elements $\langle\alpha|\,\hat{n}_p^{[1]}(1)\,|\alpha\rangle$ is straightforward. After expanding the vector plane waves in spherical waves,

$$e^{i\vec{p}\cdot\vec{r}} = 4\pi\sum_{l=0}^{\infty} i^l j_l(pr)\sum_{m_l=-l}^{+l} Y^*_{lm_l}(\Omega_p)Y_{lm_l}(\Omega_r), \tag{D.23}$$

the uncorrelated matrix elements become

$$\frac{1}{(2\pi)^3}\langle\alpha|\,d^2\Omega_p e^{i\vec{p}(\vec{r}_1-\vec{r}\,'_1)}\,|\alpha\rangle = |\phi_{n_\alpha l_\alpha}(p)|^2 \tag{D.24}$$

where $\phi_{n_\alpha l_\alpha}$ is the Fourier transform of the uncorrelated radial wave function, defined in Eq. (C.10).

The calculations of the correlated matrix elements are more extensive. After performing transformation from the uncoupled two-particle basis $|\alpha\beta\rangle_{\rm nas}$ to the relative and c.m. two-particle basis $|n(lS)jm_j\rangle\,|NLM_LTM_T\rangle$, a general matrix element has the shape

$$\begin{aligned} n^{[1]}_{AA'}(p) = \langle A\equiv n(lS)jm_jNLM_LTM_T|\,\Big[f_1(r_{12})\widehat{\mathcal{O}}^p(1,2)\Big]^\dagger\,\widehat{n}^{[1]}(1) \\ \times f_2(r'_{12})\widehat{\mathcal{O}}^q(1,2)\,\big|A'\equiv n'(l'S')j'm'_jN'L'M'_LT'M'_T\big\rangle\,, \end{aligned} \tag{D.25}$$

or the shape

$$\langle A| \left[f_1(r_{12}) \widehat{\mathcal{O}}^p(1,2) \right]^\dagger \widehat{n}^{[1]}(2) f_2(r'_{12}) \widehat{\mathcal{O}}^q(1,2) \, |A'\rangle \, . \tag{D.26}$$

Here $\widehat{\mathcal{O}}^p(1,2)$ and $\widehat{\mathcal{O}}^q(1,2)$ are the central, tensor, isospin operator of Eq. (2.32) or the unity operator $\mathbb{1}$, and $f_1(r_{12})$ and $f_2(r'_{12})$ are the corresponding central, tensor, spin-isospin correlation function or 1. For now, only Eq. (D.25) is considered, matrix element like Eq. (D.26) are addressed afterwards. For simplicity, it is also assumed that $\widehat{\mathcal{O}}^p(1,2) = \widehat{\mathcal{O}}^q(1,2) = \mathbb{1}$. The extension to the tensor or spin-isospin correlation operator is straightforward, but complicates the expressions with additional summations.

The one-nucleon momentum distribution $n^{[1]}(\vec{p}_1)$ is related to the two-body momentum distribution $n^{[2]}(\vec{p}_1, \vec{p}_2)$,

$$n^{[1]}(\vec{p}_1) = \int d^3\vec{p}_2 \; n^{[2]}(\vec{p}_1, \vec{p}_2). \tag{D.27}$$

Accordingly, the general matrix element in Eq. (D.25) can be written as

$$\begin{aligned} &\frac{1}{(2\pi)^6} \int d^2\Omega_p \int d^3\vec{p}_2 \int d^3\vec{r}_{12} \int d^3\vec{r}'_{12} \int d^3\vec{R}_{12} \int d^3\vec{R}'_{12} \; e^{i\vec{p}(\vec{r}_1 - \vec{r}'_1)} e^{i\vec{p}_2(\vec{r}_2 - \vec{r}'_2)} \\ &\quad \times \psi^*_{NLM_L}(\vec{R}_{12}) \psi^*_{nlSjm_j}(\vec{r}_{12}) f_1(r_{12}) f_2(r'_{12}) \psi_{N'L'M'_L}(\vec{R}'_{12}) \psi_{n'l'S'j'm'_j}(\vec{r}'_{12}), \end{aligned} \tag{D.28}$$

where $\psi_{NLM_L}(\vec{R})$ are the spherically symmetric three-dimensional HO wave functions defined in Eq. (2.25) and $\psi_{nlSjm_j}(\vec{r})$ the HO wave function coupled with the total spin χ_{SM_S},

$$\psi_{nlSjm_j}(\vec{r}) = \left[\psi_{nl}(\vec{r}) \otimes \chi_S \right]_{jm_j} . \tag{D.29}$$

After substituting

$$\vec{r}_1 - \vec{r}'_1 = \frac{\vec{R}_{12} + \vec{r}_{12} - \vec{R}'_{12} - \vec{r}'_{12}}{\sqrt{2}}, \tag{D.30}$$

$$\vec{r}_2 - \vec{r}'_2 = \frac{\vec{R}_{12} - \vec{r}_{12} - \vec{R}'_{12} + \vec{r}'_{12}}{\sqrt{2}}, \tag{D.31}$$

the integration over $\vec{p}_2$ gives

$$\frac{1}{(2\pi)^3} \int d^3\vec{p}_2 \; e^{i\vec{p}_2(\vec{r}_2 - \vec{r}'_2)} = \sqrt{8} \, \delta^3(\vec{R}_{12} - \vec{r}_{12} - \vec{R}'_{12} + \vec{r}'_{12}). \tag{D.32}$$

The HO wave function $\psi^*_{NLM_L}(\vec{R}_{12})$ can be rewritten as a Fourier transform,

$$\psi^*_{NLM_L}(\vec{R}_{12}) = \int \frac{d^3\vec{P}_{12}}{(2\pi)^{3/2}} e^{-i\vec{P}_{12}\vec{R}_{12}} \phi_{NL}(P_{12}) Y^*_{LM_L}(\Omega_P), \tag{D.33}$$

where ϕ_{NL} are the Fourier transformations of the radial wave functions R_{NL}. After performing the integration over $\vec{R}_{12}$ and $\vec{R}'_{12}$, Eq. (D.28) becomes

$$\begin{aligned} &\frac{1}{(2\pi)^3} \sqrt{8} \int d^2\Omega_p \int d^3\vec{r}_{12} \int d^3\vec{r}'_{12} \; e^{i\sqrt{2}\vec{p}(\vec{r}_{12} - \vec{r}'_{12})} \psi^*_{nlSjm_j}(\vec{r}_{12}) f_1(\vec{r}_{12}) \psi_{n'l'S'j'm_{j'}}(\vec{r}'_{12}) f_2(\vec{r}'_{12}) \\ &\quad \times \int d^3\vec{P}_{12} e^{-i\vec{P}_{12}(\vec{r}_{12} - \vec{r}'_{12})} \phi_{NL}(P_{12}) Y^*_{LM_L}(\Omega_P) \phi_{N'L'}(P_{12}) Y_{L'M_{L'}}(\Omega_P) \end{aligned} \tag{D.34}$$

After expending the vector plane waves in spherical waves (Eq. (D.23)) and applying the following integrals for spherical harmonics

$$\int d^2\Omega\, Y_{lSjm_j}(\Omega)Y_{l_2m_{l_2}}(\Omega)Y_{l_3m_{l_3}}(\Omega) = \sum_{M_Sm_l}(-1)^{m_j+l-S}\frac{\hat{j}\hat{l}\hat{l}_2\hat{l}_3}{\sqrt{4\pi}}\begin{pmatrix} l & S & j \\ m_l & M_S & -m_j\end{pmatrix}\begin{pmatrix} l & l_2 & l_3 \\ 0 & 0 & 0\end{pmatrix}\begin{pmatrix} l & l_2 & l_3 \\ m_l & m_{l_2} & m_{l_3}\end{pmatrix}, \quad \text{(D.35)}$$

and

$$\int d^2\Omega\, Y^*_{l_1m_{l_1}}(\Omega)Y^*_{l_2m_{l_2}}(\Omega)Y_{l'_1m_{l'_1}}(\Omega)Y_{l'_2m_{l'_2}}(\Omega) = \sum_{qm_q}\frac{\hat{l}_1\hat{l}_2\hat{q}}{\sqrt{4\pi}}\begin{pmatrix} l_1 & l_2 & q \\ 0 & 0 & 0\end{pmatrix}\begin{pmatrix} l_1 & l_2 & q \\ m_{l_1} & m_{l_2} & m_q\end{pmatrix}\frac{\hat{l}'_1\hat{l}'_2\hat{q}}{\sqrt{4\pi}}\begin{pmatrix} l'_1 & l'_2 & q \\ 0 & 0 & 0\end{pmatrix}\begin{pmatrix} l'_1 & l'_2 & q \\ m_{l'_1} & m_{l'_2} & m_q\end{pmatrix}, \quad \text{(D.36)}$$

Eq. (D.34) becomes

$$\begin{aligned}
&\frac{2}{\pi}\sqrt{8}\sum_{l_1m_{l_1}}\sum_{km_kk'm_{k'}}(i)^{L_A-L_B+k'-k}(-1)^{m_j+m_{j'}+l+l'} \\
&\times\begin{pmatrix} l & l_1 & k \\ 0 & 0 & 0\end{pmatrix}\begin{pmatrix} l & l_1 & k \\ m_l & m_{l_1} & m_k\end{pmatrix}\begin{pmatrix} l' & l_1 & k' \\ 0 & 0 & 0\end{pmatrix}\begin{pmatrix} l' & l_1 & k' \\ m_{l'} & m_{l_1} & m_{k'}\end{pmatrix} \\
&\times\sum_{qm_q}\begin{pmatrix} L & k' & q \\ 0 & 0 & 0\end{pmatrix}\begin{pmatrix} L & k' & q \\ M_L & m_{k'} & m_q\end{pmatrix}\begin{pmatrix} L' & k & q \\ 0 & 0 & 0\end{pmatrix}\begin{pmatrix} L' & k & q \\ M_{L'} & m_k & m_q\end{pmatrix} \\
&\times\hat{l}_1^2\,\hat{k}^2\,\hat{k}'^2\hat{l}\,\hat{l}'\,\hat{L}\,\hat{L}'\,\hat{j}\,\hat{j}'\int dP_{12}\,P_{12}^2\,\phi_{NL}(P_{12})\phi_{N'L'}(P_{12}) \\
&\times\chi_1(k,l_1,n,l,p,P_{12})\chi_2(k',l_1,n',l',p,P_{12}),
\end{aligned} \quad \text{(D.37)}$$

where

$$\chi_i(k,l_1,n,l,p_1,P_{12}) = \int dr_{12}\,r_{12}^2\,j_k(P_{12}r_{12})j_{l_1}(\sqrt{2}p_1r_{12})f_i(r_{12})R_{nl}(r_{12}). \quad \text{(D.38)}$$

The derivation of an expression for Eq. (D.26) is similar to the derivation of the expression (D.37) for Eq. (D.25), but in Eq. (D.28), one has

$$\int d\vec{p}_2\; e^{i\vec{p}(\vec{r}'_2-\vec{r}_2)}e^{i\vec{p}_2(\vec{r}'_1-\vec{r}_1)} \quad \text{(D.39)}$$

instead of

$$\int d\vec{p}_2\; e^{i\vec{p}(\vec{r}'_1-\vec{r}_1)}e^{i\vec{p}_2(\vec{r}'_2-\vec{r}_2)}. \quad \text{(D.40)}$$

This gives $\delta^3(\vec{R}_{12}+\vec{r}_{12}-\vec{R}'_{12}-\vec{r}'_{12})$ in Eq. (D.32) instead of $\delta^3(\vec{R}_{12}-\vec{r}_{12}-\vec{R}'_{12}+\vec{r}'_{12})$. In the counterpart of Eq. (D.37) this results in a factor $(i)^{k-k'}$ instead of $(i)^{k'-k}$.

D.4 Two-nucleon momentum distribution $n^{[2]}(\vec{k}_{12}, \vec{P}_{12})$

The two-nucleon momentum distribution $n^{[2]}(\vec{k}_{12}, \vec{P}_{12})$ is defined as

$$n^{[2]}(\vec{k}_{12}, \vec{P}_{12}) = \frac{2}{A(A-1)} \frac{1}{(2\pi)^6} \int d^{3A}\{\vec{r}_{1-A}\} d^{3A}\{\vec{r}\,'_{1-A}\} \times \sum_{i<j=1}^{A} e^{-i\vec{k}_{12}\cdot(\vec{r}\,'_{ij}-\vec{r}_{ij})} e^{-i\vec{P}_{12}\cdot(\vec{R}\,'_{ij}-\vec{R}_{ij})} \prod_{k\neq\{i,j\}} \delta^3\left(\vec{r}_k - \vec{r}\,'_k\right) \Psi^*(\vec{r}_{1-A}) \Psi(\vec{r}\,'_{1-A}) \quad \text{(D.41)}$$

The corresponding two-body operator, written in the shape of the general operator introduced in Eq. (2.40), is

$$\begin{aligned} \hat{n}_{\vec{k}_{12},\vec{P}_{12}} &= \frac{2}{A(A-1)} \sum_{i<j=1}^{A} \frac{1}{(2\pi)^3} e^{-i\vec{k}_{12}\cdot(\vec{r}\,'_{ij}-\vec{r}_{ij})} e^{-i\vec{P}_{12}\cdot(\vec{R}\,'_{ij}-\vec{R}_{ij})} \\ &= \sum_{i<j=1}^{A} \hat{n}^{[2]}_{\vec{k}_{12},\vec{P}_{12}}(i,j), \end{aligned} \quad \text{(D.42)}$$

This operator and the expansion of Eq. (2.49), determines an effective operator $\hat{n}^{\mathrm{LCA}}_{\vec{k}_{12},\vec{P}_{12}}$ from which the correlated two-nucleon momentum distribution at relative momentum $\vec{k}_{12}$ and c.m. momentum $\vec{P}_{12}$ can be computed,

$$\begin{aligned} n^{[2],\mathrm{LCA}}(\vec{k}_{12}, \vec{P}_{12}) &= \frac{1}{\mathcal{N}^{[2]}} \langle\Phi|\, \hat{n}^{[2],\mathrm{LCA}}_{\vec{p}} \,|\Phi\rangle \\ &= \frac{1}{\mathcal{N}^{[2]}} \sum_{\alpha<\beta} \mathrm{nas}\, \langle\alpha\beta|\, \hat{n}^{[2]}_{\vec{k}_{12},\vec{P}_{12}}(1,2)\, |\alpha\beta\rangle_{\mathrm{nas}} \\ &\quad + \frac{1}{\mathcal{N}^{[2]}} \sum_{\alpha<\beta} \mathrm{nas}\, \langle\alpha\beta|\, \hat{n}^{\mathrm{corr},[2]}_{\vec{k}_{12},\vec{P}_{12}}(1,2)\, |\alpha\beta\rangle_{\mathrm{nas}} \,. \\ &\quad + \frac{1}{\mathcal{N}^{[3]}} \sum_{\alpha<\beta<\gamma} \mathrm{nas}\, \langle\alpha\beta\gamma|\, \hat{n}^{\mathrm{corr},[3]}_{\vec{k}_{12},\vec{P}_{12}}(1,2,3)\, |\alpha\beta\gamma\rangle_{\mathrm{nas}} \,. \end{aligned} \quad \text{(D.43)}$$

Where $\hat{n}^{[2],\mathrm{corr}}_{\vec{k}_{12},\vec{P}_{12}}$ and $\hat{n}^{[3],\mathrm{corr}}_{\vec{k}_{12},\vec{P}_{12}}$ are the two- and three-body term of the correlated operator defined in Eq. (2.48), and $\mathcal{N}^{[2]}$ is the two-body normalization factor defined in Eq. (2.51) and discussed in appendix D.2.

D.4.1 The radial relative two-nucleon momentum distribution $n^{[2]}(k_{12})$

The radial relative two-nucleon momentum distribution $n^{[2]}(k_{12})$ is defined by

$$n^{[2]}(k_{12}) = \int d^2\Omega_k \int d^3\vec{P}_{12} n^{[2]}(\vec{k}_{12}, \vec{P}_{12}). \quad \text{(D.44)}$$

The corresponding two-body operator is then

$$\hat{n}_{k_{12}} = \int d^2\Omega_k \int d^3\vec{P}_{12} \hat{n}_{\vec{k}_{12},\vec{P}_{12}}. \quad \text{(D.45)}$$

From this operator and Eq. (D.43), the correlated radial relative two-nucleon momentum distribution $n^{[2],\mathrm{LCA}}(k_{12})$ is

$$\begin{aligned} n^{[2],\mathrm{LCA}}(k_{12}) &= \frac{1}{\mathcal{N}^{[2]}} \langle\Phi|\, \hat{n}^{[2],\mathrm{LCA}}_{k_{12}} \,|\Phi\rangle \\ &= \frac{1}{\mathcal{N}^{[2]}} \sum_{\alpha<\beta} \mathrm{nas}\, \langle\alpha\beta|\, \hat{n}^{[2]}_{k_{12}}(1,2)\, |\alpha\beta\rangle_{\mathrm{nas}} \\ &\quad + \frac{1}{\mathcal{N}^{[2]}} \sum_{\alpha<\beta} \mathrm{nas}\, \langle\alpha\beta|\, \hat{n}^{\mathrm{corr},[2]}_{k_{12}}(1,2)\, |\alpha\beta\rangle_{\mathrm{nas}} \,. \\ &\quad + \frac{1}{\mathcal{N}^{[2]}} \sum_{\alpha<\beta<\gamma} \mathrm{nas}\, \langle\alpha\beta\gamma|\, \hat{n}^{\mathrm{corr},[3]}_{k_{12}}(1,2,3)\, |\alpha\beta\gamma\rangle_{\mathrm{nas}} \,. \end{aligned} \tag{D.46}$$

After performing the transformation from the uncoupled two-particle basis $|\alpha\beta\rangle_{\mathrm{nas}}$ to the relative and c.m. two-particle basis $|n(lS)jm_j\rangle\,|NLM_LTM_T\rangle$, a general matrix element of the first term has the shape

$$\begin{aligned} \langle A \equiv n(lS)jm_jNLM_LTM_T|\, \widehat{n}^{[2]}_{k_{12}}(1,2)\, \big|A' \equiv n'(l'S')j'm'_jN'L'M'_LT'M'_T\big\rangle \\ = \delta_{NN'}\delta_{LL'}\delta_{M_LM'_L}\ \delta_{TT'}\delta_{M_TM'_T} \\ \times \delta_{ll'}\delta_{SS'}\delta_{jj'}\delta_{m_jm'_j}\ \phi_{nl}(k_{12})\ \phi_{n'l}(k_{12}), \end{aligned} \tag{D.47}$$

where ϕ_{nl} are the Fourier transformations of the uncorrelated radial HO wave functions, defined in Eq. (C.10). A general matrix element of the second term has the shape

$$\langle A|\, \Big[f_1(r_{12})\widehat{\mathcal{O}}^p(1,2)\Big]^\dagger\, \widehat{n}^{[2]}_{k_{12}}(1,2) f_2(r'_{12})\widehat{\mathcal{O}}^q(1,2)\, |A'\rangle \,, \tag{D.48}$$

where $\widehat{\mathcal{O}}^p(1,2)$ and $\widehat{\mathcal{O}}^q(1,2)$ are the central, tensor, isospin operator of Eq. (2.32) or the unity operator $\mathbb{1}$, and $f_1(r_{12})$ and $f_2(r'_{12})$ are the corresponding central, tensor, spin-isospin correlation function or 1. For now, $\widehat{\mathcal{O}}^p(1,2) = \widehat{\mathcal{O}}^q(1,2) = \mathbb{1}$ is assumed. The extension to more general correlation operators is straightforward, but extends the expressions with additional summations. Accordingly, the matrix element in Eq. (D.48) becomes

$$\delta_{NN'}\delta_{LL'}\delta_{M_LM'_L}\ \delta_{TT'}\delta_{M_TM'_T}\ \delta_{ll'}\delta_{SS'}\delta_{jj'}\delta_{m_jm'_j}\ \phi^{f_1}_{n'l,l}(k_{12})\ \phi^{f_2}_{nl,l}(k_{12}) \tag{D.49}$$

where $\phi^X_{nl,l}$ are the Fourier transformations of the correlated radial HO wave functions, defined in Eq. (C.3).

The calculation of the general matrix element of the third term

$$\mathrm{nas}\, \langle\alpha\beta\gamma|\, \hat{n}^{\mathrm{corr},[3]}_{k_{12}}(1,2,3)\, |\alpha\beta\gamma\rangle_{\mathrm{nas}} \,. \tag{D.50}$$

is less straightforward. In this appendix, only an expression for the terms

$$\begin{aligned} &\mathrm{nas}\, \langle\alpha\beta\gamma|\, f_1(r_{23})\widehat{n}^{[2]}_{k_{12}}(1,2) f_2(r_{23})\, |\alpha\beta\gamma\rangle_{\mathrm{nas}} \\ &\qquad + \mathrm{nas}\, \langle\alpha\beta\gamma|\, f_1(r_{13})\widehat{n}^{[2]}_{k_{12}}(1,2) f_2(r_{13})\, |\alpha\beta\gamma\rangle_{\mathrm{nas}} \end{aligned} \tag{D.51}$$

is derived. The other terms give the same result. First, the first term is Eq. (D.51) is calculated. The second term is considered afterwards. The nas three-body state can be written as

$$|\alpha\beta\gamma\rangle_{\rm nas} = (1-\mathcal{P}_{23})\left(|\alpha\beta\gamma\rangle + |\beta\gamma\alpha\rangle + |\gamma\alpha\beta\rangle\right). \tag{D.52}$$

The correlation functions f_1 and f_2 depend on r_{23}, therefore, the three-body states are preferable described by the same coordinate. Accordingly states are transformed from the centre-of-well particle coordinates $(\vec{r}_1,\vec{r}_2,\vec{r}_3)$ to the internal Jacobi coordinates $(\vec{r}_{23},\vec{r}_{(23)1},\vec{R}_{123})$, defined by

$$\vec{r}_{23} = \frac{1}{\sqrt{2}}(\vec{r}_2-\vec{r}_3), \qquad \vec{R}_{23} = \frac{1}{\sqrt{2}}(\vec{r}_2+\vec{r}_3), \tag{D.53}$$

$$\vec{r}_{(23)1} = \frac{1}{\sqrt{3}}(\vec{R}_{23}-\sqrt{2}\vec{r}_1), \qquad \vec{R}_{123} = \frac{1}{\sqrt{3}}(\sqrt{2}\vec{R}_{23}+\vec{r}_1). \tag{D.54}$$

In section 2.1.3, it is shown how states with the shape

$$(1-\mathcal{P}_{23})\,|\alpha(\vec{r}_1)\beta(\vec{r}_2)\gamma(\vec{r}_3)\rangle\,, \tag{D.55}$$

can be expanded into the states

$$\begin{aligned}|A\rangle \equiv & \left|n_{23}l_{23}S_{23}j_{23}m_{j_{23}}T_{23}M_{T_{23}}(\vec{r}_{23})N_{123}L_{123}M_{L_{123}}(\vec{R}_{123})\right\rangle \\ & \times \left|n_{(23)1}l_{(23)1}m_{l_{(23)1}}(\vec{r}_{(23)1})m_{s_1}t_1\right\rangle, \end{aligned}\tag{D.56}$$

Hence, a general expression for the matrix element under consideration is,

$$\begin{aligned}&\langle A|\, f_1(r_{23})\widehat{n}^{[2]}_{k_{12}}(1,2)f_2(r'_{23})\,|A'\rangle \\ &\quad = \frac{2}{A(A-1)}\frac{1}{(2\pi)^9}\int d^2\Omega_{k_{12}}\, d^3\vec{P}_{12}\, d^3\vec{k}_3\, d^9\{\vec{r}_{1-3}\}\, d^9\{\vec{r}'_{1-3}\} \\ &\qquad \times e^{-i\vec{k}_1(\vec{r}'_1-\vec{r}_1)}e^{-i\vec{k}_2(\vec{r}'_2-\vec{r}_2)}e^{-i\vec{k}_3(\vec{r}'_3-\vec{r}_3)} \\ &\qquad \times f_1(r_{23})\langle A|\vec{r}_{23}\vec{r}_{(23)1}\vec{R}_{123}\rangle\langle\vec{r}'_{23}\vec{r}'_{(23)1}\vec{R}'_{123}|A'\rangle f_2(r'_{23}).\end{aligned}\tag{D.57}$$

The momentum counterparts of the Jacobi coordinates in Eq. (D.53) are

$$\vec{k}_{23} = \frac{1}{\sqrt{2}}(\vec{k}_2-\vec{k}_3), \qquad \vec{K}_{23} = \frac{1}{\sqrt{2}}(\vec{k}_2+\vec{k}_3), \tag{D.58}$$

$$\vec{k}_{(23)1} = \frac{1}{\sqrt{3}}(\vec{K}_{23}-\sqrt{2}\vec{k}_1), \qquad \vec{P}_{123} = \frac{1}{\sqrt{3}}(\sqrt{2}\vec{K}_{23}+\vec{k}_1). \tag{D.59}$$

One can change from integral variables $d^3\vec{P}_{12}d^3\vec{k}_3$ to the variables $d^3\vec{P}_{123}d^3\vec{k}_{(12)3}$. The corresponding Jacobian determinant is one. Accordingly, the matrix element of Eq. (D.57) is in Jacobi coordinates

$$\begin{aligned}&\frac{2}{A(A-1)}\frac{1}{(2\pi)^9}\int d^2\Omega_{k_12}d^3\vec{P}_{123}d^3\vec{k}_{(12)3}d^3\vec{r}_{23}d^3\vec{r}_{(23)1}d^3\vec{R}_{123}d^3\vec{r}'_{23}d^3\vec{r}'_{(23)1}d^3\vec{R}'_{123} \\ &\qquad \times e^{-i\vec{k}_{23}(\vec{r}'_{23}-\vec{r}_{23})}e^{-i\vec{k}_{(23)1}(\vec{r}'_{(23)1}-\vec{r}_{(23)1})}e^{-i\vec{P}_{123}(\vec{R}'_{123}-\vec{R}_{123})} \\ &\qquad \times f_1(r_{23})\langle A|\vec{r}_{23}\vec{r}_{(23)1}\vec{R}_{123}\rangle\langle\vec{r}'_{23}\vec{r}'_{(23)1}\vec{R}'_{123}|A'\rangle f_2(r'_{23}).\end{aligned}\tag{D.60}$$

The vectors $\vec{k}_{(23)1}$ and $\vec{k}_{23}$ can be written in function of $\vec{k}_{(12)3}$ and $\vec{k}_{12}$:

$$\vec{k}_{23} = \frac{\sqrt{3}\vec{k}_{(12)3} - \vec{k}_{12}}{2}\,, \tag{D.61}$$

$$\vec{k}_{(23)1} = \frac{-\vec{k}_{(12)3} - \sqrt{3}\vec{k}_{12}}{2}\,. \tag{D.62}$$

The integrals over $\vec{P}_{123}$ and $k_{(12)3}$ can be readily performed,

$$\frac{1}{(2\pi)^3}\int d^3\vec{P}_{123} e^{-i\vec{P}_{123}\left(\vec{R}'_{123}-\vec{R}_{123}\right)} = \delta\left(\vec{R}_{123} - \vec{R}'_{123}\right)\,, \tag{D.63}$$

$$\frac{1}{(2\pi)^3}\int d^3\vec{k}_{(12)3} e^{-i\frac{\vec{k}_{(12)3}}{2}\left(\sqrt{3}\vec{r}'_{23}-\sqrt{3}\vec{r}_{23}-\vec{r}'_{(23)1}+\vec{r}_{(23)1}\right)} = 8\,\delta\left(\sqrt{3}\vec{r}'_{23} - \sqrt{3}\vec{r}_{23} - \vec{r}'_{(23)1} + \vec{r}_{(23)1}\right)\,. \tag{D.64}$$

The HO wave function $\psi^*_{n'_{(23)1}l'_{(23)1}m'_{l_{(23)1}}}(\vec{r}'_{(23)1})$ can be rewritten as a Fourier transform,

$$\psi^*_{n'_{(23)1}l'_{(23)1}m'_{l_{(23)1}}}(\vec{r}'_{(23)1}) = \int \frac{d^3\vec{k}}{(2\pi)^{3/2}} e^{-i\vec{k}\vec{r}'_{(23)1}} \phi^*_{n'_{(23)1}l'_{(23)1}m'_{l_{(23)1}}}(\vec{k}), \tag{D.65}$$

where $\phi_{nlm_l}(\vec{k})$ is the Fourier transform of $\psi_{nlm_l}(\vec{r})$.

Applying Eqs. (D.63), (D.64) and (D.65), and performing the integrals over $\vec{R}_{123}$, $\vec{R}'_{123}$ and $\vec{r}_{(23)1}$, Eq. (D.60) becomes,

$$\begin{aligned}\frac{8}{(2\pi)^3}\delta_{N_{123}N'_{123}}\delta_{L_{123}L'_{123}}\delta_{M_{L_{123}}M'_{L_{123}}} \int d^2\Omega_{k_{12}} d^3\vec{r}_{23} d^3\vec{r}'_{23} d^3\vec{k}\; e^{i\vec{k}_{12}\left(2\vec{r}'_{23}-2\vec{r}_{23}\right)} e^{-i\sqrt{3}\vec{k}\left(\vec{r}'_{23}-\vec{r}_{23}\right)} \\ \times \phi^*_{n_{(23)1}l_{(23)1}m_{(23)1}}(\vec{k})\phi_{n'_{(23)1}l'_{(23)1}m'_{(23)1}}(\vec{k}) \\ \times f_1(r_{23}) f_2(r'_{23}) \psi^*_{n_{23}l_{23}m_{l_{23}}}(\vec{r}_{23})\psi_{n'_{23}l'_{23}m'_{l_{23}}}(\vec{r}_{23})\end{aligned} \tag{D.66}$$

This expression is similar to the one in Eq. (D.34), and can be further calculated in the same way. The expression for the second term in Eq. (D.51) is similar. First a transformation can be made to Jacobi coordinates $(\vec{r}_{13}, \vec{r}_{(13)2}, \vec{R}_{123})$ and $(\vec{k}_{13}, \vec{k}_{(13)2}, \vec{P}_{123})$. Then, the vectors $\vec{k}_{(13)2}$ and $\vec{k}_{13}$ in function of $\vec{k}_{(12)3}$ and $\vec{k}_{12}$ is

$$\vec{k}_{13} = \frac{\sqrt{3}\vec{k}_{(12)3} + \vec{k}_{12}}{2}\,, \tag{D.67}$$

$$\vec{k}_{(13)2} = \frac{-\vec{k}_{(12)3} + \sqrt{3}\vec{k}_{12}}{2}\,. \tag{D.68}$$

In Eq. (D.66), this results in the factor $e^{-i\vec{k}_{12}\left(2\vec{r}'_{23}-2\vec{r}_{23}\right)}$ instead of $e^{i\vec{k}_{12}\left(2\vec{r}'_{23}-2\vec{r}_{23}\right)}$. The rest of the expression is identical.

D.5 One-nucleon kinetic energy $T^{[1]}$

The one-body kinetic energy operator $\hat{T}^{[1]}$ is in coordinate space defined as

$$\hat{T}^{[1]} = \frac{-\hbar^2}{2M} \sum_{i=0}^{A} \nabla_i^2, \tag{D.69}$$

or equivalently

$$\hat{T}^{[1]} = \frac{1}{2M} \sum_{i=0}^{A} \frac{1}{(2\pi)^3} \int d\vec{p}\, p^2 e^{i\vec{p}(\vec{r}_i - \vec{r}_i')}. \tag{D.70}$$

The kinetic energy of a correlated nucleus in the LCA is

$$\begin{aligned} T^{[1],\mathrm{LCA}} &= \frac{1}{\mathcal{N}^{[1]}} \langle \Phi | \hat{T}^{[1],\mathrm{LCA}} | \Phi \rangle \\ &= \frac{1}{\mathcal{N}^{[1]}} \sum_{\alpha} \langle \alpha | \hat{T}^{[1]}(1) | \alpha \rangle + \frac{1}{\mathcal{N}^{[1]}} \sum_{\alpha<\beta} \mathrm{nas} \langle \alpha\beta | \Big[\hat{T}^{[1],l}(1,2) \\ &\quad + \Big[\hat{T}^{[1],l}(1,2) \Big]^\dagger + \hat{T}^{[1],q}(1,2) \Big] | \alpha\beta \rangle_{\mathrm{nas}} \,. \end{aligned} \tag{D.71}$$

Here $\hat{T}^{[1],l}$ and $\hat{T}^{[1],q}$ are the linear and quadratic correlation operators defined in Eqs. (2.42) and (2.44), and $\mathcal{N}^{[1]}$ is the one-body normalization factor defined in Eq. (2.50) and discussed in appendix D.2. The calculation of the uncorrelated matrix elements is trivial,

$$\frac{1}{(2\pi)^3} \sum_{\alpha} \langle \alpha | \int d\vec{p}\, p^2 e^{i\vec{p}(\vec{r}_1 - \vec{r}_1')} | \alpha \rangle = (2n_\alpha + l_\alpha + \frac{3}{2})\nu, \tag{D.72}$$

The calculation of a general correlated matrix element can be broken down to the calculation of a matrix element of the shape

$$\begin{aligned} &\langle A \equiv n(lS)jm_j NLM_L TM_T | \Big[f_1(r_{12}) \hat{\mathcal{O}}^p(1,2) \Big]^\dagger \Big(\hat{T}^{[1]}(1) + \hat{T}^{[1]}(2) \Big) \\ &\times f_2(r_{12}') \hat{\mathcal{O}}^q(1,2) \, \big| A' \equiv n'(l'S')j'm_j' N'L'M_L'T'M_T' \big\rangle \,, \end{aligned} \tag{D.73}$$

where $\hat{\mathcal{O}}^p(1,2)$ and $\hat{\mathcal{O}}^q(1,2)$ are the central, tensor, isospin operator of Eq. (2.32) or the unity operator $\mathbb{1}$, and $f_1(r_{12})$ and $f_2(r_{12}')$ are the corresponding central, tensor, spin-isospin correlation function or 1. For now, $\hat{\mathcal{O}}^p(1,2) = \hat{\mathcal{O}}^q(1,2) = \mathbb{1}$ is assumed. The extension to more general correlation operators is straightforward, but complicates the expressions with straightforward additional summations.

The operator sum $\hat{T}^{[1]}(1)+\hat{T}^{[2]}(2)$ can be rewritten as

$$\begin{aligned}
&\frac{1}{2M}\frac{1}{(2\pi)^6}\int d\vec{k}_{12}\int d\vec{P}_{12}e^{i\vec{k}_{12}(\vec{r}_{12}-\vec{r}'_{12})}e^{i\vec{P}_{12}(\vec{R}_{12}-\vec{R}'_{12})}(k_{12}^2+P_{12}^2)\\
&=\frac{\hbar}{2M}\frac{4}{\pi^2}\sum_{km_k}\sum_{KM_K}\int dk_{12}\;k_{12}^2\int dP_{12}\;P_{12}^2 j_k(r_{12}k_{12})j_k(r'_{12}k_{12})\\
&\quad\times j_K(R_{12}P_{12})j_K(R'_{12}P_{12})Y_{km_k}(\Omega_{r_{12}})Y^*_{km_k}(\Omega_{r'_{12}})\\
&\quad\times Y_{KM_K}(\Omega_{R_{12}})Y^*_{KM_K}(\Omega_{R'_{12}})(P_{12}^2+k_{12}^2)\\
&=\frac{1}{2M}\frac{2}{\pi}\sum_{km_k}\sum_{KM_K}Y_{km_k}(\Omega_{r_{12}})Y^*_{km_k}(\Omega_{r'_{12}})Y_{KM_K}(\Omega_{R_{12}})Y^*_{KM_K}(\Omega_{R'_{12}})\\
&\quad\times\left(\frac{\delta(R_{12}-R'_{12})}{R_{12}^2}\int dk_{12}k_{12}^4 j_k(r_{12}k_{12})j_k(r'_{12}k_{12})\right.\\
&\qquad\left.+\frac{\delta(r_{12}-r'_{12})}{r_{12}^2}\int dP_{12}P_{12}^4 j_K(R_{12}P_{12})j_K(R'_{12}P_{12})\right).
\end{aligned}\tag{D.74}$$

The matrix element of Eq. (D.73) is then proportional to the integrals

$$\begin{aligned}
&\delta_{NN'}\int dk_{12}\,k_{12}^4\phi^1_{n'l',k}(k_{12})\phi^2_{n'l',k}(k_{12})\\
&+\int dr_{12}\,r_{12}^2R_{nl}(r_{12})R_{n'l'}(r_{12})f_1(r_{12})f_2(r_{12})\\
&\times\int dP_{12}\,P_{12}^4\phi_{NK}(P_{12})\phi_{N'K}(P_{12})
\end{aligned}\tag{D.75}$$

where ϕ_{NK} is the radial momentum distribution defined in Eq. (C.10) and $\phi^X_{nl,k}$ the correlated radial momentum distribution defined in Eq. (C.3). Using the expression of $\phi^X_{nl,k}$, the solution of the first integral is

$$\begin{aligned}
&\frac{1}{2}\left[\frac{2n!}{\Gamma\left(n+l+\frac{3}{2}\right)}\right]^{1/2}\left[\frac{2n!}{\Gamma\left(n+l'+\frac{3}{2}\right)}\right]^{1/2}\sum_{\lambda=0}^{\lambda_{max}}a_\lambda\sum_{\lambda'=0}^{\lambda'_{max}}a'_{\lambda'}\nu^{1-\frac{\lambda}{2}-\frac{\lambda'}{2}}\\
&\times\sum_{j=0}^{n}a_{nl,j}\sum_{j'=0}^{n'}a_{n'l',j'}\left(1+\frac{b}{\nu}+\frac{b'}{\nu}\right)^{-\frac{1}{2}(5+N+N')}\Gamma\left[\frac{1}{2}\left(1+N+N'\right)\right]\\
&\times\left(\left[\frac{1}{2}+\frac{b}{\nu}\right]^2\left[k+k^2-N\left(N+1\right)\right]+\left[\frac{1}{2}+\frac{b'}{\nu}\right]^2\left[k+k^2-N'\left(N'+1\right)\right]\right.\\
&\left.+\left[\frac{1}{2}+\frac{b}{\nu}\right]\left[\frac{1}{2}+\frac{b'}{\nu}\right]\left[3+2k\left(k+1\right)+3N+3N'+2NN'\right]\right),
\end{aligned}\tag{D.76}$$

where $N=2j+l+\lambda$ and $N'=2j'+l'+\lambda'$. The second integral is similar to the integrals considered in section D.2. The third integral is only different from zero for $N=N',N'\pm1$:

$$\int dP_{12}\,P_{12}^4\phi_{NK}(P_{12})\phi_{N'K}(P_{12})=\begin{cases}\sqrt{N'}\sqrt{N+K+\frac{3}{2}}\nu & N=N'-1\\ \left(2N+K+\frac{3}{2}\right)\nu & N=N'\\ \sqrt{N}\sqrt{N'+K+\frac{3}{2}}\nu & N=N'+1\end{cases}.\tag{D.77}$$

APPENDIX E

Numerical Implementation

The results contained in Chapter 3 are obtained with newly developed software. In this Appendix, a review is given of the structure of this software. The computation of the quantities presented in this work boils down to the numerical evaluation of a large amount of matrix elements between HO states. Thereby, one can discriminate three steps. First, for a given nucleus, all nucleon combinations in pairs and triplets are created. Second, a loop is performed over all pairs and triplets, and their matrix elements are calculated. However, numerical integrations are not yet performed. The algorithm keeps track of the necessary integrations. Last, all numerical integrations are performed. For some operators, the integrations are performed for multiple parameters. For example, the one-nucleon momentum distribution is calculated for a range of values for the nucleon momentum p.

Every step in the numerical implementation can be easily split up in multiple threads, which can be divided over multiple processors on a single node. The parallelization is optimized in that sense that a doubling of the number of processors, reduces the computation time with almost a factor of two. Thus far, parallelization over multiple nodes turned out unnecessary and is hence not implemented.

E.1 The nucleus

Figure E.1 gives a diagrammatic overview of the first step of the numerical calculations. A `Nucleon` class contains all the information and parameters of the considered nucleus. It generates all pair combinations $|\alpha_1\alpha_2\rangle_{\text{nas}}$ of Eq. (2.6) for a given nucleus $A(Z,N)$ by creating the corresponding `Pair` object. Every possible combination of nucleon-nucleon pair states is expanded into relative and center-of-mass (rcm) states

$$|\alpha_1(\vec{r}_1)\alpha_2(\vec{r}_2)\rangle_{\text{nas}} = C^A_{\alpha_1\alpha_2} \left| A \equiv n(lS)jm_j(\vec{r}), NLM_L(\vec{R}), TM_T \right\rangle . \tag{E.1}$$

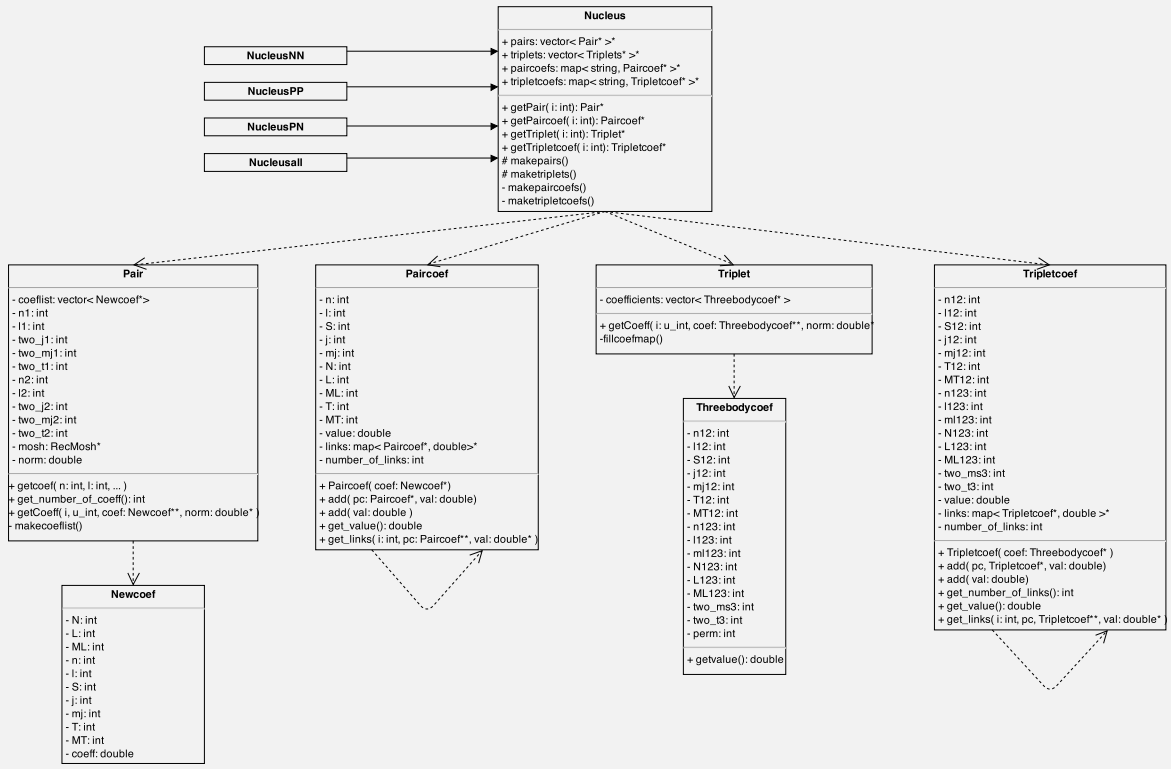

Figure E.1 – Diagrammatic overview of the classes used in the first step of the numerical computations which creates all possible combinations of nucleon pairs and triplets. For sake of readability, only the most important variables and functions are displayed.

These transformations are performed in the `Newcoef` objects. Different pairs can transform to the same rcm state A, but with a different transformation coefficients. The matrix elements between the $|\alpha_1\alpha_2\rangle_{\rm nas}$ will have non-diagonal contributions from the rcm states

$$ {}_{\rm nas}\langle\alpha_1\alpha_2|\,\Omega^{\rm eff}\,|\alpha_1\alpha_2\rangle_{\rm nas} = \sum_A \sum_B {C^A_{\alpha_1\alpha_2}}^{\dagger} C^B_{\alpha_1\alpha_2}\,\langle A|\,\Omega^{\rm eff}\,|B\rangle\,. \tag{E.2} $$

In order to speed up the calculation, the recalculation of the same $\langle A|\,\widehat{\Omega}^{eff}\,|B\rangle$ matrix element is avoided. It is computationally faster to make a set of rcm states and keep track of these non-diagonal elements with other rcm states, than to check at some later stage whether the matrix element already exists. The existence of non-diagonal elements are represented by links in the code. For every rcm state, a `Paircoef` object is generated which keeps track of these links. The value of the transformation coefficients $(C^A_{\alpha_1\alpha_2})^{\dagger}C^B_{\alpha_1\alpha_2}$ is represented by the strength of a link. In calculations involving three-nucleon states, a set of triplet combinations $|\alpha_1\alpha_2\alpha_3\rangle_{\rm nas}$ and their transformation into Jacobi coordinates and quantum numbers are performed according to the procedure outlined above.

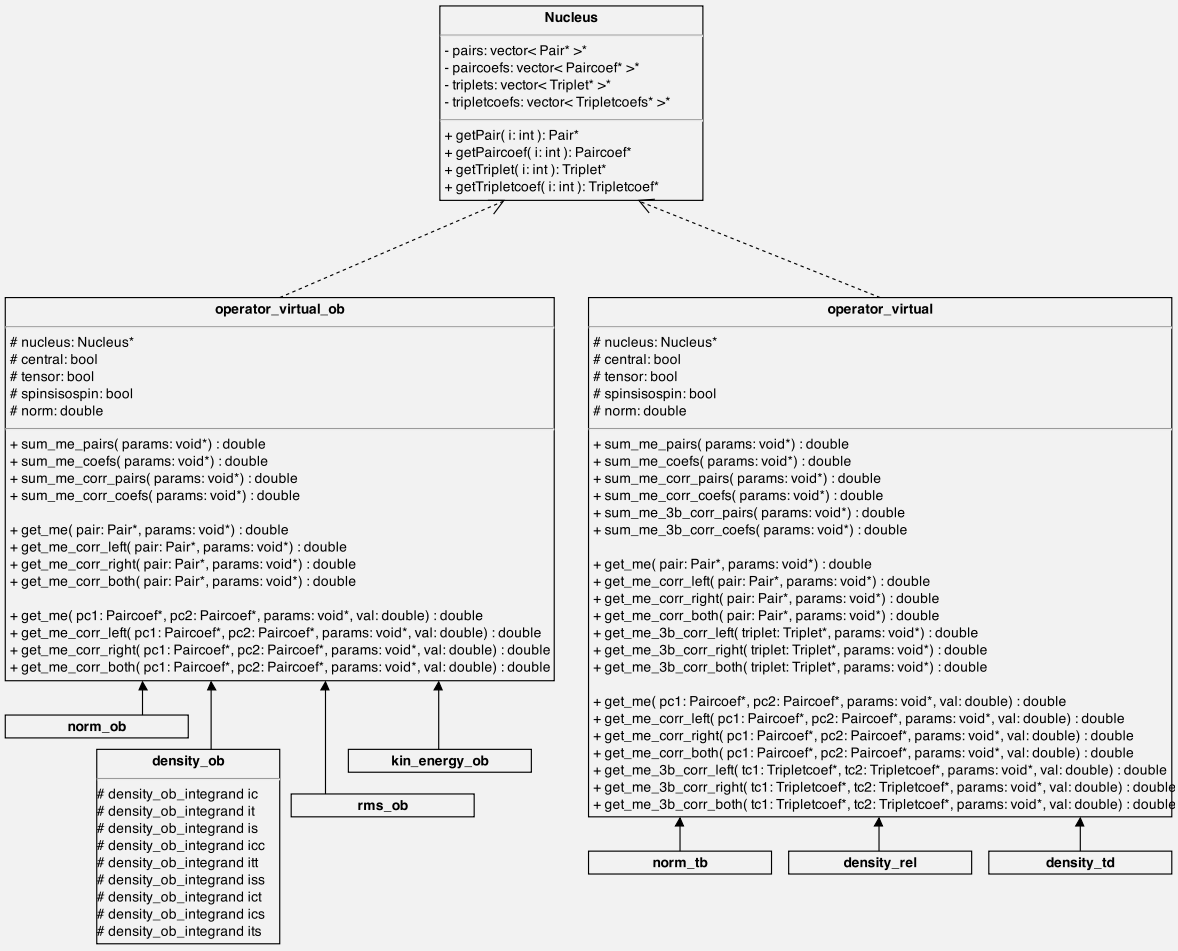

Figure E.2 – Diagrammatic overview of the classes used in the second step of the numerical computations that calculates the matrix elements. For sake of readability, only the most important variables and functions are displayed. For the one-nucleon momentum distribution operator, calculated by class `density_ob`, the member variables that keep track of the required numerical integrals are displayed. For brevity, similar variables in other classes are not shown.

E.2 Matrix elements

Figure E.2 gives a diagrammatic overview of the second step of the numerical procedure. A loop over all `Pair` objects or equivalent over all `Paircoef` objects is performed and every matrix element is calculated. When no numerically intensive operations like numerical integrations are needed, the loop sums the results of the matrix elements. When a numerical intensive operation is necessary, the operator classes keep track of the different operations. For example in the case of the one-nucleon momentum distribution, the `density_ob_integrand` objects keeps track of the integrals of Eq. (D.37). A different `density_ob_integrand` object is needed for every combination of correlation operators. For example object `ict` holds the combination of the central and tensor correlation. These objects also contain the prefactors of the integrals. For the one-nucleon momentum distribution, these are the factors given in Eq. (D.37) and the transformation coefficients $(C^A_{\alpha_1\alpha_2})^\dagger C^B_{\alpha_1\alpha_2}$. This allows the combination of

different matrix elements with the same numerical intensive operation. For every correlation function, their also exists a container which collects all the functions $\chi_i(k, l_1, n, l, p_1, P_{12})$ defined in Eq. (D.38). The function χ_1 is used by different `density_ob_integrand` objects and calculating them only once reduces computation times significantly. A similar method is applied for the relative two-nucleon density and other operators which need numerically intensive operations.

E.3 Numerical integrations

The last step is performing the numerical integrations. The integration themselves are performed using the one-dimensional methods of the GNU Scientific Library [1].

Each integral

$$I = \int_a^b f(x)dx \tag{E.3}$$

provides absolute and relative error bounds (ϵ_{abs}, ϵ_{rel}) which specify the following accuracy requirement,

$$|\text{RESULT} - I| \leq \max(\epsilon_{\text{abs}}, \epsilon_{\text{rel}}|I|), \tag{E.4}$$

where RESULT is the numerical approximation obtained by the algorithm. In case of semi-infinite interval $(a, +\infty)$. The integral is mapped onto the semi-open integral $[0, 1[$ for a variable t, using the transformation $x = a + \frac{1-t}{t}$,

$$\int_a^{+\infty} dx f(x) = \int_0^1 \frac{dt}{t^2} f(a + \frac{1-t}{t}) \tag{E.5}$$

and then integrated. The algorithm attempts to estimate the absolute error ABSERR $=$ $|\text{RESULT} - I|$ in such a way that the following inequality holds,

$$|\text{RESULT} - I| \leq \text{ABSERR} \leq \max(\epsilon_{\text{abs}}, \epsilon_{\text{rel}}|I|). \tag{E.6}$$

In short, the routines return the first approximation which has an absolute error smaller than ϵ_{abs} or a relative error smaller than ϵ_{rel}. Note that this is an either-or constraint, not simultaneous. For all integrals, at least the following accuracy is chosen

$$\epsilon_{\text{abs}} = 10^{-8}, \tag{E.7}$$

$$\epsilon_{\text{rel}} = 10^{-3}. \tag{E.8}$$

Some of this accuracy is lost by saving the χ_i functions separately. Although it is saved on a very fine grid, there is always some inaccuracy in the interpolation between two points.

The computed momentum distributions are normalized as

$$\int dp\, p^2 n^{[1]}(p) = A \tag{E.9}$$

$$\int dp_{12}\, p_{12}^2 n^{[2]}(p_{12}) = \frac{A(A-1)}{2}. \tag{E.10}$$

The preservation of the norm is a stringent test of the accomplished overall accuracy. The obtained error on the norm of the momentum distributions is at most 1%, illustrating the high level of accuracy reached.

E.4 Wigner $3j$-symbols

The calculation of the matrix elements depends heavily on Clebsch-Gordan coefficients, or equivalent Wigner $3j$-symbols. These coefficients are often reused and it is therefore more efficient to store them. An efficient scheme for storing Clebsch-Gordan, Wigner $3j$- and $6j$-symbols is presented in Ref. [2]. Thereby, use is made of the large number of symmetries which these symbols exhibit. The storage scheme has been benchmarked against well-known published programs which usually use recursion relations for the evaluation. It is shown that the storage scheme can be an order of magnitude or more faster in execution speed, maintaining full double precision accuracy.

E.5 References

[1] *GNU Scientific Library*, `http://www.gnu.org/software/gsl/`.
[2] J. Rasch and A. Yu, SIAM Journal on Scientific Computing **25**, 1416 (2004).

List of publications

Journal articles - A1

- J. Ryckebusch, W. Cosyn and M. Vanhalst,
Density dependence of quasifree single-nucleon knockout reactions,
Phys. Rev. C **83**, 054601 (2011).
- M. Vanhalst, W. Cosyn and J. Ryckebusch,
Counting the amount of correlated pairs in a nucleus,
Phys. Rev. C **84**, 031302 (2011).
- M. Vanhalst, J. Ryckebusch and W. Cosyn,
Quantifying short-range correlations in nuclei,
Phys. Rev. C **86**, 044619 (2012).
- C. Colle, W. Cosyn, J. Ryckebusch and M. Vanhalst,
Factorization of exclusive electron-induced two-nucleon knockout,
Phys. Rev. C **89**, 024603 (2014).
- M. Vanhalst, W. Cosyn and J. Ryckebusch,
Stylized features of single-nucleon momentum distributions,
Submitted for publicaten, *ArXiv e-prints*, 1405.3814 (2014).

Conference papers - C1

- M. Vanhalst, J. Ryckebusch and W. Cosyn,
Mass dependence of short-range correlations in nuclei and the EMC effect,
Nuclear Theory Vol. 31, p. 116–124 (2012), arXiv:1210.6175.
- W. Cosyn, M. Vanhalst and J. Ryckebusch,
Mass dependence of short-range correlations in nuclei and the EMC effect,
EPJ Web of Conferences **66**, 02022 (2014).

Nomenclature

3N	three-nucleon
BNL	Brookhaven National Laboratory
cm	center-of-mass
cw	center-of-well
EMC	European Muon Collaboration
FSI	final-state interactions
HF	Hartree-Fock
HO	harmonic oscillator
IPM	independent particle model
JLab	Jefferson Laboratory
LCA	low-order cluster approximation
LRC	long-range correlations
nas	normalized and antisymmetrized
NIKHEF	Nationaal Instituut voor Kernfysica en Hoge-energiefysica
nn	neutron-neutron
NN	nucleon-nucleon
pp	proton-proton
pn	proton-neutron
rcm	relative and center-of-mass
SRC	short-range correlations
STB	standard transformation brackets
WS	Woods-Saxon

Samenvatting

Het beschrijven van de kernstructuur is één van de hoofddoelen van de kernfysica. Gemiddeld-veldberekeningen geven gedetailleerde informatie over de schilstructuur voor een breed gamma van kernen en geven een verklaring voor vele nucleaire eigenschappen: de extra stabiliteit van kernen met een gesloten schilstructuur, de bindingsenergie, en de spin en pariteit van kernen met een oneven massa.

Gemiddeld-veldberekeningen houden echter geen rekening met impact van nucleoncorrelaties op de kernstructuur. Deze correlaties worden in het algemeen ingedeeld in twee categorieën. De langeafstandscorrelaties (LRC) en de korteafstandscorrelaties (SRC). De LRC induceren correlaties over een afstand van verscheidene femtometers en zijn gerelateerd aan het aantrekkend deel van de nucleon-nucleon (NN) interactie. De correcties door LRC op het schilmodel van de kernstructuur kunnen fysisch voorgesteld worden door het koppelen van de één-deeltje vrijheidsgraden tot collectieve oppervlaktemodi en grootschalige resonanties. De SRC zijn afkomstig van de afstotende kern en de tensorcomponent van NN interactie op korte afstand. Het gedrag van de NN interactie op korte afstand leidt tot sterke lokale fluctuaties. Het kan nucleonen exciteren naar hoge energieën en impulsen waar gemiddeld-veldmodellen en modellen met LRC geen substantiële sterkte voorspellen. SRC komen voor op alle één-deeltjes energieniveaus en heeft een aanzienlijke impact op de nucleaire structuur.

In de afgelopen decennia is men geëvolueerd van de zoektocht naar bewijs van SRC tot het bepalen van de sterkte en het onderzoeken van de isospinstructuur. Dit werd mogelijk gemaakt door versnellers met een hoge energie en hoge luminositiet, samen met een beter begrip van de betrokken reactiemechanismes. Verhoudingen van werkzame doorsnedes van inclusieve elektronverstrooiing $A(e, e')$ geeft een schaling in de regio waar NN en drie nucleon (3N) SRC onderzocht worden. Deze schaling bevestigt de universaliteit van de SRC en geeft een indicatie van de relatieve bijdrage van SRC in verschillende kernen. Onderzoeken naar de aard en gedetailleerde structuur van SRC vereist metingen waarbij twee uitgaande nucleonen worden gedetecteerd. Exclusieve elektronenverstrooiing $A(e, e'NN)$ waarbij zowel protonen als neutronen gedetecteerd werden, onthulden een dominantie van proton-neutron (pn) paren over proton-proton (pp) en neutron-neutron (nn) paren.

Het kwantificeren van korte-afstand correlaties in kernen

Dit proefschrift richt zich op het kwantificeren van SRC in kernen en het bestuderen van hun massa- en isospinafhankelijkheid. Er werd een werkwijze voorgesteld om SRC in een willekeurige kern te kwantificeren. Daarbij werd verondersteld dat het SRC-deel van de nucleaire golffunctie kan worden gegenereerd met correlatieoperators die inwerken op een Slaterdeterminant van onafhankelijke nucleonen. De SRC-gevoelige paren worden geïdentificeerd als de delen van de Slaterdeterminant die de grootste bijdrage leveren wanneer onderworpen aan de correlatieoperators. Er werd aangetoond dat de NN paren met een relatief radiaal en relatief angulair kwantumgetal gelijk aan nul het meest gevoelig zijn aan de correlatieoperators. Dit kan gemakkelijk begrepen worden door te beseffen dat de NN toestanden die de meeste kans hebben gecorreleerd te zijn op korte afstand, de toestanden zijn waarbij er een hoge waarschijnlijkheid is om een nucleonpaar op korte onderlinge afstand te vinden. Berekeningen van de één- en twee-nucleonmomentumdistributies bevestigen de dominatie van de SRC-gevoelige hoge-momentumstaart door deze paren.

Tellen van het aantal nucleonparen en -triples met deze kwantumgetallen biedt een methode om het aantal NN en 3N SRC te kwantificeren. Deze werkwijze is robuust, in de betekenis dat het onafhankelijk is van de keuzes van de één-deeltjegolffuncties. Het is toepasbaar voor iedere kern, van He tot Pb, en kan gebruikt worden voor het onderzoeken van de massa-afhankelijkheid en de spin- en isospinafhankelijkheid van de SRC.

De a_2 schalingscoëfficiënt verkregen uit inclusieve elektronverstrooiing $A(e,e')$ kan worden geïnterpreteerd als een maat voor het effect van SRC in kern A ten opzichte van het deuteron ^{2}H. Om de gemeten $a_2(A/^2\mathrm{H})$ coëfficiënten te relateren aan het aantal SRC paren zijn echter correcties nodig. Gepubliceerde experimentele gegevens bevatten stralings- en Coulombcorrecties. De correctiefactoren afkomstig van finaletoestandsinteracties (FSI) en van de beweging van het massacentrum van het gecorreleerde paar, zijn niet bepaald. Er werd een Monte Carlosimulatie gemaakt die de A-afhankelijkheid van de correctiefactoren schat. De simulatie is gebaseerd op algemene eigenschappen van de momentumdistributies van de nucleonen. De berekeningen voor a_2, inclusief de gesimuleerde correctiefactoren, hebben de juiste grootteorde en kunnen kwalitatief de A-afhankelijkheid bepalen. Ook het aantal 3N SRC werd bepaald en de berekeningen voor de $a_3(A/^3\mathrm{He})$ zijn van dezelfde grootteorde als de (schaarse) data. Bij de berekening van de a_3 coëfficient zijn geen correcties voor beweging van het massacentrum en FSI-effecten gemaakt en het blijft onbepaald in hoeverre deze correcties de vergelijking met de data beïnvloeden. De berekende relatieve waarschijnlijkheid per nucleon voor NN en 3N SRC heeft een zwakke A-afhankelijkheid en de pn NN SRC zijn talrijker dan de pp (nn) NN SRC. Een lineair verband tussen de grootte van het EMC effect en het voorspelde aantal pn SRC paren wordt vastgesteld. Dit biedt ondersteuning voor de rol van lokale nucleaire dynamiek op het EMC-effect.

Vervolgens werd een gefactoriseerde uitdrukking voor de werkzame doorsnede van de exclusieve $A(e,e'pN)$ reacties afgeleid en de voorwaarden voor de factorisatie werden bestudeerd. Er werd aangetoond dat de $A(e,e'pN)$ werkzame doorsnede evenredig is met de momentumdistributie van het massamiddelpunt van de nucleonparen in een toestand met relatief radiaal en angulair kwantumgetal nul. De breedte van deze voorwaardelijke momentumdistributie van het massacentrum is groter dan de overeenkomstige distributie van alle nucleonparen. De factorisatie voorspelt een zachte massa-afhankelijkheid van de breedte. Ook de robuustheid

van de factorisatie tegen kinematische randvoorwaarden en FSI werd onderzocht. Beide mechanismen hebben een bescheiden invloed op de vorm van de momentumdistributies van het massacentrum.

De lage-orde clusterbenadering

SRC manifesteren zich in de staart van de momentumdistributies. Daarom is een benaderende, flexibele methode voor het berekenen van één- en twee-nucleonmomentumdistributies voor de volledige massa-tabel ontwikkeld. De lage-orde clusterbenadering (LCA), die in dit werk voorgesteld werd, corrigeert gemiddeld-veldmodellen voor correlaties door het verschuiven van de complexiteit geïnduceerd door de SRC van de golffuncties naar de operators. Vanwege het lokale karakter van de SRC, werd aangetoond dat de expansie van deze operators afgebroken kan worden op een lage orde. De LCA bevat enkel termen lineair en kwadratisch in de correlatieoperators.

Na het in rekening brengen van de centrale en tensor correlaties, genereert de LCA de SRC-gerelateerde kenmerken van de één- en twee-nucleonmomentumdistributies, zoals de hoge-momentumstaarten. Deze worden gedomineerd door correlaties van de gemiddeld-veldparen met relatief radiaal en angulair kwantumgetal nul. De één-nucleonmomentumdistributie verklaart de dominante rol van de pn paren in het genereren van SRC en voorspelt verhoudingen van gecorreleerde pp op pn paren die in overeenstemming zijn met de waarnemingen. In de hoge-momentumstaart van de twee-nucleonmomentumdistributie, maakt de LCA duidelijk onderscheid tussen de directe bijdrage van gecorreleerde paren en de bijdrage van correlaties via een derde mediator. Bijgevolg zijn de eigenschappen van een nucleonpaar met een hoog relatieve momentum niet de eigenschappen van een gecorreleerd nucleonpaar. Dit werd geïllustreerd door de ST-afhankelijke twee-nucleonmomentumdistributies.

De LCA kan ook gebruikt worden voor de berekening van andere observabelen. SRC verhogen de gemiddelde kinetische energie van kernen met een factor twee tot drie en in asymmetrische kernen zijn de correlaties verantwoordelijk voor het feit dat de gemiddelde kinetische energie van de minderheidsnucleon groter is dan die van de meerderheidsnucleonen. Verder werd ook aangetoond dat SRC de nucleaire rms straal $2-7$ % verminderd.

Vooruitzicht

In de nabije toekomst wordt nieuwe data voor de verhouding van $A(e,e'pp)$ werkzame doorsnedes verwacht van het *data mining* initiatief in JLab. De data zal toelaten de massa-afhankelijkheid van de reactie verder te bestuderen. Hierbij kan gebruik gemaakt worden van de afgeleide gefactoriseerde uitdrukking voor de werkzame doorsnede. Maar hierbij zal ook rekening gehouden moeten worden met het effect van FSI.

Tot nu toe lag de focus vooral op elektrongeïnduceerde reacties. Recente geladen quasi-elastische neutrino-verstrooiingsexperimenten raporteren afwijkingen eigen aan nucleoncorrelaties. In vele neutrino-experimenten wordt de initiële energie gereconstrureed op basis van de gedetecteerde muonenergie. Er wordt verwacht dat deze reconstructie gevoelig is aan nucleoncorrelaties.

De LCA kan ook gebruikt worden voor de berekening van andere momentumdistributies zoals de hoekafhankelijke radiële twee-nucleonmomentumdistributie en de momentumdistributie van het massacentrum. Deze distributies zullen kenmerken van SRC bevatten.

De LCA is afhankelijk van een model voor de correlatiefuncties. Daarom kan het interessant zijn de modelafhankelijkheid van de beschouwde distributies te bestuderen. Tot slot kan de LCA ook gebruikt worden voor het berekenen van vele andere SRC-gerelateerde observabelen die ons meer kunnen leren over de impact van SRC op de nucleaire dynamica.